February 2016

K43: Field Development Report

Technical: Storage

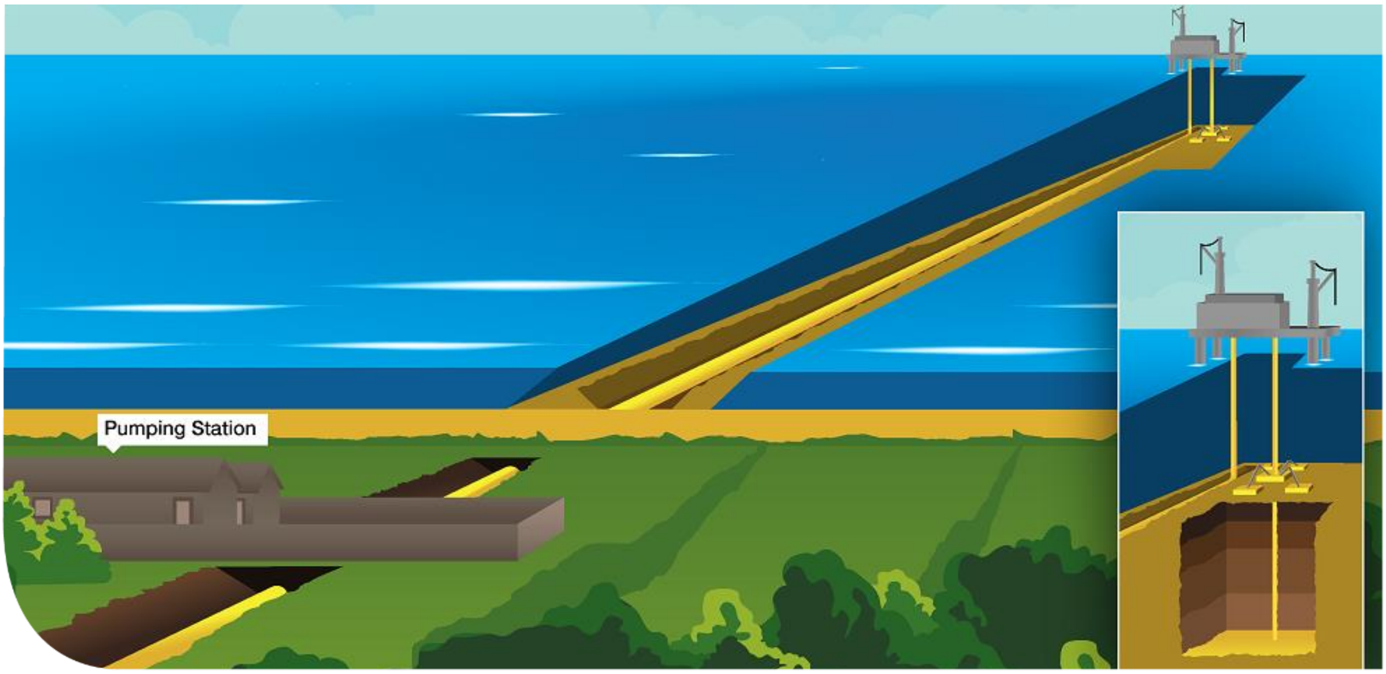

IMPORTANT NOTICE

The information provided further to UK CCS Commercialisation Programme (the Competition) set out herein (the Information) has been prepared by Capture Power Limited and its sub-contractors (the Consortium) solely for the Department of Energy and Climate Change in connection with the Competition. The Information does not amount to advice on CCS technology or any CCS engineering, commercial, financial, regulatory, legal or other solutions on which any reliance should be placed. Accordingly, no member of the Consortium makes (and the UK Government does not make) any representation, warranty or undertaking, express or implied, as to the accuracy, adequacy or completeness of any of the Information and no reliance may be placed on the Information. In so far as permitted by law, no member of the Consortium or any company in the same group as any member of the Consortium or their respective officers, employees or agents accepts (and the UK Government does not accept) any responsibility or liability of any kind, whether for negligence or any other reason, for any damage or loss arising from any use of or any reliance placed on the Information or any subsequent communication of the Information. Each person to whom the Information is made available must make their own independent assessment of the Information after making such investigation and taking professional technical, engineering, commercial, regulatory, financial, legal or other advice, as they deem necessary.

Contents

Key Words

Key Word	Meaning or Explanation
Well	Subsea, this is a penetration of the seabed, using specialised drilling techniques, to penetrate impervious rock formations into other rock structures such as sandstone which hold fluids such as natural gas, oil and brine.
Storage	Deposition of the CO_2 in the reservoir.
Reservoir	The subsurface rock formation into which the CO_2 would be deposited.
Subsurface	Below the seabed.

Executive Summary

This report is one of a series of reports; these "key knowledge" reports are issued here as public information. These reports were generated as part of the Front End Engineering Design Contract agreed with the Department of Energy and Climate Change (DECC) as part of the White Rose Project.

The White Rose CCS Project plans to develop an integrated power and carbon capture and storage demonstration project with a gross output of 448MW of electricity where over 90% of the plant's carbon dioxide (CO_2) emissions up to 2.68MTPA for a period of twenty years will be transported through a dedicated pipeline offshore for permanent underground storage in the UK Sector of the North Sea, specifically the Endurance Structure located in blocks 42/25 and 43/21.

Delivery of the full-chain project is be provided by National Grid Carbon Limited (NGCL), which is responsible for the T&S network and Capture Power Limited (CPL), which is responsible for the Oxy Power Plant (OPP) and the Gas Processing Unit (GPU).

The Endurance structure is a four-way dip-closure within the Bunter Sandstone Formation of the Southern North Sea. It is a saline formation, approximately 22km long, 7km wide and over 200m thick. The crest of the reservoir is located at a depth of approximately 1020m below the sea bed. Reservoir datum pressure and temperature (at 1300mTVDSS) were determined as 140.0bar and 55.9°C, respectively. A layer of mudstone called the Röt Clay provides the primary seal. This in turn is overlain by more than 90m of a salt layer known as the Röt Halite at the base of the 900m thick Haisborough Group which provide the secondary sealing capability. None of the overburden faults visible on seismic penetrate the Röt Halite.

The proposed oxyfuel power plant (OPP) will be connected by a short 12" diameter 150barg MAOP pipeline to a junction manifold, the Camblesforth Multi-Junction, which is provided to allow easy connection of other regional CO_2 emitters. From the Multi-Junction a 60km 24" diameter 150barg MAOP pipeline buried to at least 1.2 m will be connected to the Barmston booster pumping station situated close to the proposed beach crossing. A 90km 24" diameter 200barg MAOP pipeline will be laid offshore to the platform location in Block 42/25d. The pipeline from Camblesforth to the platform will have a capacity of up to 17MTPA of CO_2 to allow for future expansion.

The normally unmanned installation (NUI) platform is designed to have six well slots, filters for the injected CO_2, flow meters for well allocation measurement, provision for temporary equipment for well maintenance as well as providing control and measurement interfaces.

The injection wells, to be drilled by jack-up rig through the platform, will be moderately deviated to optimise the separation of their bottom hole locations within the Bunter Sandstone reservoir. The CO_2 will be injected into the Bunter Sandstone reservoir through perforation in the lower (deeper) half of the reservoir thickness in order to maximise the residual trapping of CO_2. The CO_2 plume will develop and migrate, initially vertically towards the top of the reservoir, and then laterally towards the crest of the structure in an east-south-easterly direction.

The Storage Complex comprises the Storage Site, its Triassic underburden down to the base of the Zechstein Halite and the overburden up to the top Jurassic Lias. Conformance of the observed and predicted response of the Storage Site to CO_2 injection will be monitored during the injection period under a comprehensive Measurement, Monitoring and Verification Plan (MMV Plan). If the operation of the Storage Site behaves as forecast and the dynamic capacity is confirmed, consideration may be given to increasing the quantity of CO_2 to be stored in the Endurance Structure. After injection ceases, the Storage

Site and Storage Complex will be monitored for a number of years after which the platform and wells will be decommissioned before responsibility for the Storage Complex will be transferred to the designated Competent Authority.

This document provides a summary of the methodologies and conclusions of the geological and reservoir engineering analysis of the regional and site-specific information for the characterisation of the Endurance structure and its behaviour as CO_2 is injected into it. It also includes a description of the offshore infrastructure and asset management plan.

Her Majesty's Government (HMG) Autumn Statement and Statement to Markets on 25 November 2015 regarding the Carbon Capture and Storage Competition confirmed that the £1 billion ring-fenced capital budget for the Carbon Capture and Storage Competition was no longer available. This meant that the Competition could not proceed on the basis previously set out. A notice of termination of the White Rose FEED Contract was issued to CPL on 23 December 2015 and the FEED Contract was terminated on 25 January 2016; a date which was earlier than the expected completion date. The Government, CPL and National Grid are committed to sharing the knowledge from UK CCS projects, and this Key Knowledge Deliverable represents the learning achieved up to the cancellation of the CCS Competition and termination of the FEED Contract and therefore does not necessarily represent the final and completed constructible project.

1 Introduction

1.1 General

National Grid Carbon Limited (NGC) is a wholly owned subsidiary of the National Grid group of companies. Capture Power Limited (CPL) is a special purpose vehicle company, which has been formed by a consortium consisting of General Electric (GE), Drax and BOC, to pursue the White Rose CCS Project (the WR Project).

CPL have entered into an agreement (the FEED Contract) with the UK Government's Department of Energy and Climate Change (DECC) pursuant to which it will carry out, among other things, the engineering, cost estimation and risk assessment required to specify the budget required to develop and operate the WR Assets. The WR Assets comprise an end-to-end electricity generation and carbon capture and storage system comprising, broadly: a coal fired power station utilising oxy-fuel technology, carbon dioxide capture, processing, compression and metering facilities; transportation pipeline and pressure boosting facilities; offshore carbon dioxide reception and processing facilities, and injection wells into an offshore storage reservoir.

CPL and NGC have entered into an agreement (the KSC) pursuant to which NGC will perform a project (the WR T&S FEED Project) which will meet that part of CPL's obligations under the FEED Contract which are associated with the T&S Assets. The T&S Assets include, broadly: the transportation pipeline and pressure boosting facilities; offshore carbon dioxide reception and processing facilities, and injection wells into an offshore storage reservoir.

A key component of the WR T&S FEED Project is the Key Knowledge Transfer process. A major portion of this is the compilation and distribution of a set of documents termed Key Knowledge Deliverables (KKDs). This document is one of these KKDs and its specific purpose is summarised below.

1.2 Reservoir Geology

The structure of interest (identified now as "Endurance" and formally as "5/42") is a four-way dip-closure within the Bunter Sandstone Formation of the Southern North Sea. It is a saline aquifer, approximately 22km long, 7km wide and over 200m thick. A layer of mudstone called the Röt Clay provides the primary cap rock or seal over the aquifer. This in turn is overlain by more than 90m of a salt layer known as the Röt Halite which should provide additional sealing capability.

The crest of the reservoir (the highest point of the top of the seam) is located at a depth of approximately 1020m below the seabed. A datum level of 1300m below the mean sea surface level (1300mTVDSS) was chosen, for which the pressure and temperature were determined as 140bar and 56°C, respectively.

The subsurface description of the Endurance structure has been provided by regional seismic data and the results obtained from the drilling of three wells on the structure. Two of these wells are abandoned hydrocarbon (oil/natural gas) exploration wells; the third was a dedicated CCS appraisal well drilled by National Grid Twenty Nine Limited which had a comprehensive data evaluation programme designed to quantify and characterise various aspects of the structure with regard to its possible use for permanent, secure CO_2 storage.

The Bunter sandstone reservoir within the structural closure (the "Storage Site") is estimated to have a net pore volume of over four and a half billion cubic meters (more than 4,500,000,000$m^{3)}$. This should provide storage for of the order of twenty-six-thousand million tons (2600MT) of CO_2. The planned production by the White Rose power plant, over a 20 year operational period, would total just 53.6 MT of CO_2; this would occupy approximately just 2% of the estimated storage capacity.

The maximum aquifer pressure increase (no more than 40bar) resulting from the injection of CO_2 injection produced by the OPP is estimated to be substantially lower than that required to fracture the Röt Clay primary seal; an uplift of only 9 cm at the crest of the structure is predicted.

Approximately 90% of the injected CO_2 is predicted to be trapped structurally for hundreds of years following injection, forming a 25m thick CO_2 gas cap beneath the Röt Clay cap rock due to the buoyancy of the CO_2 relative to the native brine. The amount of CO_2 trapped by capillary forces between the injection wells and the structure crest is considered to be relatively small, less than 5% of the total injected volume, in view of the high reservoir quality. In the longer term, over thousands of years, the structurally trapped CO_2 will diffuse and dissolve into the underlying brine and create a CO_2-rich, denser brine phase, which will then initiate a convection process, that will gradually deplete the CO_2 cap and thereby enhances dissolution trapping. Simulation indicates, that CO_2-rich brine will reach the base of the structure in about 10,000 years (assuming no temperature anomalies and no reactivity of the dissolved CO_2 with the formation), at which point approximately 25% of total White Rose CO_2 is predicted to have been dissolved.

The main geochemical reactions resulting from an increase in the acidity (decrease in the pH value) of the brine due to CO_2 dissolution would result in some dissolution of dolomite and precipitation of halite and calcite minerals. Since dolomite occurs within the formation as isolated nodules, no impact on rock mechanical properties is considered likely from dissolution reactions whilst precipitation reactions are predicted to sequester (take up) less than 1% of total injected CO_2 in the first 10,000 years.

1.3 Description of the Offshore Facilities

1.3.1 Platform

The offshore platform shall consist of a conventional fixed 4-leg liftable jacket structure, similar to many installations in the North Sea (Figure 1.1) It shall have 4 decks housing the different equipment and spare risers and J-tubes to allow for the drilling of additional wells and an extension pipeline to another storage facility if required in future. Construction of these spare risers as part of the initial installation will minimise the costs of future works as well as ensuring that the original design is sufficient to cope with the additional weight that future extensions will impose on the jacket.

A detailed description of the platform is provided by the KKD K36 Offshore Installation Plot Plan report.

Figure 1.1: Jacket Schematic

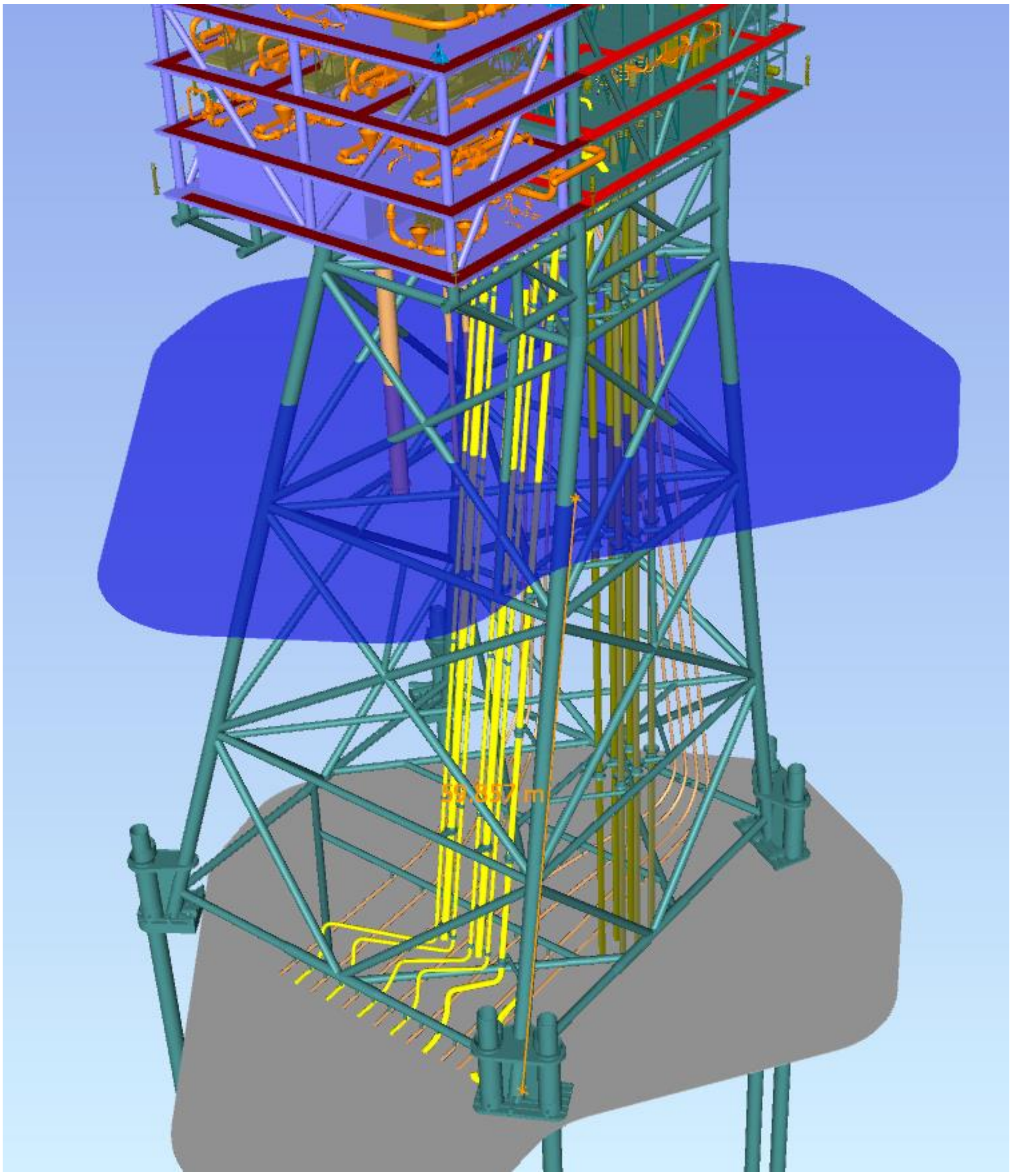

1.3.2 Pipeline

The offshore pipeline has a design life of 40 years and a maximum capacity of 17MTPA of CO_2.

The upstream boundary limit is defined as downstream of the pumping station, 5 m outside the boundary fence of the pumping station. The downstream boundary limit is the upstream flange of the injection well trees located on the offshore platform facility, downstream of the wellhead choke valve.

The building of the section of pipeline between the discharge of the pumping station and the mean low water mark including works in the designated route corridor are subject to the parameters set by the Development Consent Order (DCO) application.

Offshore, 90km pipeline route corridor between landfall and the storage site where the water depth is in the range from 50m to 60m has been defined and surveyed. It is shown in Figure 1.2 below.

Figure 1.2: Offshore Pipeline Route Corridor

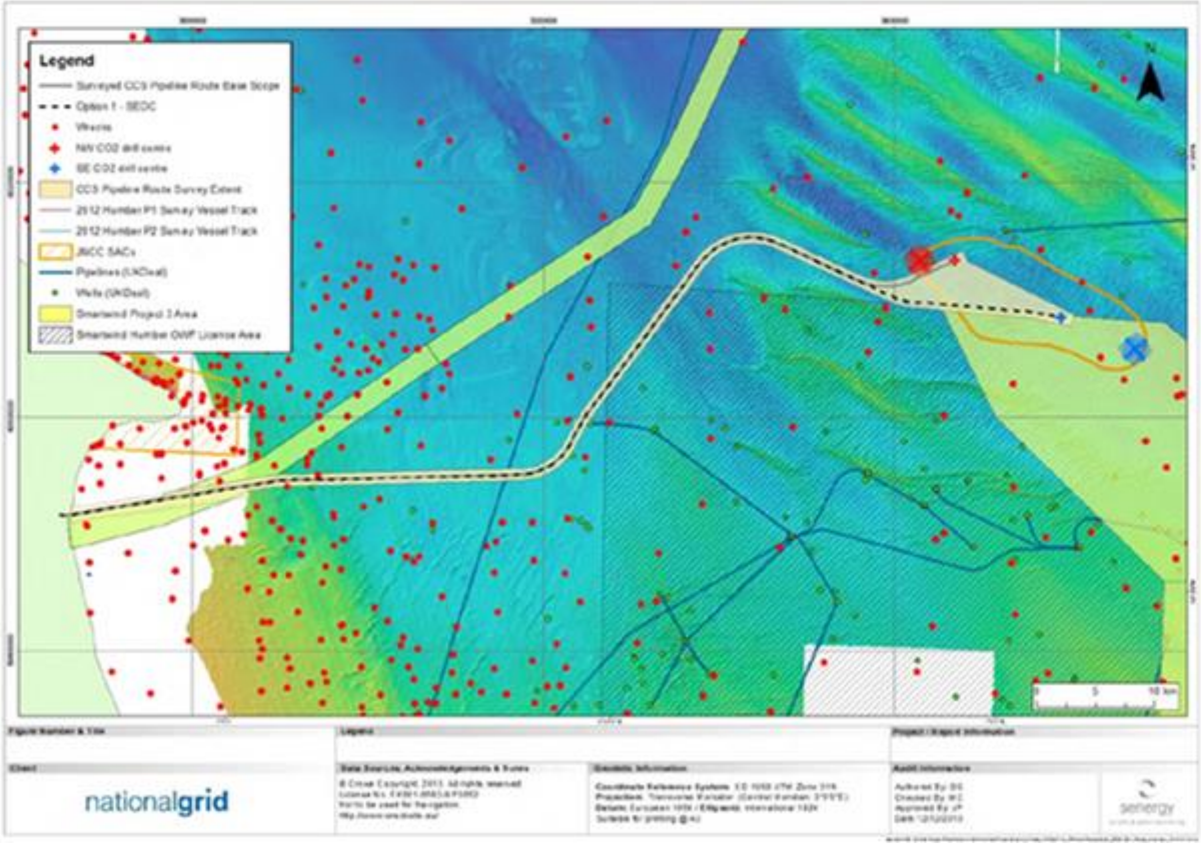

Further details are provided by K37 Offshore Infrastructure and Design Confirming the Engineering Design Rationale report.

1.4 Purpose of this Report

This report summarises the details of the reports which were prepared in line with regulatory guidelines for submission to regulatory authorities in relation to gaining approval for the proposed storage development.

The KKD will include:

- subsurface description; and
- facilities description;
- well drilling and completion;
- well and reservoir management plan;
- Asset Reference Plan;
- Field Development Plan; and
- Technology Maturation Plan.

2 Project Overview

The White Rose CCS Project is to provide an example of a clean coal-fired power station of up to 448mW gross output, built and operated as a commercial enterprise.

The project comprises a state-of-the-art coal-fired power plant that is equipped with full CCS technology. The plant would also have the potential to co-fire biomass. The project is intended to prove CCS technology at a commercial scale and demonstrate it as a competitive form of low-carbon power generation and as an important technology in tackling climate change. It would also play an important role in establishing a CO_2 transportation and storage network in the Yorkshire and Humber area. Figure 2.1 below gives a geographical overview of the proposed CO_2 transportation system.

Figure 2.1: Geographical overview of the transportation facility

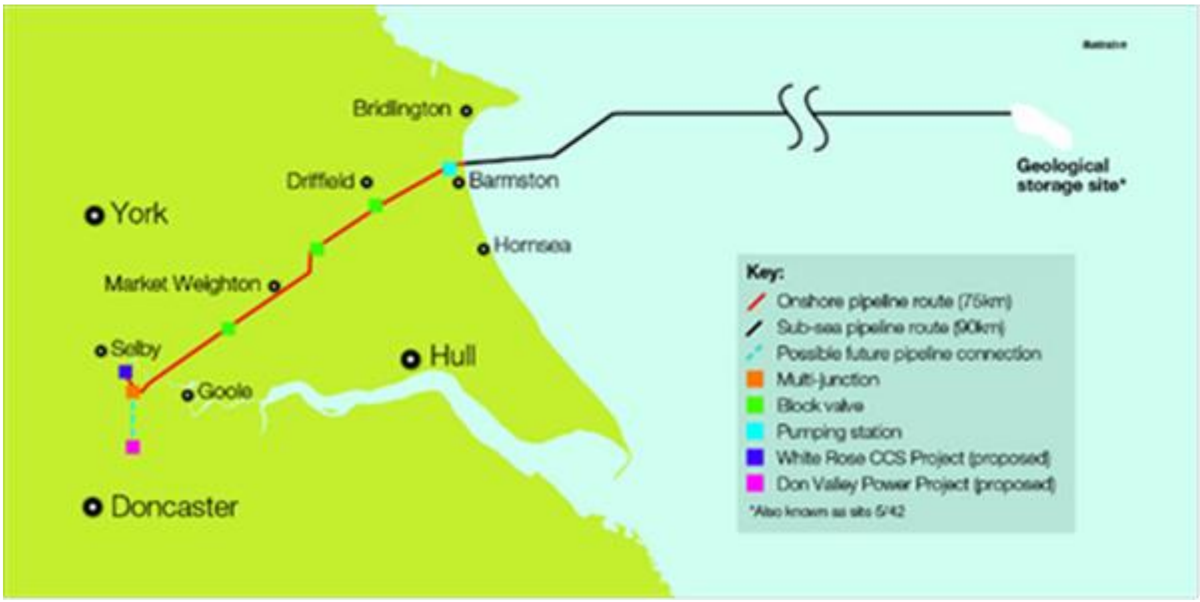

The standalone power plant would be located at the existing Drax Power Station site near Selby, North Yorkshire, generating electricity for export to the Electricity Transmission Network (the “Grid”) as well as capturing approximately 2 million tonnes of CO_2 per year, some 90% of all CO_2 emissions produced by the plant. The by-product CO_2 from the Oxy Power Plant (OPP) would be compressed and transported via an export pipeline for injection into an offshore saline formation (the reservoir) for permanent storage.

The power plant technology, which is known as Oxyfuel combustion, burns fuel in a modified combustion environment with the resulting combustion gases being high in CO_2 concentration. This allows the CO_2 produced to be captured without the need for additional chemical separation, before being compressed into dense phase and transported for storage.

The overall integrated control of the End-to-End CCS chain would have similarities to that of the National Grid natural gas pipeline network. Operation of the Transport and Storage System would be undertaken by NGC. However, transportation of carbon dioxide presents differing concerns to those of natural gas; suitable specific operating procedures would be developed to cover all operational aspects including start-up, normal and abnormal operation, controlled and emergency shutdowns. These procedures would include a hierarchy of operation, responsibility, communication procedures and protocols. Figure 2.2 below provides a schematic diagram of the overall end-to-end chain for the White Rose CCS Project.

Figure 2.2: End-to-End Chain Overall Schematic Diagram

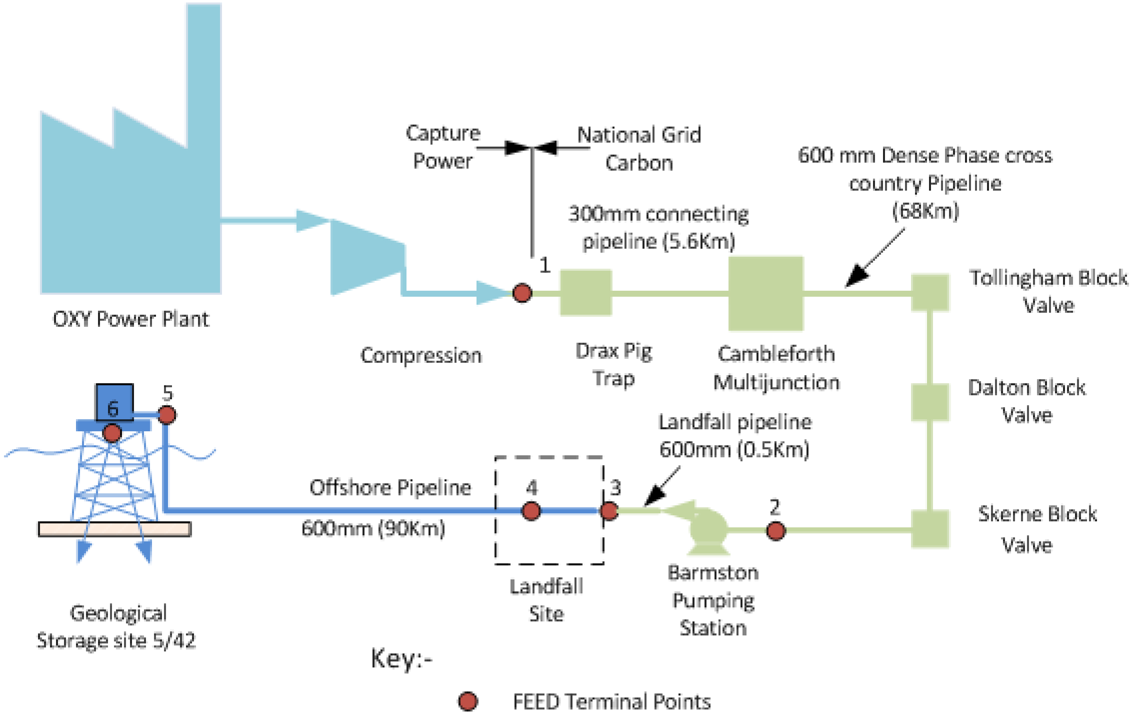

NGC have taken the strategic investment decision to design the transportation and storage system for future expansion beyond the initial First Load CO_2 supply. The intention would be to create an onshore and offshore hub to reduce incremental costs for future entrants into the pipeline system. This is why the proposed onshore pipeline from the Camblesforth Multi-Junction and the offshore pipeline from Barmston to the Normally Unmanned Installation (NUI) are 600mm with an approximate capacity of 17MTPA, which would be well in excess of First Load supply of 2.68MTPA and the 10MTPA expected maximum injection capacity into the proposed subsea storage reservoir, which is identified as Endurance.

3 Geological Characterisation of the Endurance Storage Site and Storage

3.1 Geological and Structural Setting

The Endurance structure is one of several structural closures of the Bunter Sandstone Formation (BSF) found within the Triassic Southern North Sea (SNS) basin. It is a large four-way dip closure and acquired its current structural configuration as a result of the development of the underlying Zechstein Halite diapir (Figure 3.2 and Figure 3.3). It is situated between Blocks 42/25d and 43/21, and has been penetrated by three exploration and appraisal wells drilled between 1970 and 2013. Several other exploration and appraisal wells drilled with various objectives surround the structure as shown in Figure 3.2.

The development of the SNS Basin is characterised by a complex history of basinal subsidence and episodes of uplift and erosion (Ref 7). The Triassic is divided into three main sedimentary successions that include the Bacton Group, the Haisborough Group and the Penarth Group. Figure 3.4 shows the lithostratigraphic nomenclature for the Triassic. Top Bunter is one of largely coarse-grained deposits, comprising red sandstones, shales and mudstones that make up the Bacton group. The Bunter Shale formation which underlies the BSF provides a basal seal. The Bacton Group is immediately overlain by the Haisborough Group which comprises mainly alternating beds of fine-grained clastics and evaporates that act as excellent top seals for CO_2 injected into the Endurance structure. The Haisborough group comprises the Dowsing, Dudgeon, and Triton formations. The Dowsing formation is Dolomitic and at its base is the Rot Halite member which is well developed throughout the SNS basin. There is a thin basal transgressive unit within the Rot Halite called the Rot Clay. The Rot Clay directly overly the Endurance structure and is also generally considered to be of considerable extent (Ref 1). The Penarth group at top Triassic is representative of the marine transgression that marks the transition from the Triassic to the Jurassic.

Figure 3.1: Endurance Storage Site Showing Lease Boundry

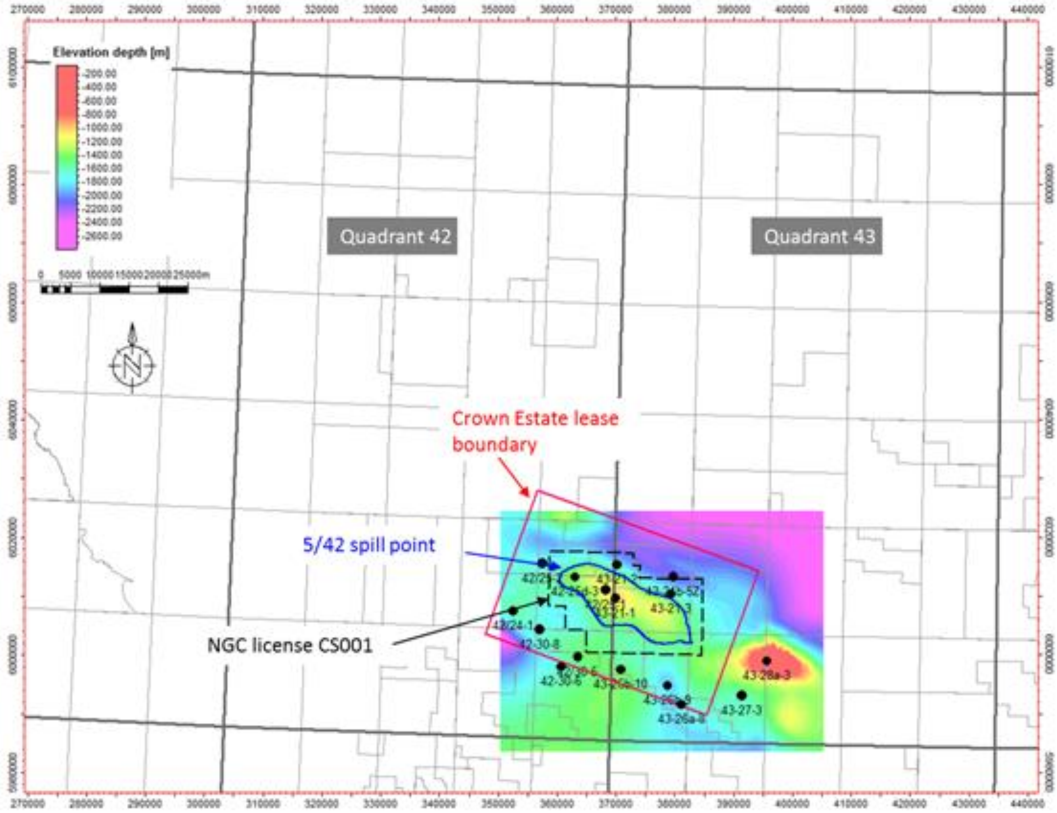

Figure 3.2: Top Bunter depth structure map over Endurance Storage Site showing NGC CCS licence block boundary (black dotted line) and wells .

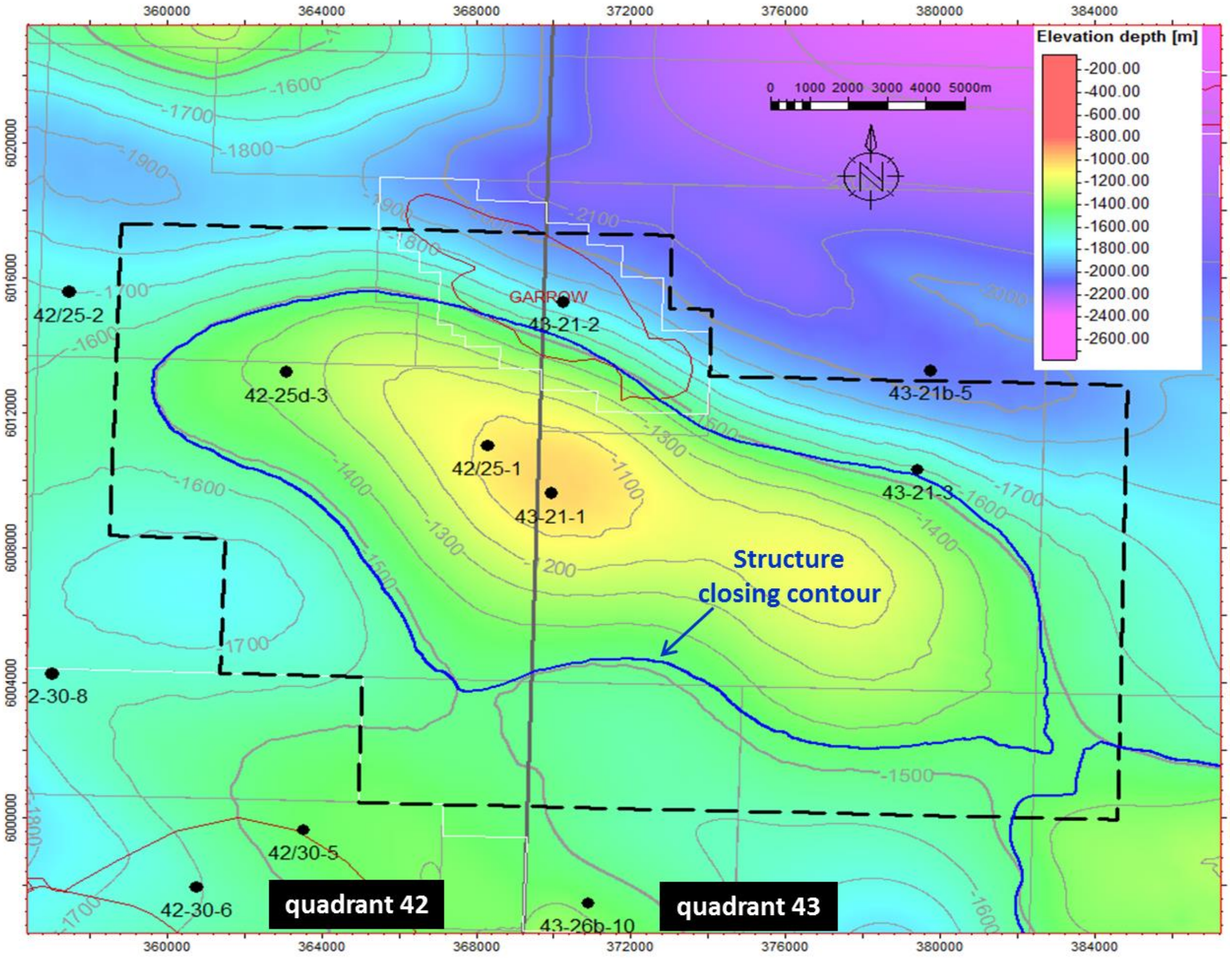

Figure 3.2 shows the Top Bunter depth structure map over Endurance Storage Site showing licence block boundaries (broken black line) as well as exploration and appraisal wells within the area of interest (AOI). Note only wells 42/25d-3, 42/25-1, and 43/21-1 have penetrated the Endurance structure. Note outline of the Garrow field located below the Endurance structure.

Movement of the Zechstein salt dominates the structural morphology of the Endurance structure. Zechstein movement was initiated at various times during the history of the SNS basin. The majority of the salt movement is likely to have begun in late Jurassic and early Cretaceous times and the mechanism is well understood. It is related to underlying faulting. The general model is one of extensional faulting being accommodated by the overlying salt but weakening the overburden through differential loading. Once the overburden becomes weaker than the increasing buoyancy force of the underlying salt, the salt itself will start to flow.

Another salt diapir is present to the southeast of the Endurance structure and the Triassic sands and shales outcrop at the seabed around the salt core (Figure 3.3). Interpretation of seismic data suggests that the Bunter sandstone is continuous in the saddle between the Endurance structure and this diapir.

Tertiary structural inversion (uplift following deep burial) has brought much of the SNS to shallower levels and this has led to poorer quality reservoirs than would be the case in the absence of this inversion. Structural inversion followed by glacial erosion has also resulted in the absence of most of the post Middle Jurassic interval within the vicinity of the Endurance structure and beyond.

Figure 3.3: WNW-ESE cross-section through Endurance structure and salt diapir to SE

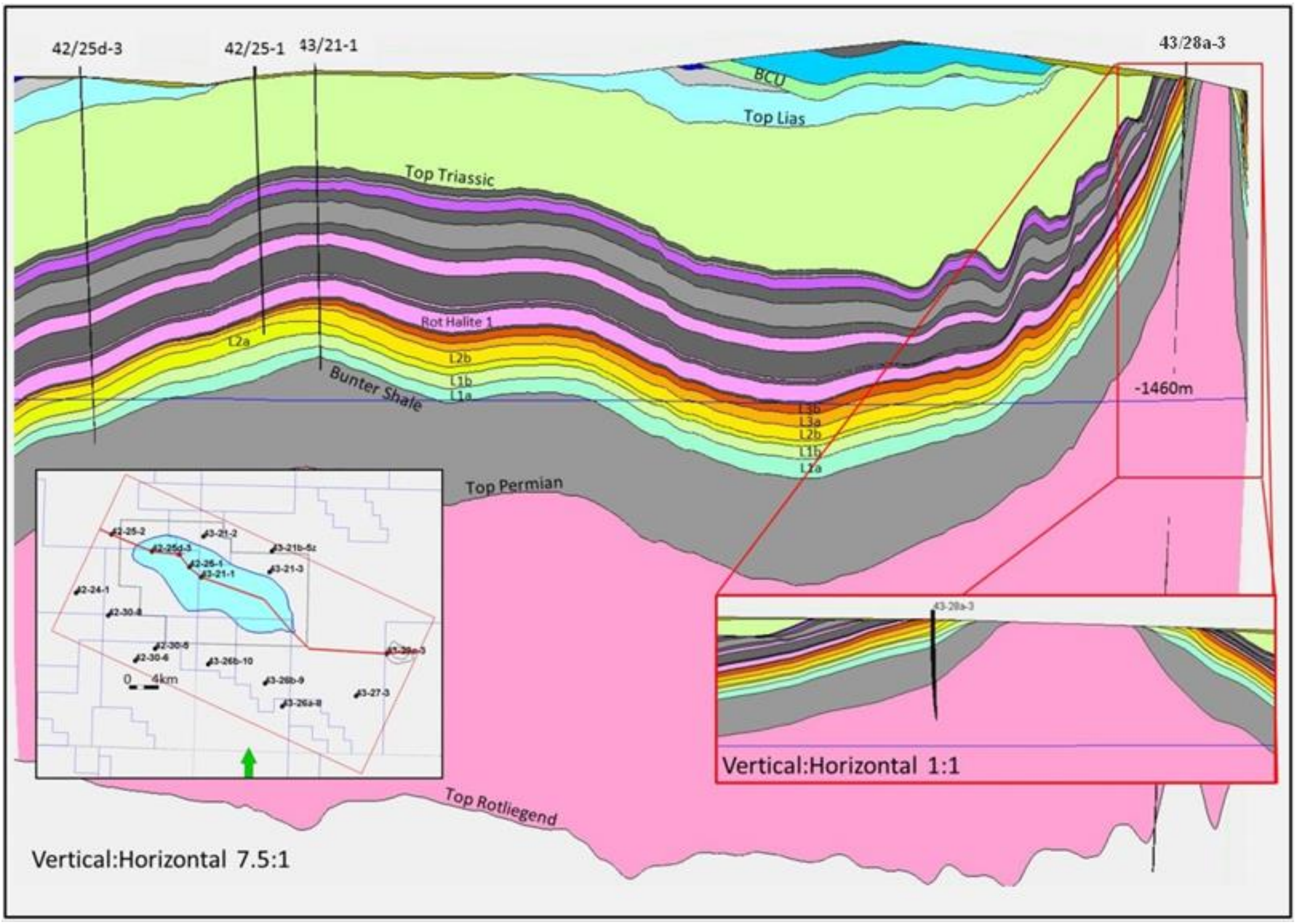

Figure 3.4: Lithostratigraphic nomenclature scheme for the Triassic of the Southern North Sea (after Ref 9)

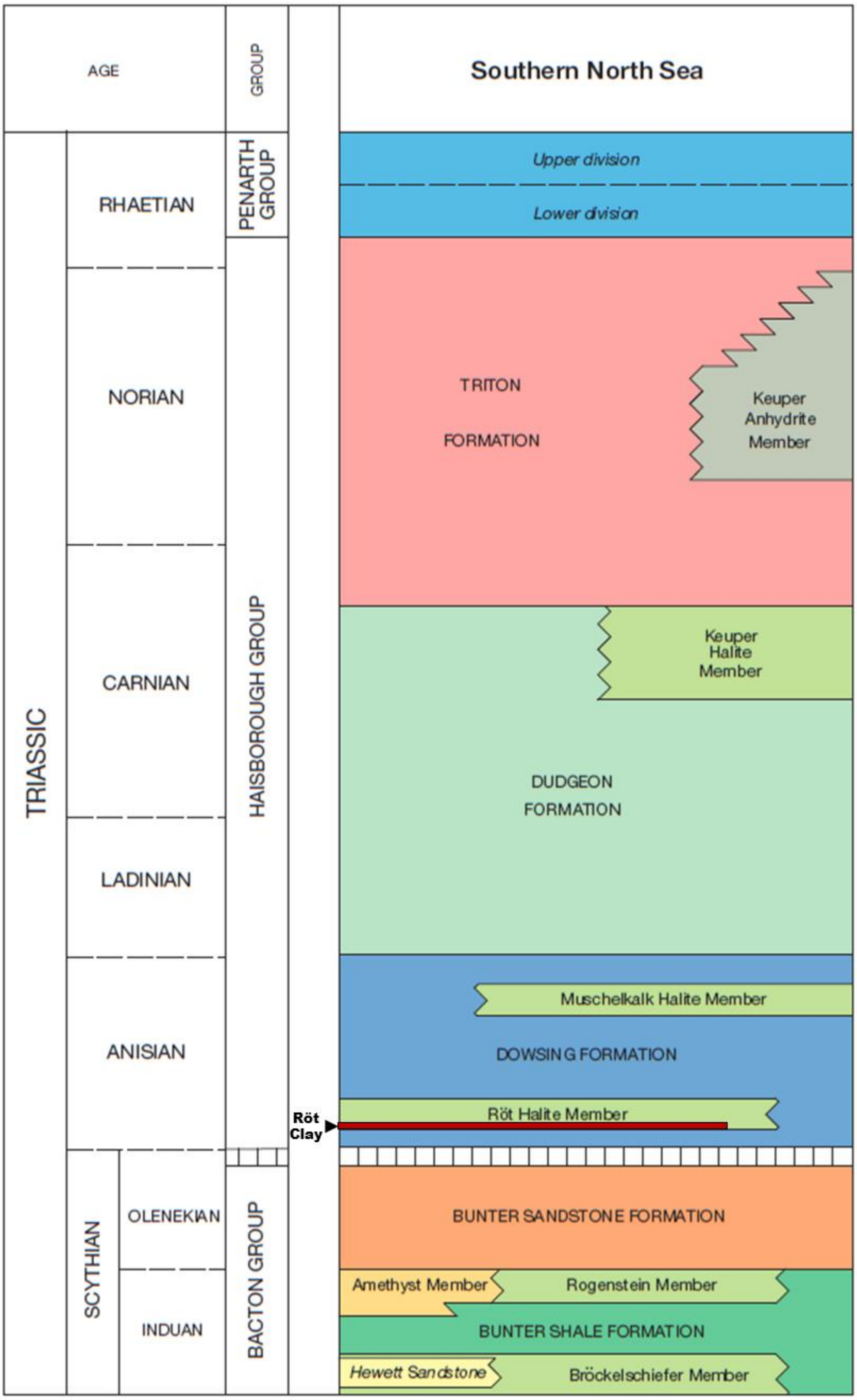

Interpretation of seismic data has provided further insight into the relative sequence of events that led to the present day structural configuration. Figure 3.5 highlights the subdivision of the Endurance structure into three overlapping volumes mainly for the purposes of the MMV (Monitoring, Measurement and Verification) plan and this is adopted henceforth in this document. These are summarised below.

3.1.1 Endurance Storage Site

For the Endurance structure, the Storage Site comprises the BSF within the Endurance structure. The lithologies above and below Bunter sandstone are mainly shales and evaporites, hence they are all envisaged to have a good sealing quality (Figure 3.7). The areal dimensions of the Storage Site shown in Figure 3.8 are taken from the most likely Top Bunter depth map which closes at 1460mTVDSS (see Section 3.2.1.1).

Figure 3.5: Section illustrating the limits of Storage Site, storage complex & monitoring area (a) Crossection of Site (see Plan below, Figure 3.6)

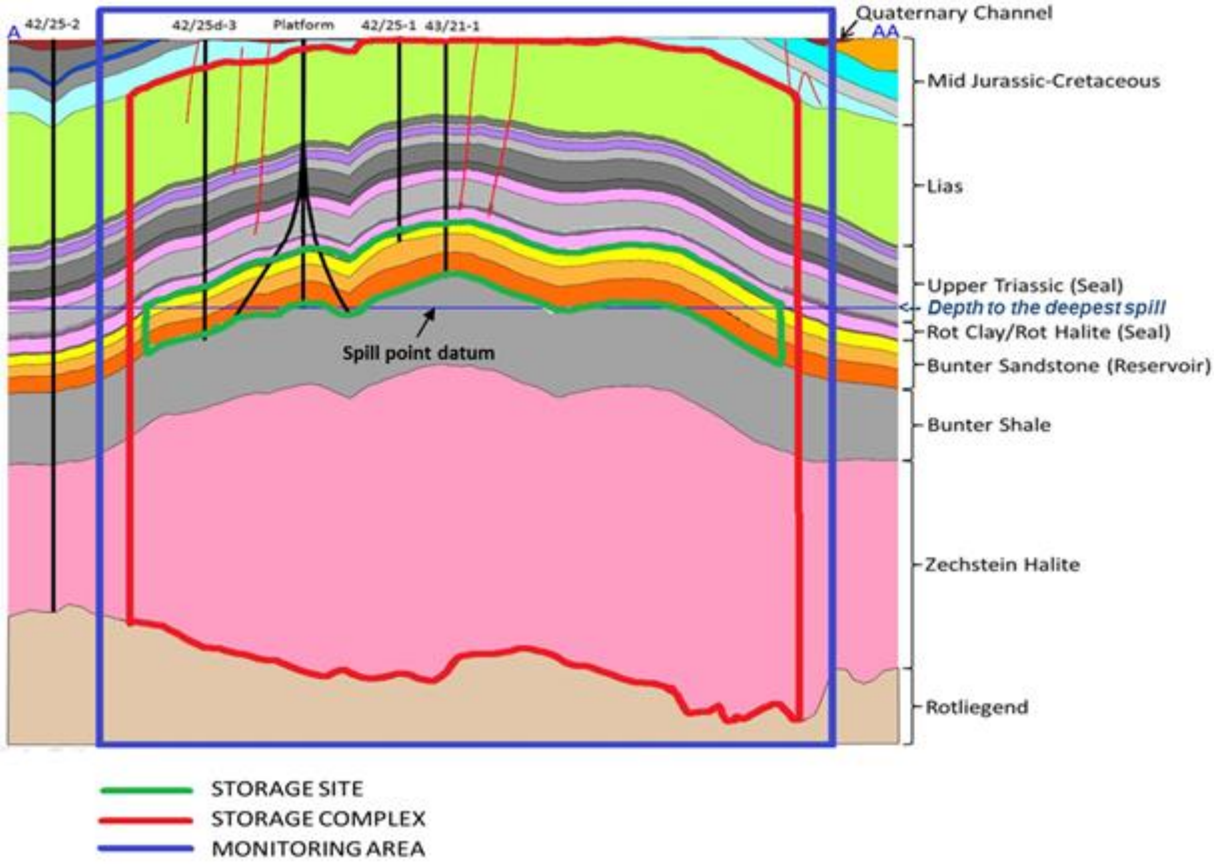

Figure 3.6: **Section illustrating the limits of Storage Site, storage complex & monitoring area (b) Plan of Site**

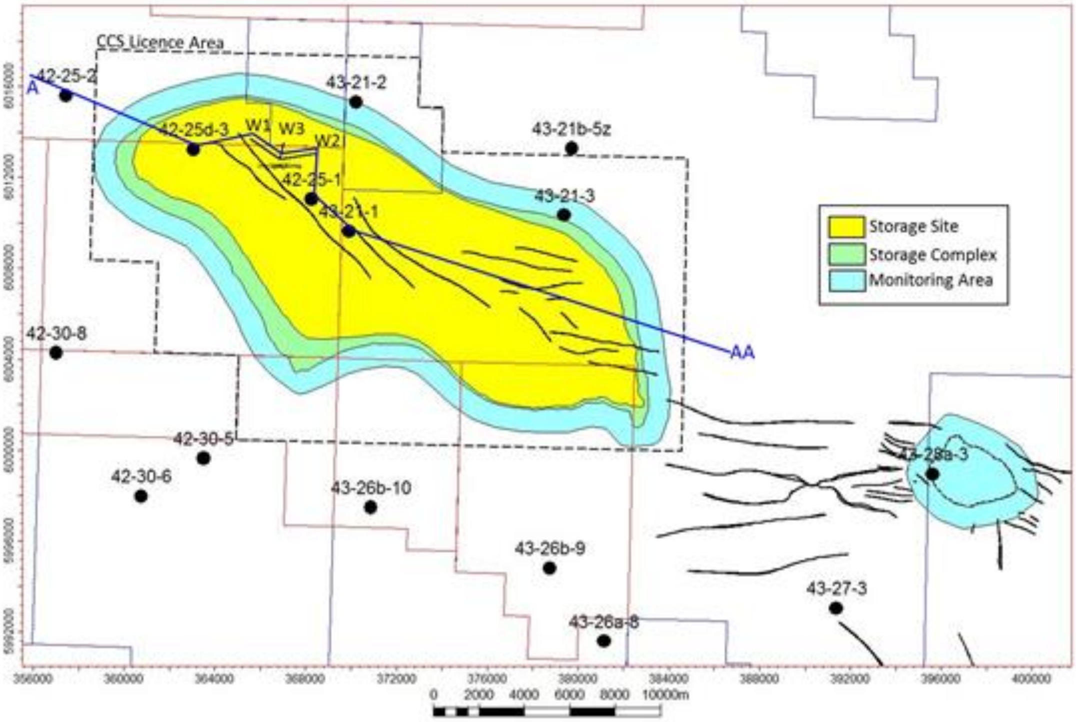

Figure 3.7: Lithostratigraphy of the Storage Site and complex

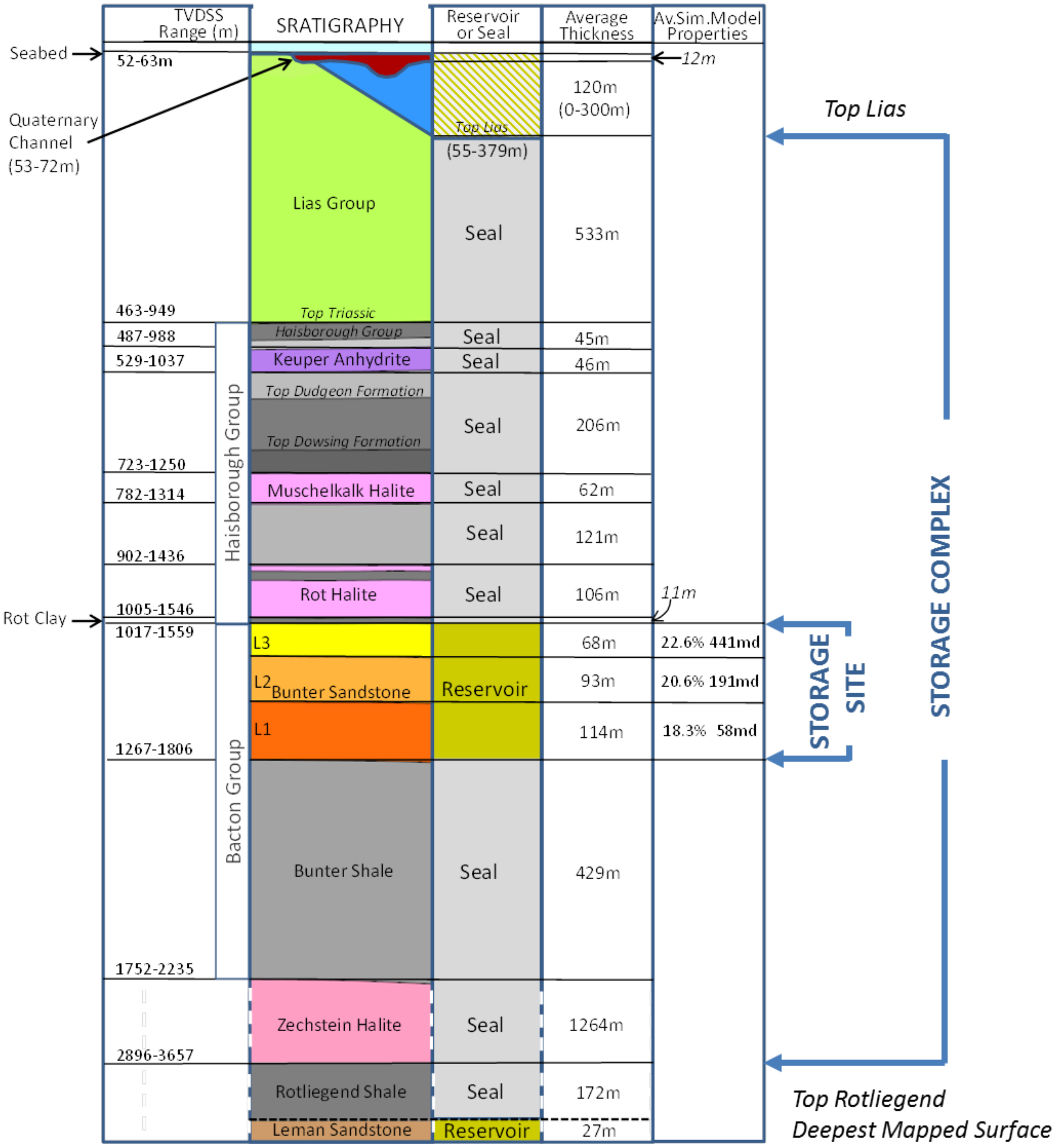

Figure 3.8: Map view of CO_2 Storage Definitions

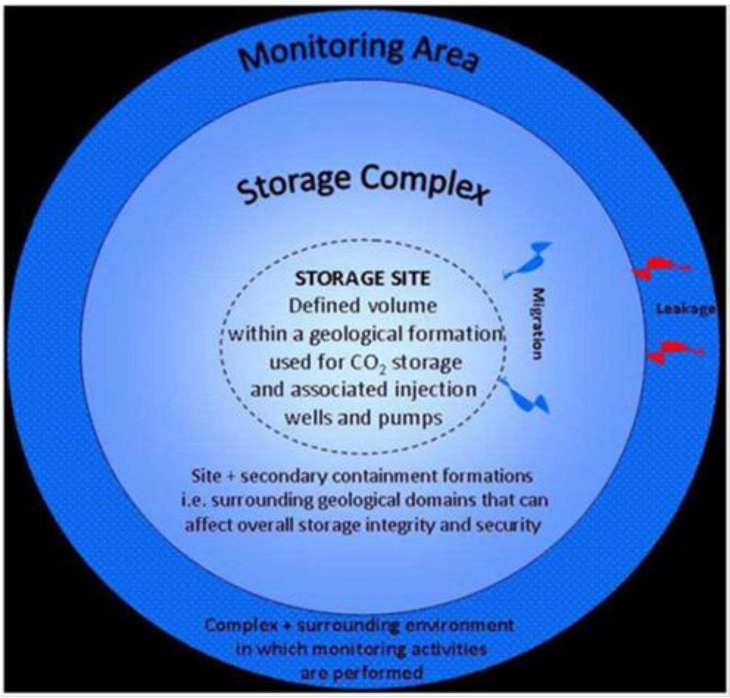

3.1.2 Endurance Storage Complex

The Storage Complex is defined from the Top Rotliegend to the top of the Liassic and encompasses the Storage Site. The Upper Rotliegend is likely to provide a further basal seal; however, the base of the formation and the top of the underlying Leman Sandstone reservoir could not be mapped seismically with any confidence. Consequently the base of the storage complex has been placed at the deepest confidently mappable horizon, namely the Top Rotliegend.

The areal dimensions of the Storage Complex for the Endurance structure is taken from the closure of the high NPV (Net Pore Volume) case on the top Bunter Sandstone at -1553 mTVDSS. The Storage Complex includes all the overburden geological formations directly above the Röt Clay seal up to the Top of the Liassic, the shallowest sealing interval.

3.1.3 Endurance Monitoring Area

The Monitoring Area will include the Storage Site and Complex – both vertically and areally. The areal extent will ensure that any Lateral migration of CO_2 beyond the Bunter Sandstone spill point which lies to the east and south of the structure is highly unlikely to occur as a result of White Rose CO_2 injection (see Section 5). The areal extent of the Monitoring Area will, however, ensure that any such migration would be detected.

Vertically the monitoring area includes stratigraphy outwith the Storage Complex area. This includes the Middle Jurassic to Cretaceous strata which outcrop at the seabed on the margins of the salt diapir core west of the Endurance anticline. It also includes Quaternary channels which locally erode older stratigraphy.

The following sections give summaries of the structural interpretations.

3.2 Geological Horizon Mapping

The seismic responses of the key stratigraphic intervals from the 3D OBC survey and the 2D survey (covering the seabed outcrop to the South-East of Endurance) were calibrated to data obtained from approximately 20 wells in the Area of Interest (AOI). A total of 6 seismic horizons were interpreted from these extensive seismic to well ties, they are:

Top Chalk; Top Chalk is marked by an increase in acoustic impedance and is represented by a low amplitude trough (red) on seismic. The trough varies in amplitude and continuity, becoming more discontinuous in shallower sections.

Base Cretaceous; The Base Cretaceous was difficult to interpret because of the poor quality of the shallow 3D seismic section. It was picked on a prominent peak throughout the 3D and 2D surveys. It is interpreted to outcrop on the seafloor on the flanks of the structure.

Top Triassic; The Top Triassic is represented as a high amplitude peak which varies considerably, from strong and continuous in the 3D J07 tile of the PGS Mega Merge data, to weak and indistinct in the West K06 and J06 tiles and 2D surveys.

Top Bunter Sand; The Top Bunter Sandstone was the main horizon of interest and this horizon was correlated with well control through synthetic seismograms. It was picked on the prominent blue peak tied into the synthetic seismogram in well 43/21-1 where the upper part of the Bunter Sand has low acoustic impedance associated with high porosity of the sand (Figure 3.9). However, on the flanks of the structure there is an abrupt change in the polarity of the reflection so that it becomes a strong red trough (Figure 3.10).

The Top Bunter Sand horizon was picked as a peak in the high parts of the structure and as a trough in the lower parts. The change from peak to trough occurs almost instantaneously. The boundary is shown on the Top Bunter Sand two-way time structure map in Figure 3.11. The interpretation was continued on the 2D surveys to the southeast and an additional well tie was achieved at 43/27-1, in which the Top Bunter Sand is also a peak.

Top Zechstein; Top Zechstein Group represents the top of evaporite and carbonate rocks of Late Permian age. The Top Zechstein is represented by a sharp impedance contrast between the Bunter Shales and anhydrites of the Top Zechstein, resulting in a strong, continuous trough on seismic across the majority of the survey area.

Top Rotliegend (base Zechstein); Decrease in acoustic impedance resulting in a high amplitude peak on seismic was observed where anhydrites of the Zechstein group overlie clastics of the Rotliegend. The Top Rotliegend is a consistent pick through the area of interest with the exception of regions below salt walls and swells, where the horizon becomes steeply dipping due to time pull-up leading to more uncertainty in the horizon pick.

Figure 3.9: Synthetic Seismogram Well 43/21-1, Illustrating Top Bunter Peak

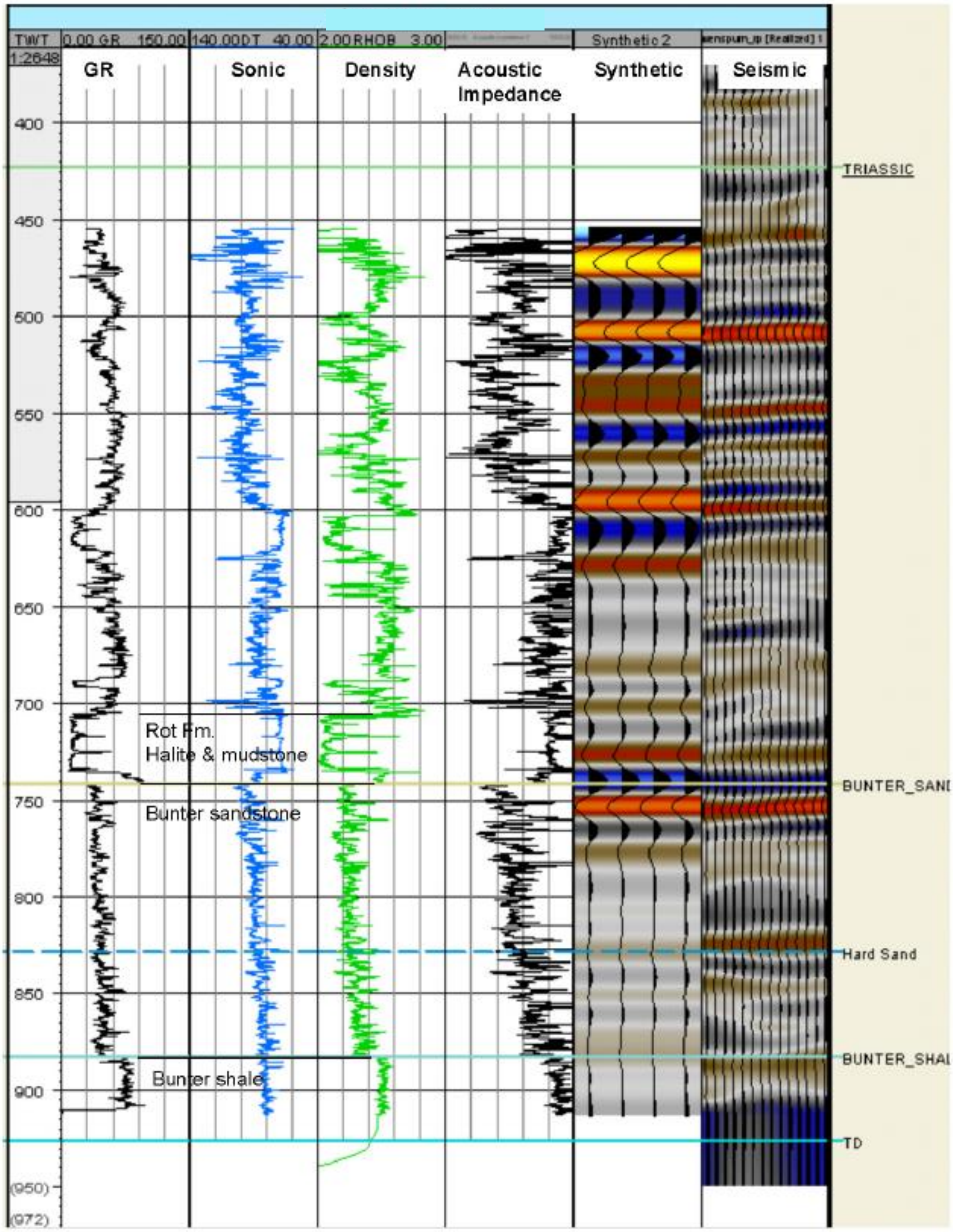

Figure 3.10: Seismic Correlation from 43/21-1 to 43/21-2

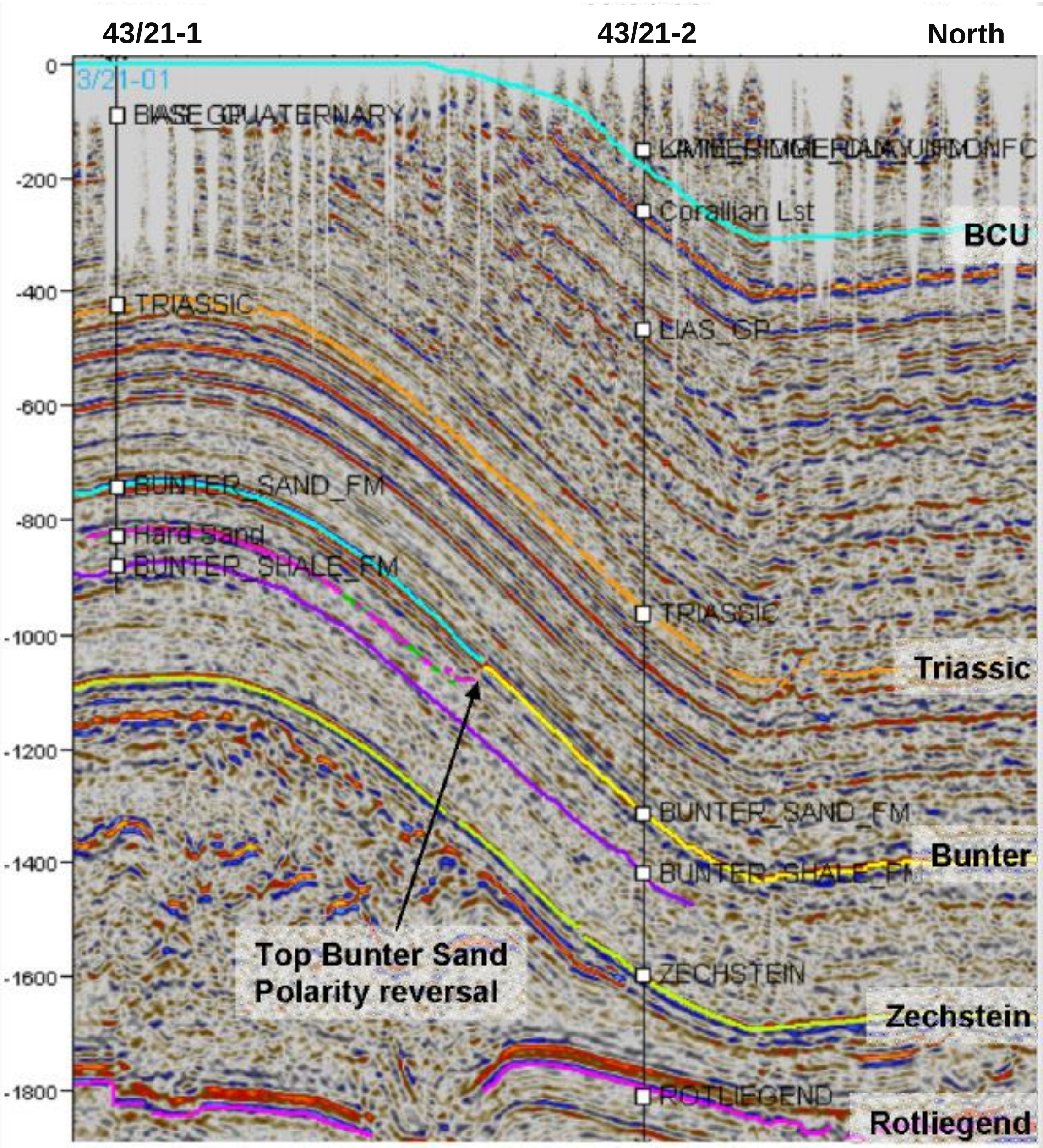

Figure 3.11: Endurance Top Bunter depth surface with wells and PRP (Phase Reversal Polygon)

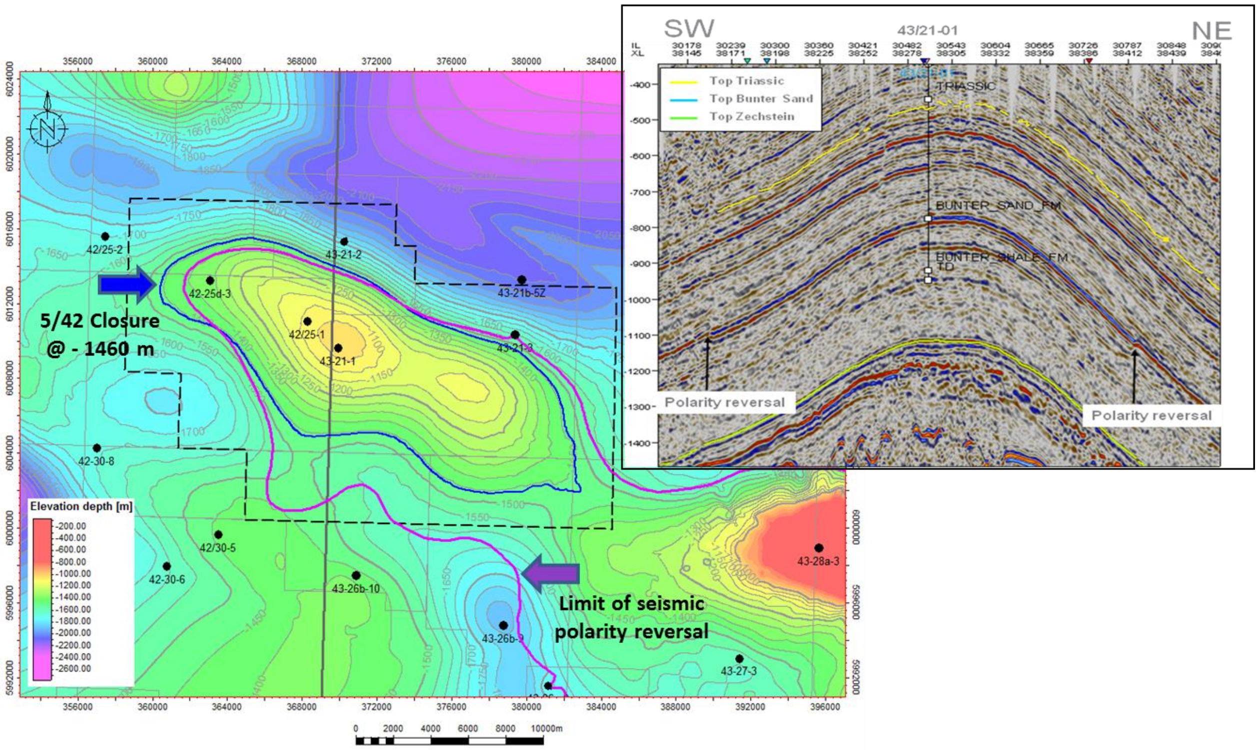

Figure 3.12 shows a West-East oriented crossline from the 3D OBC survey. Due to insufficient spatial sampling by the seabed receiver cables of the near surface geology, seismic gaps are observed in the shallowest 500ms of two way travel time (equivalent to about 590mTVDSS). The survey sampling was sufficient to image the top of the Triassic interval and deeper geological intervals down to Carboniferous depths. Figure 3.12 shows interpreted horizons for top Triassic (light green), top Bunter Sand (cyan), top Zechstein (green) and top Rotliegend (blue). The line intersects the 43/21-1 well at the crest of the Endurance Bunter Sand structure which provides control for the interpretation.

In the context of the seismic gaps in the shallowest data from the OBC survey it is worth noting that a new 3D seismic streamer based data set taken and processed during 2012-14 became commercially available in early 2015 and a 5km x 5km pilot area over the crest of Endurance was acquired for assessment. This assessment has indicated that the structural differences seen in this 5km x 5km pilot study area with the new data set have minimal impact on the objectives of site characterisation and would have no or minimal impact on the established static, dynamic and geomechanical modelling workflows.

Figure 3.12: 3D OBC Xline 38296 with well 43/21-1 on the crest and projected well 43/21-3 on the north eastern flank

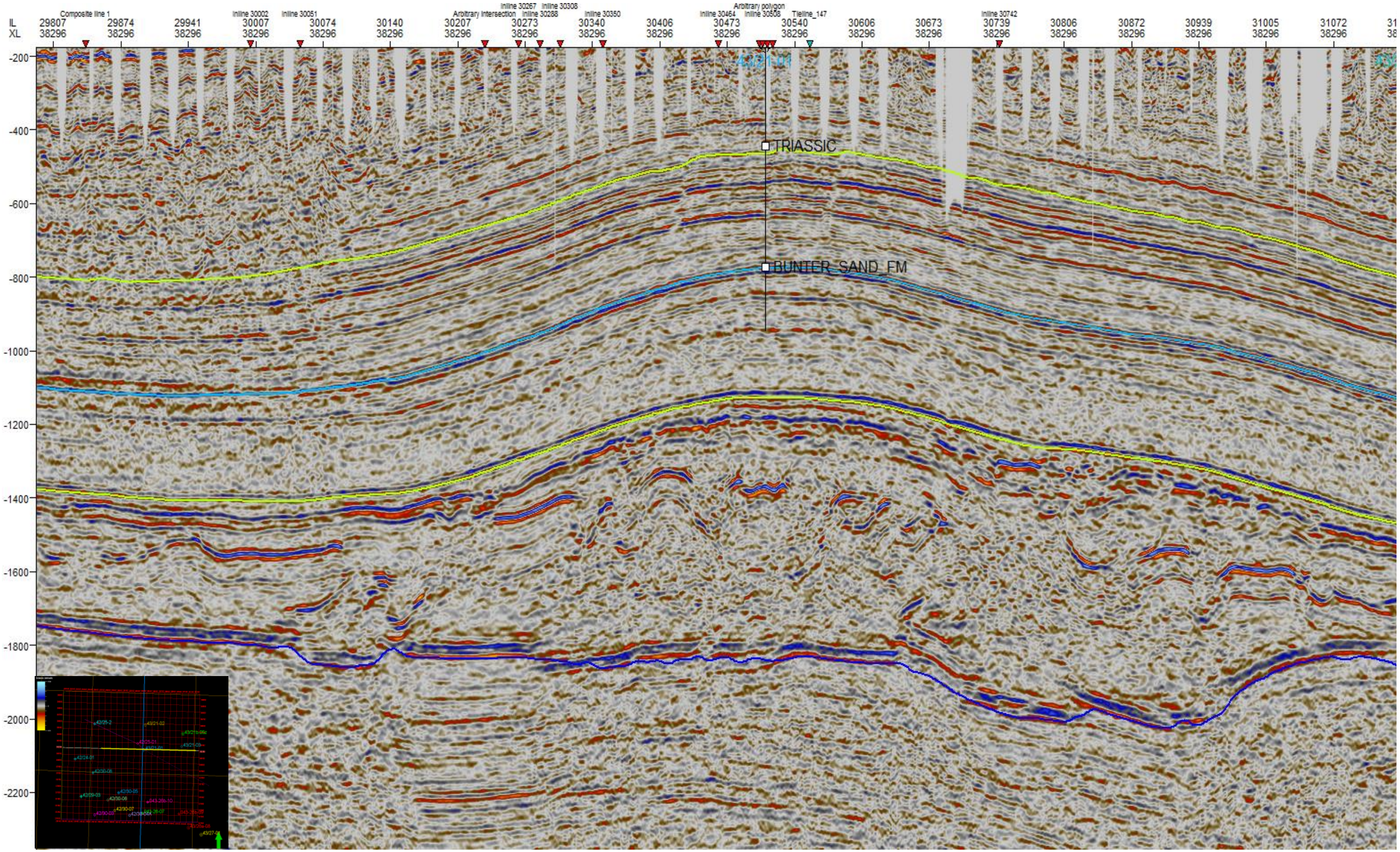

The Cretaceous chalk interval and all younger stratigraphic units are absent over the crest due to uplift and erosion as a consequence of basin inversion during the Tertiary and subsequent glacial erosion.

Figure 3.13 is a 2D seismic tie line running North-West to South-East across the main longitudinal axis of the Endurance anticline (through the 43/21-1 crestal well) and down to the Bunter seabed outcrop (43/28a-3 "outcrop" well). As well as the top Triassic, top Bunter Sands, top Zechstein and top Rotliegend interpreted on the 3D OBC data, overlying reflectors have been interpreted: base Quaternary channels (red), top Chalk (light blue), base Cretaceous (pale purple), Lower Jurassic Lias (blue). The sea bed (yellow) has also been interpreted on this line and sand waves over the core of the anticline can clearly be observed.

A series of TWT (Two Way Time) base maps for Top Triassic, Top Bunter sand, Top Zechstein and Top Rotliegend horizons are shown in Figure 3.14 through to Figure 3.17. For each map, polygons delimiting the static model AOI (red) and the live data area for the 3D OBC grid (blue) are also shown to highlight the total data coverage afforded by the various seismic volumes and thus the degree of grid interpolation required for each horizon. For the Top Triassic, Top Bunter sand and Top Zechstein maps, the original gridded surfaces from the 3D Ravenspurn seismic grid are included and show elements of data interpolation outside the live OBC area.

Figure 3.13: 2D Site Survey Tie Line (147) [change colour of structural close]

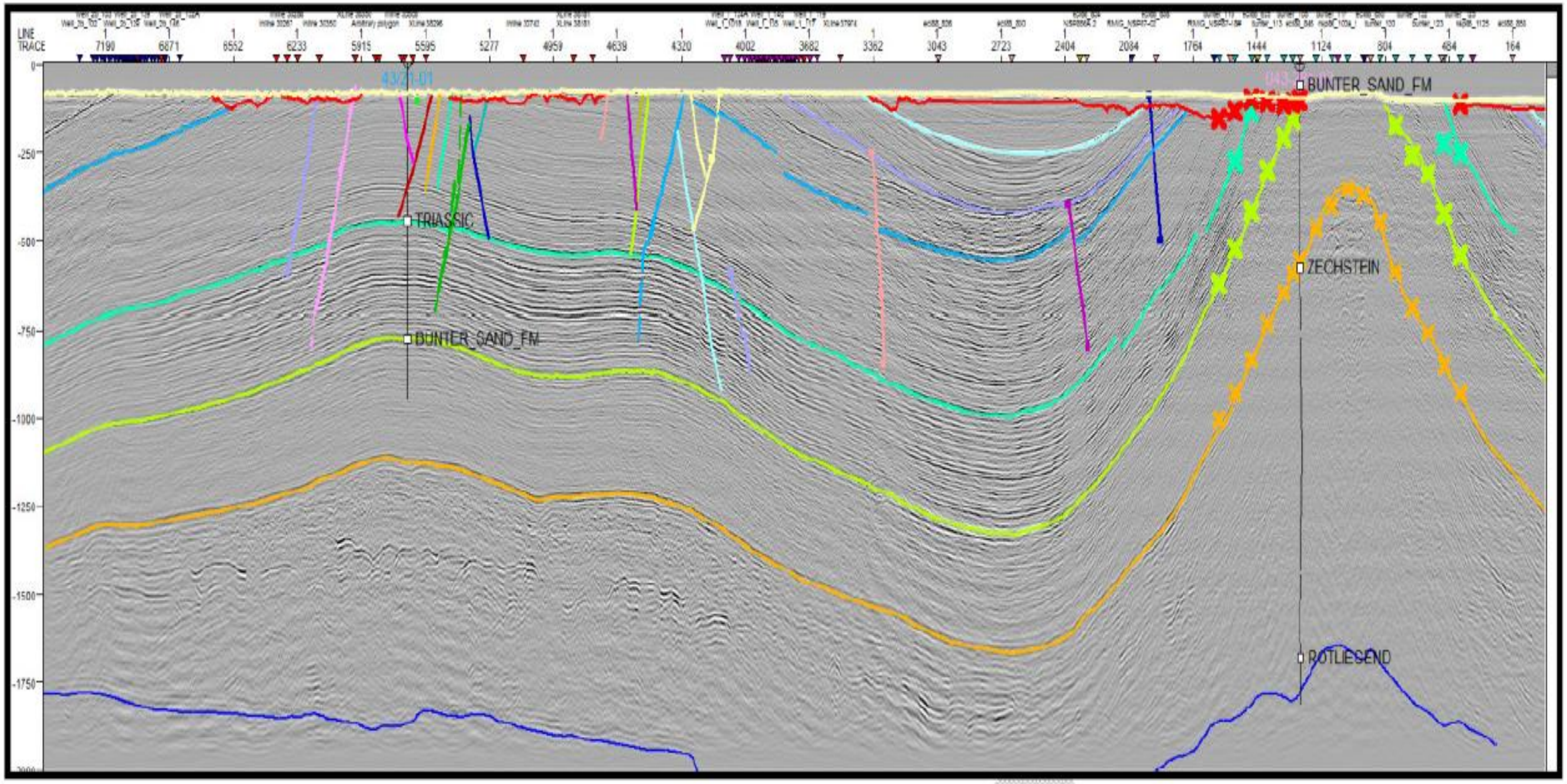

Figure 3.14: Composite Top Triassic TWT Interpretation

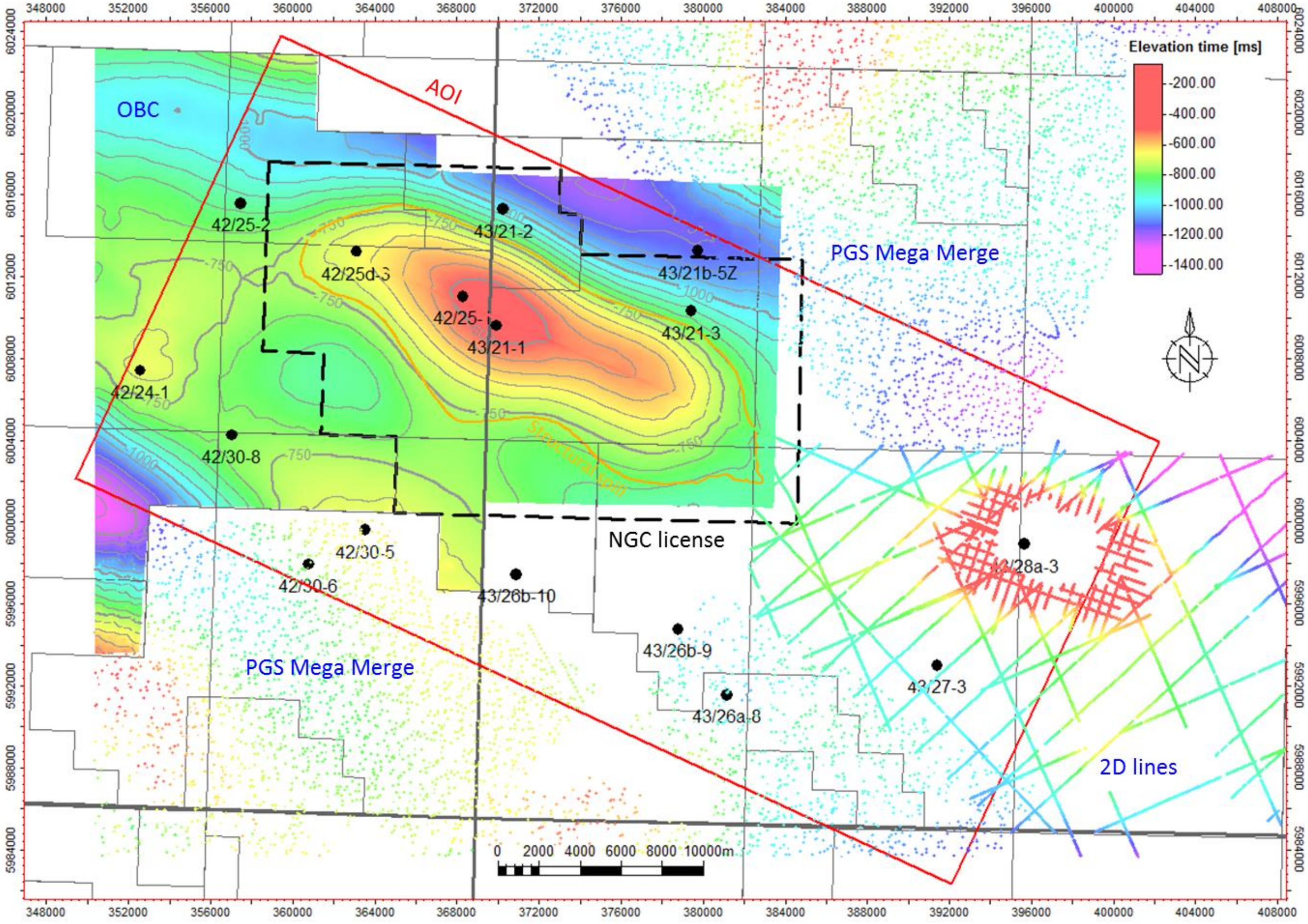

Figure 3.15: Composite Top Bunter Sand TWT Interpretation

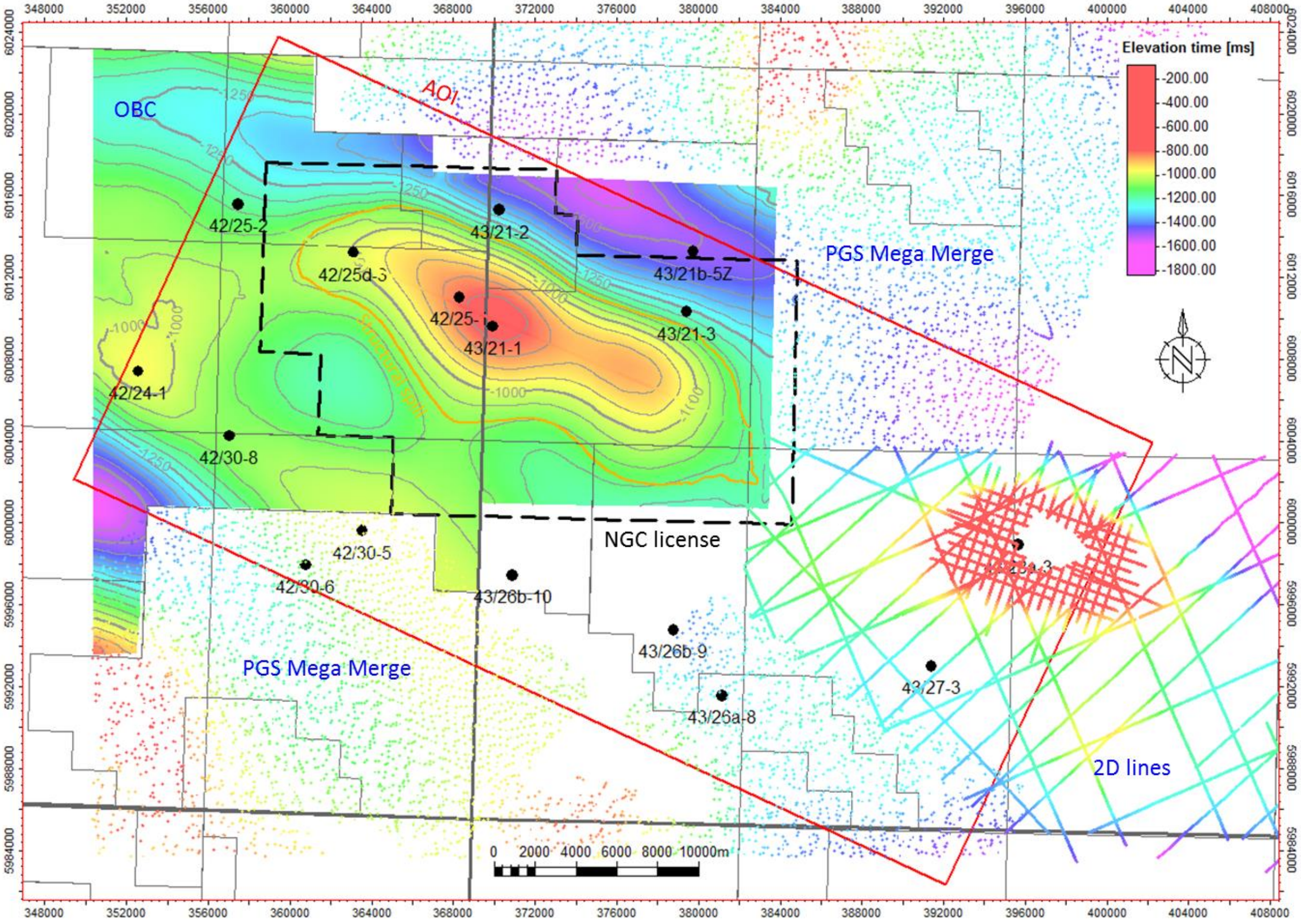

Figure 3.16: Composite Top Zechstein TWT Interpretation

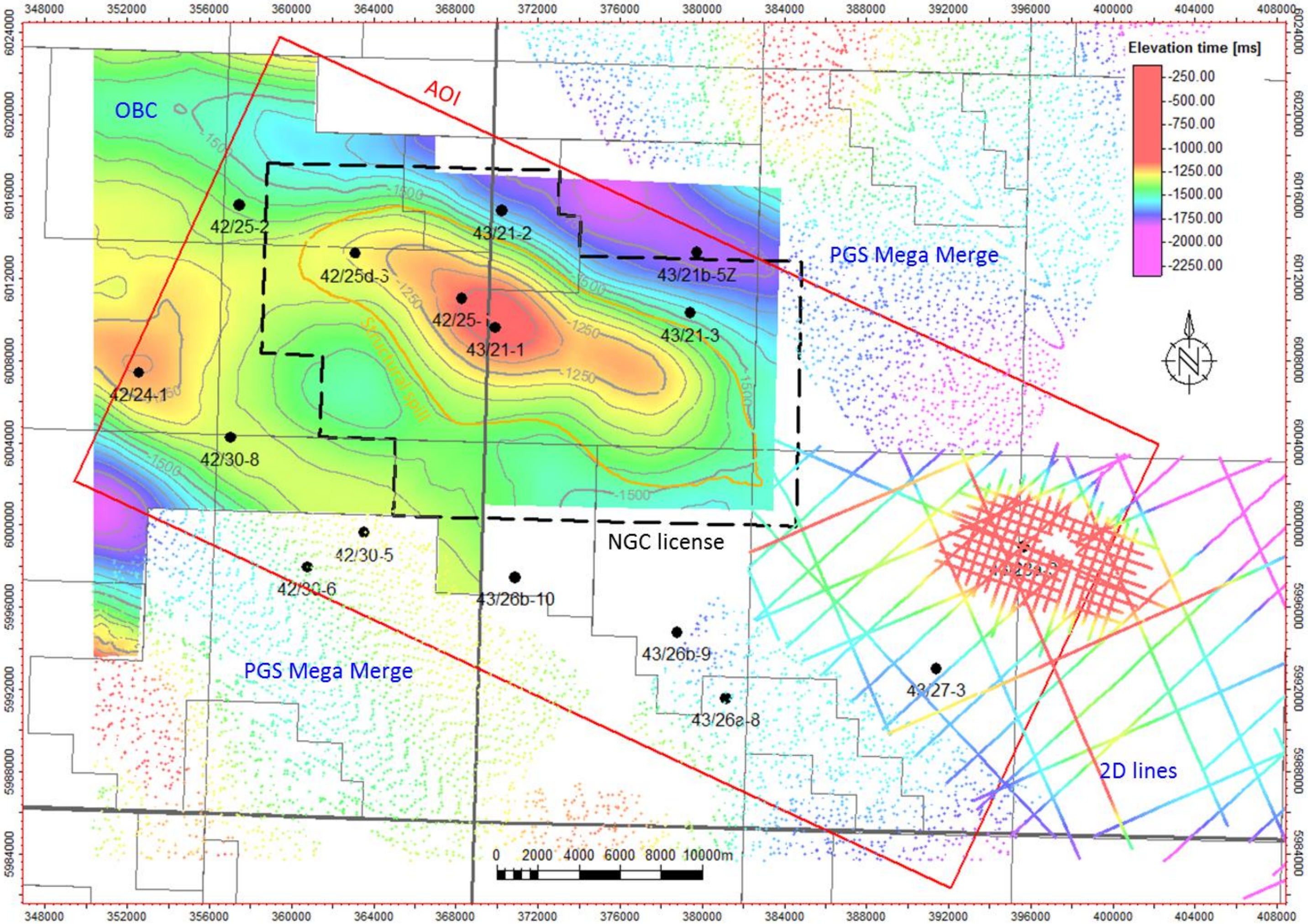

Figure 3.17: Composite Top Rotliegend TWT Interpretation

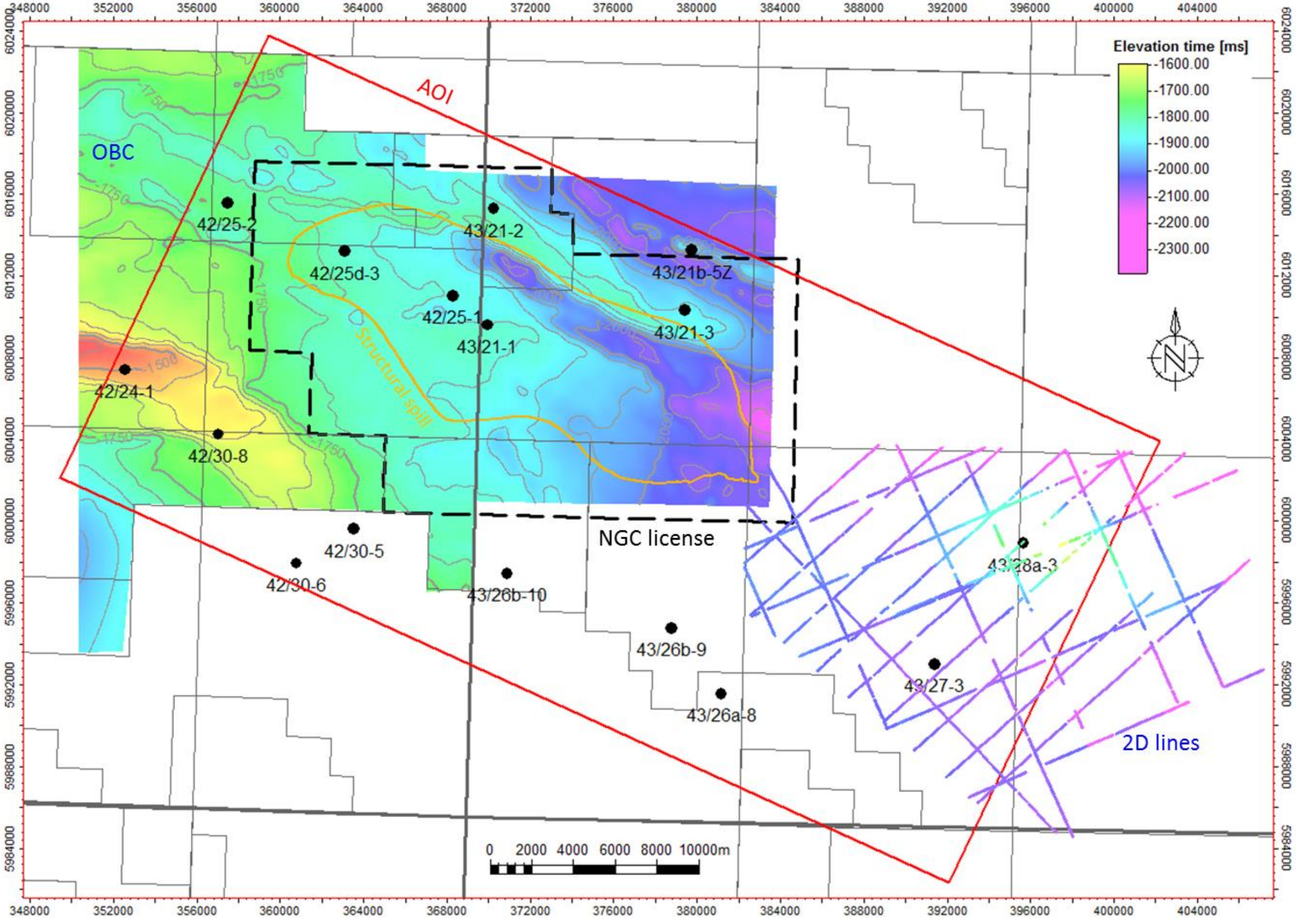

3.2.1 Depth Conversion and Uncertainties

Time horizons have been depth converted using a V0k type layer-cake model based on well checkshot velocities. Interval velocity grids were calculated for each layer from the well depths and seismic times.

A constant sea velocity of 1480m/s was used to the seabed, then velocity layers modelled to Top Triassic, then to Top Bunter Sand, and then to Top Zechstein. For these layers, a linear regression analysis of well velocities estimated the interval velocity at the top of the layer (V0 or intercept) and the acceleration term of the velocity within the layer (k or gradient). Figure 3.18 shows the initial layer-based linear fit (shown as solid black lines) of the V0k function to the well velocities. V0 points were then gridded over the area of interest while the k term was held fixed. Each of the bounding horizons were then depth converted in turn, top down, with depth residuals (between predicted and actual well tops) projected back onto the V0 velocity grids before proceeding down to the next horizon. This process creates a 3D velocity model through which seismic time objects can be converted to depth and vice versa.

This method was used prior to drilling the 42/25d-3 appraisal well in summer 2013 to prognose depths for the two seismic reflectors (Top Triassic and Top Bunter Sands). Other prognosed depths were derived from isochoring from surrounding wells (Table 3.1). The uncertainties quoted in Table 3.1, below are ±25m and ±29m, these being derived from 1 standard deviation (SD) of well top residuals. The wellsite tops for Top Triassic came in 11.5 m deep to prognosis and the Top Bunter Sands 32.6 m deep. Figure 3.19 is the data acquisition summary for the 42/25d-3 well and shows the actual versus prognosed differences.

Figure 3.18: Initial linear fit of well velocities

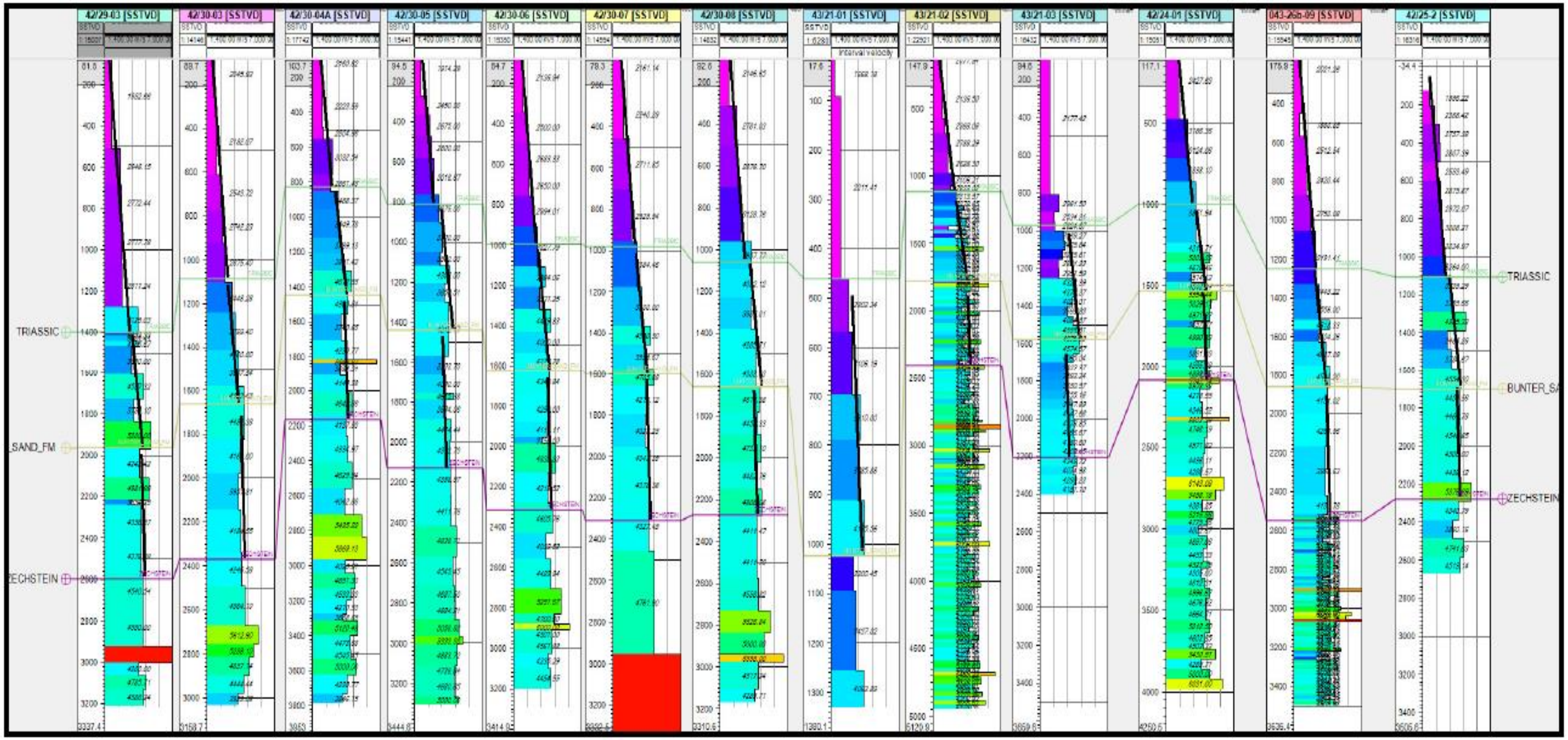

Table 3.1: Prognosed Depths Compered with Actual Depths as Reported at the 42/25d-3 Wellsite

Lithostratigraphical Prognosis				Actual Depth (wellsite)	
Formation Top	TWT [s]	Depth [m SS]	Uncertainty [m SS]	Depth [m SS]	Difference [m] (-=deep to prognosis)
Seabed		-56 (LAT)		-61.3	
Middle Jurassic		-56	+9 to -25m	-61.3	-5.3
Lias Group		-196	+/- 25m	-199.6	-3.6
Top Triassic (Haisborough Group)	0.680	-759	+/- 25m	-770.5	-11.5
Triton Anhydritic (Stag FWR)		(-759)		-783.0	-24
Top Keuper Anhydrite Member		-811	+/- 25m	-812.6	-1.6
Base Keuper Anhydrite Member		-854	+/- 25m	-862.0	-8.0
Dudgeon Formation		-900	+/- 25m	-913.5	-13.5
Dowsing Formation		-999	+/- 25m	-1015.9	-16.9
Muschelkalk Halite Member		-1043	+/- 29m	-1068.9	-25.9
Base Muschelkalk Halite Member		-1107	+/- 29m	-1129.3	-22.3
Upper Röt Halite Member		-1225	+/- 29m	-1250.0	-25.0
Main Halite Member				-1286.0	
Röt Clay Member		-1326	+/- 29m	-1358.2	-32.2
Bunter Sandstone Formation	0.997	-1336	+/- 29m	-1368.6	-32.6
Bunter Shale Formation		-1575	+/- 29m	-1592.0	-17.0
TD		-1655		-1655.7	-0.7

Figure 3.19: Overview of 42/25d-3 data acquisition and results including actual compared to prognosed depths

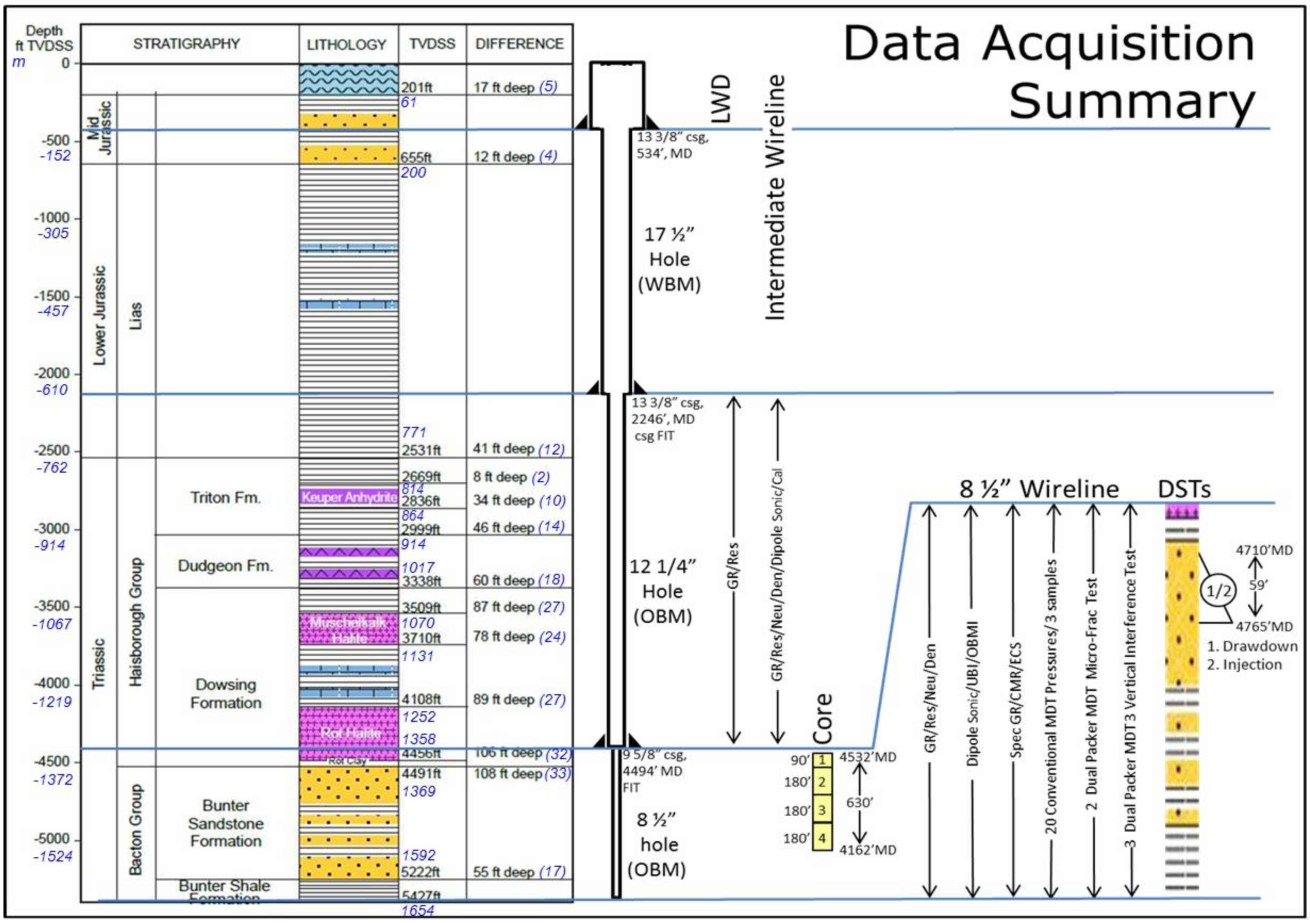

Alternative depth conversion methods were explored post-drilling the 42/25d-3 appraisal well as a means of providing a range of depth map predictions. Predicted depths from these alternative methods were found to be in the range already established by modifying parameters in the V0k method and thus confirm V0k as a reliable method for generating the geological structural model depths.

The uncertainty in depth conversion is reflected directly in the estimates of the structure volume and the NPV of the Storage Site. NPV uncertainty analysis shows that the GRV (Gross Rock Volume) is the most uncertain parameter, creating an NPV range of -16% to 11%. NPV uncertainty is discussed further in Section 3.8.2. It is however appropriate here to outline the workflow used to generate the gross rock volume.

3.2.1.1 Gross Rock Volume Uncertainty Workflow

The Petrel workflow (see Section 3.8.6) used for generating the range of gross rock volume is illustrated in Figure 3.20. Five hundred (500) realisations have been created in which multiple Top Bunter structures and Bunter Sandstone isochores are combined to estimate the GRV uncertainty range. The key elements of the workflow are summarised below.

Figure 3.20: Gross rock volume uncertainty workflow

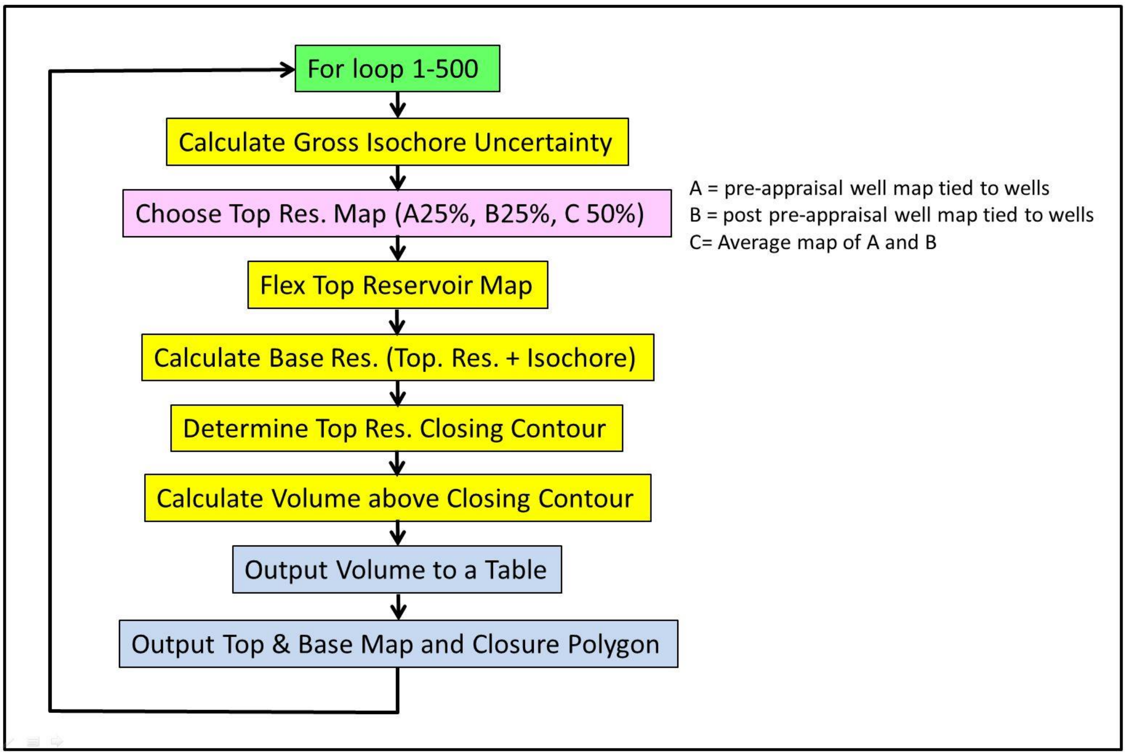

Three maps have been input into the workflow:

1. **Low Case Map (MAP A):** represents the pre 42/25d-3 map, tied to the Top Bunter depth point in this well using a 2km radius of adjustment (Figure 3.21). This map was depth converted without the northern flanking wells 43/21-2 and 43/21-3 which were seen to have anomalous velocities. The spill point for this map was -1460mTVDSS.
2. **High Case Map (MAP B):** represents a post 42/25d-3 map (Figure 3.22). For this case the depth conversion was revised incorporating northern flanking wells 43/21-2 and 43/21-3, creating a deeper structure that moved the spill down to -1520mTVDSS.
3. **Mid Case Map (MAP C):** is an average of the low and high cases (Figure 3.23) and was created to provide a realisation over the middle ground between the end member cases. It has a spill point of -1490mTVDSS.

Figure 3.21: Low Case Top Bunter Structure depth map (Map A)

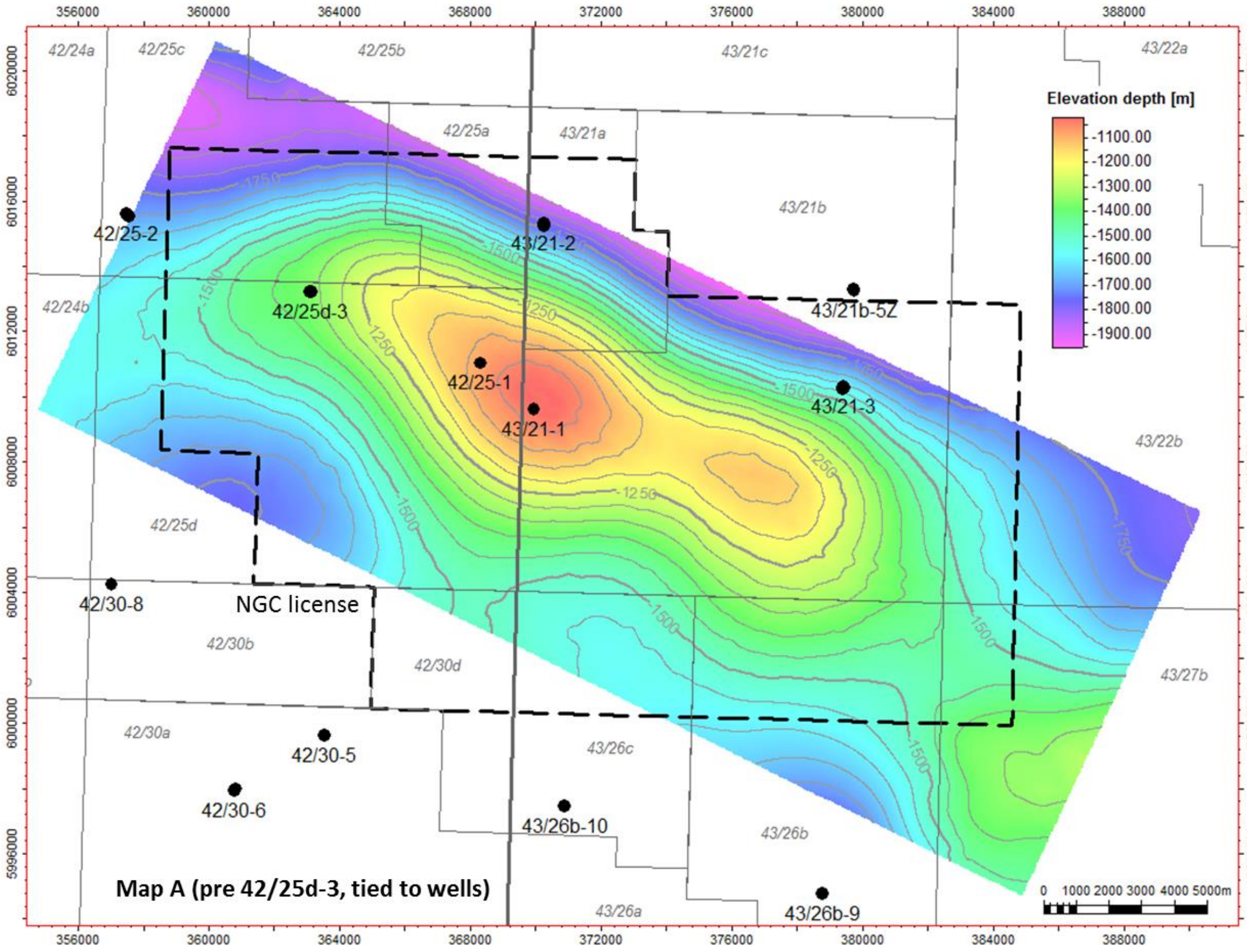

Figure 3.22: High Case Top Bunter Structure depth map (Map B)

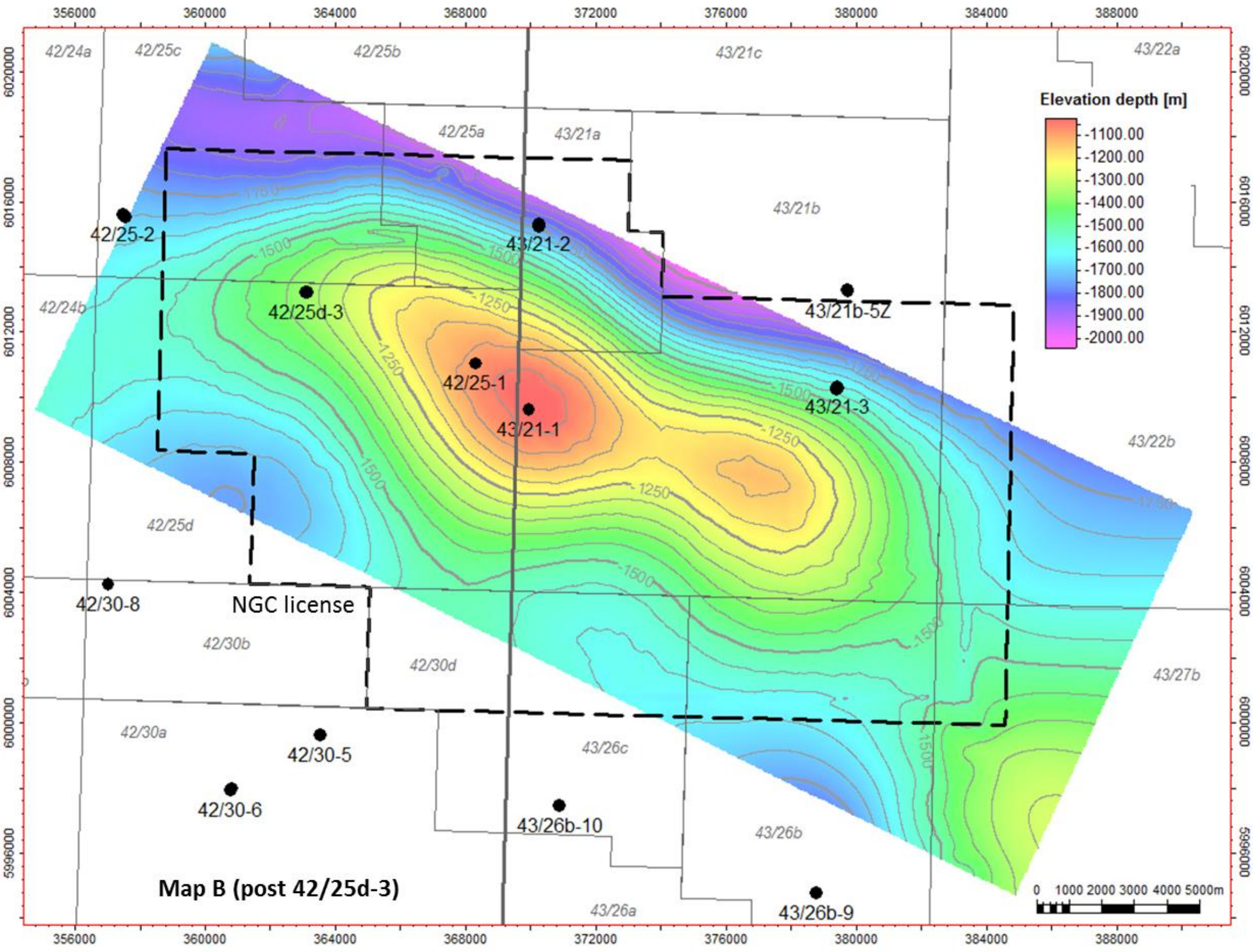

Figure 3.23: Mid Case Top Bunter Structure depth map (Map C)

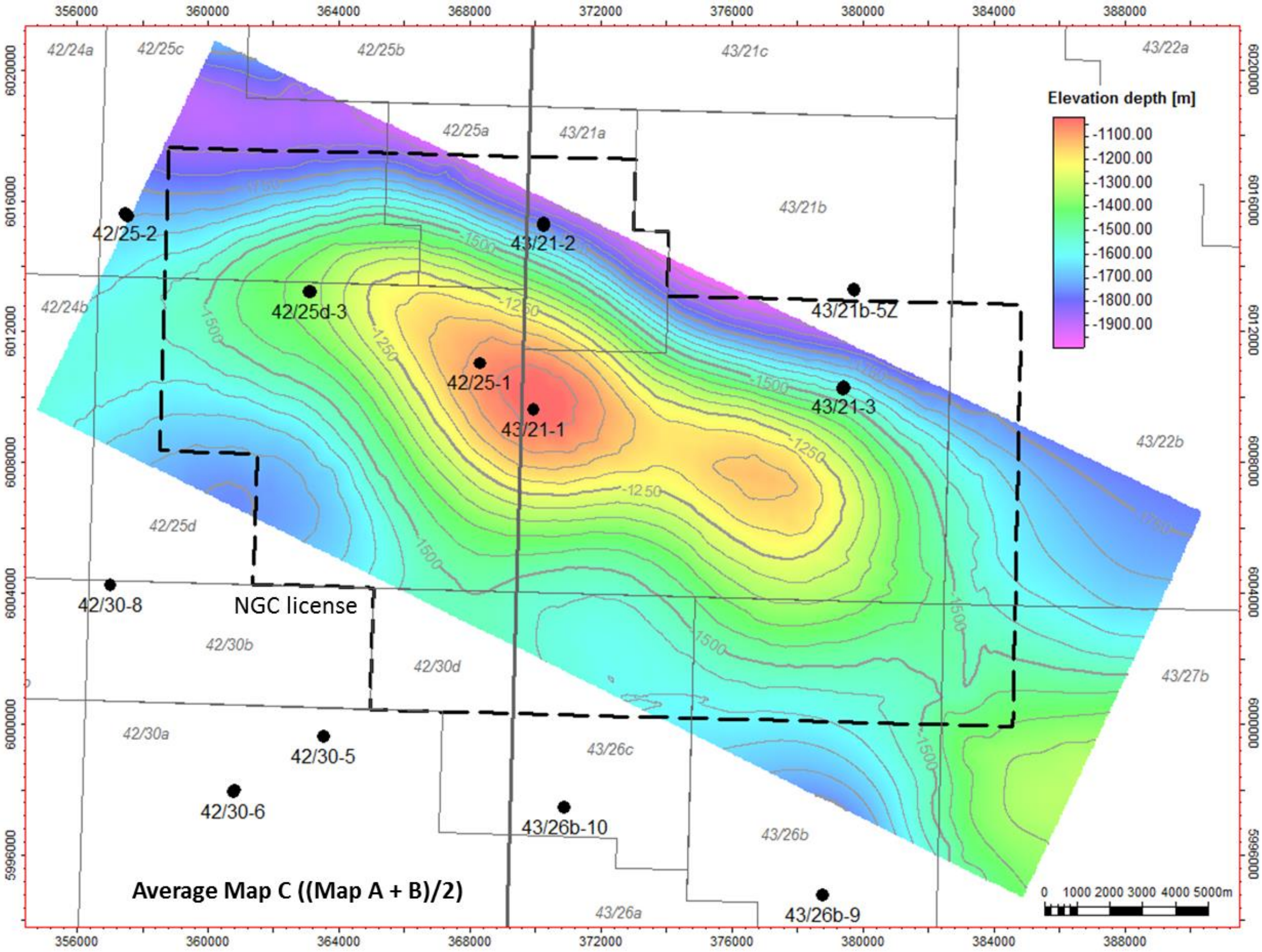

In the first part of the workflow a Bunter Sandstone isochore is generated whose thickness was ±10% of the base case isochore thickness. This isochore is then added onto to a Top Bunter structure to create a Base Bunter structure. The top structure map is based on either a low, mid or high Top Bunter structure cases (Maps A, C or B). The low and high case maps were each chosen 25% of the time leaving the mid case map being selected 50% of the time.

Once a map has been selected it is flexed in the workflow to create top reservoir depth variation. The method of flexing the map is similar to the method used to vary isochore thickness described above. A maximum top reservoir depth error surface is multiplied by a factor that ranges between -1 and +1 and then added to the selected top reservoir depth surface:

Uncertainty Top Structure = Top Structure + (Error Surface x Factor)

The error surface was based on the maximum depth error of 44.6m derived from the pre 42/25d-3 depth conversion process. The west-east cross section in Figure 3.24 illustrates the three input maps (Maps A, B and C) and the maximum and minimum depth surfaces that have been created by the uncertainty workflow. The depth uncertainty is greatest to the south east of the structure in the vicinity of the saddle that separates Endurance from the outcrop diapir structure. The estimated Endurance closing contours ranges from -1416m to -1553mTVDSS (137m range).

A similar cross section in Figure 3.25 shows the complete range of top and base reservoir structural uncertainty maps created by 500 runs of the Petrel GRV uncertainty workflow.

Figure 3.24: West-East cross-section across the Endurance structure illustrating the input depth surfaces and structural uncertainty

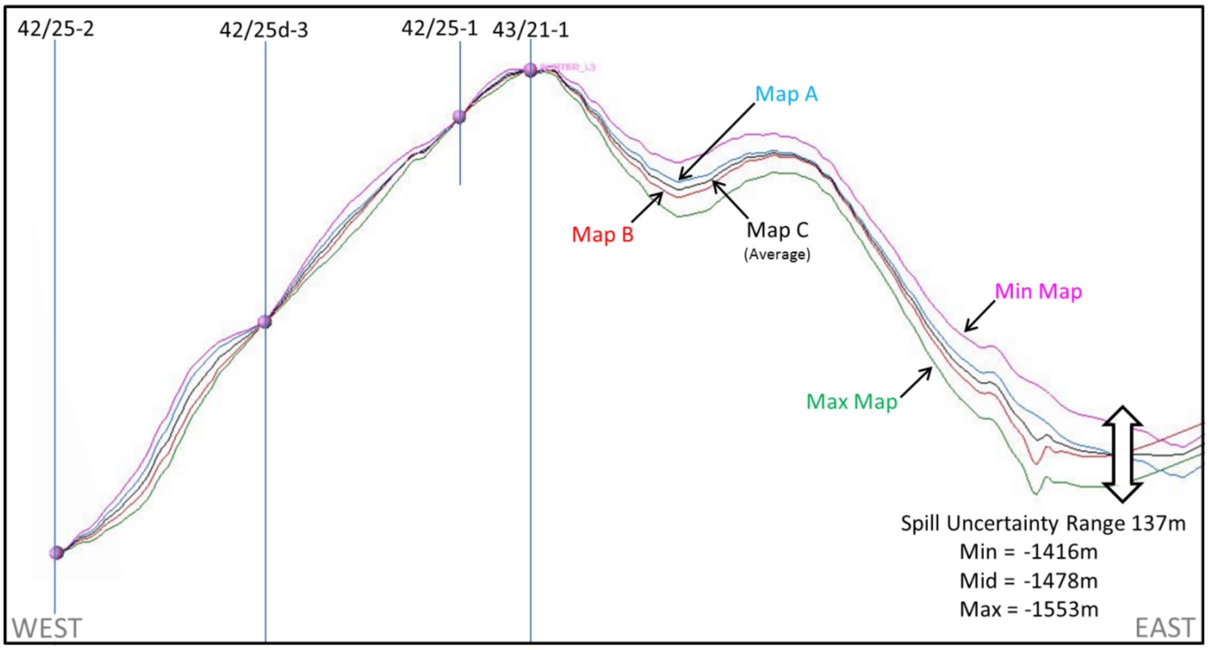

Figure 3.25: West-East cross section across the Endurance structure illustrating the complete range of top and base reservoir depth structures created by 500 runs of the uncertainty workflow.

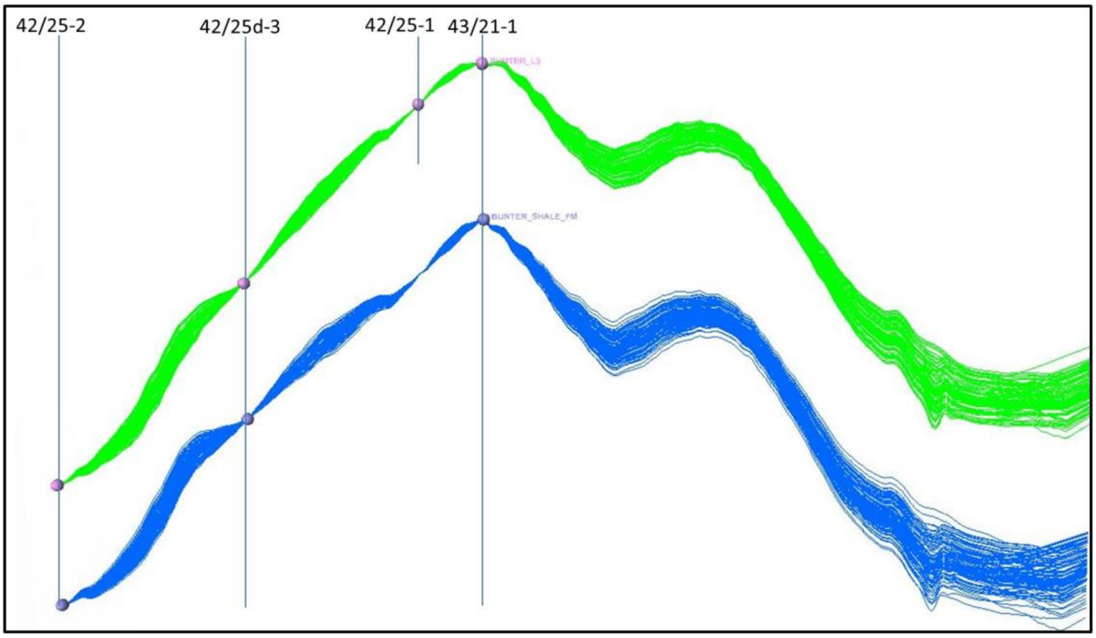

Once a structure has been selected and flexed for structural uncertainty, the lowest closing contour was determined using a simple routine that tests for volume in a narrow polygon beyond the maximum possible spill of -1553 m at progressively shallower levels (Figure 3.26). The spill point in the workflow is defined at the level where volume is no longer detected within the spill volumetrics polygon. Spill occurs mostly to the east but some of the larger structures spill to the south (Figure 3.27a). At this point the workflow saves the spill level for the particular realisation and uses it to calculate GRV of the Bunter interval.

Figure 3.26: Routine for determining the maximum closing spill contour of a structure.

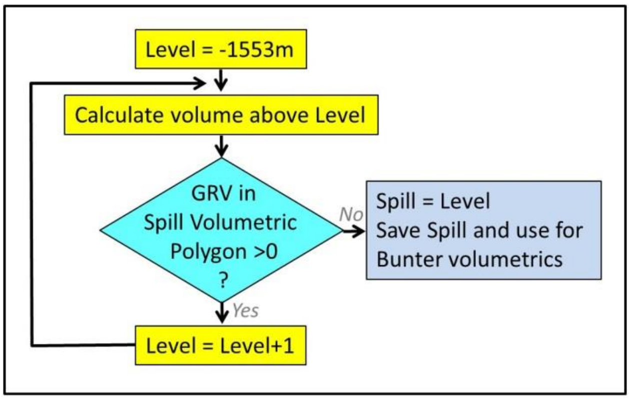

Figure 3.27: Top reservoir structure for the maximum (a) and minimum (b) maps illustrating the spill volumetrics polygon

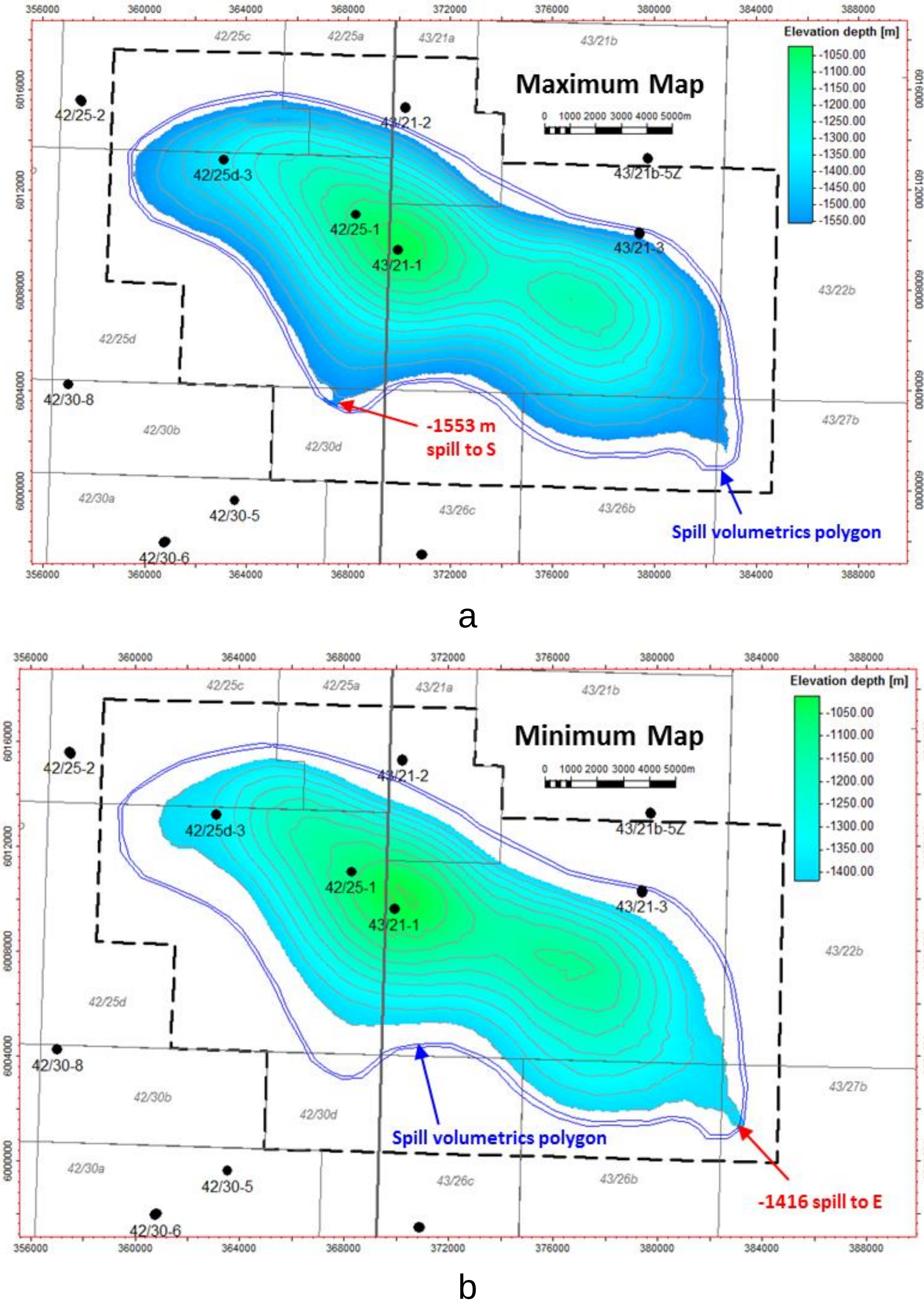

3.2.2 Structural Configuration and Faulting

Over the Endurance structure a North West - South East grain is observed consistent with the deeper Palaeozoic trend observed at Carboniferous/Permian level. Normal displacements in top Triassic reflectivity can clearly be traced down towards top Bunter but appear to sole out above the Röt Halite interval (Figure 3.28). There is no evidence of faults extending into the Bunter aquifer within the closure of the Endurance anticline. Even with the data dropouts affecting near surface continuity, it is likely that these faults would extend vertically up close to seabed, and this is confirmed on 2D high resolution appraisal well site survey seismic (Figure 3.29). Further interpretation using lately acquired Polarcus 3D seismic data provide additional confidence in this interpretation. Figure 3.30 shows comparison of fault interpretation for 2D Tieline, 3D Polarcus and 3D OBC data sets.

Faulting appears constrained to the axial part of the crest and this is thought to be related to sediment cover extensional forces due to underlying Zechstein salt swelling. Fault offsets in general appear relatively small and in the order of 10m to 40m, the lower limit representing the resolution of the seismic data. With increased proximity to the large Zechstein salt diapir to the south-east of Endurance, the faulting style increases in its complexity and frequency with a "concertina" style noted from many of the 2D lines that traverse the area surrounding this feature. A series of upward and downthrown Triassic blocks are noted here over the crest of the salt swell.

Figure 3.28: SW-NE arbitrary section (3D OBC volume)

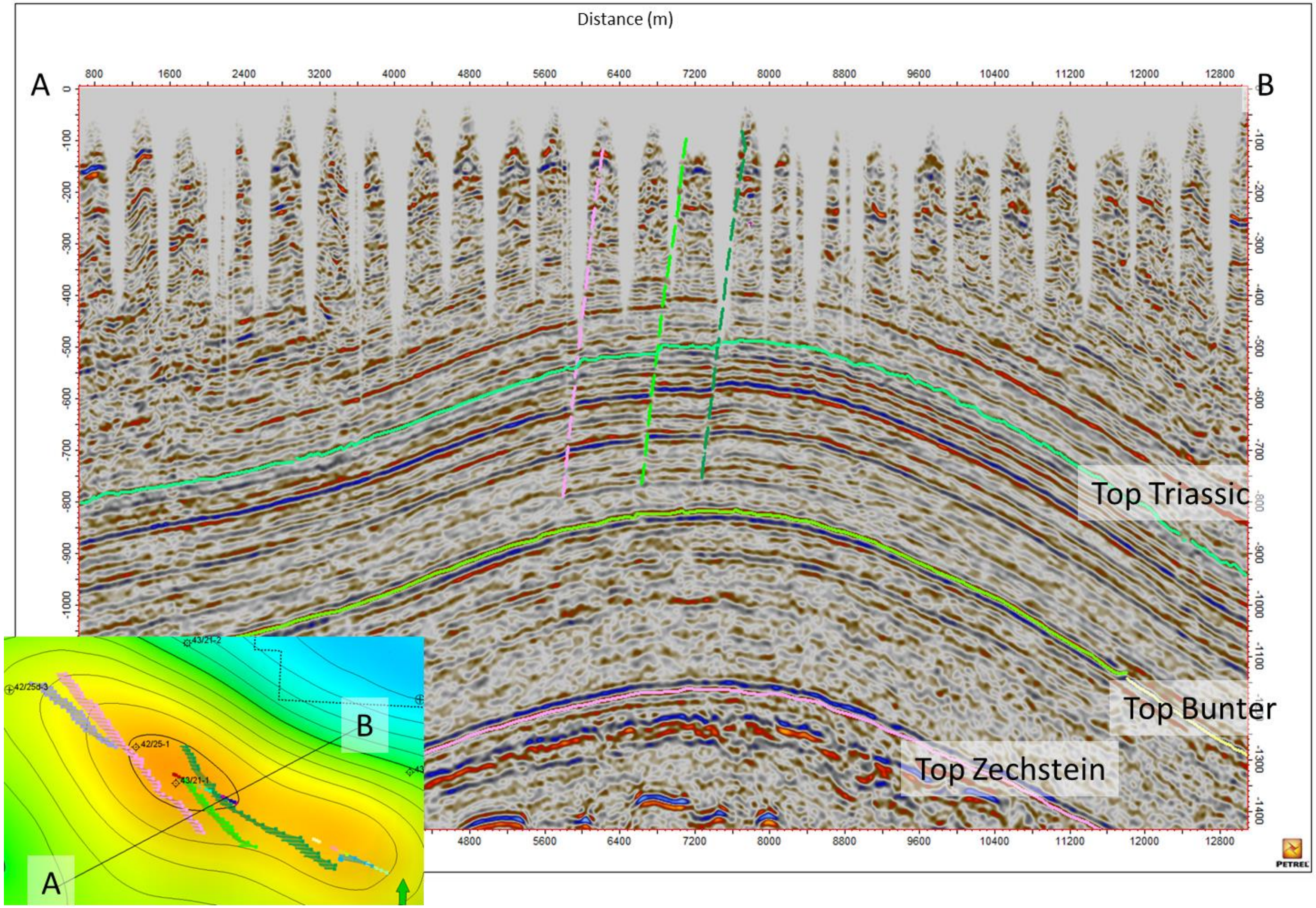

Figure 3.29: 43/21-3 P2 Site Survey Tie Line

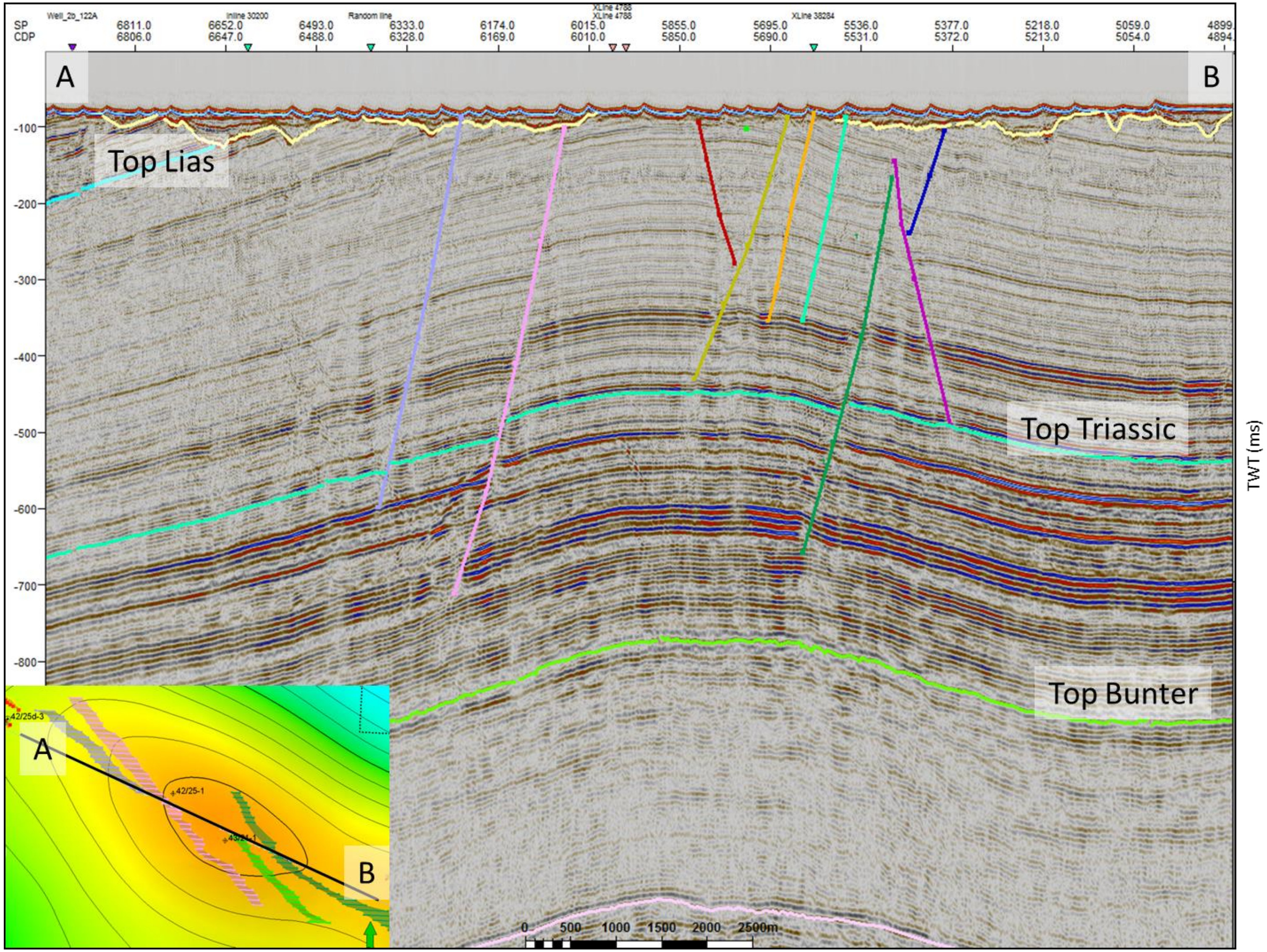

Figure 3.30: (A) Tieline 2D interpretation, (B) Polarcus interpretation, (C) OBC interpretation with OBC faults and Tieline faults

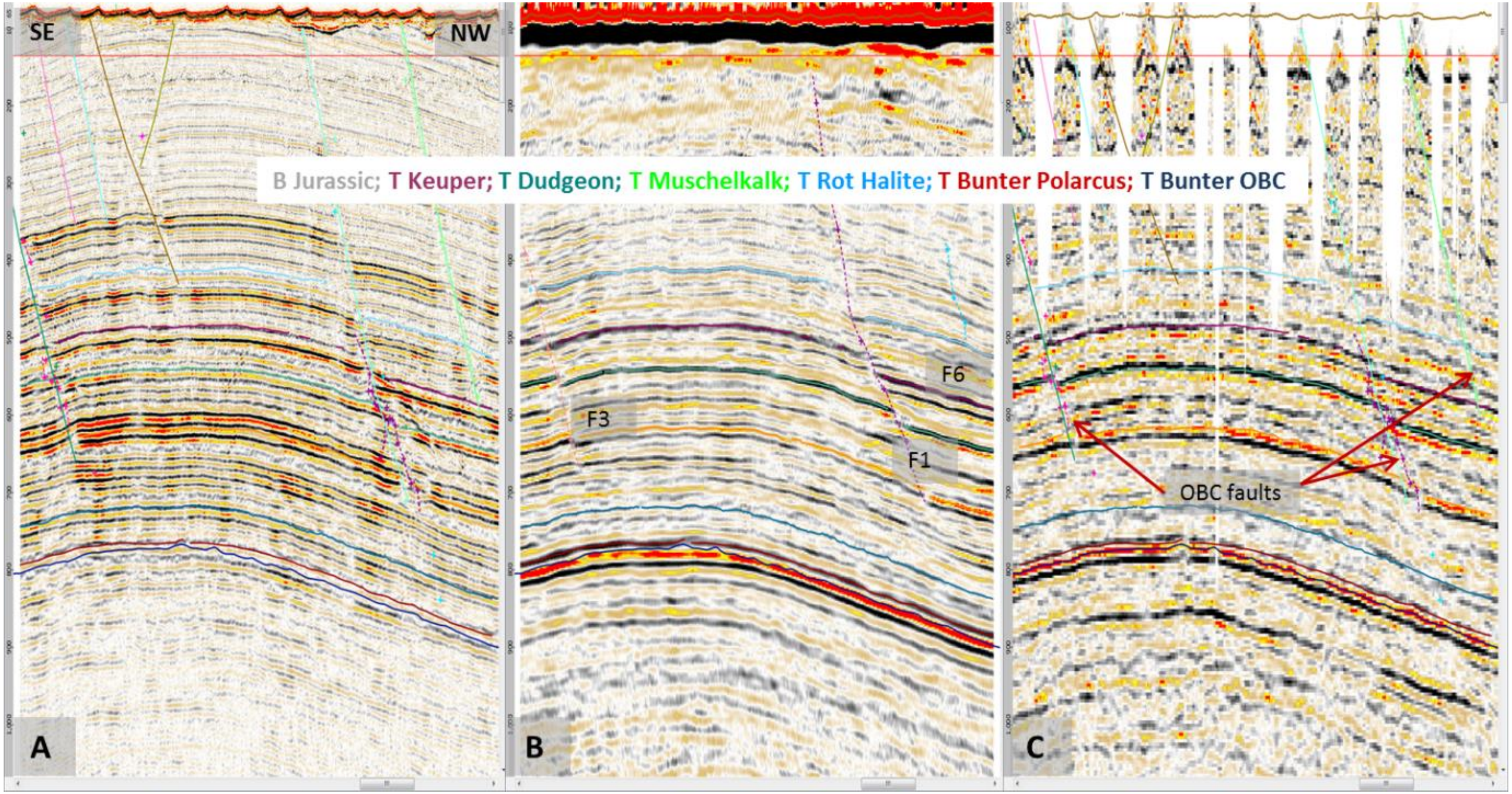

3.3 Depositional Setting and Sedimentological Framework

The Bunter Sandstone was deposited in a broad, land locked and gradually subsiding basin situated between 20º and 30º north of the equator. The climate was semi-arid with rivers and streams draining into the basin from surrounding highs and terminating in a playa lake situated within the basin centre. During drier periods, aeolian processes redistributed the sands, and mudstones were desiccated. Expansion of the playa lakes during wetter periods resulted in deposition similar to that of the underlying Bunter Shale Formation and presumably also similar to that of the overlying Röt Clay. Figure 3.31 illustrates the gross regional palaeo geographic setting during Bunter deposition.

The Bunter Sandstone comprises a number of large-scale fining-upwards units in which predominantly fluvial and aeolian sandstones fine upwards into siltstone and claystone alternations of the playa margin facies. Low permeability facies such as clay rich playa mudstones and playa margin flood plain siltstones, deposited during periods of low energy or lake expansion, are abundant in the Lower Bunter. Coarser-grained deposits are more common in the middle and upper parts of the Bunter Sandstone.

Sedimentological logging of the Bunter section in 42/25d-3 supports a depositional model with a general preponderance of coarser-grained fluvial and Aeolian facies. This is probably due to the proximal position of the 42/25d-3 in relation to the regional transport directions (Figure 3.31 and Figure 3.32) compared to the wells examined by Leppard. Well 44/26-1 for example lies farther south than 42/25d-3 and consists exclusively of siltstones, very fine sandstones and minor mudstones and therefore represents a more distal location. Sedimentological interpretation from the short core (16m) recovered from well 42/25-1, the closest well to 42/25d-3, show sandstones that comprise finely interbedded sequence of sand sheet, playa margin, aeolian and fluvial laminated facies. The absence of well-developed finer-grained facies in 42/25d-3 has hindered the subdivision of the Bunter Sandstone into lower-order stratigraphic units based on sedimentology. This has, however, been achieved using chemostratigraphy, where the BSF has been divided into three main units (L1, L2, & L3 from the base up, equivalent to P1, P2, & P3).

The 42/25d-3 core log has been split into six facies successions which include fluvial deposits (mainly sheetfloods) subject to occasional aeolian reworking. The dominant lithology is very-fine to fine-grained sandstone. The only Mudstone bed seen in 42/25d-3 is about 0.35 ft (10 cm) thick, comprising muddy siltstones with irregular top and base, and interpreted as laterally inextensive. A bed of presumed reworked ooids from the underlying Rögenstein section is thought to be regionally extensive, and forms a distinct calcareous horizon several feet thick. Nodular anhydrite cement is common at numerous horizons.

Although the depositional interpretation has centred around the 42/25d-3 appraisal well, data and analysis from wells around the Endurance structure, have been used to constrain the interpretation.

Figure 3.31: Schematic representation of Bunter Sandstone depositional environments in the region around the 42/25d-3 well

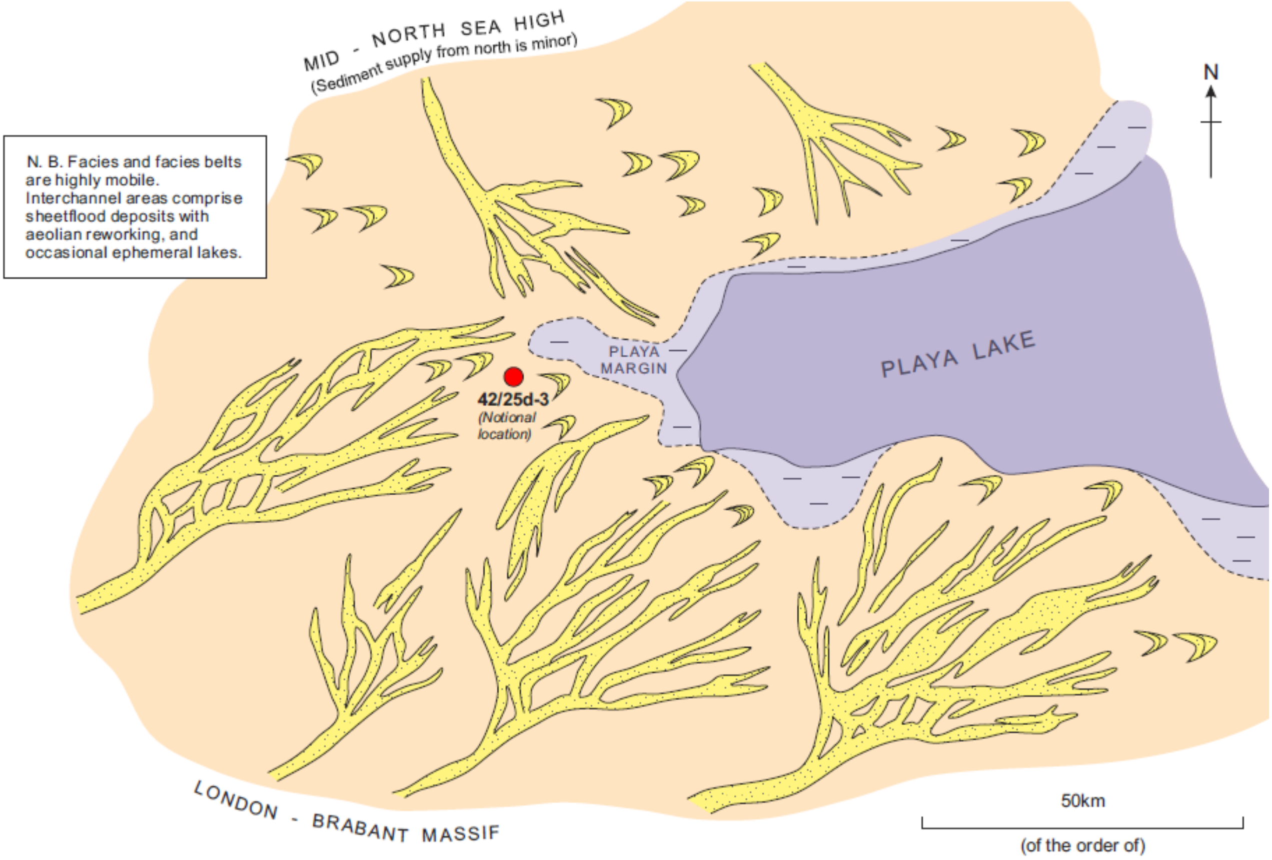

Figure 3.32: Location map

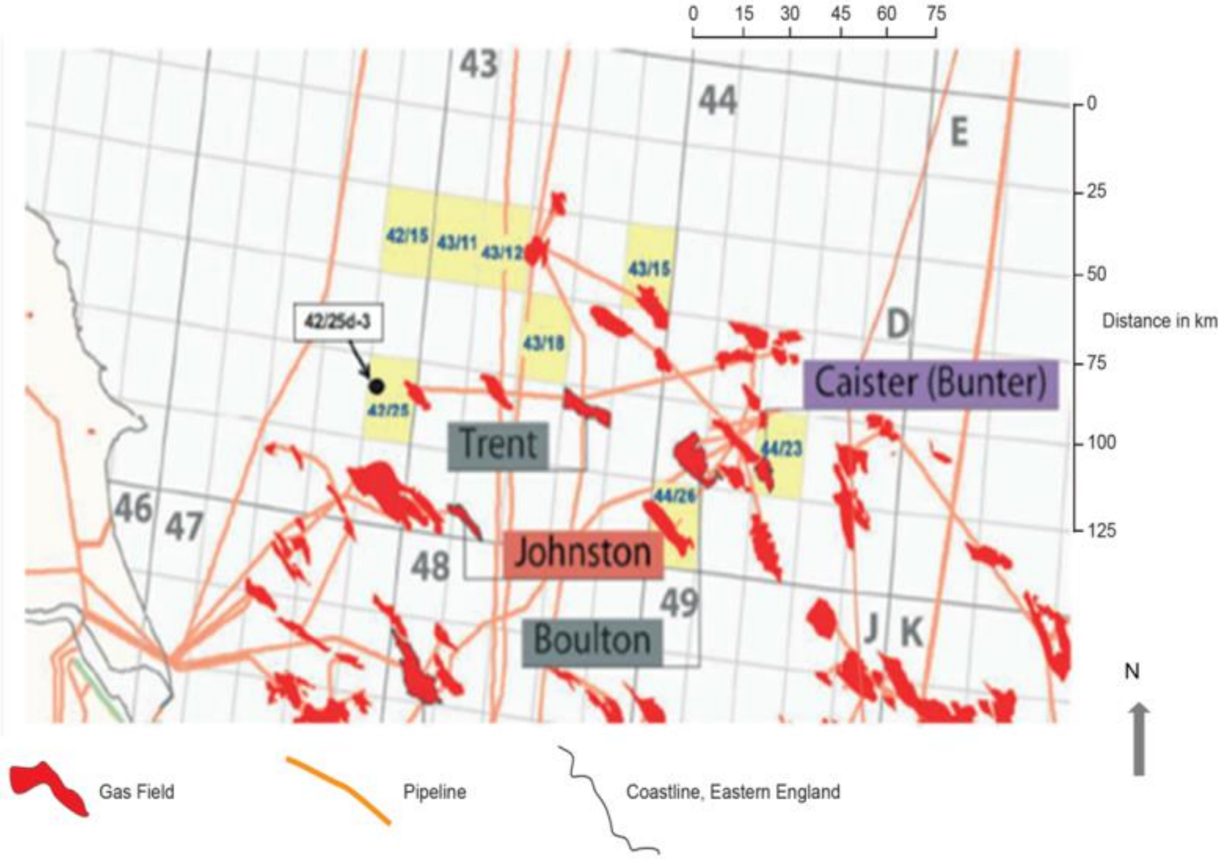

The location map shown in Figure 3.32 is an extract highlighting (in yellow) the blocks that include wells studied by Leppard's "Sedimentology Study of Regional Model Building for an Aquifer Storage System in the Bunter Formation" (2011). The position of well 42/25d-3 is also indicated.

3.3.1 Petrographic and Chemostratigraphic Input

3.3.1.1 Chemostratigraphic Input

In the absence of microfossils, obvious regional shale breaks and repeatable log character, Chemostratigraphy provided the best means of correlating the sandstone packages. Mineral characterisation of rock samples from the Triassic Bunter Sandstone successions encountered by wells 42/25d-3, 42/25-1, 42/30-6, 43/21-1, 43/21-2 and 43/21-3, established four chemostratigraphic packages and six chemostratigraphic units within the study interval as outlined in Table 3.2. The mineral characterization was based on changes in the feldspar, heavy mineral and mica content within the study interval as shown in Figure 3.33 and Table 3.2 (which shows the key elemental ratios used in the chemostratigraphic interpretation).

Two hundred and ninety-five Bunter sandstone samples have been analysed for this study, using Inductively-Coupled Plasma - Optical Emission Spectrometry (ICP-OES) and Inductively-Coupled Plasma - Mass Spectrometry (ICP-MS), with the samples prepared by an alkali fusion procedure. Data was acquired for ten major elements, e.g., Si, Ti, Al, etc., twenty-four trace elements, e.g., Ba, Be, Co, etc., and fourteen rare earth elements, e.g., La, Ce, Pr, etc. . The precision error in data acquisition for the majority of these elements is found to be c. 5%, though the precision error for the W, Ti and Sn data ranges from 10% to 20% and these have been excluded from later interpretations. With respect to the standard reference materials, the absolute accuracy of all the data were generally considered to lie within the range of error achieved for multi-determinations of the same sample.

The chemostratigraphic zonations have formed the foundation for the correlation of the study wells as illustrated in Figure 3.38. The main features of the chemostratigraphic correlation are as follows:

- Package P3/L3 occurs in all wells and is consistently defined by its low Be/Al and high K/Rb, implying that it has increased levels of k-feldspar and decreased mica content than package P2/L2. Unit P3a/L3a is recognised in all wells and is characterised by higher K/Al values than the overlying P3b/L3b. Unit P3b/L3b is absent in well 42/25d-3.
- Package P2/L2 is defined in all wells by its high Be/Al and lower K/Rb values. These geochemical characteristics imply package P2/L2 has lower K-feldspar contents than the underlying P1/L1 and overlying P3/L3 packages. Unit P2a/L2a is well defined in all wells by an increased Be/Al values and decreased K/Al values compared to the overlying unit P2b/L2b (also defined in all wells).
- Package P1/L1 is consistently defined in all wells except well 42/25-1 (which did not penetrate the full sequence) by high K/Rb coupled with low Be/Al. Unit P1a/L1a is generally recognised in all wells except 42/25-1 by an increase in K/Al and Be/Al compared to the overlying unit P1b/L1b. Unit P1b/L1b is characterised by low Be/Al values which increase over this unit to a high on the boundary with package P2/L2.
- Package P0 is defined in wells 42/25d-3, 43/21-1 and 43/21-3 by both low K/Rb and Be/Al values, with the top of the package defined by increased K/Rb values. This change probably implies that package P1/L1 contains more K-feldspar than P0, with P0 considered to be equivalent to the Bunter Shale which underlies the Bunter Sandstone.

Table 3.2: Chemostratigraphic zonation of wells 42/25d-3, 42/25-1, 42/30-6, 43/21-1, 43/21-2 and 43/21-3 within the Bunter sandstone

Heading Left	Heading Right	Heading Right	Heading Right	Heading Right	Heading Right	Heading Right	Heading Right
P3	P3b		1113	1667	1056	1818	1614
	P3a	1406	1125	1712	1077	1859	1642
P2	P2b	1425	1141	1781	1095	1893	1670
	P2a	1470	1172	1832	1153	1917	1714
P1	P1b	1534		1856	1201	1950	1751
	P1a	1578		1921	1258	2012	1796

All depths are in metres and are measured depths. Note P0 is not included because it lies within the Bunter shale.

Figure 3.33: Key geochemical profiles for well 42/25d-3.

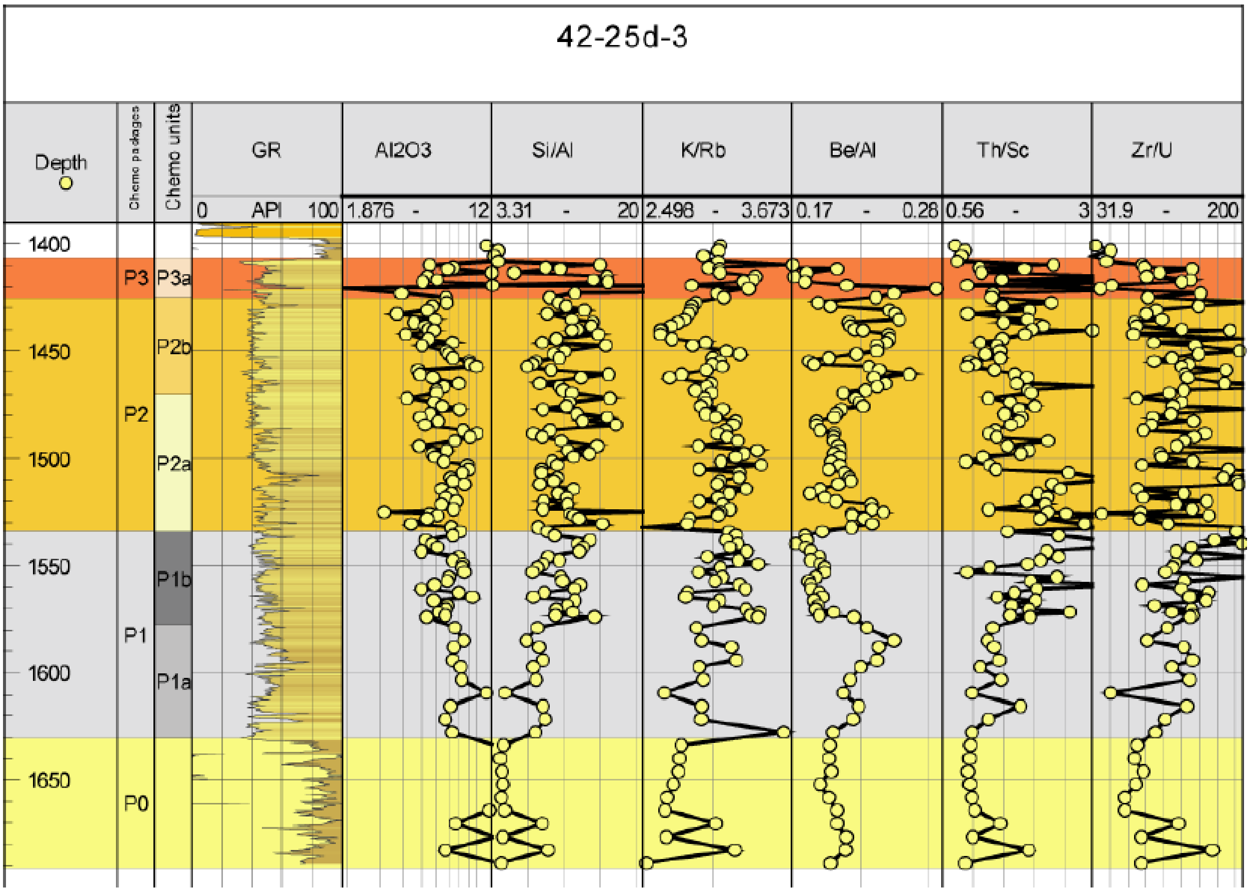

Table 3.3: Key Elements Ratios and Their Mineral Affinities

Element Ratio	Interpretation
K/Al	K feldspar/illite mica
K/Rb	K feldspar/illite mica
Be/Al	Micas/clay
Si/Al	Sand/clay
Zr/U	Zircons

Figure 3.34: A 6 Layer Inter-Well Correlation Incorporating Chemostratigraphic Sub-Layers

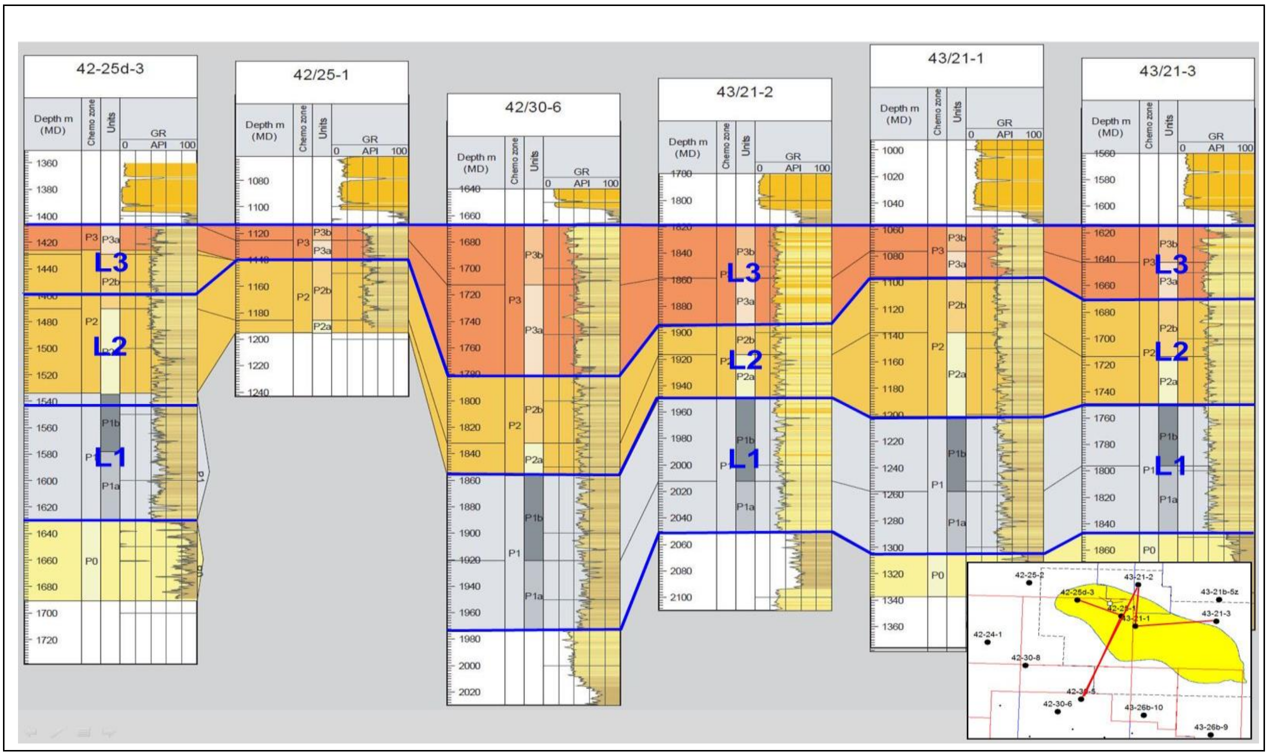

3.3.1.2 *Petrographic Input*

Optical petrographic analysis was performed on fifty core plugs recovered from the Triassic section of well 42/25d-3 to aid sedimentological interpretation and characterisation of reservoir and sealing quality. The four cores cover the lower part of Röt Halite, and the full Röt Clay section and a significant proportion (167 m) of the Bunter Sandstone.

Within the Bunter Sandstone, detrital grains are dominated by quartz and feldspar, with lithic fragments of varying granitic compositions and altered volcanic material. Small volumes of mica and heavy minerals occur. Major authigenic cements include dolomite and anhydrite. Calcareous ooids reworked from underlying Rögenstein are abundant near the top, forming a distinct horizon with potentially reactive calcite mineralogy.

The petrography of the Röt Clay shows detrital grains comprising illite-rich clays and silt-grade quartz, with subordinate plagioclase and traces of alkali feldspar. Cements within the Röt Clay include dolomite, anhydrite and minor halite.

The Röt Halite is made up of coarsely crystalline halite with anhydrite present in trace amounts.

3.3.2 Reservoir Quality and Correlation

The average porosity of the extensively cored appraisal well 42/25d-3 ranged from 0.17 in the Lower Bunter to 0.24 in the Upper Bunter, with corresponding estimated average permeabilities of 100md and 800md. Similar values were observed in the crestal wells 42/25-1 (>0.13 porosity and 100mD horizontal permeability) and 43/21-1 (0.20 – 0.33 porosity and 205mD to 2100mD permeability) . The high values of porosity and permeability are suggestive of a post-depositional dissolution of detrital grains (most notably feldspars) and halite cements. Furthermore, although the reservoir lies at a relatively shallow level (1000-1500m) it is well documented that the Bunter Sandstone in the SNS was buried to a much deeper depth prior to being inverted in the Late Cretaceous to Early Tertiar. Based on the distribution of facies porosity from well 42/35d-3 core, reservoir quality was found to be largely independent of depositional facies. Apart from an overall slight reduction in reservoir quality downwards through the sequence, which results primarily from a reduction in grain size and an increase in the proportion of impermeable mudstone beds, the reservoir quality is remarkably uniform on large scales (Figure 3.35). The formation as a whole can be approximated to a single “tank”, with occasional laterally impersistent barriers to vertical permeability associated with thin mudstone horizons, and more widespread baffles associated either with concentrations of such mudstones (e.g. within playa margin facies), or cemented horizons.

The overriding control on reservoir quality appears to be diagenetic, related to post-depositional cementation and possibly dissolution. Anhydrite, dolomite and halite have all been recognised as potential cementing phases. Wells with cemented sandstone (wells 42/24-1, 42/25-2, and 43/21-3 in Figure 3.35) occur on the margin of the Endurance anticline where porosity ranges from being completely occluded to very low (0.05). This cementation appears to be more strongly developed at the top of the reservoir and creates a strong phase reversal on seismic data at the Top Bunter level. The phase reversal boundary is approximately conformant with the Endurance structure, lying close to the structural spill at least at the western end of the structure (Figure 3.11).

The Bunter sands have excellent porosity and permeability within the PRP boundary and are heavily cemented – and thus reservoir quality significantly deteriorates – outwith the PRP. Figure 3.35 shows the large differences in porosity (right hand track) between cemented and uncemented wells. The precise origin of the sharp interface between cemented and uncemented Bunter sandstone as represented by the PRP is not clear. The Thermohaline Circulation Model (TCM) to explain the absence of significant halite cement within the PRP in Endurance. The model envisages convection currents of lower salinity brine preferentially removing halite by dissolution. These convection currents are driven by differential heating of the reservoir through the underlying Zechstein salt.

Simulation of temperature distribution within the Endurance storage complex using highly idealised models have been performed to test the predictions of the TCM. The results agree broadly with the TCM predictions. The seabed above the salt diapir (outcrop) was predicted to be slightly warmer than further away. The temperature difference decreases down to 10°C within a 3km radius around the diapir centre – 10°C being the assumed seabed annual average temperature (Figure 3.36).

The resulting temperature trends confirm the differential heating of the Bunter Sandstone through the underlying Zechstein Salt, producing brine density variation of up to 3 kg/m^3 across the structure which is sufficient to trigger thermal convection. The temperature values, ranges and distributions used for this analysis are subject to significant uncertainty and depend on the grid resolution and various assumptions employed in the modelling. Nevertheless the work has been useful in that it lends support to the TCM mechanism.

All available data also show no evidence to support an interpretation of the PRP as a palaeo-GWC. Whilst the PRP boundary is approximately conformant with the Endurance structure, this is not the case regionally, see Figure 3.37, particularly at the 3/44 structure to the east of Endurance which is water bearing, but has the phase reversal cutting across the structure close to the crest. Gas chromatograph readings and processed logs failed to show any evidence of trapped residual gas which would be anticipated if hydrocarbon gas had been present in the structure. Similarly water samples from 42/25d-3 appraisal well recorded no evidence of hydrocarbon gas. Rock strength data from a mini-frac in Röt Clay cap rock from 42/25d-3 appraisal well indicate it is geomechanically strong. Wireline logs suggest the Röt Clay is consistent in both thickness and shale quality. Seismic interpretation shows no faults penetrating the Bunter reservoir over the Endurance structural closure that could act as potential leak paths for hydrocarbons.

The PRP boundary was used in reservoir models as a limit to the extent of better reservoir quality rock. The cemented sandstone margin of the Endurance structure is referred to as the hardground.

Figure 3.35: Cementation in the Endurance area wells. Note the L1, L2, L3 zonations are equivalent to P1, P2, P3 chemostratigraphic packages

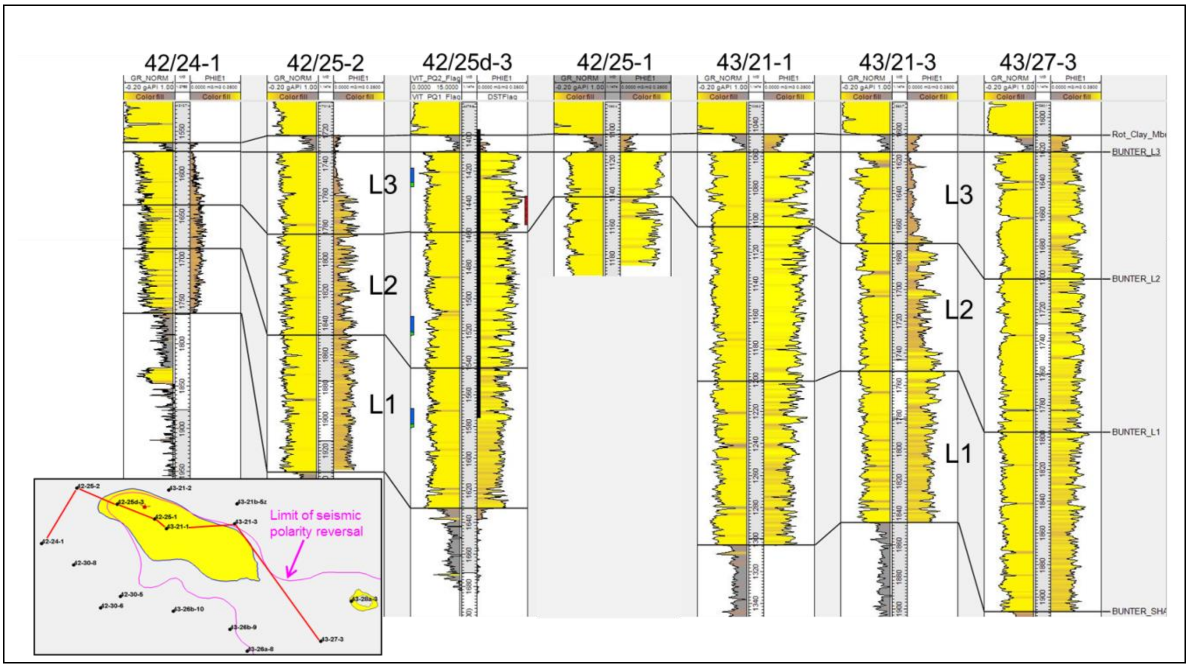

The explanation as to why the Endurance structure did not receive any hydrocarbon charge is that it is isolated from the regional source ‘kitchen’ by the Zechstien salt. There are a number of connected closures nearby and to the east (up to 50 km distant) which also are shown not to contain hydrocarbon gas and these structures are also underlain by thick Zechstein salts. The salts create a migration ‘shadow’.

The nearest connected Bunter sandstone structure that does contain hydrocarbons is the Esmond field 40km to the north. It is on the sub-basin margin and the Zechstein thins and is faulted in this area allowing charge to migrate up from below.

This theory is supported by:

a) analysis (isotopic) of the water samples obtained from the appraisal well that show the formation water to be predominately of Triassic age; and

b) The complete absence of even residual hydrocarbon, which would have been present if the sands had ever even had hydrocarbon passing through them. Special care was taken to sample and to identify any traces of hydrocarbon, which may have been present, but none was observed during the drilling and testing operations on the 43/25d-3 appraisal well.

Figure 3.36: Estimated Temperature Distribution along North West-South East Cross-Line

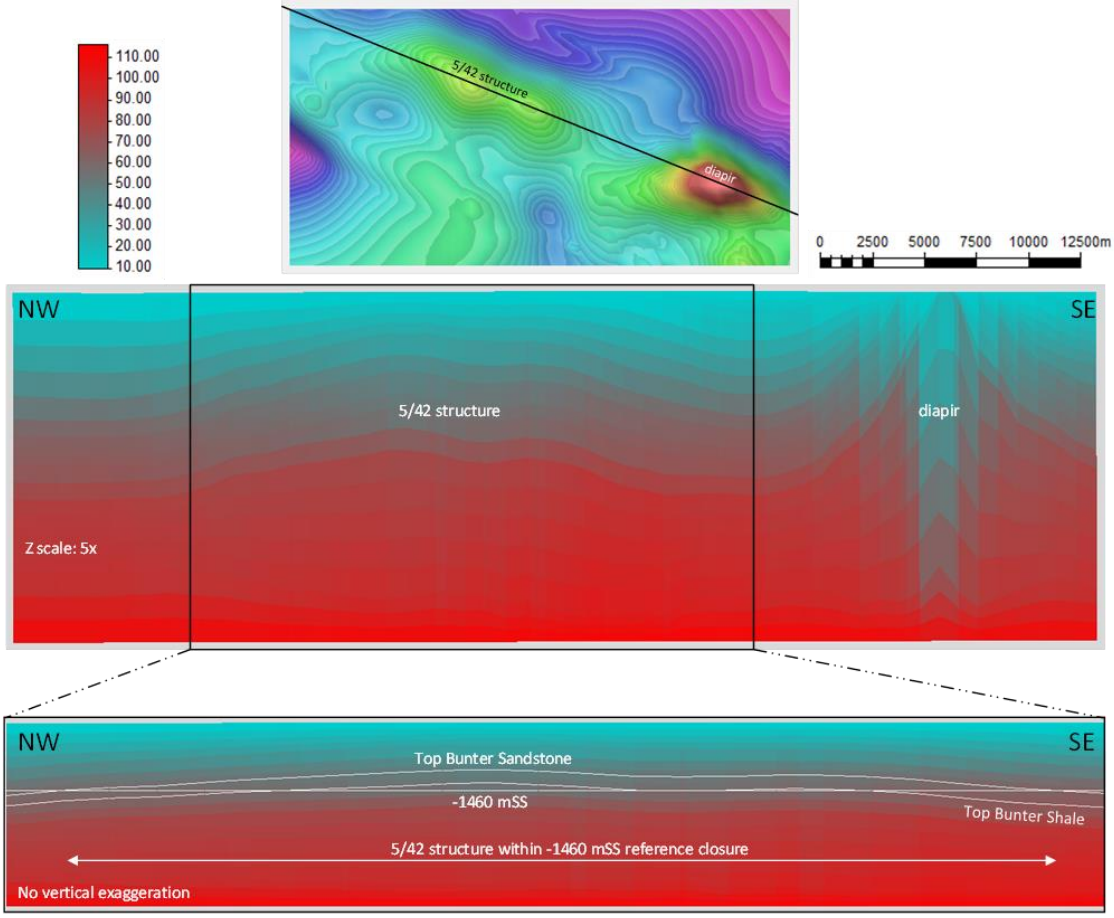

Figure 3.37: Outline of Endurance and the regional extent of the PRP

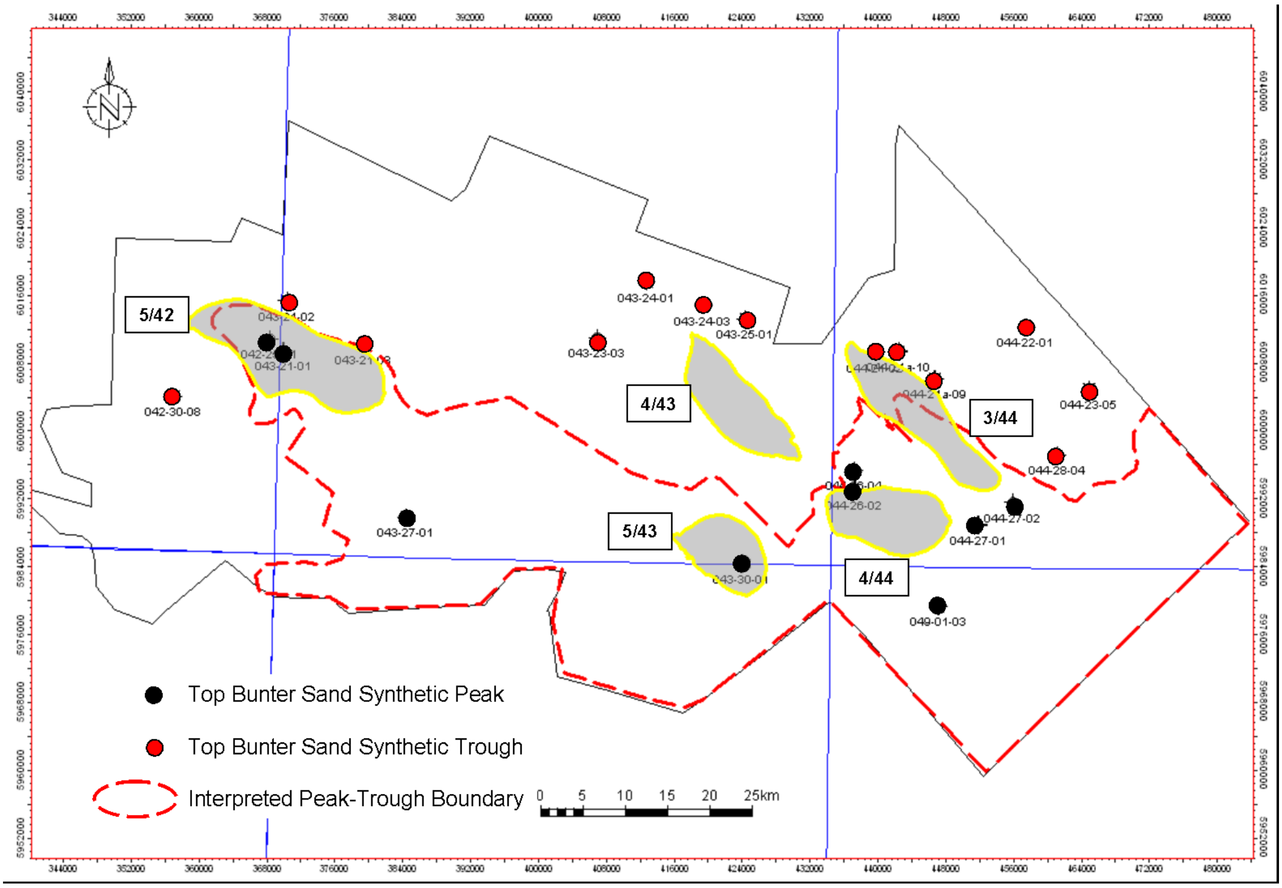

As already noted in the section on Chemostratigraphic input, the Bunter sandstone has been subdivided into 3 main zones, P1/L2 at the base, P2/L2 in the middle and P3/L3 at the top of the Bunter Sandstone. Each of these zones have been further split into two sub-zones; a lower “a” zone and an upper “b” zone. The Chemostratigraphic correlation in Figure 3.35 was expanded by interpolation to the wells without chemostratigraphic analysis, as illustrated in Figure 3.38 (note again the redesignation of the original chemostratigraphic zonations as L1, L2 and L3).

Figure 3.38: Endurance area Bunter Sandstone correlation

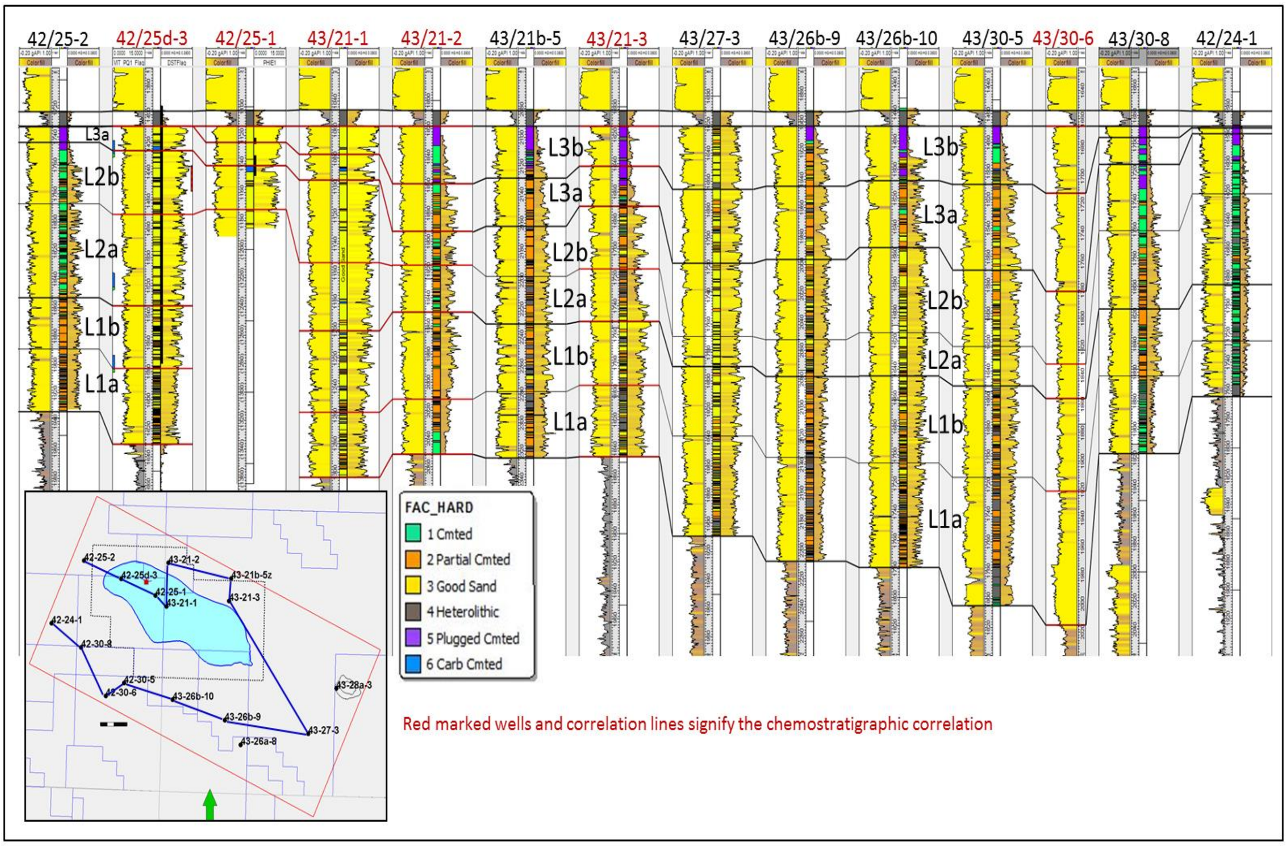

Red marked wells and correlation lines signify the chemostratigraphic correlation

3.4 Stratigraphic and Structural Framework

A Regional Structural Framework Model (RSFM) covering the full stratigraphic column from seabed to Top Rotliegend was built using the Build Simple Model process in Petrel, without faults. The RSFM provides a common platform for the geological, simulation and geomechanical models. The structural framework shared by the RSFM and the geomechanical models is shown in Figure 3.39. The geological and simulation models focus only on the horizons in the black rectangle except the geomechanical model which uses the entire RSFM (see Figure 3.57). The overburden faults described in Section 3.2.2 have only been included in the geomechanical model.

Figure 3.39: Petrel RSFM horizons

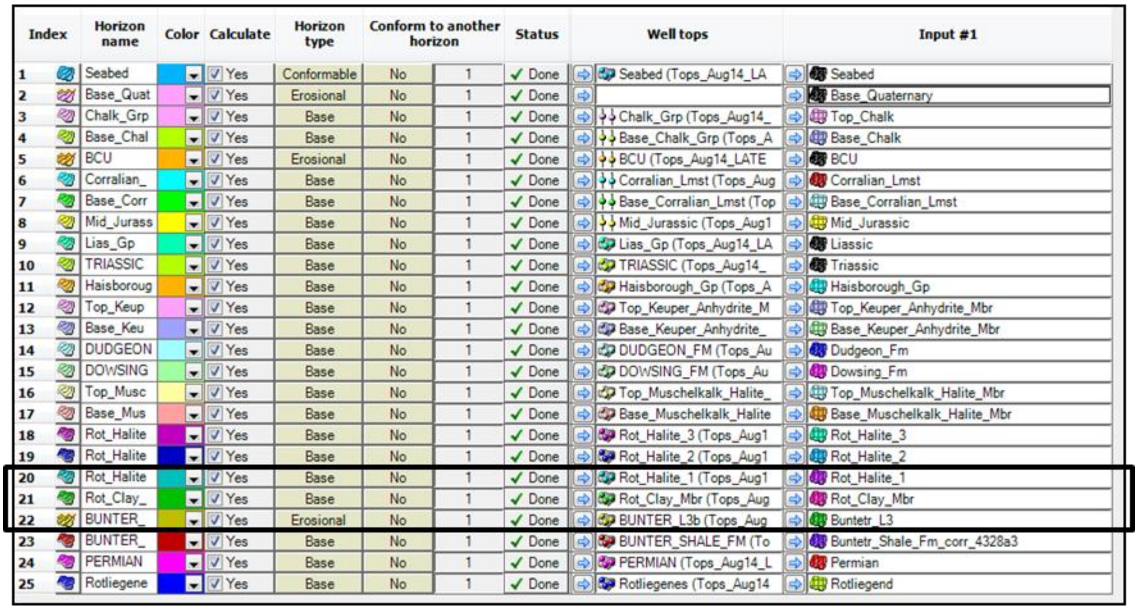

Index	Horizon name	Color	Calculate	Horizon type	Conform to another horizon		Status	Well tops	Input #1
1	Seabed	■	☑ Yes	Conformable	No	1	✓ Done	Seabed (Tops_Aug14_LA	Seabed
2	Base_Quat	■	☑ Yes	Erosional	No	1	✓ Done		Base_Quaternary
3	Chalk_Grp	■	☑ Yes	Base	No	1	✓ Done	Chalk_Grp (Tops_Aug14_	Top_Chalk
4	Base_Chal	■	☑ Yes	Base	No	1	✓ Done	Base_Chalk_Grp (Tops_A	Base_Chalk
5	BCU	■	☑ Yes	Erosional	No	1	✓ Done	BCU (Tops_Aug14_LATE	BCU
6	Corralian_	■	☑ Yes	Base	No	1	✓ Done	Corralian_Lmst (Tops_Aug	Corralian_Lmst
7	Base_Corr	■	☑ Yes	Base	No	1	✓ Done	Base_Corralian_Lmst (Top	Base_Corralian_Lmst
8	Mid_Jurass	■	☑ Yes	Base	No	1	✓ Done	Mid_Jurassic (Tops_Aug1	Mid_Jurassic
9	Lias_Gp	■	☑ Yes	Base	No	1	✓ Done	Lias_Gp (Tops_Aug14_LA	Liassic
10	TRIASSIC	■	☑ Yes	Base	No	1	✓ Done	TRIASSIC (Tops_Aug14_	Triassic
11	Haisboroug	■	☑ Yes	Base	No	1	✓ Done	Haisborough_Gp (Tops_A	Haisborough_Gp
12	Top_Keup	■	☑ Yes	Base	No	1	✓ Done	Top_Keuper_Anhydrite_M	Top_Keuper_Anhydrite_Mbr
13	Base_Keu	■	☑ Yes	Base	No	1	✓ Done	Base_Keuper_Anhydrite_	Base_Keuper_Anhydrite_Mbr
14	DUDGEON	■	☑ Yes	Base	No	1	✓ Done	DUDGEON_FM (Tops_Au	Dudgeon_Fm
15	DOWSING	■	☑ Yes	Base	No	1	✓ Done	DOWSING_FM (Tops_Au	Dowsing_Fm
16	Top_Musc	■	☑ Yes	Base	No	1	✓ Done	Top_Muschelkalk_Halite_	Top_Muschelkalk_Halite_Mbr
17	Base_Mus	■	☑ Yes	Base	No	1	✓ Done	Base_Muschelkalk_Halite	Base_Muschelkalk_Halite_Mbr
18	Rot_Halite	■	☑ Yes	Base	No	1	✓ Done	Rot_Halite_3 (Tops_Aug1	Rot_Halite_3
19	Rot_Halite	■	☑ Yes	Base	No	1	✓ Done	Rot_Halite_2 (Tops_Aug1	Rot_Halite_2
20	Rot_Halite	■	☑ Yes	Base	No	1	✓ Done	Rot_Halite_1 (Tops_Aug1	Rot_Halite_1
21	Rot_Clay_	■	☑ Yes	Base	No	1	✓ Done	Rot_Clay_Mbr (Tops_Aug	Rot_Clay_Mbr
22	BUNTER_	■	☑ Yes	Erosional	No	1	✓ Done	BUNTER_L3b (Tops_Aug	Buntetr_L3
23	BUNTER_	■	☑ Yes	Base	No	1	✓ Done	BUNTER_SHALE_FM (To	Buntetr_Shale_Fm_corr_4328a3
24	PERMIAN	■	☑ Yes	Base	No	1	✓ Done	PERMIAN (Tops_Aug14_L	Permian
25	Rotliegene	■	☑ Yes	Base	No	1	✓ Done	Rotliegenes (Tops_Aug14	Rotliegend

The RSFM has lateral cells dimensions of 100mx100m within the 44 x 47km AOI and is rotated by -25º to be parallel to the Endurance structural grain. No layering was applied so each zone is in effect one layer thick. The RSFM is designed to include 16 surrounding Bunter Sandstone well penetrations (Figure 3.40). A cross section through the RSFM is given in Figure 3.3.

Figure 3.40: Top Bunter depth structure with the RSFM AOI

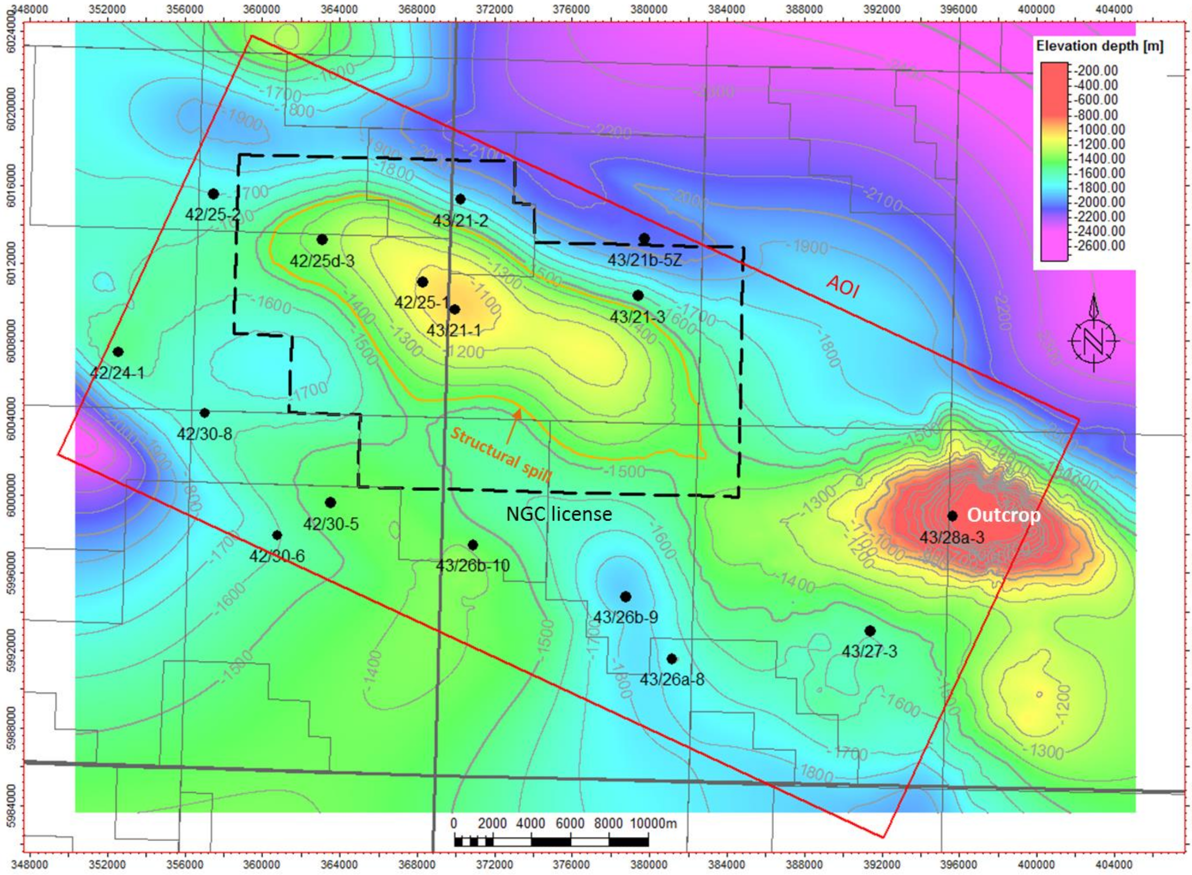

Note the full RSFM spans an area of 42 x 47km.

Out of a total of 16 wells in the AOI (Figure 3.41), 13 were subjected to petrophysical analysis for rock properties; the remaining three have incomplete data sets and have been used for correlation only. Additionally, the AOI includes the Bunter Sandstone seabed outcrop that overlies a Zechstein salt diapir 14km southwest of the Endurance structure.

Figure 3.41: Well database

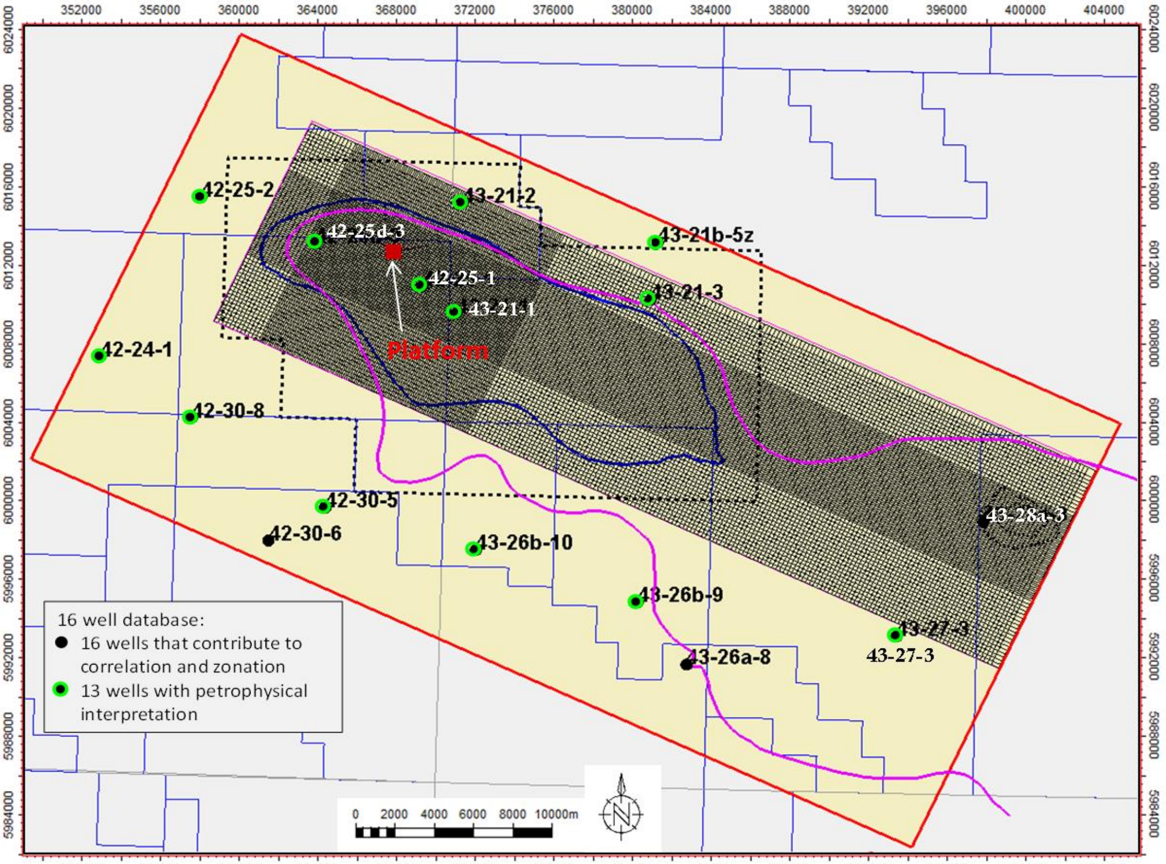

3.5 Primary and Secondary Seals

Above the Bunter Sandstone lies a thick sequence of shales and evaporites belonging to the Haisborough Group which constitutes the main regional sealing unit (Figure 3.42 and Figure 3.43). The overburden formations have consistent lithologies and only subtle thickness variations. In 43/21-1 a Muschelkalk thinning is attributed to a fault that is visible on the seismic.

Figure 3.42: Triassic lithostratigraphy (after SNS Atlas)

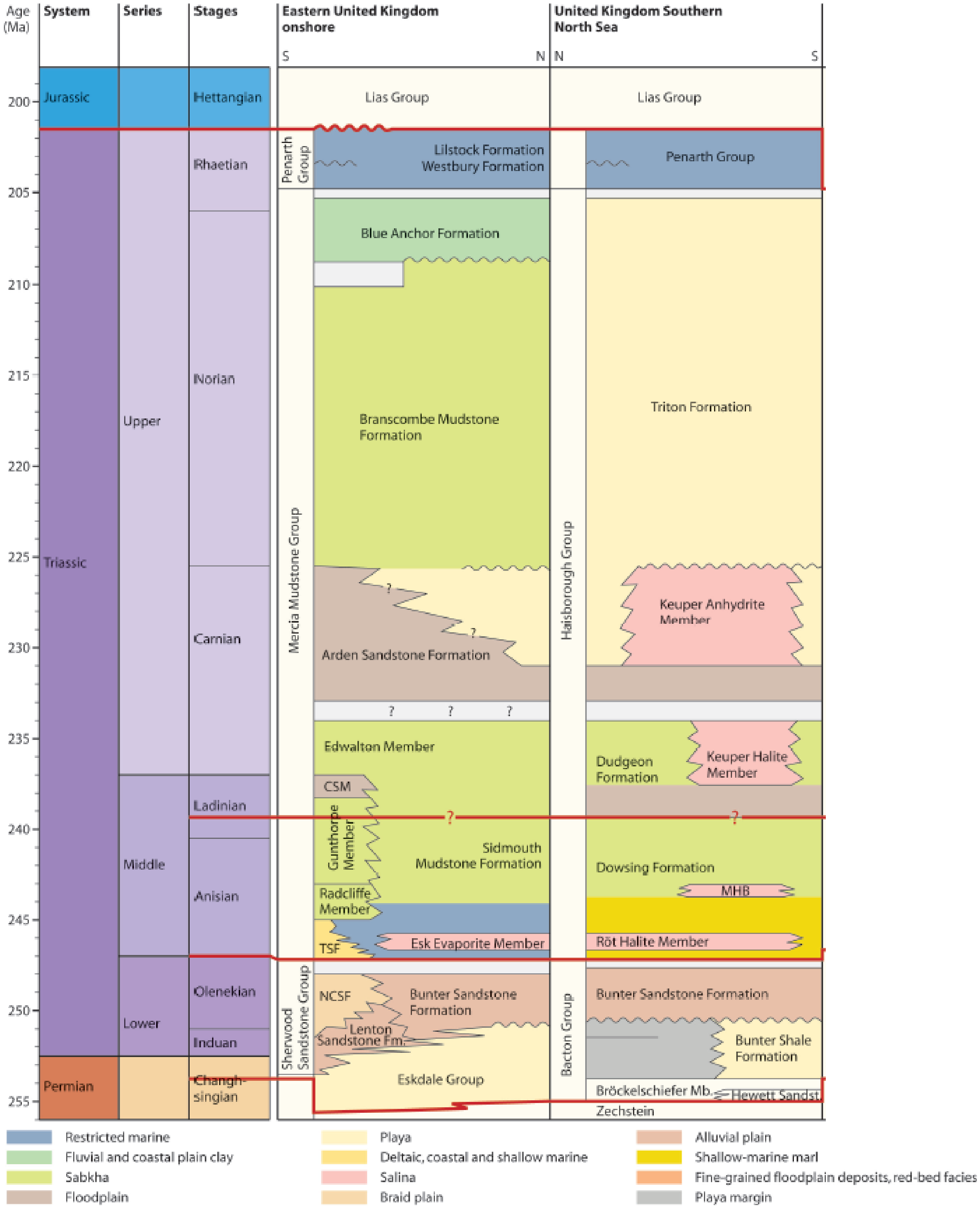

Figure 3.43: Overburden correlation in the regional wells. Note the thinning of Muschelkalk in 43/21-1 due to a fault

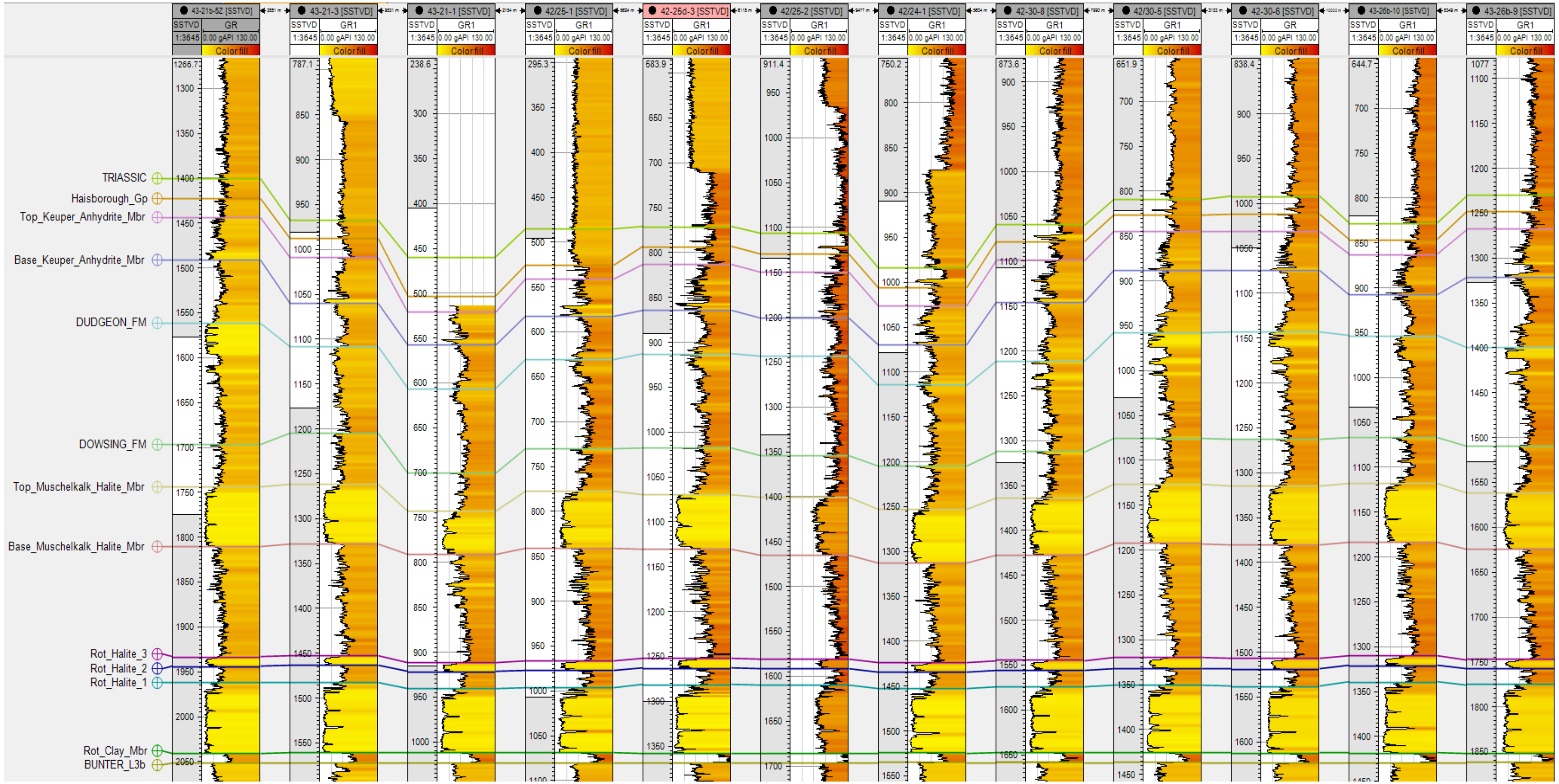

At the base of the Haisborough Group and directly overlying the Bunter sands lies the Röt Clay Member approximately 10m thick (as an average) over the Endurance structure. This constitutes the cap rock as well as the primary seal and it is immediately overlain by the Röt Halite Member with interbedded shales and halite layers. The Röt Halite is at the base of a 800m thick sequence of anhydrites and shales comprising, *inter alia*, the Muschelkalk Halite, the Dowsing Shale, the Dudgeon Formation, and the Keuper Anhydrite, that constitute the secondary sealing unit (see Figure 3.5 and Figure 3.7).

Long term (>10,000 years) exposure of the Röt Clay to a CO_2 cap is expected to cause minimal diffusion into the Röt Clay and will not result in any measurable migration outside the Storage Site nor any change in the mechanical properties of the Röt Clay.

The Röt Clay shale appears to be a competent seal based on all available data: 42/25d-3 mini-frac data, Esmond Field analogue, petrography and geomechanics.

3.5.1 Characterisation

The fracture closure pressure of the Rot Clay – a measure of sealing potential – recorded during a MDT (Modular Formation Dynamic Tester) mini frac test that was conducted on the appraisal well 42/25d-3 is 264bar (3830 psi) at -1362.8mTVDSS (4471 ft TVDSS). This is the best direct evidence that the Röt Clay is geomechanically strong and theoretically capable of trapping a sizeable CO_2 column and also withstanding a significant increase in differential pressure due to CO_2 injection.

Figure 3.44 shows the Endurance structure being capable of supporting a theoretical hydrocarbon gas column in excess of 2500ft (760m).

Figure 3.44: Esmond and Endurance pressure data

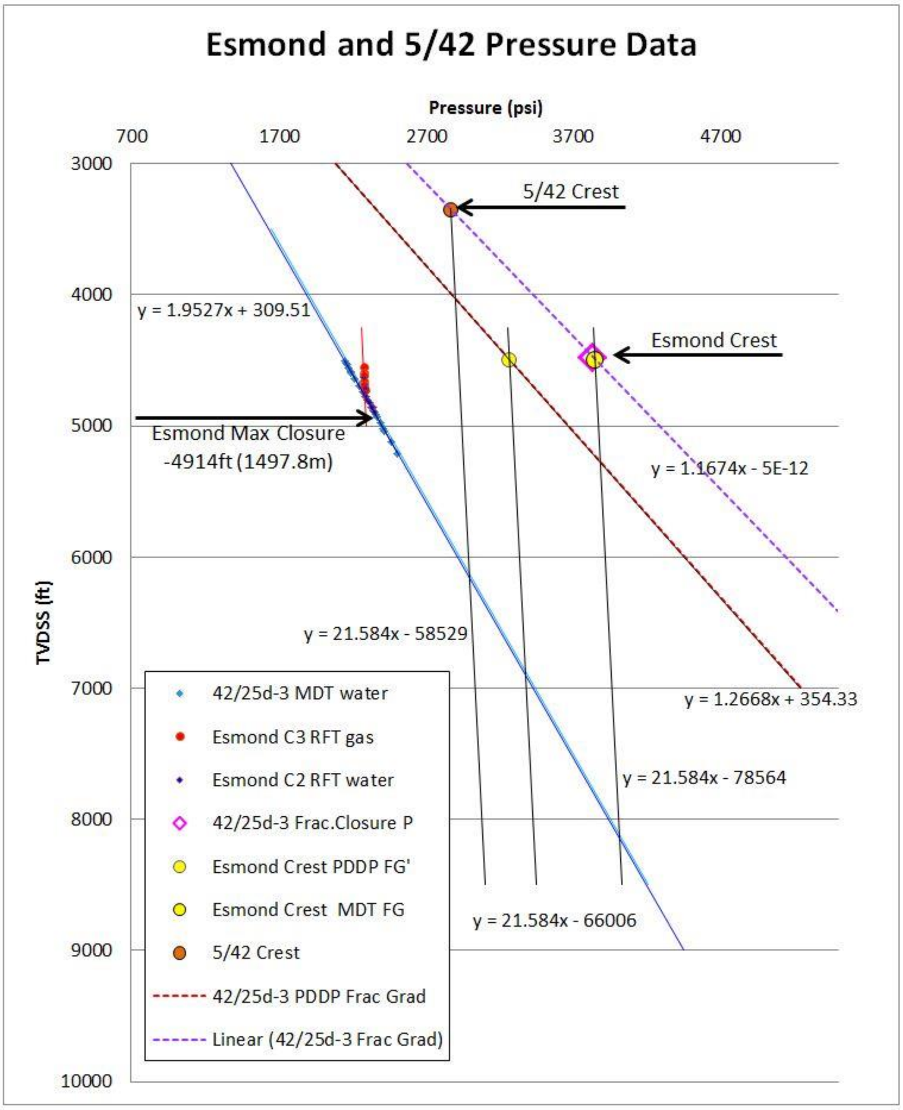

The Esmond Gas Field lies about 45km northeast of Endurance (Figure 3.45). It is a simple 4-way dip anticlinal closed Bunter Sandstone reservoir formed by swelling of underlying Permian salt. The reservoir is around 100m thick and sealed by the Rot Claystone about half the thickness of that seen in Endurance region. The Rot Clay interval actually comprises two shales separated by a thin 7 m sandstone which has been labelled the Rot Sandstone (RSS) (Figure 3.46). The lower shale has been labelled Rot Clay 1 (RC1) and is 6 m thick (43/13a-C1). The Upper Shale has been labelled Rot Clay 2 (RC2) and is 12m thick. The crest of the reservoir is about 350m deeper than Endurance at -1369 m. The initial Gas-Water Contact (GWC) lay at -1453.8 m, yielding an initial gas column of 85 m. Estimated GIIP was 325 bcf, of which 313 bcf is has been recovered at a recovery factor of 93% (Encore 2009). Eight crestal producers were drilled with production commencing in 1985 and finishing in 1995 when the field was abandoned. An appraisal drilled into the Esmond reservoir 13 years after production had ceased found that the Bunter sandstone had recovered from an abandonment pressure of 10.3bara (150 psia) in 1995 to 120.7bara (1750 psia) in 2008, indicating the presence of an active connected aquifer (initial pressure was 157.2bara i.e. 2280 psi). More importantly, formation pressure data shows differential pressures across the Rot Clay interval with the Rot Sandstone having maintained its abandonment pressure of 10.3bara, suggesting that the thin Rot Sandstone is clearly isolated from the main Bunter Sandstone Reservoir and that the thin 6 m of Rot Clay 1 is acting as a seal in its own right, holding back a differential pressure of 110bar (1600 psi) between Rot Sandstone and Bunter Sandstone. This provides a useful analogue for the Endurance structure where the Röt Clay is approximately twice as thick and it will be required to withstand a pressure increase of no more than 40bar due to CO_2 injection from the First Load (White Rose).

The Gamma Ray (GR) logs in the Esmond Field and Endurance wells suggest similar shale character and sealing capability for the Röt Clay (Figure 3.46). Spectral GR does show some subtle differences in clay mineralogy between the two structures . The Endurance area show a higher Rot Clay GR region to the south, around well 42/30-5, which suggests a higher shale content and similar if not better sealing potential than Esmond.

Also, the sonic log data from Esmond ties in with an increasing westerly transit time trend observed in the Endurance area which suggests a greater degree of burial and compaction thus a greater sealing capability of the Röt Clay at Endurance compared to Esmond.

Figure 3.45: Block boundary and wells map illustrating the location of the Esmond Gas Field relative to the 5/42 structure (now call Endurance).

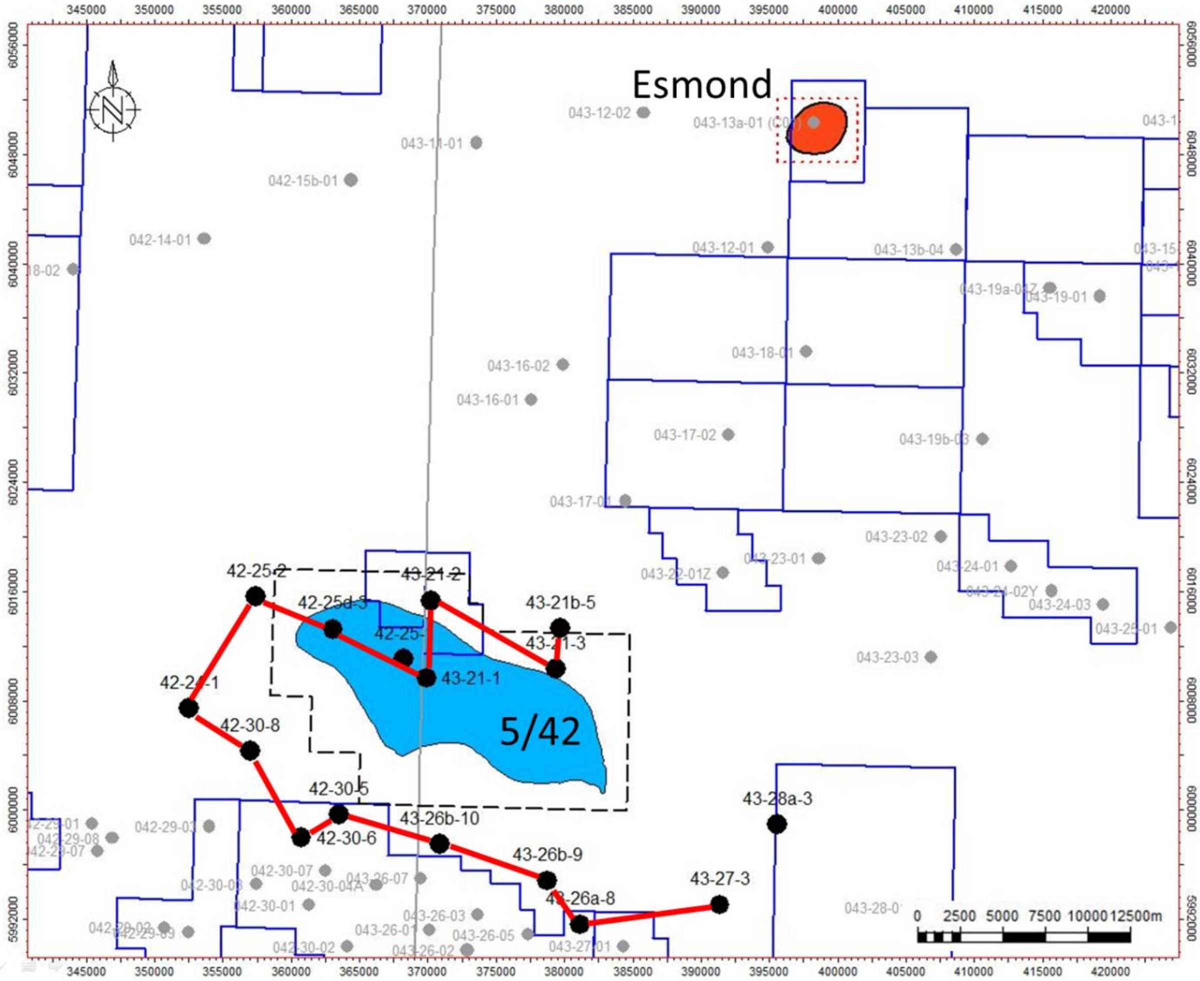

Figure 3.46: Normalised GR correlation of wells from the 5/42 (Endurance) and Esmond areas over the Röt Claystone

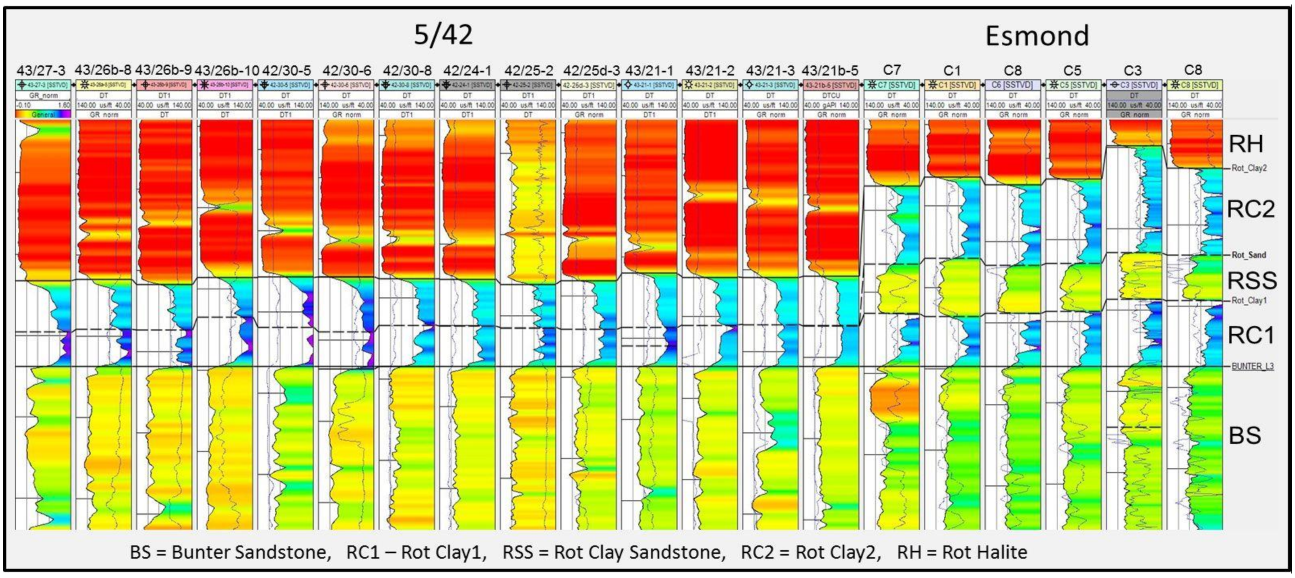

BS = Bunter Sandstone, RC1 – Rot Clay1, RSS = Rot Clay Sandstone, RC2 = Rot Clay2, RH = Rot Halite

3.5.2 Core & Cuttings Analysis

The sedimentological and petrographic work undertaken by Blackbourn and Robertson (2014) on the 42/25d-3 cores concluded that the Röt Clay and the succeeding Röt Halite have been deposited in a playa lake environment.

The red mudstones of the Röt Clay were interpreted as a transgressive horizon at the base of the playa lake. A significant amount of dolomite cement (up to 27%) intimately mixed with the clays was also reported in the three Röt Clay samples analysed. Other components identified are silts and anhydrite that mix with the illite (main clay mineral) in varying proportions depending on the sample.

The evaporitic sequence of the Röt Halite comprises mostly halite with inclusions and irregular thin laminae of anhydrite. Small proportions of silts, clays and dolomite may also be present although there is uncertainty regarding their presence.

3.6 Reservoir Facies Modelling

In the absence of a meaningful correlation between the primary depositional facies and the reservoir quality (see Section 3.3.2), a set of “electro facies” was defined based on wireline log data alone and was used in the facies modelling. Six electro facies (Figure 3.47) were picked on the gamma-ray, sonic and resistivity logs in 13 wells within the greater Endurance area, including 42/25d-3, and interpreted for trends that could be then used for modelling. The facies are interpreted to relate primarily to post-depositional diagenetic processes that occlude the original porosities.

Figure 3.48 illustrates the porosity distributions for the six facies types. Two of the six facies represent varying degrees of cemented sand (Facies 3 and Facies 4), whilst four are un-cemented facies (Facies 1, Facies 2, Facies 5, and Facies 6). The porosity range, cut off and definitions applied to each facies (Figure 3.48) have been informed by results of 42/25d-3 core sedimentology, petrography and chemostratigraphy.

The Heterolithic facies is truncated at 0.17 porosity because 42/25d-3 core sedimentology showed that the bulk of the low porosity facies (<0.17) are playa margin facies.

Petrography provided clarification on the partially Cemented facies which comprise both dolomite and anhydrite cements. The dolomitic cements occur in the three Endurance wells 42/25-1, 42/25d-3 and 43/21-1, near the top of the reservoir. Their lateral continuity is uncertain but they are likely to be patchy as the 42/25d-3 well test indicated (There was no evidence of boundaries in the volume investigated by the test, which was calculated to extend to a radius of 1.2km.). Chemostratigraphy suggested that halite is more prevalent in cemented wells (42/25-2 and 43/21-3) than in un-cemented wells (42/25d-3 and 43/21-1).

Figure 3.47: GR, electrofacies and porosity in cemented and uncemented wells

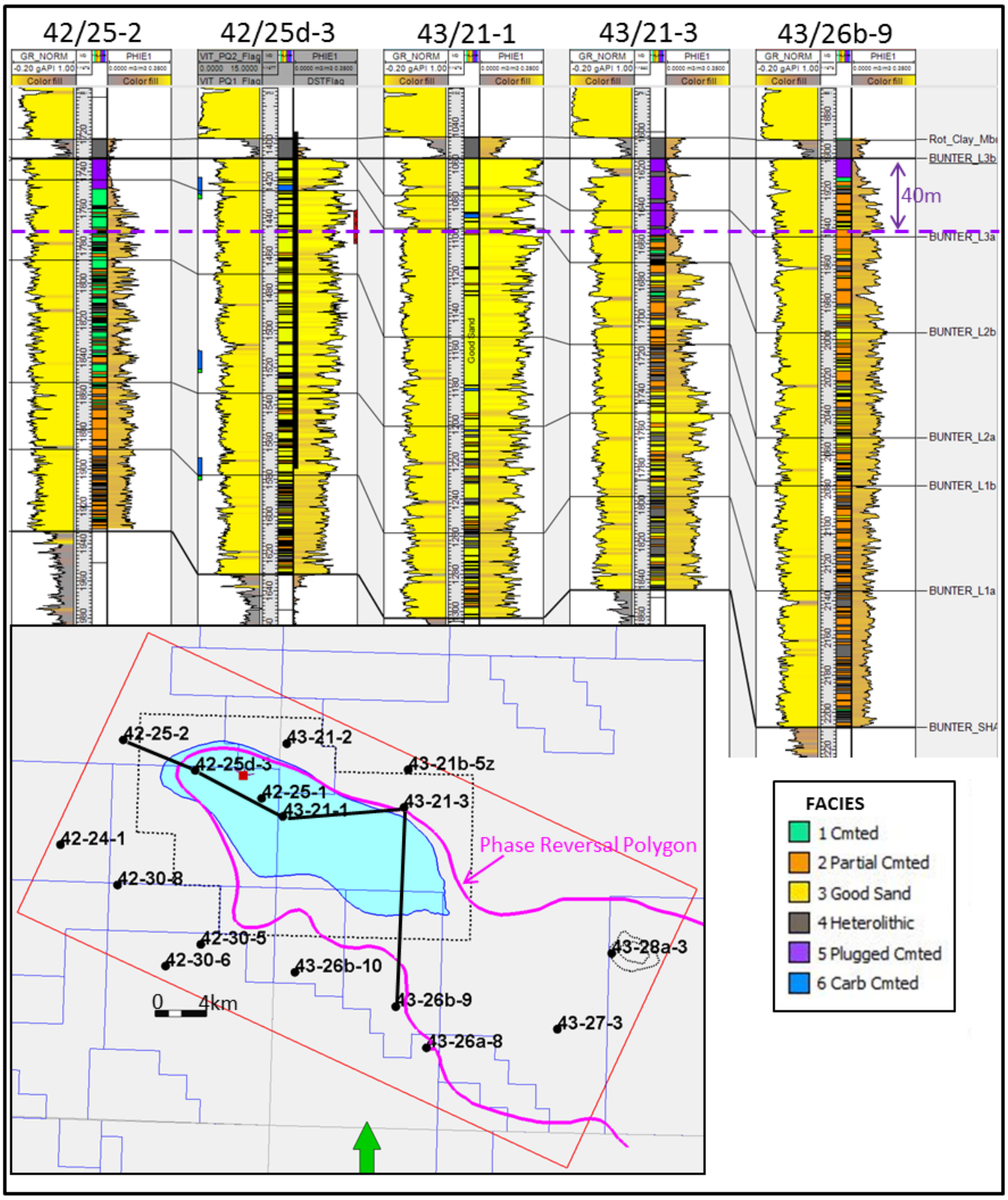

Figure 3.47 shows cemented wells outside the PRP (phase reversal polygon): 42/25-2, 43/21-3 and 43/26b-9; and uncemented wells inside the PRP: 42/25d-3 and 43/21-1.

Figure 3.48: Facies porosity distributions

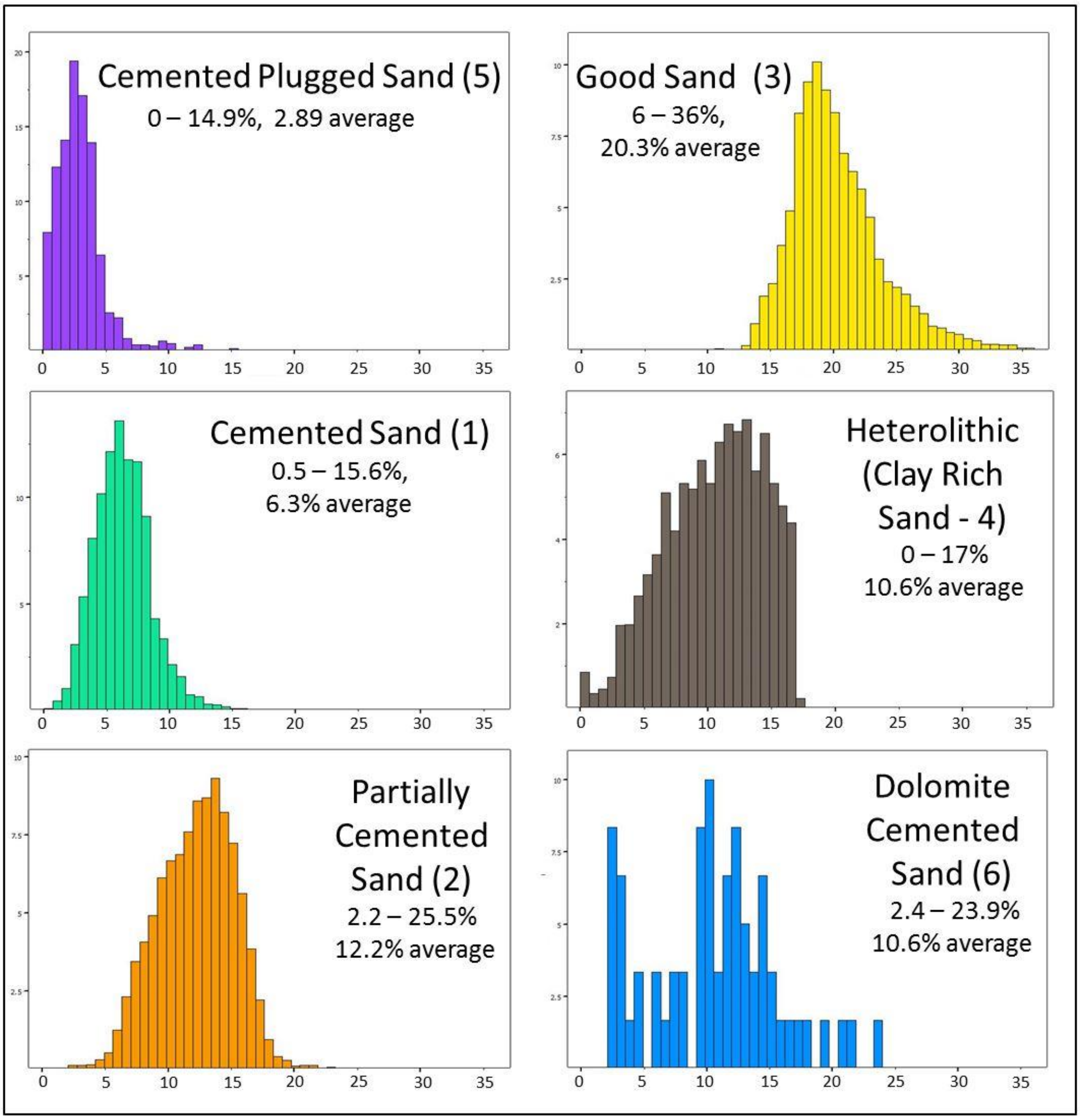

The electrofacies and the cementation trends described above were captured in the facies modelling. The primary aim in facies modelling was to capture the seismic phase reversal boundary (i.e. the phase reversal polygon (PRP)) that appears to control the distribution of cemented facies as discussed above. All other facies trends are secondary to this major trend. The PRP was modelled as a vertical boundary between the cemented and un-cemented sands. Various sensitivities cover the PRP geometry and the amount and lateral distribution of cemented sands within the Endurance structure (Figure 3.49). Facies modelling follows four steps:

1. Creation of a Hardground Region Parameter: Five hardground parameters were created in order to capture, as illustrated in Figure 3.49, the phase reversal boundary uncertainty which are then used in step 2 to distribute the facies types. These hardground parameters are:

    I. Vertical Hard Region (VHM): created with the seismic phase reversal polygon defining a “cookie cutter” style region of un-cemented rock surrounded by cemented rock (Figure 3.49A).
    II. Diffuse Vertical Hardground Region (DVHM): similar to the Vertical Hardground Model except that it has a fuzzy margin (Figure 3.49B). This model acknowledges the fact that Good Sands do exit outside the phase reversal polygon in small proportions that get smaller away from the polygon.
    III. Patchy Hardground Model 1: distributes patches of cemented sand within the phase reversal polygon with a trend probability parameter that shows the 25% probability of cemented sand with the phase reversal polygon (Figure 3.49C).
    IV. Patchy Hardground Model 2: is similar to the PHM1 except the probability parameter used to distribute patches of cemented sand was increased to 50% within the phase reversal polygon (Figure 3.49D).
    V. Easterly Trending Hardground Model (ETHM): distributes progressively higher proportions of cemented sand toward the east of the AOI (Figure 3.49E).

2. Distribution of sand facies types within the cemented/un-cemented areas of the Hardground Region. Five individual facies trends were included in this step, namely: (a) Gross facies trends related to the seismic phase reversal boundary (b) Plugged Cemented Trend (c) Cemented Sand Trend (d) Dolomite Cemented Sand Trend (e) Heterolithic Trend.
3. Distribution of Heterolithic Facies which are independent of the Hardground Region: Heterolithics are distributed using Truncated Gaussian Distribution (see the cross section in Figure 3.50B for an illustration).
4. Final Facies Model - Combination of the sand facies model created in step 2 and the Heterolithic model created in step 3. Heterolithic facies were allowed to overwrite sandstone “facies”. Figure 3.50C provides an illustration of the combined final facies model.

Figure 3.49: Hardground Facies Models

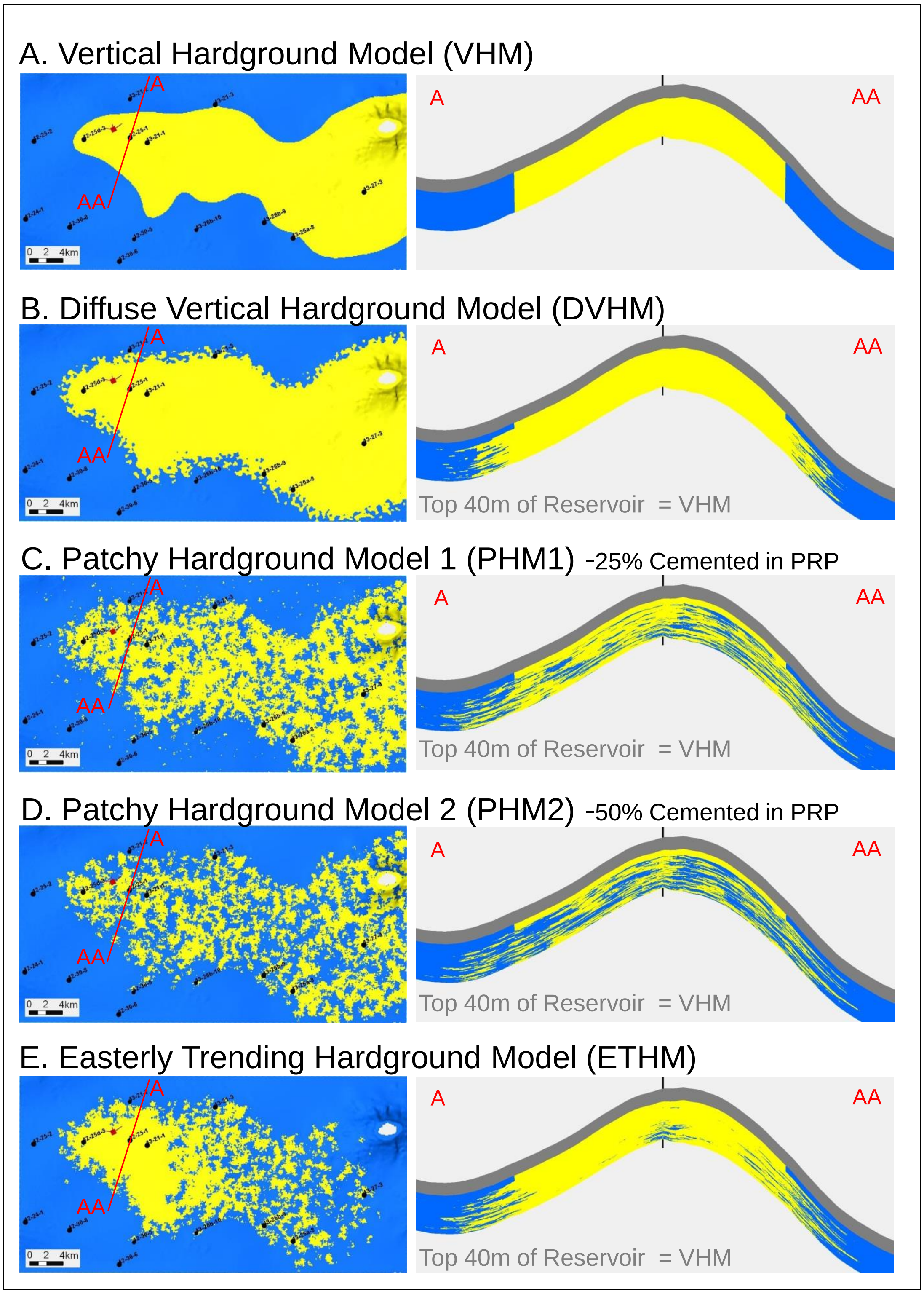
A. Vertical Hardground Model (VHM)

B. Diffuse Vertical Hardground Model (DVHM)

C. Patchy Hardground Model 1 (PHM1) -25% Cemented in PRP

D. Patchy Hardground Model 2 (PHM2) -50% Cemented in PRP

E. Easterly Trending Hardground Model (ETHM)

Figure 3.50: Southwest to northeast cross section across the Endurance model illustrating the sand “facies” model (A), the heterolithic model (B) and the combined facies model (C).

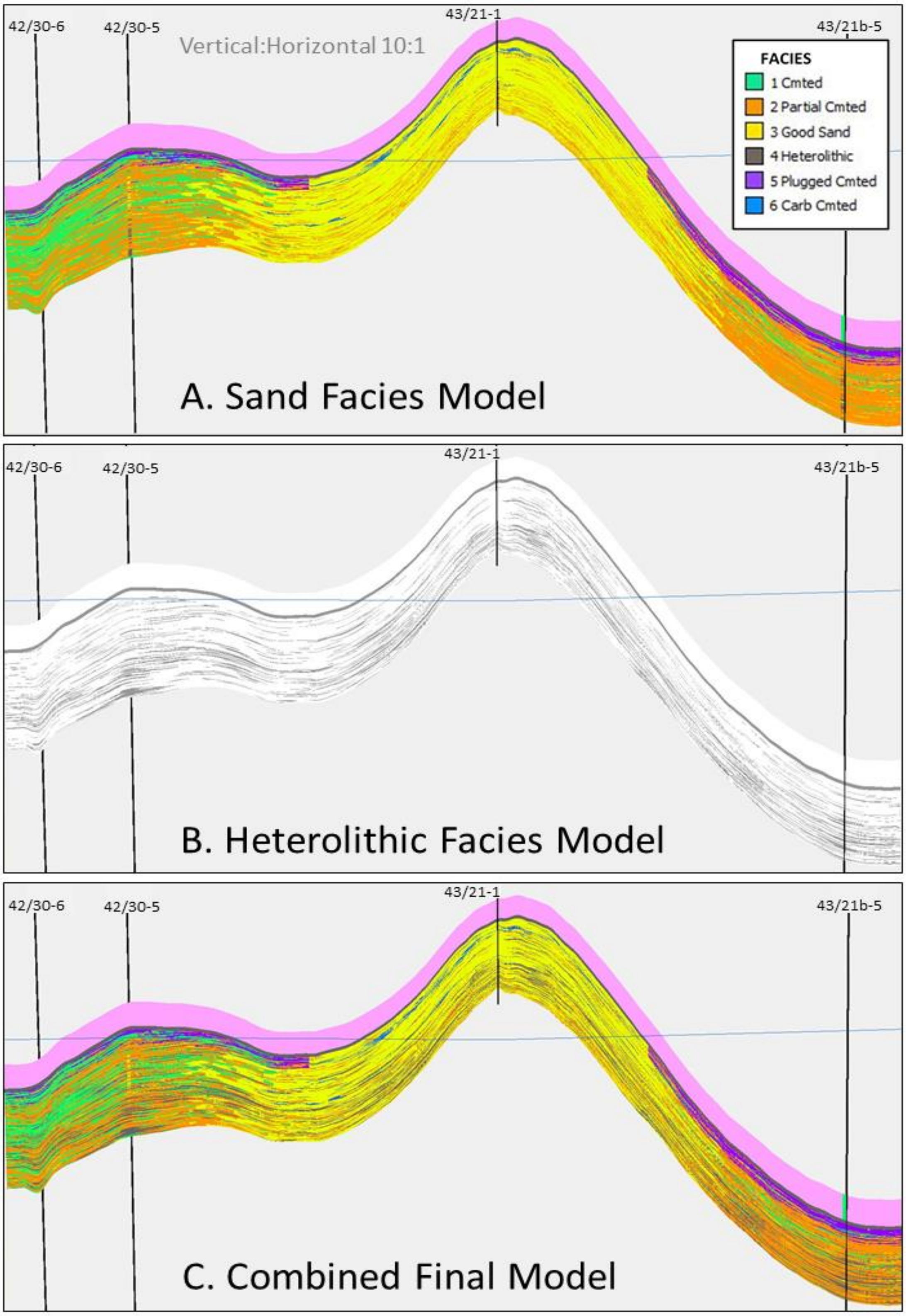

3.7 Reservoir Properties

Reservoir porosity and permeability were determined using a combination of logs from 13 wells and core analysis data from two wells (42/25-1 and 42/25d-3).

3.7.1 Porosity

The sonic log was the only porosity curve common to all wells and in conjunction with the core data was used to calculate porosity across the structure. Where available, the density log was used to confirm the sonic porosity. The method involved the integration of a set of preliminary matrix and fluid coefficients in the wells with strong core control and a range of available curves (cored wells and wells with density as well as sonic logs). A preliminary porosity was then calculated and compared to a 'resistivity porosity', after which final adjustments to the matrix coefficients were made. Figure 3.51 shows an example of the excellent agreement achieved between core porosity and porosity calculations from the sonic, density and resistivity logs.

Porosity was modelled in the Geological Model stochastically within each of the six facies described above. The variogram ranges are half the ranges used for facies modelling to capture the heterogeneity observed within each facies. Porosity depth trends were applied for facies that showed porosity decreasing with increasing depth.

Figure 3.51: Petrophysical summary of upper part of Bunter sandstone section.

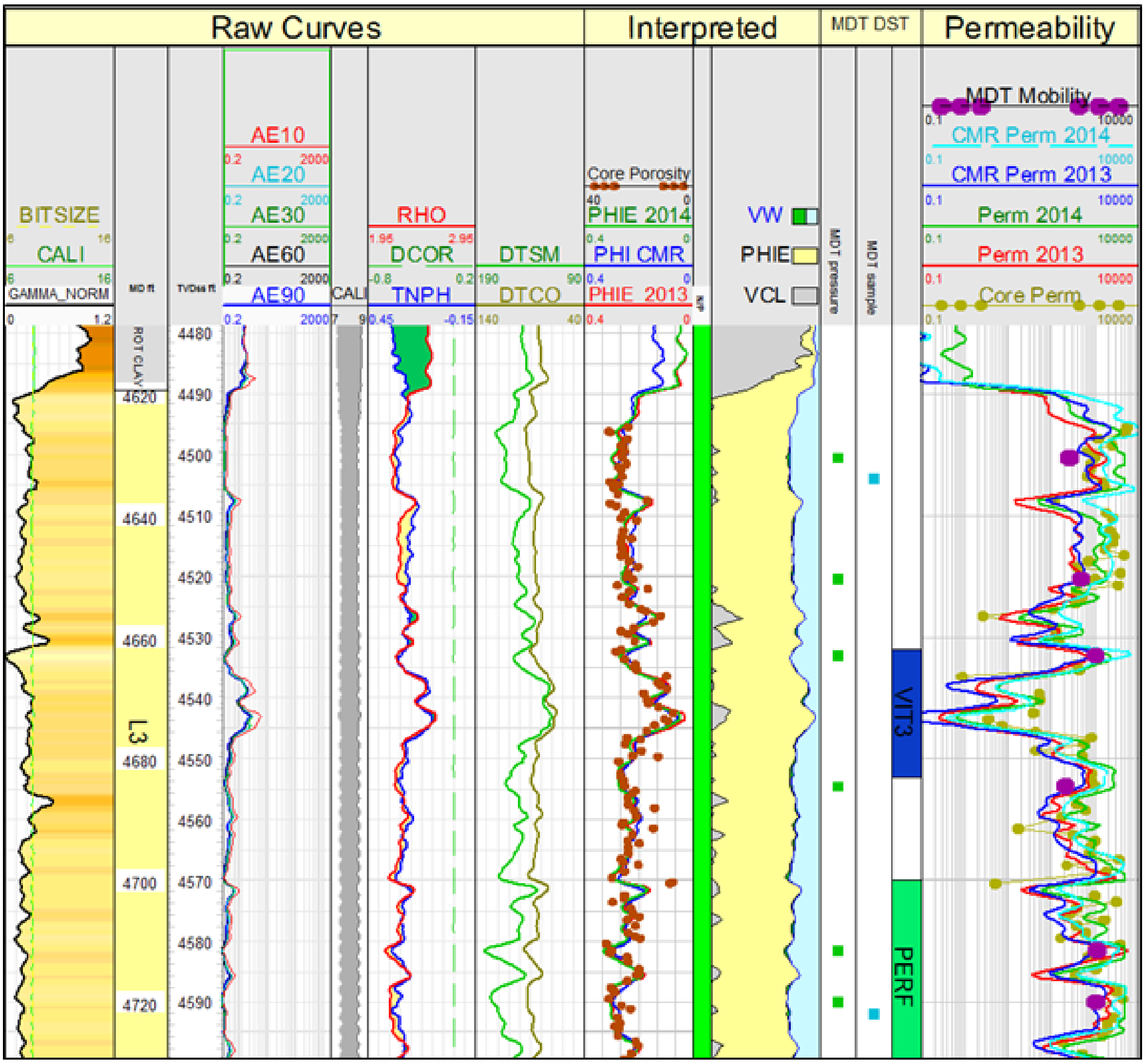

Note: in track 8 comparison of core porosity with calculated porosity curves using density, sonic and resistivity logs.

3.7.2 Permeability

Permeability was based on a permeability prediction algorithm derived from a porosity-permeability cross-plot of core data from wells 42/25-1 and 42/25d-3. Figure 3.52 shows the resulting function fitted to the binned data on a semi-log plot (top plot) and against the raw data cloud (bottom plot). It should be noted that the power function based on the binned data shown in Figure 3.52 has been the one adopted for model development because it gives a reasonable fit at very low permeabilities as compared to a conventional linear or exponential functions.

Figure 3.52: RCA (Routine Core Analysis) permeability vs porosity trend function

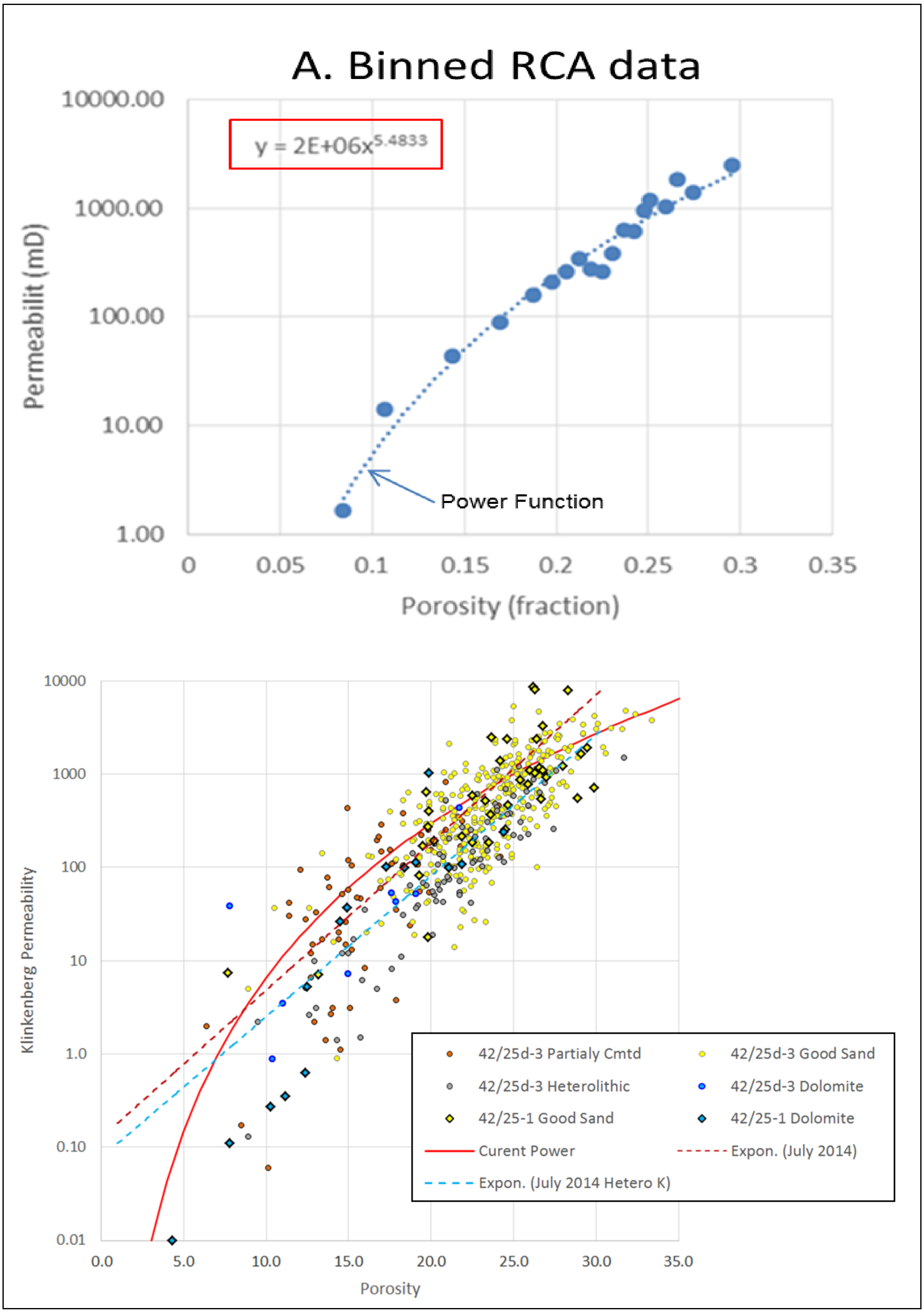

3.7.3 Net to Gross

The Net-To-Gross (NTG) cut-off is uncertain in CO_2 storage given the short period of injection compared to hydrocarbon charge. This uncertainty was captured using a range of porosity cut-offs, following established standards in oil and gas exploration using the poro-perm power function shown in Figure 3.52:

- 4.56% - (0.1 mD) – equivalent to typical light natural gas threshold;
- 7% - (1 mD) – equivalent to a typical light oil threshold; and
- 12% (17.9mD) – defined as being a threshold above which the reservoir volumes are insensitive.

In the NPV uncertainty analysis, 4.56%, 7%, and 12% were treated as low, mid and high cases, respectively. The porosity cut-offs yielded deterministic minimum, maximum and average NTG values of 0.752, 0.993, and 0.927 respectively. The 7% cut-off is viewed as the reference case for deterministic estimates of NPV. The contribution of NTG to the NPV uncertainty range was relatively low (-5.3 to +0.7%).

3.7.4 Temperature

The temperature gradient has been estimated as 3.05 C/100m and equates to a temperature of 55.9 ^{o}C at a reference depth of 1300mTVDSS.

A number of temperature measurements were made in the 42/25d-3 appraisal well. The reliability of the measurement varies depending on the accuracy of the various tools and the time spent by the tools at the depth of interest during measurement. This latter point relates to the time required for the tool to heat (if moving down the hole) or cool (if moving up the hole) to the local temperature. The sets of measurements at which the tools were given most time at any given depth were those associated with:

- the Modular Dynamic Tester (MDT) measurements of pressure i.e. the MDT long duration test (20 depths);
- Wireline Head Thermometer (WHT) measurements (6 depths, the first two measurements were anomalous and therefore excluded from the final analysis; the anomaly was probably caused because the thermometers were not reset from those used in the previous hole section);
- water sampling (3 depths) – see Section 3.9.3.1;
- Mini-frac (1 depth in Röt Clay and 1 depth in Lower Bunter sands) – see Section 5.3; and
- the Vertical Interference Tests (VIT) (3 depths) – see Section 4.3.2.

Measurements associated with the highest tool running speeds include:

- Logging Head Thermometer measurements – made after a short circulation time and could therefore have been affected by frictional heat generated during drilling as well as the relatively low volume of drilling fluid used which had insufficient time to cool at the surface; and
- Quartz gauge measurements – MDT short duration points (20 depths).

The MDT long duration temperature measurements are considered most representative of the geothermal gradient and a plot of the data is shown in Figure 3.53.

Re-arranging the Equation shown on this figure gives:

Equation 3.1 $T_c = 0.0305D + 16.29$,

where T_C is the temperature (C), D is the True Vertical Depth Sub-Sea (TVDSS m) from which the datum pressure above was estimated.

3.7.5 Pressure

The MDT pressure data are shown in Figure 3.54 in which the gradient of the line is displayed along with that obtained from the Repeat Formation Tool (RFT) run in the 42/25-1 crestal appraisal well run in 1990. For a reference depth of 1300mTVDSS on Figure 3.53, the pressure was determined to be 140.0 ± 0.4bar.

Figure 3.53: Temperature Gradient Measured in 42/25d-3

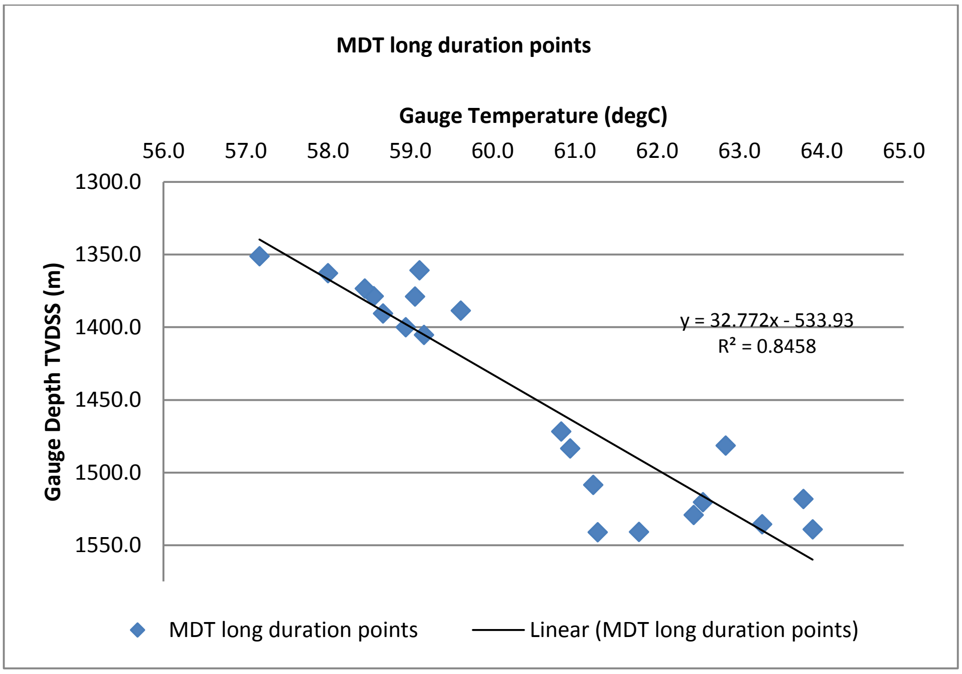

Figure 3.54: RFT Pressure Data from 42/25-1 and MDT Pressure Data from 42/25d-3

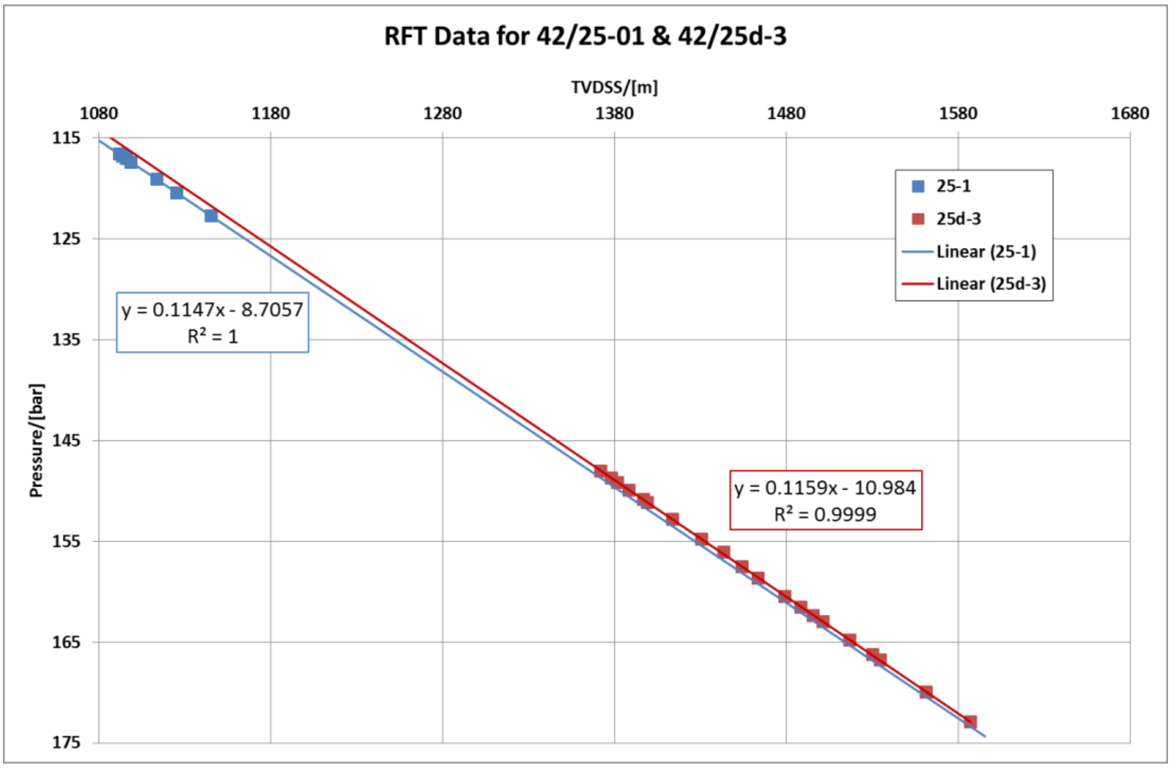

The decrease in reservoir pressure seen between the two fitted trendlines is about 0.8bar at 1300mTVDSS. There is a suggestion that this drop in pressure is due to expansion of the Greater BSF to fill the void created by gas production from some of the Bunter hydrocarbon gas fields, in particular the Esmond field some 50km to the north of Endurance. This important observation suggests that Endurance is connected to an aquifer volume around 100 times larger than itself and thus indicating the availability of a large pressure “sponge” during CO_2 injection.

3.8 Volumetric Ranges and Uncertainties

3.8.1 Net Pore Volume Range

The deterministic NPV analysis has been based on the seven facies models and three NTG models as illustrated in Table 3.4. The NPV ranges from 3.6 to 5.1 Bm^3, with an average of 4.5 Bm^3. The DVHM model with a mid-case porosity cut-off of 7% which yielded NPV of 4.6 Bm^3 is regarded as the most likely case because it distributes predominantly un-cemented rock throughout the model within the Phase Reversal Polygon (PRP) (Figure 3.47) – the 4 wells within the PRP (42/25d-3, 42/25-1, 43/21-1 and 3/37-3) having largely un-cemented Bunter intervals. The structural uncertainty has been assessed via Petrel uncertainty workflows that calculate the spill point for each of the 500 maps generated as already discussed in Section 3.2.1. The current model spill is -1460m with a range of -1416 m to -1553 m resulting from the uncertainty workflow.

Given that the area within the PRP in Figure 3.47 is very large and only penetrated by 4 wells, most of the modelling has focussed on downside scenarios where poorer quality cemented sands could be present away from the wells. The PHM2 model that yields a NPV of 3.6 Bm^3 with a low case porosity cut-off (12%) is therefore regarded as an extreme low case.

Table 3.4: Deterministic model volumetrics and average properties

Model	Cut Off %	GRV Bm^3	NRV Bm^3	NPV Bm^3	N:G	Por
DVHM_up	4.7	24.6	24.4	5.097	0.993	0.209
DVHM_up	7.0	24.6	24.2	5.087	0.987	0.210
DVHM_up	12.0	24.6	23.4	4.999	0.951	0.214
VHM	4.7	24.6	24.2	4.629	0.987	0.191
VHM	7.0	24.6	23.7	4.596	0.964	0.194
VHM	12.0	24.6	21.2	4.347	0.863	0.205
DVHM	4.7	24.6	24.2	4.654	0.986	0.192
DVHM**	7.0	24.6	23.7	4.621	0.964	0.195
DVHM	12.0	24.6	21.3	4.384	0.866	0.206
ETHM	4.7	24.6	24.1	4.583	0.981	0.190
ETHM	7.0	24.6	23.2	4.517	0.974	0.194
ETHM	12.0	24.6	20.7	4.267	0.842	0.206
PHM1	4.7	24.6	24.0	4.380	0.976	0.183
PHM1	7.0	24.6	23.1	4.326	0.940	0.187
PHM1	12.0	24.6	19.9	4.011	0.810	0.202
PHM2	4.7	24.6	23.7	4.098	0.964	0.173
PHM2	7.0	24.6	22.5	4.026	0.915	0.179
PHM2	12.0	24.6	18.5	3.636	0.752	0.197
Minimum			18.5	3.636	0.752	0.173
Maximum			24.4	5.097	0.993	0.214
Average			22.8	4.459	0.927	0.196

**Most likely case.

The NPV uncertainty range was established by Monte Carlo simulation using representative distributions of Gross Rock Volume (GRV), NTG and porosity. To create the GRV range, a combination of structure, spill level and gross Bunter isochore were varied. The most likely NTG value was taken from the deterministic base case (with 7% NTG cut off) and minimum and maximum values from the extreme values of the deterministic range.

NPV ranged from a minimum of 3.281 Bm^3 to a maximum of 6.195 Bm^3 with a P50 case of 4.793 Bm^3 (Figure 3.55). The most likely deterministic case (DVHM with a 7% porosity NTG cut off) has an NPV of 4.621 Bm^3 and represents a P64 case on the distribution range.

Figure 3.55: Stochastic distribution of 5/42 (Endurance) NPV (DVHM denotes the most likely deterministic case)

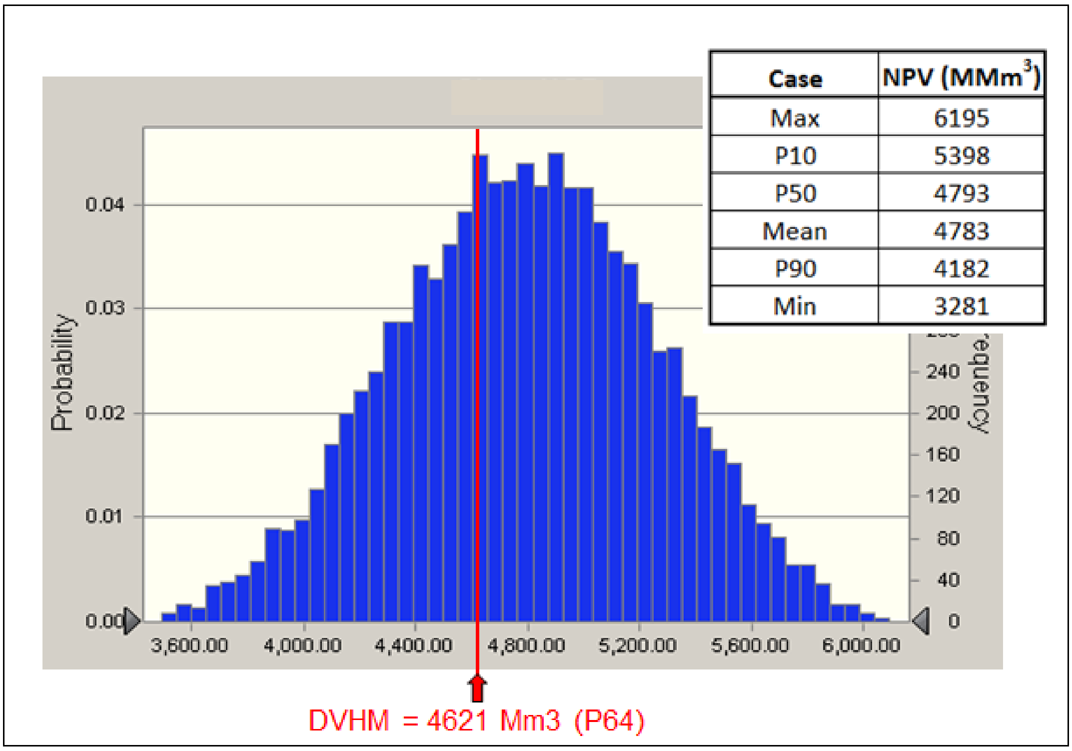

Case	NPV (MMm^3)
Max	6195
P10	5398
P50	4793
Mean	4783
P90	4182
Min	3281

3.8.2 Net Pore Volumetric Uncertainty

Figure 3.56 shows a tornado plot illustrating the net pore volume uncertainty. The reference value is based on a gross rock volume (GRV) of 26.307 Bm^3 (mid case result of the structural uncertainty workflow) combined with the reference values for facies, porosity, NTG and the gross Bunter isochore. Top Bunter reservoir structure has the greatest impact on the NPV followed by the facies model and average porosity.

Figure 3.56: Tornado chart illustrating the effect of the key volumetric parameters on NPV

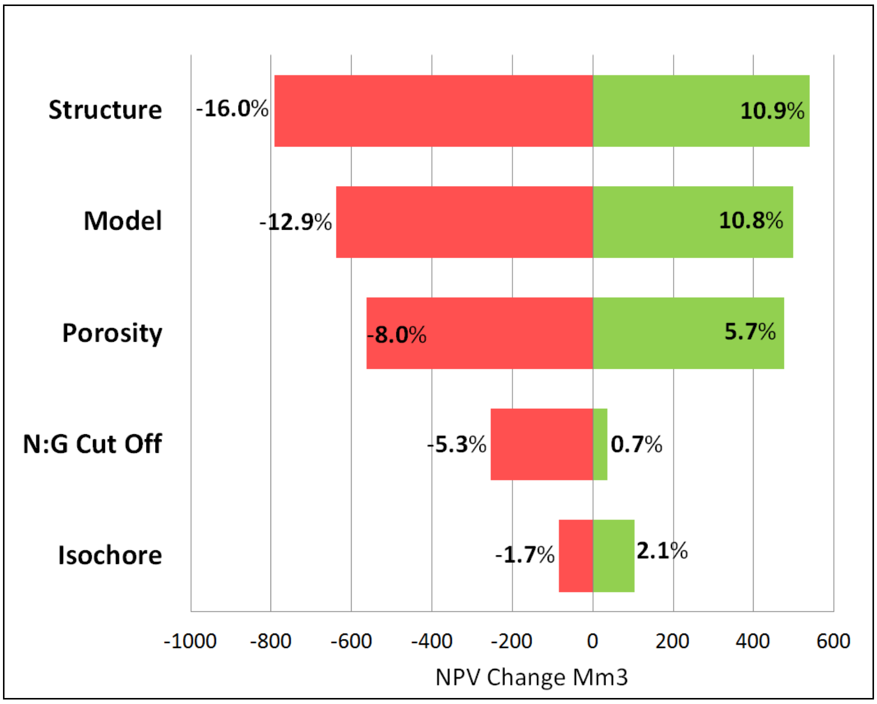

3.8.3 Geological Models

A number of Petrel models that represent sectors of the RSFM have been built (Figure 3.57). These models have different lateral and vertical extents depending on the objective and the spread of the inputs constraining them, and are described in more detail in the following sections.

Figure 3.57: Extent of the Geological Models

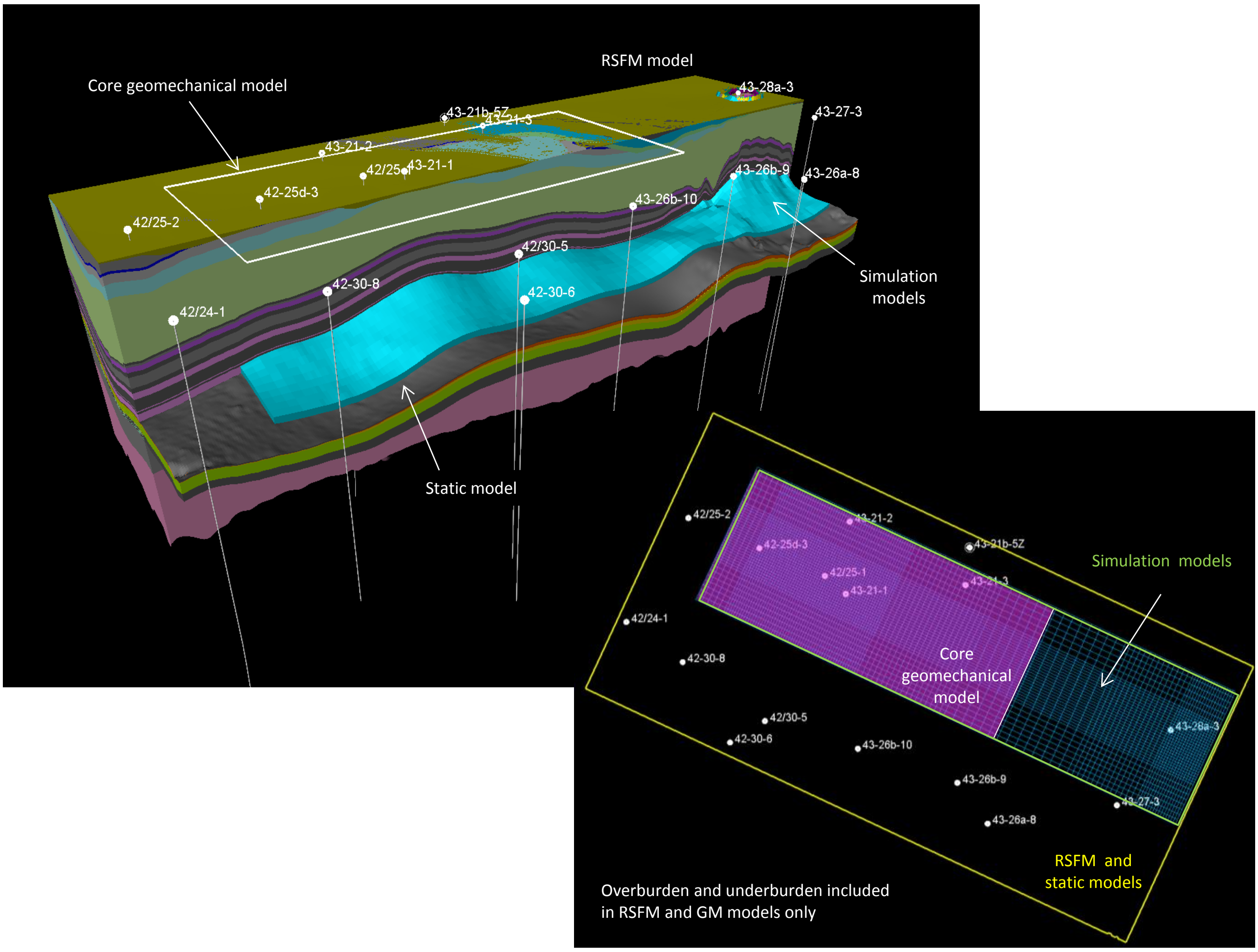

3.8.4 Regional Structural Framework Model

The RSFM has been described in Section 3.4. The stratigraphy includes the latest chemostratigraphic correlation that shows L3b pinching out in the west of the structure.

3.8.5 Static (Geological) Model

The static model has the same areal extent as the RSFM but it extends only from Top Röt Halite to Top Bunter Shale. The reason for such a large areal extent is to include all the regional wells that constrain the stratigraphy and inform the rock property modelling (Figure 3.58).

The model includes the following zones: Röt Halite 1, Röt Clay, Bunter L3b, L3a, L2 and L1, each of them further divided in layers. The lateral resolution is 100m x 100m (same as RSFM) with an average layer thickness of just over 1 m. Figure 3.58 illustrates the zonation in a cropped view of the static grid (top, in colours) whilst the base skeleton (bottom, in green) gives a visual of the horizontal resolution.

Figure 3.58: Static Model Geometry

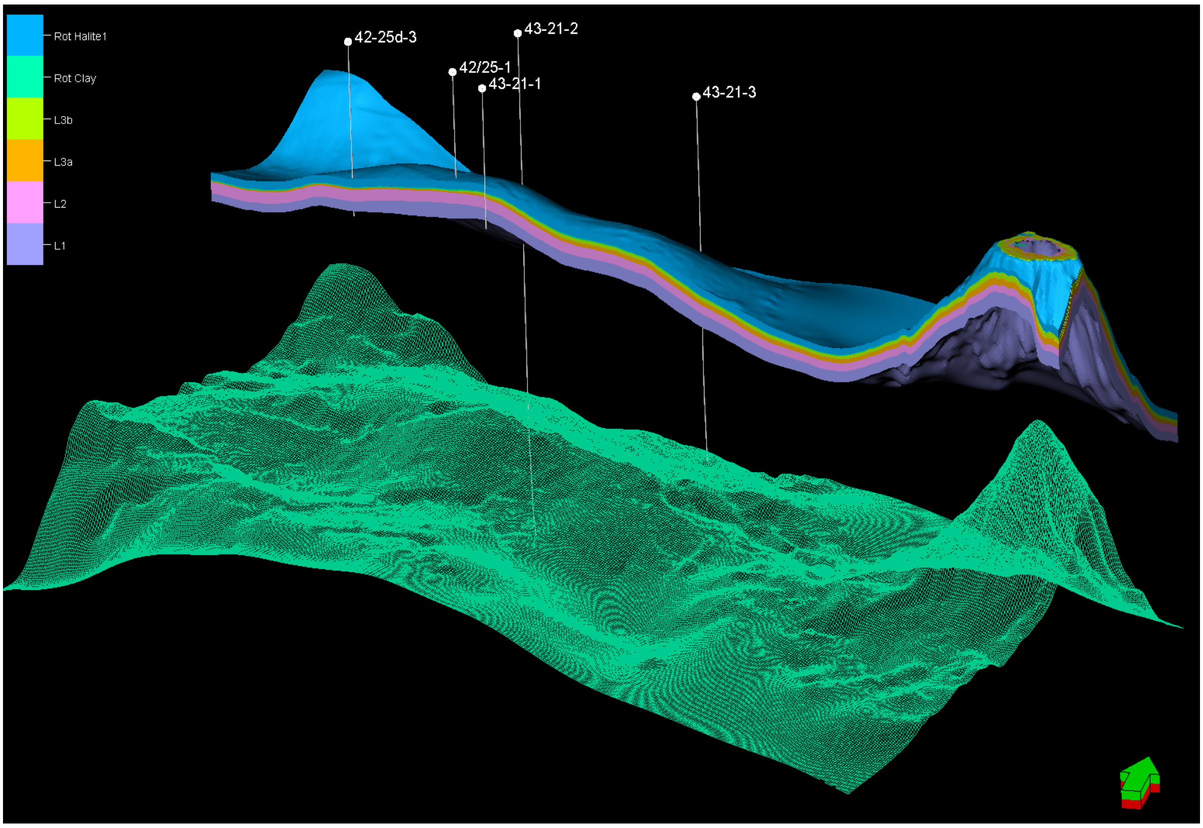

The model contains five facies models or sensitivity cases as described in Section 3.6. The porosity parameters (arrays) are conditioned to the facies; thus five porosity models have also been generated. Each of the facies – porosity pairs is associated with three NTG parameters: low, reference and high, corresponding to the different porosity cut-offs, hence a total number of 25 facies and rock property models are part of the geological model.

3.8.6 Simulation Models

The Schlumberger geoscience modelling suite has been used. The static geological model has been implemented in Petrel; the Dynamic Reservoir Model in Eclipse (see Section 4.6) and the Geomechanical Model in Visage (see Section 5.1). These models operate together using common definitions for the Regional Structural Framework Model and using specific outputs as required.

The simulation grids are less areally extensive covering only the Endurance structure width and extending as far as the outcrop to southeast (Figure 3.59). Unlike the other grids that have constant cell size, the simulation grids are tartan-like with smaller cells over the main structure and the outcrop, and larger cells on the flanks.

This approach enables a proper evaluation of the areas of interest whilst still maintaining a manageable total number of cells and simulation run times. Relatively quick simulation runs are key to evaluating as many sensitivity cases as required to properly understand the dynamic uncertainties.

Figure 3.59: Reference Simulation Grid

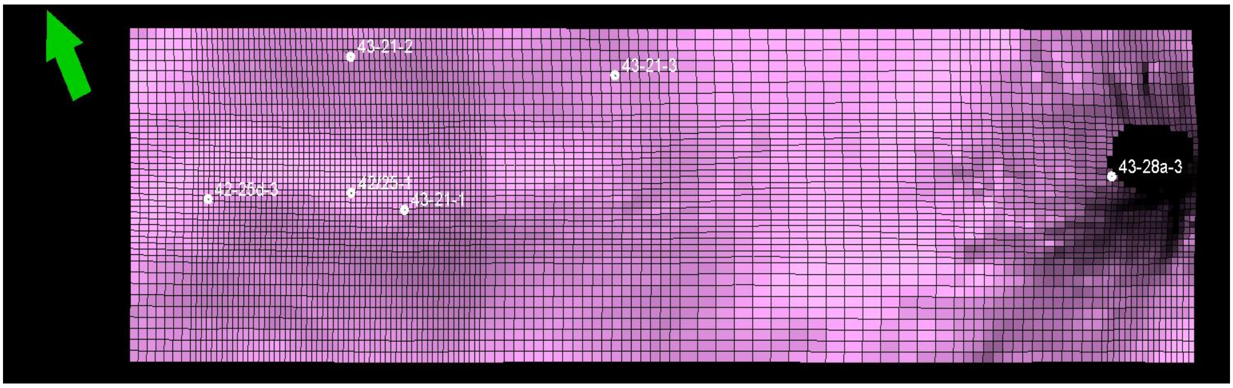

These grids are usually described by the resolution in the core, finer areas (Endurance crest and around the outcrop) as the cell sizes are variable outside. Different 'tartan' geometries have been tried during this study and three, all following the pattern shown in Figure 3.59, but with different resolutions, have been exported to Eclipse and used in the dynamic simulations:

- Fine Grid: approximately 100m x 100m;
- Reference Grid: approximately 200m x 200m; and
- Coarse Grid: approximately 400m x 400m.

All static rock property models for porosity and NTG have been upscaled onto the simulation grids and then exported for simulation. The corresponding permeability arrays have been generated directly in Eclipse by applying the porosity – permeability transform (see Section 3.7.2) to the 3D porosity models. The resulting permeability models are then scaled to match appraisal well 42/25d-3 average well test permeability of 271 md.

3.8.7 Geomechanical Models

Two geomechanical (GM) models have been built:

- large GM grid that extends further than the RSFM (not shown Figure 3.57) to incorporate the log properties from all the regional wells. These properties are then sampled into the smaller core GM grid; and

- core GM grid that covers only the Endurance structure (shown in Figure 3.57). Due to the smaller size, this is the grid used in all the geomechanical runs.

These grids are populated with parameters as part of the geomechanical modelling described in Section 5. As with the simulation models, three different resolutions (at constant cell size) have been generated: 100 x 100, 200 x 200 , and 400 x 400m.

3.9 Geochemistry

Insights into the geochemical interactions between the Endurance Storage Site and injected CO_2 during the injection as well as the longer term post-closure phases were obtained using both laboratory testing and numerical modelling.

3.9.1 Laboratory Testing

The tests described below form part of a larger core analysis programme, but are being highlighted here because of their relevance to the understanding of the potential geochemical processes that may occur within Endurance upon CO_2 injection.

3.9.1.1 Permeability as a function of throughput

The test was performed to establish the effect on Bunter sandstone permeability to continuous exposure to mobile CO_2.

It involves continuous injection of CO_2 through three brine-saturated Bunter sandstone samples, each at a non-damaging flow rate of 10ml/min for a maximum of 25 Pore Volumes (PVs) and under Endurance temperature and pressure conditions. The three samples: 4H (28.7 mD, 0.181 porosity), 8D (483 mD, 0.215 porosity), and 8E (1104 mD, 0.256 porosity), represent low, medium and high permeability values respectively.

Comparison of pre and post-flow sample permeability measurements indicate permeability in all three samples reduced by an average of -19.2% – sample 4H, with the lowest permeability, showing the greatest reduction of -26.1% whilst sample 8E, with the highest permeability, showing the least reduction of -12.6%. SEM (Scanning Electron Microscope) analysis of sample #8D (4936.30’) showed expelled particles during flow, consisting mainly of illite/mica, quartz, potassium feldspar, plagioclase and other mineral fragments in a matrix of iron carbonate precipitate.

This test suggests that exposure of the Endurance formation to supercritical CO_2 under *in situ* conditions will lead to salt deposition in the pore throats. Injected CO_2 will absorb water from the formation brine causing solid salt to precipitate. As the formation brine is highly saline, this process occurs very quickly. The SEMs of samples and filters all show mobilised clay fines and also amorphous/microcrystalline iron carbonate (likely to have been leached from the iron minerals present in the rock e.g. hematite, chlorite) which may have contributed to the reduction in the permeability. This reduction in permeability is not considered sufficient to cause permanent impairment of CO_2 injectivity and further assessment of this phenomenon along with likely mitigation measures has been performed using numerical modelling (see Section 3.9.2).

3.9.1.2 Impact of CO_2 exposure on rock mechanical properties

A range of rock mechanical characterisation tests have been performed to evaluate the potential for weakening of the Bunter sandstone and the Röt Clay as a result of exposure to supercritical CO_2. No CO_2 exposure tests were carried out on the Röt Halite.

The samples were first saturated in simulated formation water and then surface dried to ensure the CO_2 would contact the face of the core samples and invade into the pore spaces under pressure. Samples were exposed to CO_2 for up to 60 days at 1500psi pressure and 40°C.

Tests completed for the Bunter sandstone sample included Thick Walled Cylinder (TWC), Advanced Thick-Walled Cylinder (ATWC), and triaxial testing. For the Röt Clay, Single Stage Triaxial Testing (SST) and

Acoustic Travel Time Testing (ATT) have been performed in addition to Brazilian tensile strength and Brinell hardness testing. The findings may be summarised as follows:

- Bunter sandstone: exposure to CO_2 produced differing effects as both decreases and increases in rock strength have been observed. Increases in Unconfined Compressive Strength (UCS) tend to be greater in magnitude than when a decrease occurs; but a marked increase is seen at 1543.6 m as shown in Table 3.5 for the TWC test. Such variations are likely to be facies/mineralogy related; and

- Röt Clay: exposure to CO_2 increased the surface hardness as measured by the Brinell hardness test, especially with increased exposure time. The Brazilian tensile strength test results however showed no clear trends. SST tests run on 3 sets of CO_2 30 day aged claystone plugs showed UCS values of 348bar to 825bar.

Table 3.5: Comparison between Bunter sandstone rock strength pre and post-exposure to CO_2

Plug Ref.	Plug Depth M brt	TWC Yield bar	TWC Collapse bar	Plug Ref.	Plug Depth m brt	TWC Yield bar	TWC Collapse bar	Delta Yield bar	Delta Collapse bar
Fresh sate (connate brine) saturated plugs				30-day scCO2 aged plugs					
4	1438.42	293.0	306.8	5	1438.46	355.7	378.0	62.7	71.2
13	1458.95	509.5	555.9	14	1459.00	479.0	513.9	-30.5	-42.0
28	1501.48	452.3	470.5	29	1501.53	486.1	504.6	33.8	34.1
D1	1538.52	495.5	562.9	D2	1538.56	518.6	575.1	23.1	12.2
E1	1543.85	765.6	860.5	E2	1543.90	907.8	1009.4	142.2	148.9
F1	1556.35	611.0	656.0	F2	1556.42	583.5	651.3	-27.5	-4.7

Notes:
Delta Yield (TWC) = TWC Yield (CO_2 exposed – TWC Yield (fresh state)
Delta Collape (TWC) = TWC Collapse (CO_2 exposed – TWC Collapse (fresh state)

3.9.2 Geochemical modelling and simulation

The numerical models incorporate detailed mineralogical descriptions of the Bunter Formation (derived mainly from petrographic analysis) and of the Endurance brine composition from a comprehensive analysis of formation water samples taken during testing of the 42/25d-3 appraisal well testing. Simulations were performed using a thermodynamic model called PHREEQC (Ref 2), and the GEM-GHG^{TM} reservoir simulator with coupled geochemical code which has been adapted specifically for use in Green House Gas storage modelling. These models have been used to assess the risk to Storage Site integrity of the dissolution of primary cements in the Röt Clay and the Bunter Sandstone, the potential of carbonation reactions to permanently sequester CO_2, and the extent of near-well brine evaporation and associated halite precipitation on CO_2 injectivity and the effectiveness of water-wash as a possible remediation measure.

3.9.2.1 Mineralogy and Fluid Chemistry

This section summarises the mineral composition of the Endurance Storage Site and its overlying seals and also the fluid chemistry of the formation brine.

3.9.3 Geochemical composition of Bunter Formation

The mineralogy data came from petrographic and diagenetic analysis of representative cores of the Röt Halite, the Röt Clay, and the Bunter Sandstone recovered from the 42/25d-3 appraisal well as presented in . Sample depths and the corresponding volume fractions are listed in Table 3.6. The average composition for each zone was used in the simulation model.

Based on the mineralogy analysis in Table 3.6, eight mineral components were chosen for the conceptualisation of mineralogy in the geochemical model. They are quartz, illite, calcite, dolomite, K-feldspar, anhydrite, halite, and albite. Among these albite is used as a surrogate for plagioclase as it is not included in the GEM database.

Table 3.6: Mineral Composition of Bunter Formation from Petrographic Analysis

plug	Depth (ft)		Illite/Smectite	Illite+Mica	Kaolinite	Chlorite	Quartz	K Feldspar	Plagioclase	Calcite	Dolomite	Siderite	Magnesite	Halite	Anhydrite	Pyrite	Hematite	Total
20	4551.00	Röt Halite	0.0	0.0	0.0	0.0	TR	0.0	0.0	0.0	0.0	0.0	0.0	99.7	0.3	0.0	0.0	100.0
34	4565.15		0.0	0.0	0.0	0.0	0.5	0.0	0.0	0.0	0.0	0.0	1.4	28.0	70.1	0.0	0.0	100.0
56	4586.90	Röt Clay	0.0	23.6	0.0	4.2	11.5	TR	1.9	0.0	14.8	0.0	0.0	0.0	43.2	0.0	0.8	100.0
76	4607.55		0.0	36.8	0.0	3.2	20.9	TR	4.8	0.0	27.2	0.0	0.0	0.0	5.5	0.0	1.6	100.0
84	4615.00		0.0	35.2	0.0	2.4	31.1	2.2	2.3	0.0	18.5	0.0	0.0	2.5	4.0	0.0	1.8	100.0
86	4616.90		0.0	TR	0.0	TR	62.7	5.9	2.1	0.0	1.3	0.0	0.0	1.9	26.0	0.0	TR	99.9
139	4670.00	L3	0.0	5.0	TR	0.7	15.3	0.7	1.6	62.8	4.2	0.0	0.0	0.0	8.7	0.0	1.1	100.0
170	4701.00	L2	0.0	3.3	0.0	0.8	66.4	7.1	6.3	0.3	3.9	0.0	0.0	7.1	4.3	0.0	0.4	99.9
219	4749.95		0.0	3.9	TR	0.6	75.0	4.9	5.6	0.0	6.8	0.0	0.0	2.6	0.0	0.0	0.6	100.0
269	4800.10		0.0	13.1	TR	2.1	56.2	4.2	11.8	0.0	4.3	0.0	0.0	2.8	2.9	0.0	2.6	100.0
343	4874.00		0.0	9.5	TR	2.1	64.4	4.4	10.8	0.0	1.4	0.0	0.0	3.6	2.0	0.0	1.9	100.0
399	4929.95		0.0	7.9	TR	1.2	63.1	6.1	8.8	6.1	1.3	0.0	0.0	3.2	1.5	0.0	0.7	99.9
459	4990.00		0.0	7.3	TR	1.5	67.2	4.6	8.0	4.4	1.3	0.0	0.0	2.8	2.0	0.0	1.1	100.0
521	5052.20	L1	0.0	5.0	TR	0.8	69.8	7.1	8.2	TR	1.9	0.0	0.0	5.2	1.3	0.0	0.7	100.0
573	5104.00		0.0	12.1	0.0	0.8	63.5	4.0	10.6	3.8	1.0	0.0	0.0	2.4	1.1	0.0	0.9	100.0

3.9.3.1 *Formation water composition*

The analysis of water samples taken from 42/25d-3 appraisal well shows all water samples were highly saline sodium chloride dominated brines (TDS 300,000 ± 10,000mg/L) with significant concentrations of common rock constituents, calcium, magnesium and sulphate.

Comparing the depth at which samples were taken for water analysis in Table 3.7 and Table 3.8 with the depth where the cores were sampled for mineralogical analysis in Table 3.6 it is found that three water samples match or are close to the core samples; two in Bunter Sandstone L1 and L2 (4722 ft and 5167 ft) and one in Röt Clay (4589 ft). As the thermodynamic model is 0D (zero dimensional), and as the 2D radial geochemical model is a homogeneous model, the initial aqueous concentration data were chosen based on the rock and formation water data from the three depths.

Table 3.7: Physicochemical Parameters

	units	L1a	L2a	L3b		Röt Clay
Sample Reference		1.04	1.09	1.13	2.1	2.14
Sampling Point / Depth	ft	5167.5	4722	4634	Separator Water Line	4589.37
Physicochemical Parameters						
pH immediate @ 20.7 ± 1.2°C Initial		6.20	5.25	5.34	-	4.55
Resistivity @ 20°C	ohm.m	0.0461	0.0466	0.047	0.0466	0.0465
Density @ 20.00 ± 0.08°C	kg/L	1.1958	1.1881	1.1868	1.1976	1.1976
TDS - Measured @ 0.2 µm - By Mass	mg/kg	256146	247659	247730	259680	258925

3.9.3.2 *CO_2 composition*

The normal White Rose CO_2 stream composition is discussed in Section 4.2. For the geochemical modelling, however, the injection stream was assumed 100% CO_2 and other components in the normal stream were ignored.

Table 3.8: Formation water composition

Sampling Point / Depth	ft	5167.5	4722	4634	Separator Water Line	4589.37
Chloride	mg/kg	154146	148780	148164	155600	155405
Fluoride	mg/kg	0.15	0.12	0.1	0.13	0.14
Sulphate	mg/kg	296	359	385	360	364
Bromide	mg/kg	473	460	444	438	470
Nitrate	mg/kg	<4	<4	<4	<4	<4
Iodide	mg/kg	<4	<4	<4	<4	<4
Phosphate	mg/kg	<20	<20	<20	<20	<20
Total Carbonate (as Bicarbonate) Immediate	mg/kg	38	37	43	-	39
Formate	mg/kg	<2	<2	<2	<2	<2
Acetate	mg/kg	<2	<2	<2	<2	<2
Propionate	mg/kg	<3	<3	<3	<3	<3

Sampling Point / Depth	ft	5167.5	4722	4634	Separator Water Line	4589.37
Butyrate	mg/kg	<4	<4	<4	<4	<4
iso	mg/kg	<4	<4	<4	<4	<4
Cl:Br	mg/kg	326	323	334	355	331
Lithium	mg/kg	7.9	8	7.6	8.4	8.5
Barium	mg/kg	2	1	1	1	1
Strontium	mg/kg	108	111	103	117	116
Calcium	mg/kg	8858	8610	8037	8985	9129
Magnesium	mg/kg	2543	3014	3192	3138	3103
Sodium	mg/kg	85512	79664	79953	83763	84792
Potassium	mg/kg	1400	1469	1483	1553	1525
Iron	mg/kg	<1	<1	<1	2	1
Copper	mg/kg	3.9	1.7	1.3	1	1.7
Zinc	mg/kg	7.8	8.5	7.9	8.9	8.8
Manganese	mg/kg	2.6	1.6	1.5	1.7	1.7
Aluminium	mg/kg	<0.6	<0.6	<0.6	<0.6	<0.6
Ammonium	mg/kg	<10	<10	<10	<10	<10
Lead	mg/kg	1.1	1.3	1.4	1.4	1.5
Chromium	mg/kg	0.3	0.4	0.4	0.7	0.7
Nickel	mg/kg	<0.2	1.8	1.6	<0.2	0.4
Cadmium	mg/kg	0.2	0.2	0.2	0.1	0.2
Cobalt	mg/kg	0.15	0.16	0.16	0.09	0.08
Silver	mg/kg	<0.04	<0.04	<0.04	<0.04	<0.04
Vanadium	mg/kg	0.07	0.07	0.08	0.07	0.06
Arsenic	mg/kg	1.2	1.3	1.5	2.1	2.4
Boron	mg/kg	9	10	9	10	10
Phosphorus	mg/kg	<6	<6	<6	<6	<6
Silicon	mg/kg	3	3	3	4	4
Sulphur	mg/kg	84	104	112	107	106
Total Barium	mg/kg	2	2	1	2	1
Total Iron	mg/kg	<1	1	<1	3	1
Soluble Mercury	µg/kg	0.4	0.2	0.2	0.3	<0.2
Total Mercury	µg/kg	0.3	0.2	0.2	0.3	<0.2
Total Cl- equivalent	mg/kg	154597	149271	148670	156071	155906
Total Na+ equivalent		101403	96204	96174	101021	102133
Total NaCl equivalent		255999	245474	244845	257092	258039

3.9.3.3 Thermodynamic data

The rate law used for the mineral dissolution and precipitation reaction is (Bethke, 1996):

Equation 3.2 $$r_\beta = \hat{A}_\beta k_\beta \left(1 - \frac{Q_\beta}{K_{eq,\beta}}\right)$$

where r_β is the rate, $\hat{A}_\beta$ is the reactive surface area for mineral β; k_β is the rate constant of mineral reaction β, $K_{eq,\beta}$ is the chemical equilibrium constant for mineral reaction β and Q_β is the activity product of mineral reaction β.

The CMG-GEM software models changes to formation porosity due to mineral dissolution and precipitation by tracking the associated changes in void volume.

The phase behaviour and properties of reservoir fluids are modelled in the WinProp pre-processor within the CMG-GEM package.

3.9.3.4 Porosity-permeability relationship in dynamic simulation

The Kozeny-Carman perm-poro model (K-C model) was used to predict permeability change induced by mineral dissolution or precipitation. Comparison of simulation results generated using the K-C model and the Verma and Pruess's 'tubes-in-series' model (V-P) showed no noticeable difference between the two – even though this is not apparent from Figure 3.60.

The poro-perm correlation presented in Figure 3.52 has not been used in the prediction of permeability following salt precipitation or dissolution reactions because although this function holds for the consolidated formation rock it may not be applicable for permeability changes that occur as a result of halite precipitation, where it is not known where the halite will deposit (in pore bodies and/or pore throats, and whether once precipitated it will be static, mobile, or mobile until hydrodynamically trapped).

Figure 3.60: Comparison of K-C and V-P permeability-porosity models when ϕc=0.90ϕo when k=0, and n=8

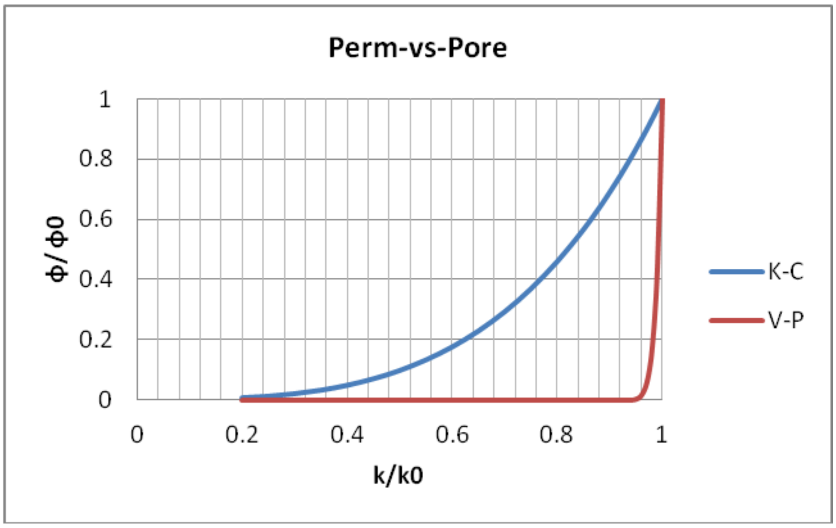

3.9.3.5 Interaction among CO_2, formation water, reservoir and seal facies

The chemical reactions for the PHREEQC modelling were chosen based on the minerals identified in Figure 3.60 and the brine composition in Table 3.8. The primary concern is formation damage in the near wellbore zone and the impact that CO_2 saturated brine could have on the integrity of the cap rock. Thus only the precipitation/dissolution of halite, dolomite, anhydrite and calcite minerals was considered in the main thermodynamic modelling activity.

3.9.3.6 Equilibrium batch 0D modelling (PHREEQC)

PHREEQC was used to run batch geochemical simulations to identify the main chemical reactions in the formation and to validate the equilibrium state based on the water composition data and rock mineral analysis data before building the more complex 2D GEM geochemical model.

In total, six sets of calculations were performed using PHREEQC. Initial calculations were performed to identify the initial equilibrium water composition, and how this varied compared to the supplied water composition. Subsequent calculations then considered the impact of dissolving CO_2 in this brine. The six sets of calculations correspond to six locations in the sequence at various depths, and their corresponding water compositions. These include the Röt Halite, Röt Clay (two intervals) and L3, L2 and L1 intervals of the Bunter sandstone. All simulations were performed using 1L of water @ 57.2°C and 142bar. The conditions are identified in Table 3.9.

Table 3.9: Selected brine and aquifer sections for PHREEQC simulations

Simulation 1	Simulation 2	Simulation 3	Simulation 4	Simulation 5	Simulation 6
Brine @ 5167 feet	Brine @ 4722 feet	Brine @ 4634 feet	Brine @ 4634 feet	Brine @ 4589 feet	Brine @ 4589 feet
L1 @ 5104 feet	L2 @ 4750 feet	L3 @ 4670 feet	Röt Clay 1 @ 4617 feet	Röt Clay 2 @ 4587 feet	Röt Halite @ 4565 feet

Figure 3.61 shows the new mineral compositions as a result of the equilibration process (identifying only minerals that are present in fractions > 10%).

Figure 3.61: Equilibrium mineral fractions from PHREEQC simulations in graphical format

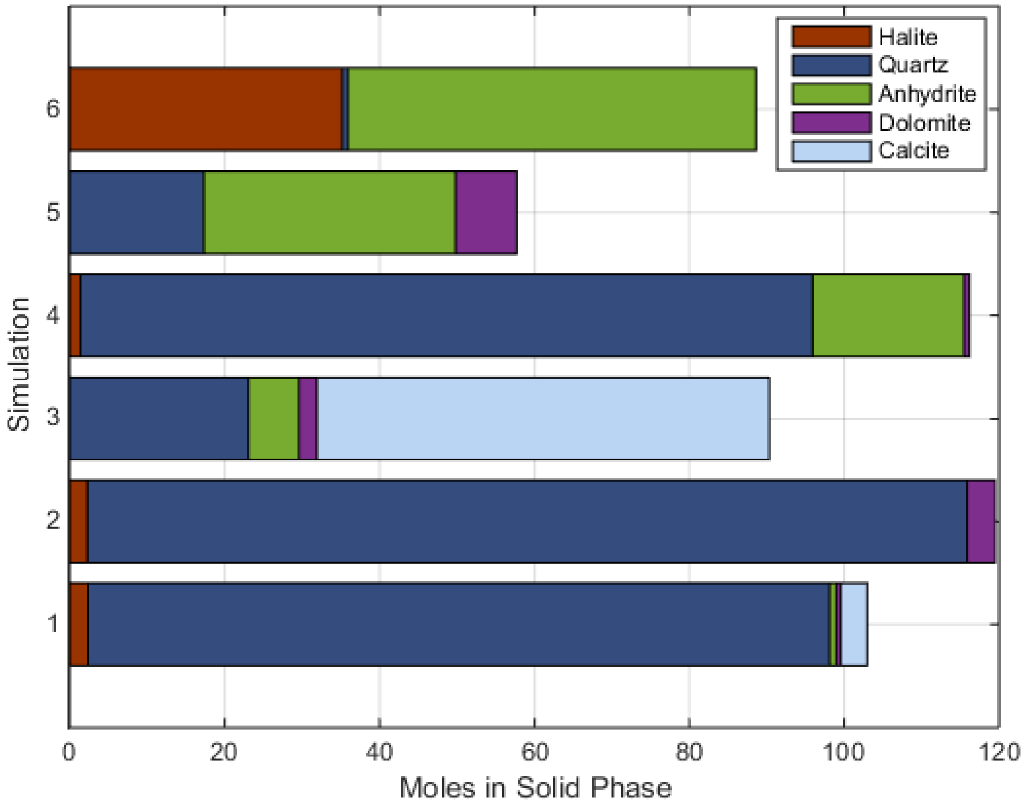

Having established the initial equilibrium conditions, the effect of varying CO_2 concentration on the mineral composition of each of the six scenarios was simulated. The CO_2 solubility for the analysed system is between 0.4 and 0.5 mol/kgw for all intervals. The addition of CO_2 to the formation brine creates carbonic acid, and this results in a drop in brine pH, as shown in Figure 3.62. The pH decreases for increasing amounts of CO_2 (dissociation of carbonic acid). For the Röt Halite, lower pH values are reached because there are no carbonate minerals present to buffer the brine.

Figure 3.62: pH vs CO_2 concentration for 6 scenarios

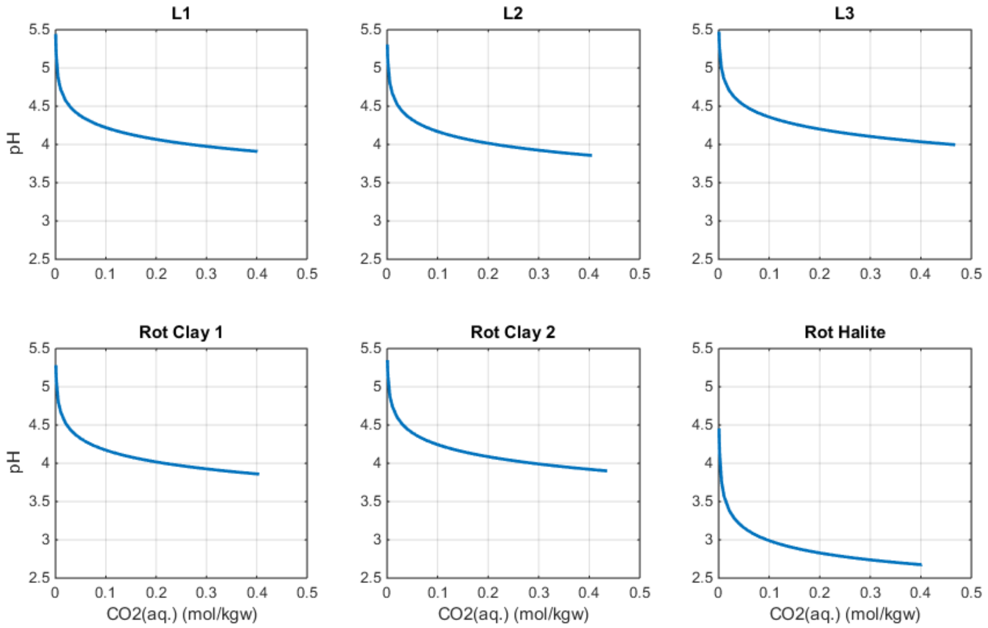

Na and Cl ions have the largest molalities within solution (with molalities an order of magnitude larger than Ca, Mg, and K ions) and represent the dominant species (they set the maximum CO_2 solubility). Increasing CO_2 concentration increased the number of other ions (especially H and HCO_3 ions and led to further dissociation of carbonic acid) in addition to carbonate dissolution (dolomite) and precipitation (calcite). On the other hand, SO_4 ion concentration decreased as anhydrite precipitated (see Figure 3.63).

Figure 3.63: Molalities of HCO_3 and SO_4 ions vs CO_2 concentration for 6 scenarios

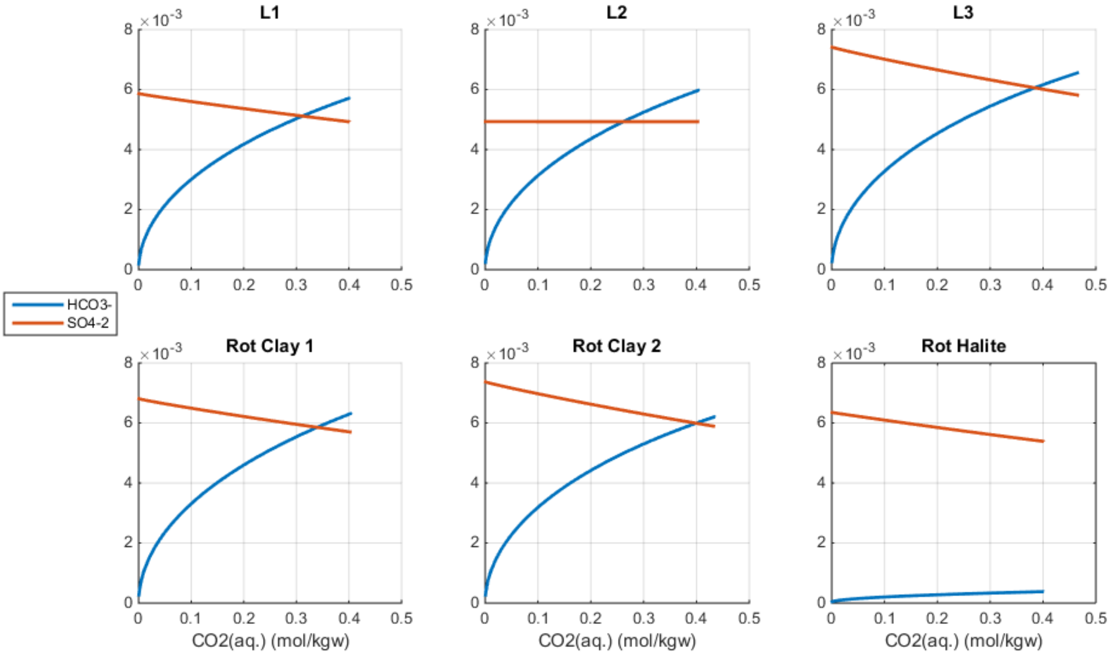

The changes in brine composition are driven by the mineral reactions, and these are shown in Figure 3.64.

Figure 3.64: Mineral changes resulting from increase in CO_2 concentration for 6 scenarios

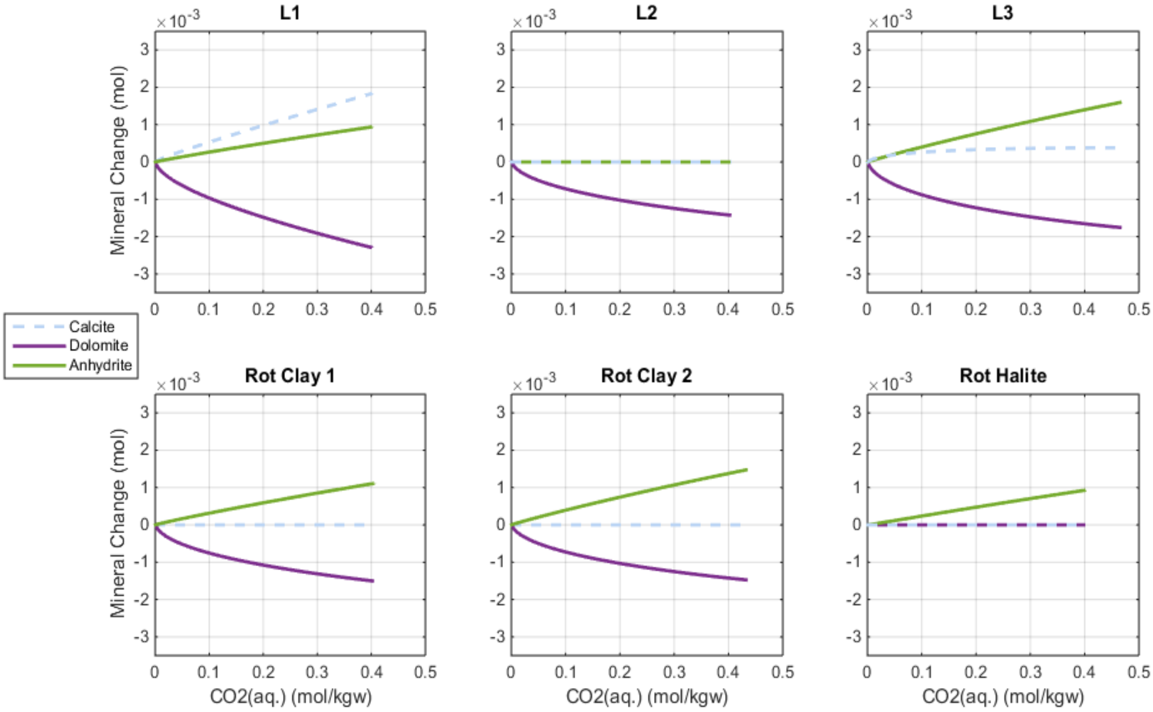

The simulations predict, in general, that only dolomite may dissolve under conditions applicable in Endurance, with all other minerals precipitating.

3.9.3.7 Kinetic batch 0D modelling (PHREEQC)

The last section has identified equilibrium endpoint conditions for a range of CO_2 concentrations. The next sets of calculations include kinetic reaction rates and are used to identify the evolution of the mineralogy over a 10,000 year period.

The Pitzer database was used in all quantitative predictions as it is the database applicable for the conditions in Endurance. However, the Pitzer database includes only a limited set of minerals and sensitivities were therefore performed with the default PHREEQC database to assess the long term evolution of secondary minerals such as hematite, chlorite, kaolinite and K-feldpar which are not included in the Pitzer database.

Simulation was initialised by equilibrating the formation water with the minerals present in each reservoir section. Then, 0.5 mol/kgw of CO_2 was added and kinetic calculations performed for a period up to 10,000 years. Because the final state of the system was reached before 200 years, results have been plotted for this transient period only.

From Figure 3.65, the amount (moles) of dissolved dolomite is higher than the precipitated calcite for all reservoir sections except for Röt Halite where neither mineral is present. Therefore, there is no net mineralisation of CO_2 in the reservoir. From Figure 3.66, halite precipitation is predicted as the fastest mineral reaction and stops after 5 years. Wherever halite precipitation occurs it has a mineral change that is many orders of magnitude larger than the combined mineral change of the remaining three primary minerals (i.e. dolomite, calcite, and anhydrite).

The rock volume changes over the course of the reactions indicate that the decrease in volume due to dolomite dissolution was higher than the increase in volume due to precipitation of calcite and anhydrite combined. This means that porosity is likely to increase in areas where halite does not precipitate, namely L3 and Röt Clay 2. However, this porosity increase would be below detectable limits (<0.001%1 pore volume of fluid) Halite precipitation is the main reaction likely to cause a measurable porosity change – a porosity decrease of approximately 0.1% for 1 pore volume of fluid.

Figure 3.65: Calcite, dolomite and anhydrite precipitation (positive) and dissolution (negative) vs time

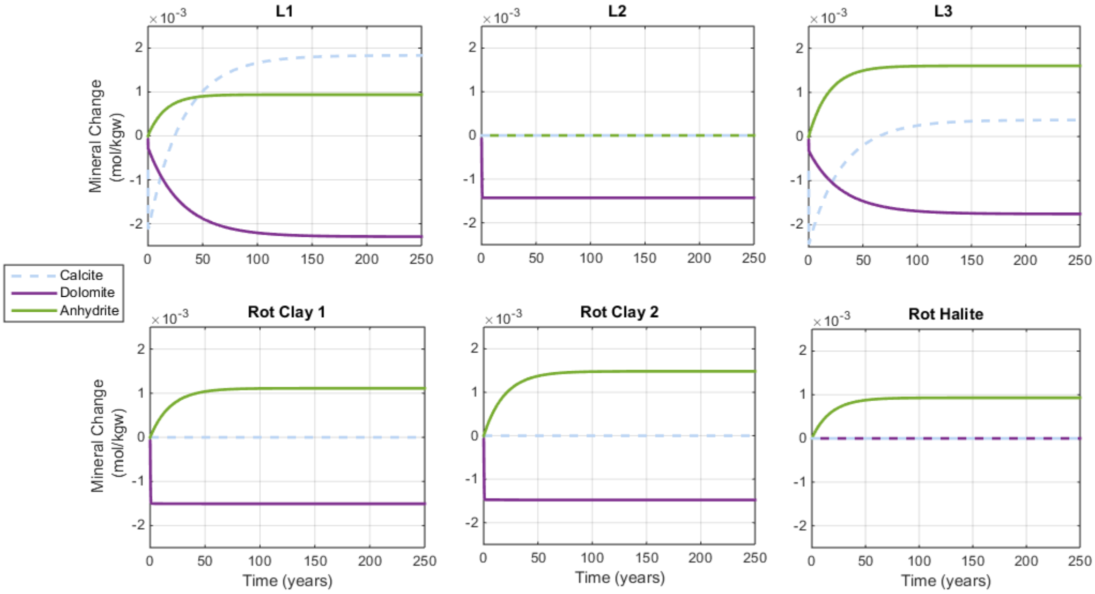

Figure 3.66: Halite precipitation (positive) and dissolution (negative) vs time

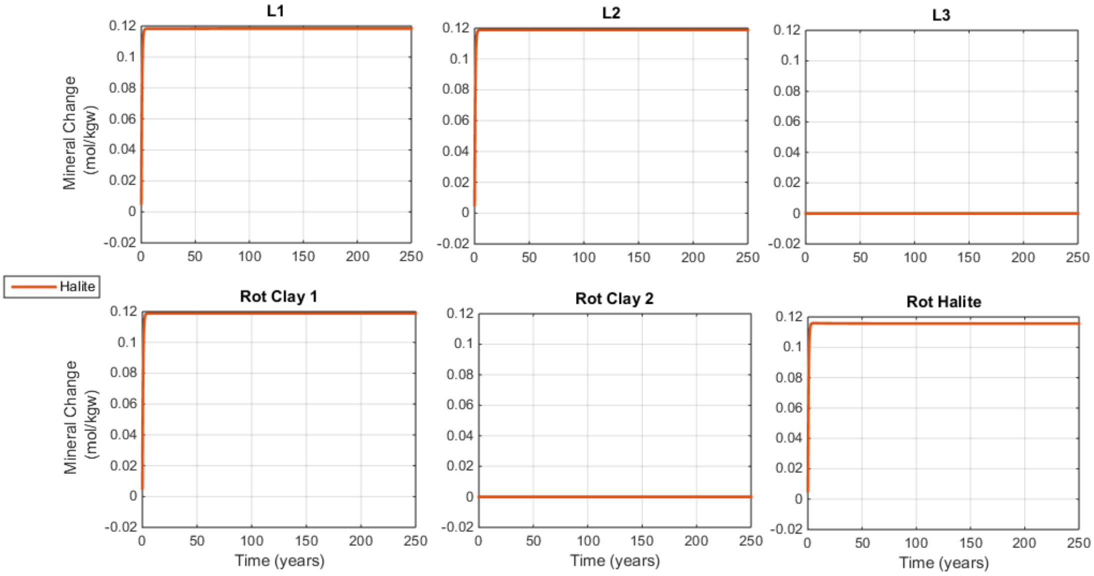

Kinetic Simulation Using PHREEQC default database: the above calculations have been repeated using the default PHREEQC database, but now including other minerals that may be involved in reactions not included in the Pitzer database. The results of this second set of calculations are considered as qualitative only since the PHREEQC database is applicable for salinity conditions only up to 1 mol/kgw, whereas the Pitzer database can handle salinities of over 6 mol/kgw – 4/52 aquifer salinity is approximately 4.3 mol/kgw.

Of the original reactions, calcite, dolomite and anhydrite all undergo dissolution whilst halite was precipitated (Figure 3.67). The other mineral reactions, including dissolution of chlorite and K-feldspar, and precipitation of kaolinite were much slower (Figure 3.68). Note that mineral reactions are shown for the full 10,000 years of the calculations, since the slow reaction kinetics mean that equilibrium is not reached over that period.

Although the default PHREEQC database is not as accurate for Endurance salinity system as compared to the Pitzer database, there is no predicted long term dissolution of major minerals that would affect reservoir or cap rock integrity. Chlorite dissolution at a very low rate may continue for 10,000 years but the volume change is likely to be very small.

Figure 3.67: Calcite, dolomite, anhydrite and halite precipitation (positive) and dissolution (negative) vs time using the default database, and with inclusion of other mineral reactions in the calculation

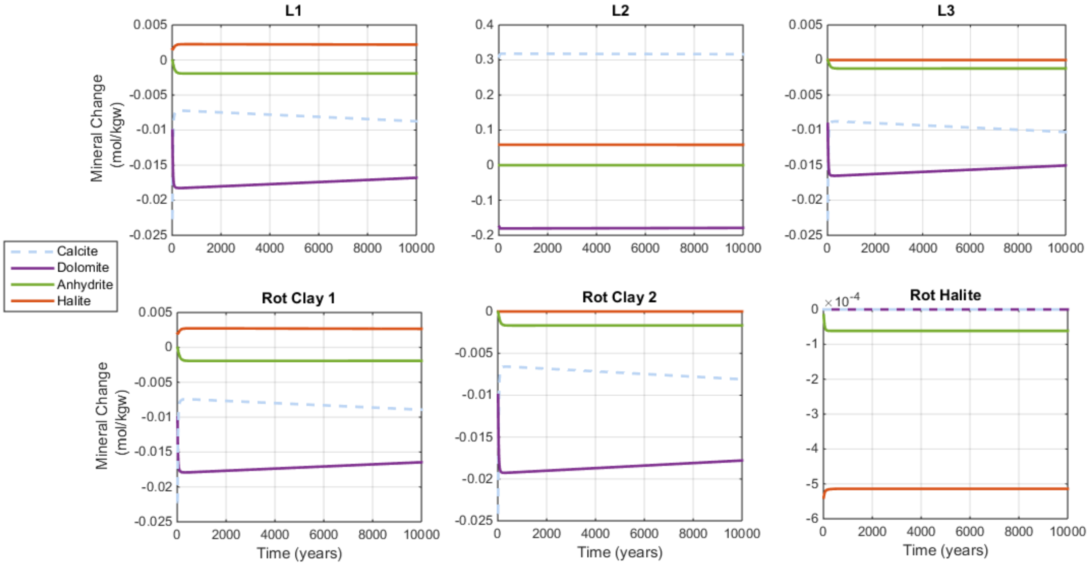

Figure 3.68: Quartz, hematite, chlorite, kaolinite and K-feldspar (positive) and dissolution (negative) vs time using the default database

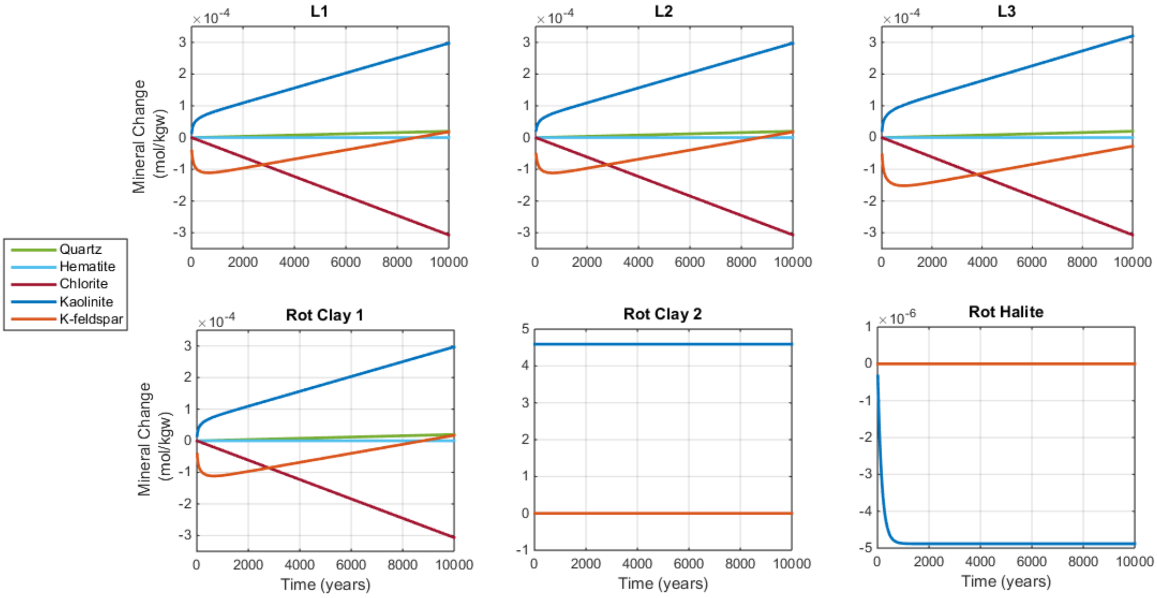

3.9.3.8 *Summary of Kinetic batch 0D modelling (PHREEQC)*

The more accurate Pitzer modelling identifies that halite and anhydrite precipitation is likely to occur (even excluding the effects of evaporation), and that short term calcite dissolution may give way to calcite precipitation, driven by the more long term effects of dolomite dissolution. No dissolution reactions are predicted when CO_2 saturated brine contacts the Röt Halite. Contact of CO_2 saturated brines with the Röt Clay may lead to early time dissolution of dolomite, but this is likely to stop by the end of White Rose CO_2 injection period. Long term dissolution of dolomite would only take place in the Bunter sandstone intervals, and the volume changes due to this reaction are predicted to be small. Furthermore, dolomite cement exists as isolated nodules in the Bunter sandstone and does not contribute significantly to the overall rock strength, its dissolution is unlikely to have any impact on Storage Site integrity. The net trapping of CO_2 as a solid mineral phase is likely to be less than 1 % of White Rose CO_2 injection.

3.9.3.9 *Fluid Flow and Geochemical Reaction Coupled Modelling (GEM)*

The coupled flow and geochemical simulations were performed using GEM-GHG software by Computer Modelling Group Ltd. GEM-GHG is a general Equation-of-State (EoS), three-dimensional compositional reservoir simulator for modelling multi-phase flow of multi-component fluids, and specifically adapted for use in Green House Gas (GHG) storage modelling.

The 2D simplified model is built with a radial mesh of 48 layers: 2 layers of cap rock, 45 layers of Bunter Sandstone, and one layer of underburden. Two regions were defined to represent cap rock (Röt Halite and Röt Clay) and Bunter Sandstone. The underburden had the same properties as the cap rock. The dimension of the model is 4000m in radius, 375 m in thickness with a dip angle of 2 degrees. The top of the model is at the depth of 1200m. A numerical aquifer is connected at the out boundary of the model and the spill point is at the outermost column of cells at a depth of about 1480m. The injector is in the centre of the model as shown in Figure 3.69. The perforations go through the L2 and L3 zone (layer 22 to

47). Injection of CO_2 is simulated at 0.6MTPA for 15 years. A pre-injection run was carried out for formation equilibrium.

Figure 3.69: Model geometry and cross-section with porosity distribution for the 2D GEM model

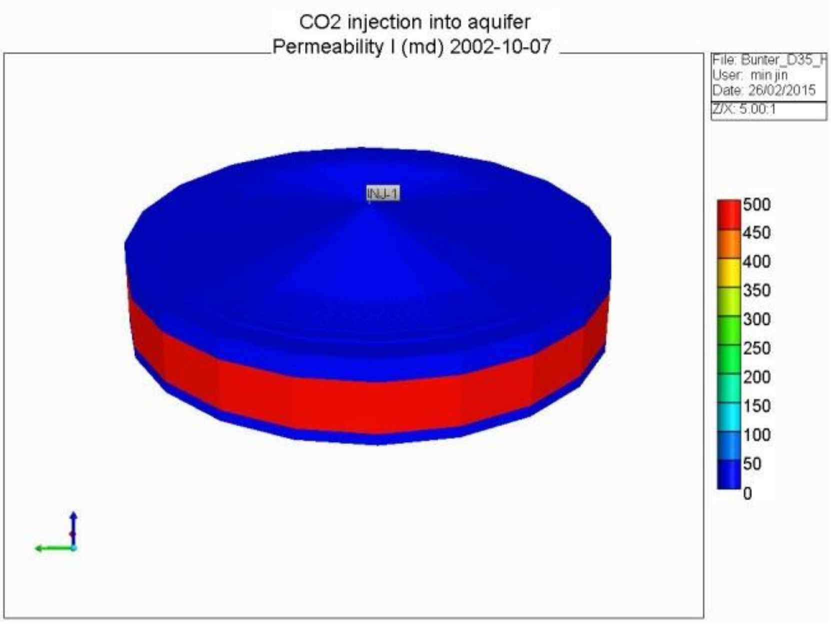

Fluid flow and rock properties: Table 3.10 gives a summary of the rock and fluid properties for the two model geometries used. Measured Endurance relative permeability and capillary pressure curves (Figure 3.68) have been used for the simulations whilst the Viking-2 data was used as a sensitivity.

Table 3.10: Input data for simulation models illustrated in Figure 3.69

Grid type		1D Radial model	2D Radial model
Grid dimension	I x J x K	699x1x3	
grid size	ni x di	495x0.02	642x5
Röt Fm.	nk x dk	1x100	1x80, 1x20
BSS Fm.	nk x dk	1x225	45x5
Under burden	nk x dk	1x50	1x50
datum	m	1300	1300
Pressure	kPa	14120	14120
Pressure gradient	bar/m	0.115	0.115
Temperature	C	57.2	57.2
Temperature gradient	Degree C/m	0.0316	0.0316
Pore compressibility	1/kPa	$5.0x10^{-7}$	$5.0x10^{-7}$
Porosity (o/u burden)		0.1	0.1
Porosity (BSS)		0.22	0.22
Permeability (o/u’ burden)	mD	0.0001	0.0001
Permeability (BSS)	mD	500	500
Deepest inj. point	m	1459	1459

Grid type		1D Radial model	2D Radial model
Top perforation	m	1292	1292

Chemical reaction model: three aqueous reactions and six mineral reactions were selected, based on the PHREEQC modelling above and reactions reported in the literature for minor minerals.

Results:

Figure 3.70 shows the porosity change due to mineral reactions. The main porosity change induced by CO_2 injection was from halite precipitation (mainly from brine evaporation) because of a combination of relatively high Na and Cl concentrations relative to the other components and the relative low rates of other reactions.

Figure 3.70: Porosity change due to CO_2 injection and salt precipitation after 100 and 5000 days. The figure indicates the gradual formation of a low permeability flow barrier near the perforations which forced a change in CO_2 migration path during the rest of injection

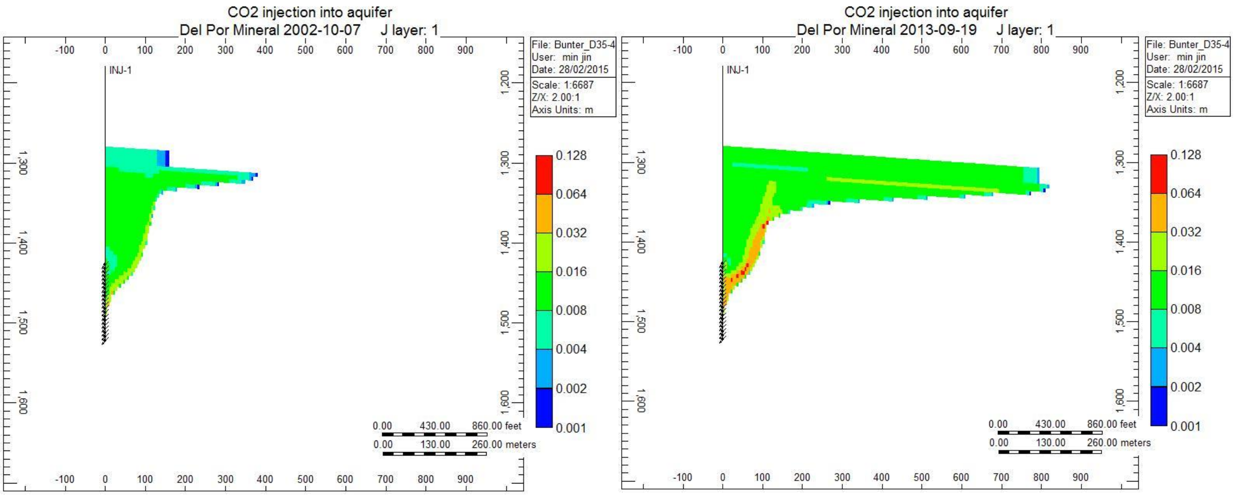

As shown in Figure 3.70, a low porosity zone was formed gradually at the edge of CO_2 plume in the 2D model. The pronounced vertical solid saturation trend and the emergence of a localized region with very large salt precipitation near the lower portion of the dry-out front was caused by a backflow of brine towards the injector under capillary force, which provides a continuous supply of salt that increase the local salinity and the precipitatable salt. Gravity override effects accelerated the accumulation of solids.

The permeability reduction due to halite precipitation at different time steps is shown in Figure 3.71. The permeability in the front at 5000 days was predicted to reduce to about 1/3 - 1/2 of its initial value whilst a region with an impaired permeability can be seen to develop along the top perforations.

Figure 3.71: Permeability reduction due to the halite precipitation at different time steps (a) 1000, (b) 2000, (c) 3000, and (d) 5000 days. The permeability at the front after 5000 days reduced to about 40% of its initial value

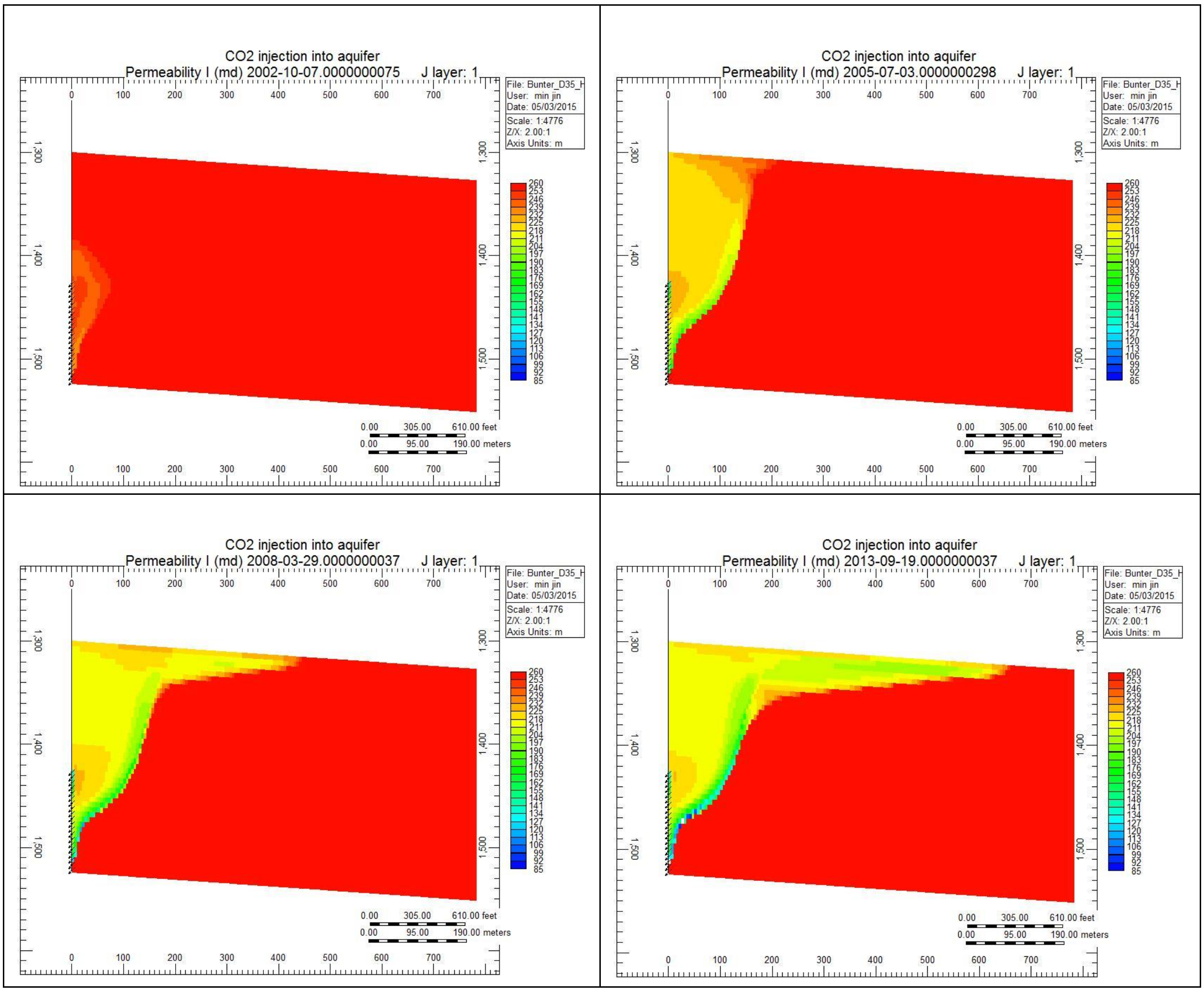

A freshwater flush, which reduces the brine salinity near the wellbore before CO_2 injection (re-injection water flushing), was simulated to assess its effectiveness in alleviating injectivity impairment, caused by salt precipitation during CO_2 injection. The pre-flush water was injected for 10 days. Figure 3.72 shows a comparison of the permeability reduction in the model without pre-flush (left) and with pre-flush (right) after 600 days. In the model with pre-flush a low salinity region was created that established a pathway for CO_2 migration and pressure release. The maximum well Bottom Hole Pressure (BHP) after 3 years of CO_2 injection was reduced by about 40% compared to the model without the pre-flush.

Figure 3.72: Comparison of permeability reduction between (a) no water flush model and (b) pre-flushed model, after 600 days

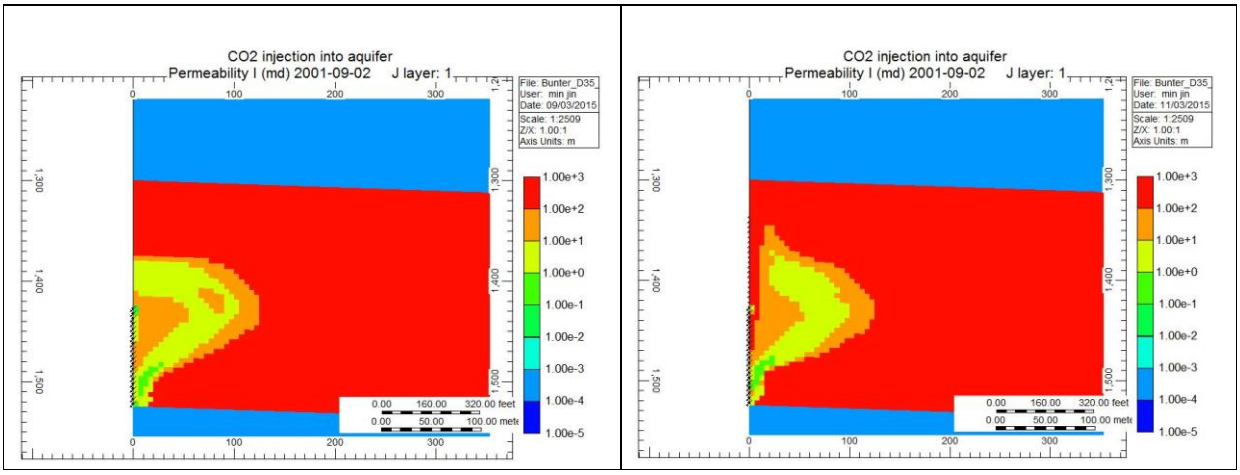

3.9.4 Summary of Fluid Flow and Geochemical Reaction Coupled Modelling

The impact of halite deposition was to channel the CO_2 but there was no significant change in injection pressure. Where extreme modelling assumptions have been made, a 20% reduction in injectivity was predicted over a three year period. The coupled flow and geochemical simulations suggest that the impact of halite precipitation on injectivity during continuous and sustained injection of CO_2 at a constant rate will not be significant.

3.9.4.1 CO_2 Exposure in Analogous Reservoirs: Literature survey

Published works have been examined to understand the interaction of CO_2 with sandstone reservoirs that share key features (sandstone mineralogy, highly saline brine, halite seal, etc) with the Endurance Storage Site to discover relevant lessons that could be incorporated into operational planning.

The introduction of CO_2 into saline aquifers could give rise to geochemical processes such as CO_2 dissolution in brine forming a weak acid which reacts with the minerals of the aquifer and the caprock, leading to mineral precipitation and dissolution reactions that span varying timescales.

In the short term it is near-well precipitation of minerals that presents the greatest challenge since this can lead to reduced porosity and permeability and thus decrease the injectivity. Although salt precipitation due to CO_2 injection have been observed to reduce rock permeability by up 70% in reservoir condition laboratory experiments using brine salinities ranging from 150,000 – 350,000mg/l , all the instances of CO_2/reservoir interactions examined by the review (including CO_2 Storage Sites as well as CO_2-EOR operations) relate to brine with salinities that are much lower than found in the Endurance reservoir (~300, 000mg/l) (see Figure 3.73).

Only one out of the six studied sites reported injectivity problems (Snohvit), however, this particular case was mainly due to fluvial reservoir heterogeneities and limited high permeability channel sandstone connected to large volume of poorer injectivity reservoir. At Snohvit, the extent of good reservoir was less than predicted because of the presence of faults which sealed lateral connectivity and blocked access to the larger reservoir volume. The dislodging of fine particles (i.e. clays and other particles not contributing to the grain framework) due to CO_2 injection in addition to salt precipitation were also claimed to have contributed to the reduction in injectivity at Snohvit (Ref 3). The injectivity impairment was temporarily ameliorated by injection of MEG (monoethylene glycol) (Ref 4). However, no data on the actual levels of overall injectivity change nor on the geochemical reactions involved has been published but it was stated that the impact of mineral precipitation was “minor”.

Petrographic analysis indicate the Endurance Storage Site contains high amounts of detrital feldspar (13.8% K-feldspars and 10.9% plagioclase) as well as carbonate (9.6%) and anhydrite (2.2%) cements and trace amounts of diagenetic halite . Geochemical modelling of Endurance (Section 3.9.2) suggests that only dolomite carbonate cements will dissolve as a result of brine acidification due to injected CO_2 dissolusion. However, dolomite occur in relatively small amounts as isolated nodules and is not part of the load-bearing framework of the Endurance Bunter sandstone and therefore the impact of its dissolution on injectivity or Storage Site integrity is likely to be immeasurably small. The detrital feldspars are on the other hand integral to the load-bearing framework but alteration of siliciclastic minerals takes much longer than carbonate alteration and it’s unlikely to have an impact on the injection phase timescales. Studies of analogue reservoirs which remain water wet have, however, shown that over geological time-scales all feldspars can be dissolved and replaced by authigenic clays. For example, the average feldspar content in reservoir sandstones in the Otway Basin, Australia, is highly dependent on the CO_2 content of the reservoir – high CO_2 reservoirs have <1% feldspar whilst low CO_2 reservoirs have ~25% detrital feldspar (Higgs et al, 2014). Long term geological modelling of CO_2 interaction with the Endurance Storage Site suggests that K-feldspar will dissolve rapidly in the first few hundred years followed by a long period of slower precipitation which will restore the initial K-feldspar content after approximately 10, 000 years (see Figure 3.67, Section 3.9.3.7).

Experimental studies on CO_2 injection into Rotliegend gasfields (alluvial fan Slochteren Formation) of Netherlands, Germany, and Poland also holdsome lessons for the Endurance Storage Site even though the reservoir mineralogies of these fields differ from that of Endurance. Short term effects (30 day, 300bar, and 100ºC) include partial dissolution of feldspar, anhydrite, carbonate, kaolinite (Ref 5); followed by precipitation of halite as the porewater dries into the CO_2. Addition of 100 ppm and 5000 ppm H_2S trace quantities produced significant growth of anhydrite with pyrite, and severe halite precipitation. The injection of pure CO_2 led to 10 – 30% increase in reservoir permeability whilst caprock permeability increased by 3x to 10x – although it was still in the micro Darcy range and provided a good seal. With 100 ppm and 5000 ppm H_2S added to the CO_2 stream, permeability increased after 30 – 80 days by between +3% for reservoir and 30% for the caprock as halite precipitation come to be dominated by mineral dissolution of the rock framework. The CO_2 stream specification for transportation to and storage at Endurance precludes processing streams with these high levels of H_2S.

Figure 3.73: Bar chart illustrating the brine salinity of the 5/42 (Endurance) reservoir compared to other CO_2 storage and CO_2-EOR operations. Red at Snohvit indicates injectivity problems partly related to near well mineral precipitation. Ketzin not included due to gas phase injection

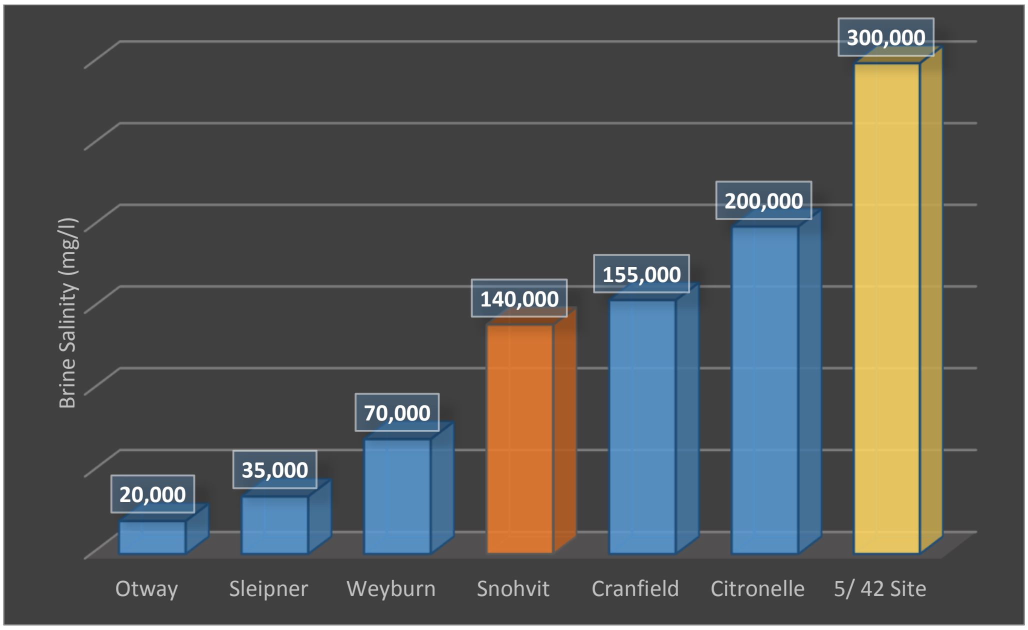

4 Reservoir Engineering

4.1 Core Analysis

Four cores were recovered from well 42/25d-3 totalling a length of 192.51 m (631.6 ft) (Figure 4.1). Core 1 (84.6 ft.; 25.79 m) recovered the lower part of the Röt Halite and the whole of the Röt Clay unit including the first few feet of the top Bunter sandstone, whilst Cores 2, 3, and 4 recovered 166.73 m (547 ft) of the Bunter sandstone section. All cores were delivered to Weatherford Laboratories (UK) Limited in July, 2013 for core analysis. The core analysis was divided into broadly two parts: the conventional, Routine Core Analysis (RCA) and the Special Core Analysis (SCAL).

The RCA involved photographing, CT scanning, spectrographic gamma ray, as well as core plug permeabilty, probe permeametry measurements, porosity, grain density and particle size analysis in addition to plug selection for further SCAL work. A cleaning study to determine the effect cleaning agents had on the halite within the core plugs and Mercury Injection Capillary Pressure tests were also completed.

The SCAL study was preceded by an Interfacial Tension study to determine how a synthetic formation water would react with CO_2 at reservoir conditions, as well as a study to determine the effect of critical flow velocity. Subsequently the SCAL study identified irreducible water saturation and relative permeability curve parameters for use in dynamic modelling based on capillary pressure and 1-D core performance modelling results.

Figure 4.1: 42/25d-3 well schematic showing cored interval

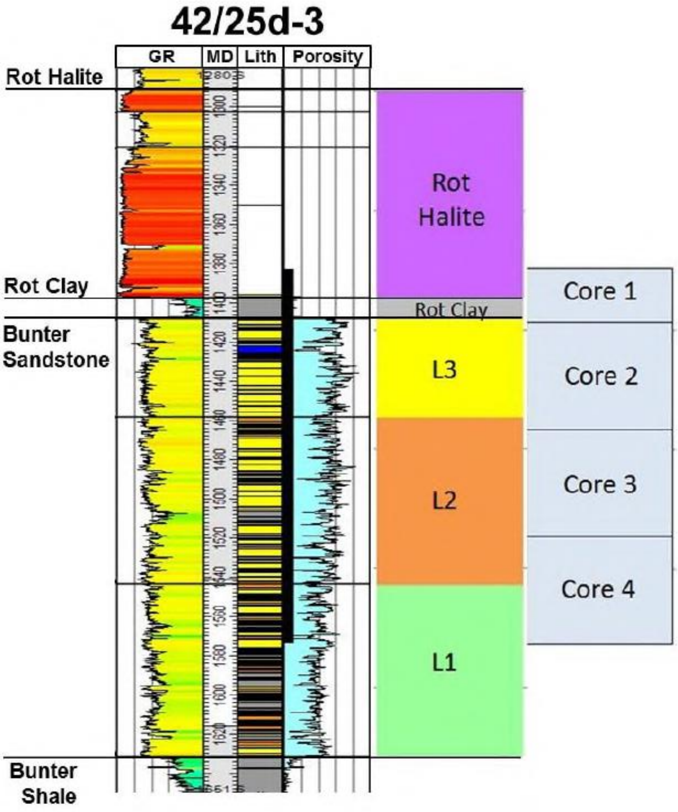

4.1.1 Conventional Core Analysis

The main objective of the RCA was to determine basic rock properties of the cores recovered from appraisal well 42/25d-3 and to prepare plug samples for use in more specialised core analyses. The basic rock properties measured during RCA include porosity, permeability, grain density and grain size distribution. The following sections give brief summaries of the RCA programme in a broadly chronological order.

4.1.1.1 Core Preparation

Core 1 was cored using 4” diameter half-moon sleeves and delivered to the laboratory cut into 3 ft lengths, immersed in plastic tubes containing a bland mineral oil, capped at each end. Following CT scanning, these were removed from the tubes and transferred to custom made stainless steel troughs, immersed under Isopar L oil. This prevented the core from de-hydrating whilst allowing its surface to be viewed as required. Cores 2, 3 and 4 were approximately 3.5” in diameter and arrived at the laboratory in 30 ft aluminium inner sleeves which were then cut into 3 ft lengths to enable the core sections to be handled. Other operations associated with core preparation: Core Gamma run, CT Scanning, Core Handling, Samples Preservation, Conventional Core Plug Sample Preparation, Special Core Analysis (SCAL) Plugs Preparation, and Plug Sample Analysis.

4.1.1.2 Permeability

Permeability was determined by use of a Weatherford Laboratories DGP-300B Steady State Nitrogen Permeameter at an effective confining pressure of 400 psig. These were used in conjunction with the callipered length and diameter to calculate permeability from Darcy's equation.

As an internal quality control, one in ten plugs were re-run during analysis of the samples, and prior to running the plugs, check plugs of predetermined permeability covering a range from 0.18mD to 6000mD were analysed, with each check plug corresponding to a mass flowmeter in the permeameter.

4.1.1.3 Helium Porosity and Grain Density

Porosity of the clean, dry unsleeved plug samples was determined by direct measurement of grain volume at ambient conditions and bulk volume determined by mercury displacement. The sleeved plugs underwent an additional direct pore volume measurement using a confining pressure of 400 psig.

Grain volume was determined using a Weatherford Laboratories DHP-100 Boyle's Law porosimeter. Bulk volume for the mounted plugs was calculated from the sum of the measured grain volume and direct pore volume. Grain density was calculated from the weight and measured grain volume, taking care that all sleeving materials volume and weight were subtracted. The porosity measurements were repeated to ± 0.02 psi.

Cross plots of horizontal permeability and vertical permeability vs. porosity are presented in Figure 4.2 and Figure 4.3.

Figure 4.2: 42/25d-3 Helium Porosity vs Horizontal Permeability

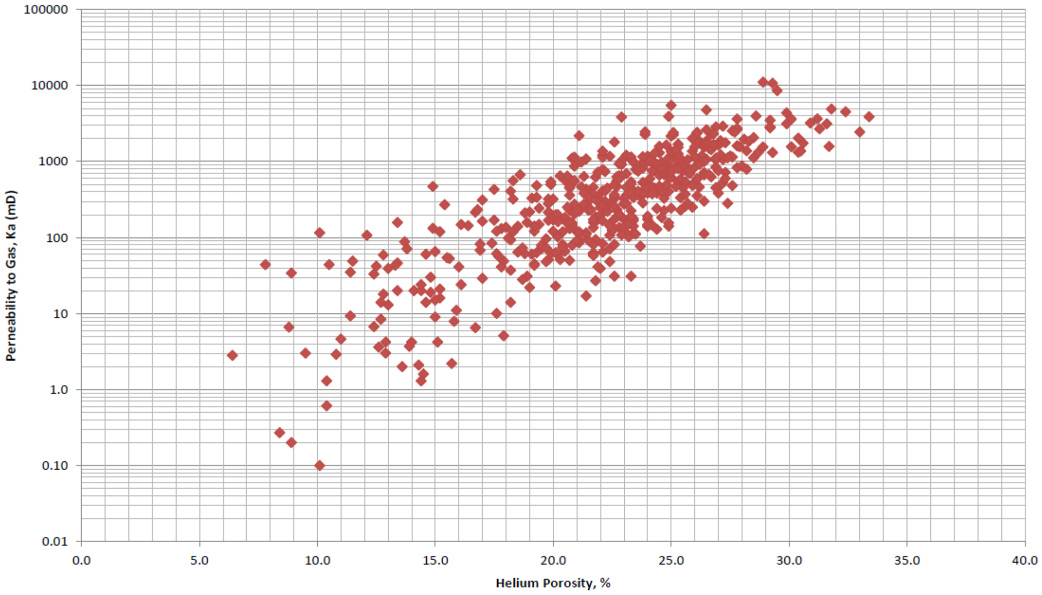

Figure 4.3: 42/25d-3 Helium Porosity vs Vertical Permeability

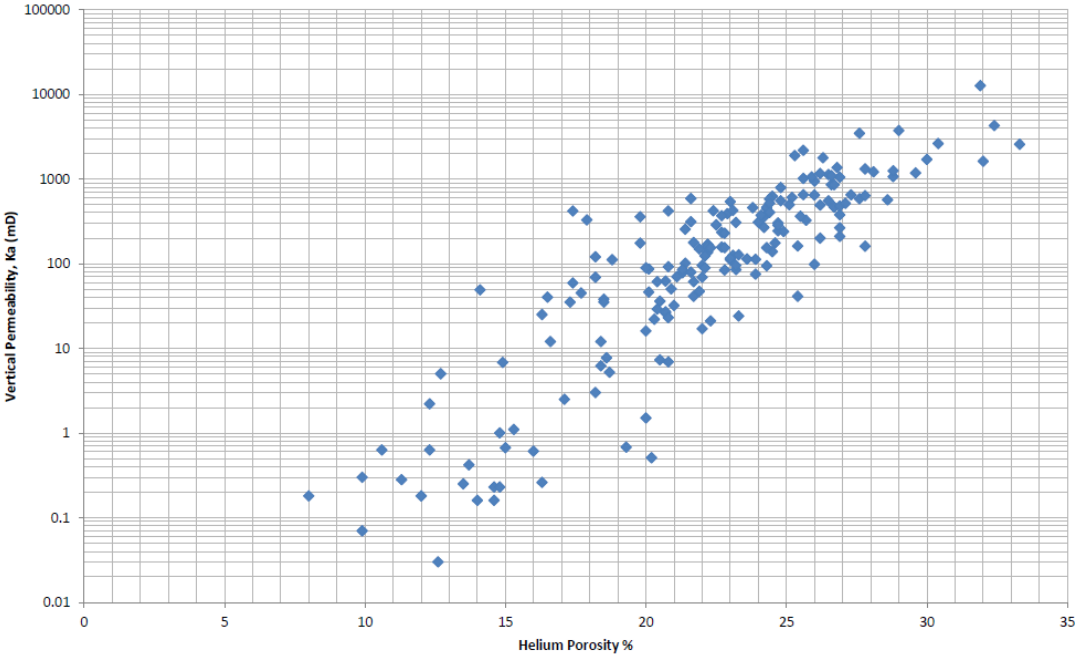

Fifteen plugs were re-measured independently for porosity after an assessment of the original preliminary data showed that the measured porosities for these samples fell outside the accepted error margins in comparison to the calculated length x area porosities. Re-measurement put back the new lengths, diameters and porosities into the accepted error margin. The initial deviations were attributed to plugs misshaped by chipped edges or sides, fractures or slight ridges along plug lengths.

4.1.1.4 Klinkenberg Permeability

Klinkenberg Permeability was determined by use of a Weatherford Laboratories DGP-300B Steady State Nitrogen Permeameter at two minimum sleeve pressures of 400 psig (28barg) and 2600 psig (179barg).

Measurements were repeated a minimum of four times on each sample at different mean pore pressures to enable the calculation of Klinkenberg permeability (Kl). Permeability to CO_2 was plotted vs 1/mean pore pressure and the best fit line extrapolated to infinite mean pore pressure to provide the Kl.

Example Klinkenberg permeability data are presented in Figure 4.4 and Figure 4.5 for sample 94 (4624.90ft) at confining pressures of 28barg and 179barg respectively.

Figure 4.4: Klinkenberg plot for sample 94 (4624.90 ft) at a confining pressure of 28barg

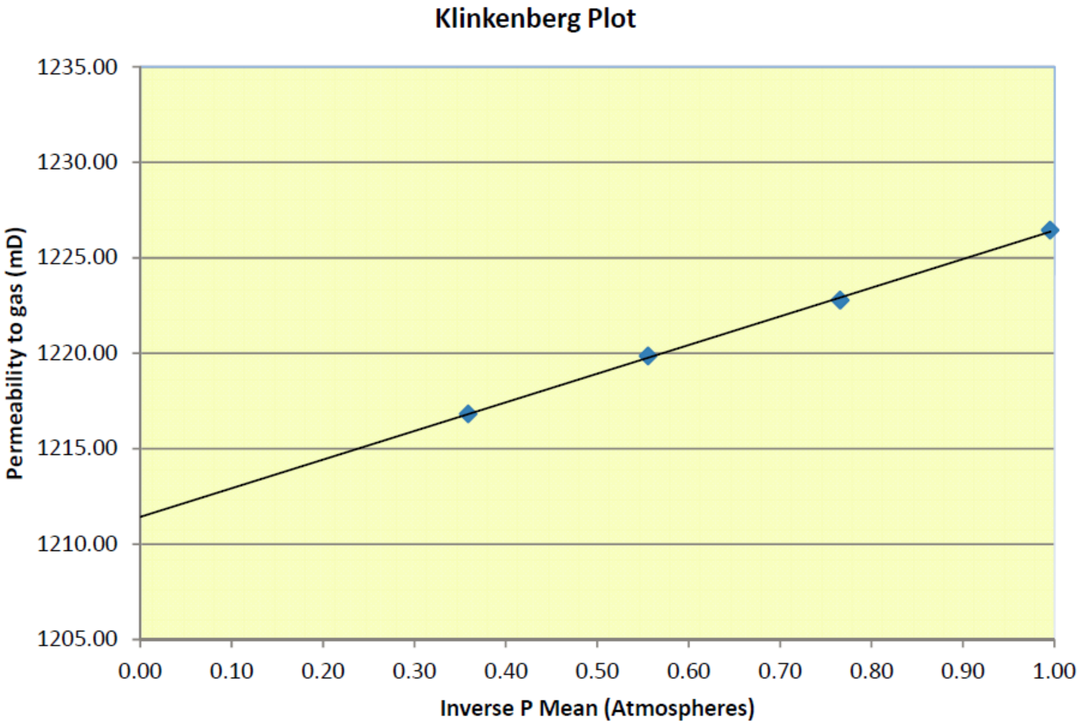

Figure 4.5: - Klinkenberg plot for sample 94 (4624.90 ft) at a confining pressure of 179barg

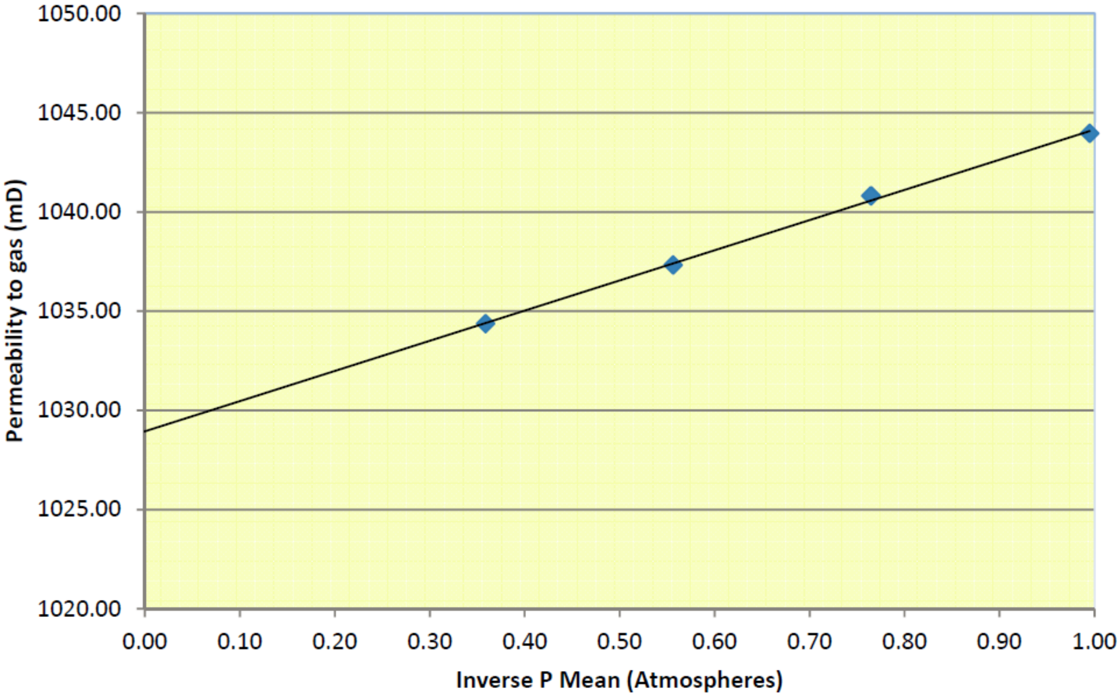

4.1.1.5 Slabbing

On completion of all sampling and plugging the core was slabbed 1/3 to 2/3 to expose maximum dip dry. The slabbed core was placed into plastic gutters to support it without movement.

4.1.1.6 Core Photography

Following slabbing, salt was leaching to the surface of the core, obscuring the sedimentological features. In order to improve this, each section was carefully sanded and smoothed prior to quickly taking the core photograph under white light.

4.1.1.7 Resination

Following core photography, a second slabbing cut was performed. A 2cm thick “biscuit-slice” was taken along the entire cored interval from the photographed face of the 1/2 cut core section. The slice was placed into plastic presentation trays, labelled with well name, core number, box number, and all routine porosity and permeability data. Clear Epoxy resin was then used to seal the core into the trays for archive purposes.

4.1.1.8 Particle Size Analysis

Laser particle size analysis and sieve analysis were performed on 17 plug samples. Sieve Analysis is a procedure used to assess the particle size distribution of a granular material by weight whilst Laser Particle Size Analysis (LPSA) is used to assess the particle size distribution of a granular material by laser diffraction.

Sieve analysis is applicable for particles larger than coarse silt (45 microns) whilst Laser particle size analysis is applicable for particles from 2 mm to 0.02 microns.

Graphical LPSA and sieve analyses data is presented in Figure 4.6.

Figure 4.6: - Particle size distribution from laser and sieve grain size analysis

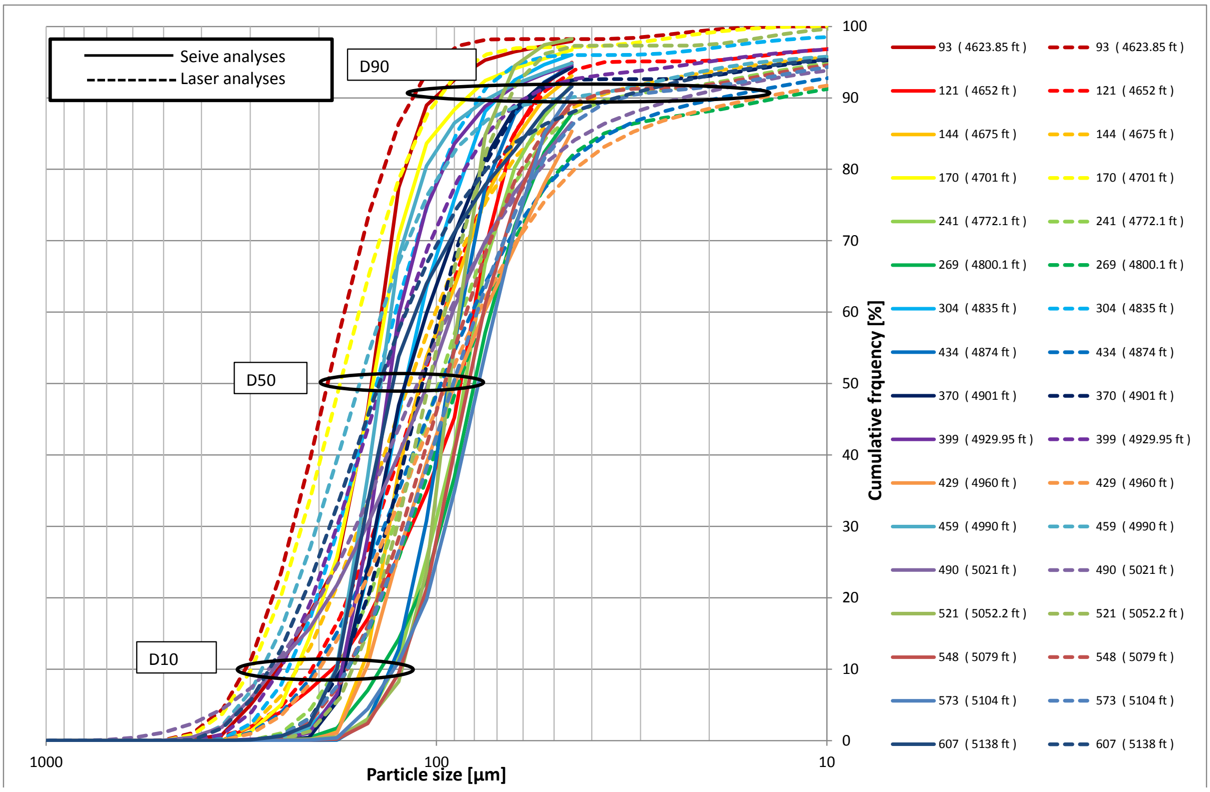

4.1.1.9 Unconventional RCA Studies

Additional studies (which may be termed unconventional RCA) have been performed at Weatherford Laboratories in Norway to support the routine core analysis carried out in the UK using 30 core plugs. The main outlines of the study are:

1. Perform a non-standard cleaning study on plug samples and sister end trims, perform basic rock properties on plugs samples, and prepare sister end trims for Scanning Electronic Microscope.

   The Bunter formation contains potential native halite minerals and has a highly saline formation water. This study was meant to assess the extent to which the removal of native and/or precipitated salts produced changes in basic rock properties and to ascertain the most appropriate method of cleaning Bunter core for RCA.

   Trims from samples were taken through three cycles of cleaning and basic petrophysical properties determined after each cleaning cycle. All the samples that survived through all cycles of cleaning show a tendency to an increase in permeability but the increase was not significant (see Figure 4.7).

Standard cleaning procedures were therefore considered appropriate for cleaning Bunter cores for RCA.

2. Seal unit-cap rock tests meant to determine pore throat size distributions and as a characterisation tool for geological and petrophysical parameters including:
    a. Water permeability measurements at 400 psi net confining pressure
    b. Pore squeeze to 2600 psi net confining pressure
    c. Water permeability measurements at 2600 psi net confining pressure
    d. Measurement of bulk volume by Archimedes principal
    e. Grain volume and porosity measurements

This test program was shared between Weatherford’s Stavanger and Trondheim laboratories. Tests **a**. to **d**. above were performed at the Stavanger lab, and the remaining at the Trondheim lab. The original test program at Trondheim lab had to be curtailed because of damage (ranging from complete plug dissolution to fracturing) to all but one of the 19 samples due to prolonged storage in cold isopropanol. It is therefore important to note that even if great care was taken when collecting grains of the damaged samples stored in isopropanol into the thimbles prior to soxhlet cleaning, some grains would have been lost. This will affect the interpretation of the results for grain density and porosity. The results are summarised in Figure 4.8 and Figure 4.9.

3. Capillary pressure by mercury injection or Mercury Injection Capillary Measurements, MICP: This is to determine pore throat size distributions and for use as a characterisation tool for dynamic models.

Before performing MICP, cleaned Bunter core samples were oven dried and their pore volume, density, and porosity determined.

Figure 4.10 shows the plot of mercury pressure versus mercury saturation. The pore throat size distribution is given as a plot in Figure 4.11. The pore throat distribution size varies from 0.752 microns to 13.463 microns, corresponding to an injection pressure that varies from 2.52 psia to 62.25 psia. The J-function is plotted against saturation in Figure 4.12.

Table 4.1 is a summary of the measured petrophysical properties obtained as part of the additional RCA study. The table shows the range (from minimum to maximum values) of each measurement and also indicates the applicable test program.

Figure 4.7: Klinkenberg corrected CO_2 permeability, kL, vs. Helium porosity, ϕHe

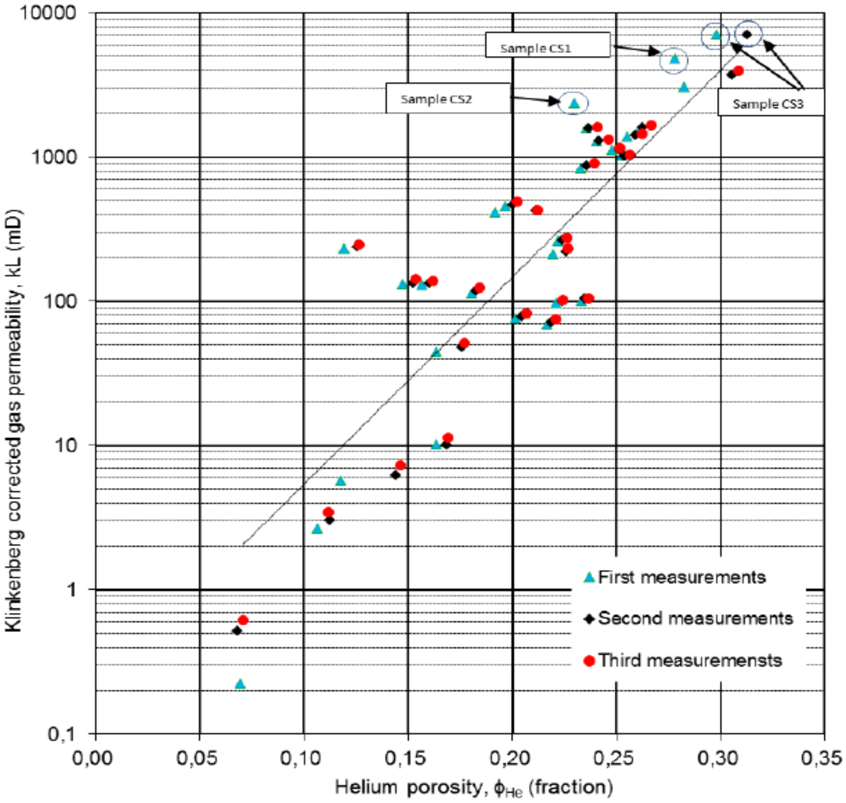

Figure 4.8: kw at 400 psi NCP vs. porosity obtained at Trondheim Lab

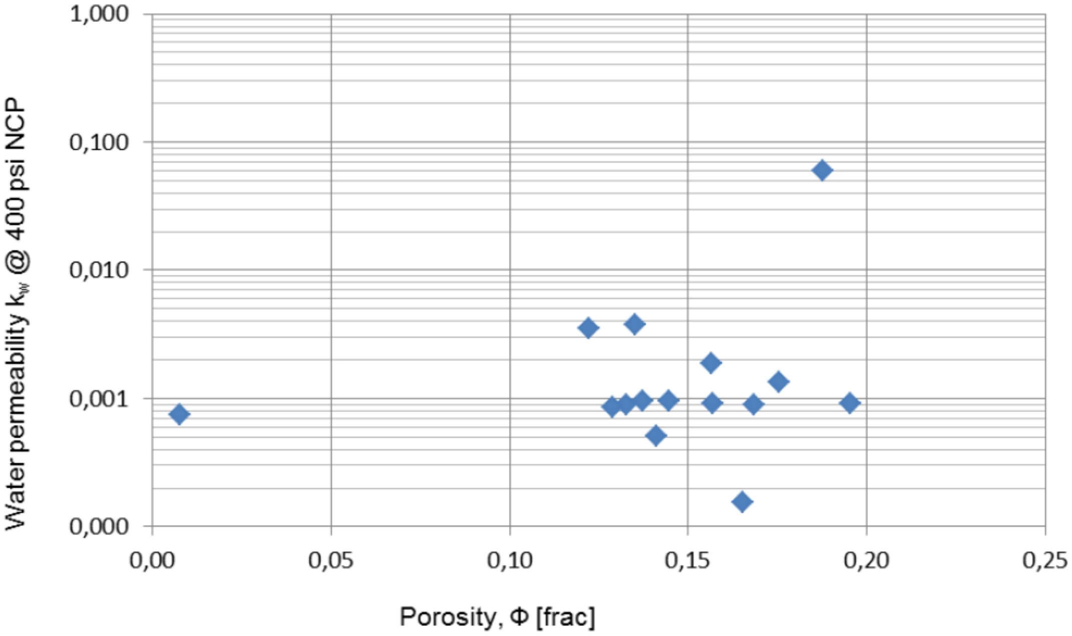

Figure 4.9: kw at 2600 psi NCP vs. porosity calculated at 2600 psi NCP

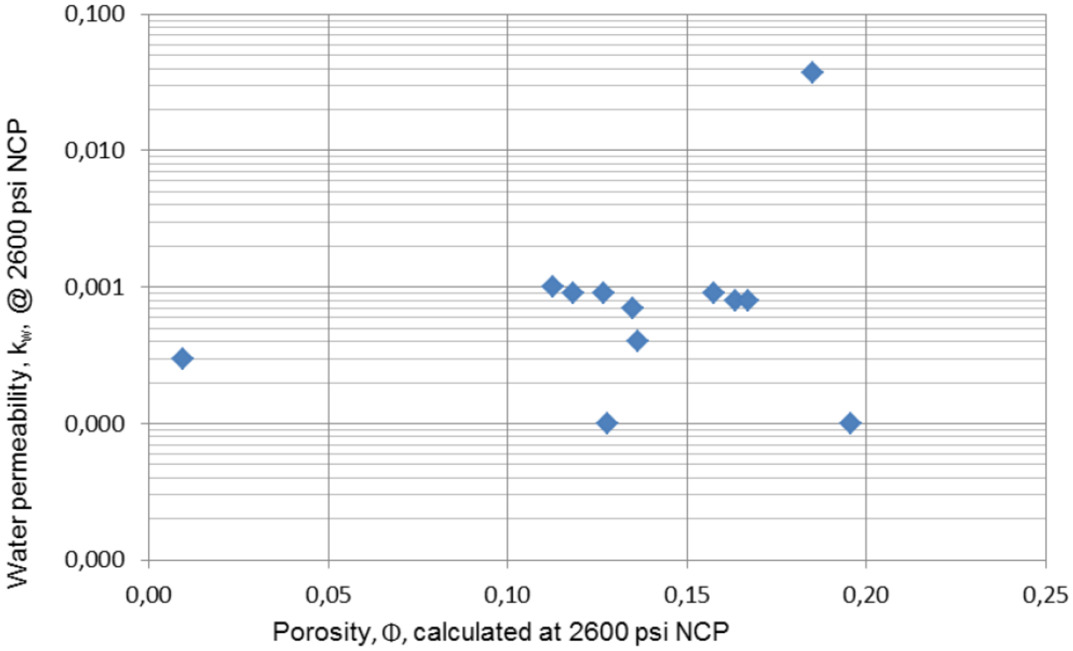

Figure 4.10: Pressure vs. saturation obtained from MICP

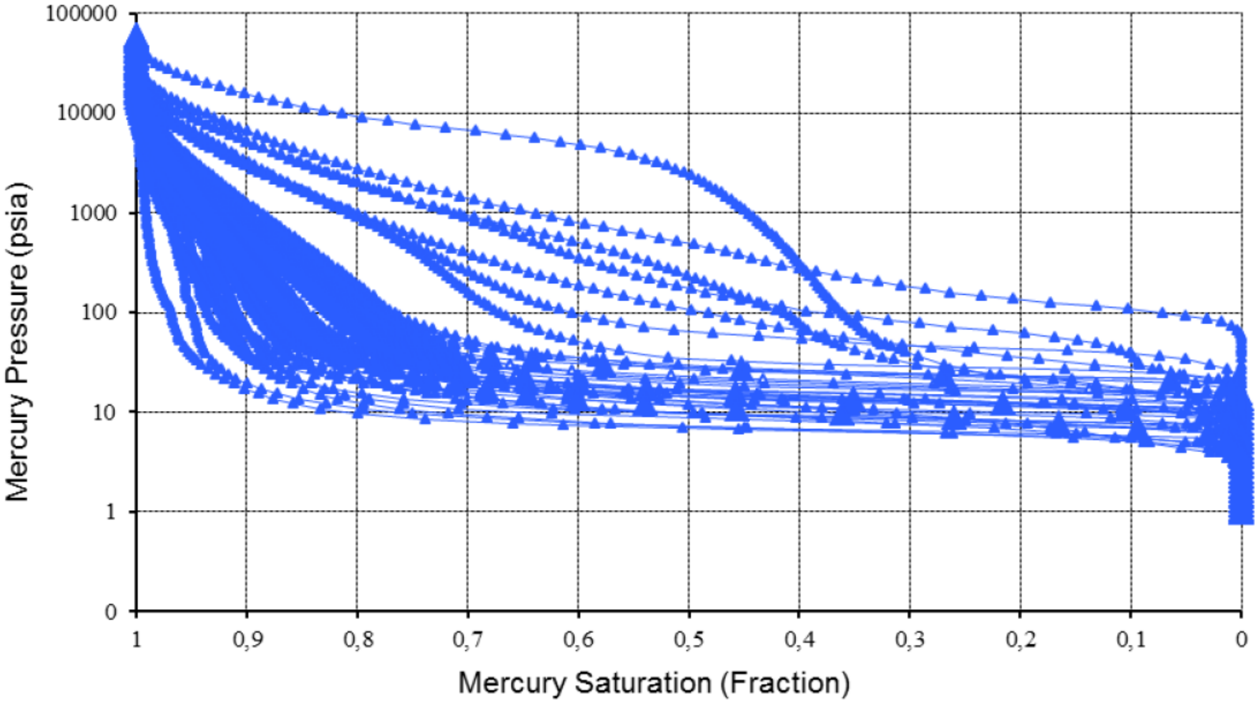

Figure 4.11: dSw/dLog pore throat size vs. Pore throat size obtained from MICP

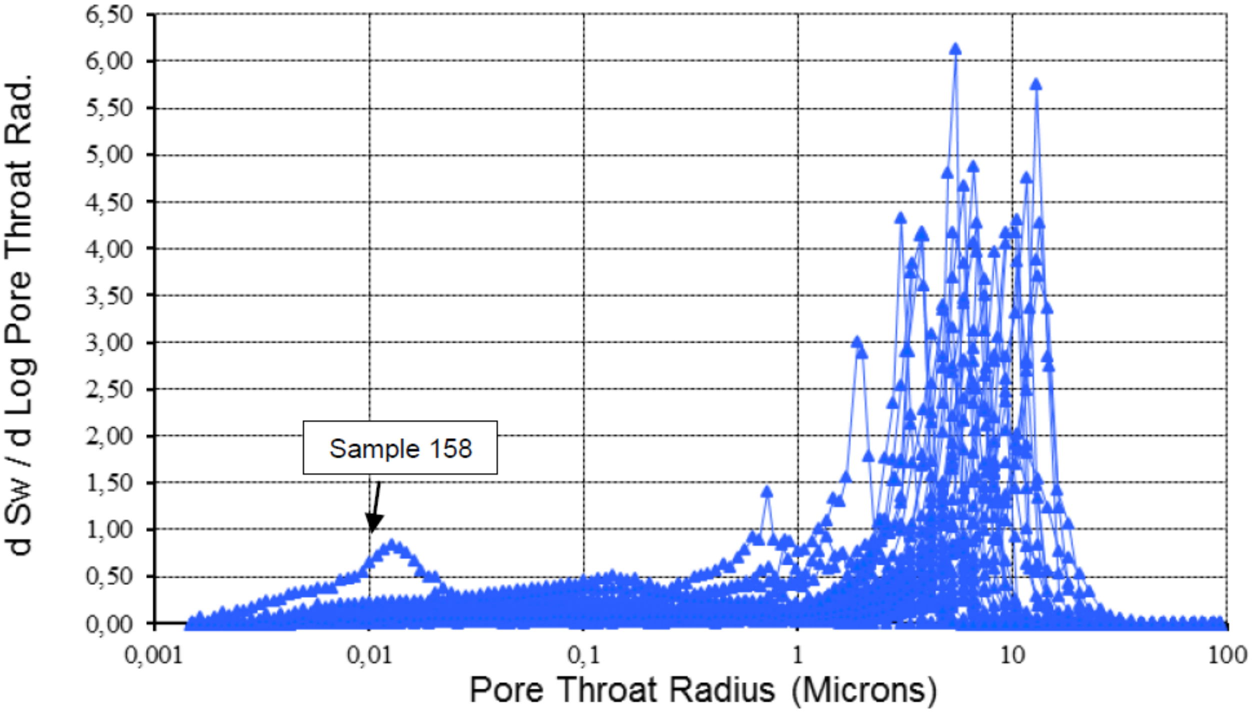

Figure 4.12: J-Function plot (J(1-SHg) vs. Saturation)

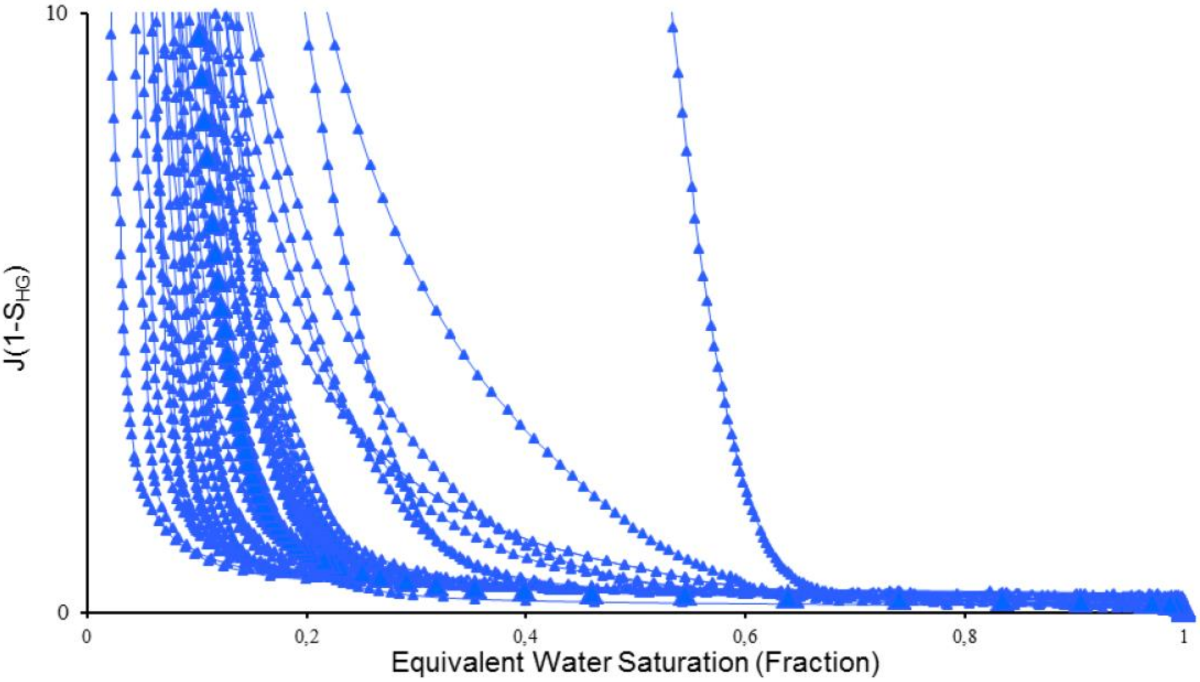

Table 4.1: Measured Petrophysical Properties from Additional RCA study

Petrophyscial Properties	Range	Test Programme
Cleaning study: first measurement Klinkenberg corrected gas permeability, K_L, [MD]	0.225 - 3061	(1)
Cleaning study: first measurement Helium porosity [%]	6.90 – 28.2	(1)
Cleaning study: second measurement Klinkenberg corrected gas permeability, K_L, [MD]	0.519 – 3758	(1)
Cleaning study: second measurement Helium porosity [%]	6.80 – 30.5	(1)
Cleaning study: third measurement Klinkenberg corrected gas permeability, K_L, [MD]	0.615 – 3969	(1)
Cleaning study: third measurement Helium porosity [%]	7.10 – 30.9	(1)
Water permeability @ 400 psi	0.0002 – 2.7	(2)
Porosity at ambient	1.0 – 20.0	(2)
Archemedes bulk volume [ml]	14.93 – 68.77	(2)
Water permeability at reservoir net confining pressure, 260 psi	0.0001 – 0.037	(2)
Porosity at reservoir net confining pressure, 260 psi [%]	0.93 – 15.6	(2)
MICP porosity [%]	2.60 – 30.20	(3)

4.1.2 Special Core Analysis

The Special Core Analysis (SCAL) programme was undertaken to measure the range of trapped CO_2 saturation, CO_2 and water relative permeability data relevant to dynamic modelling of CO_2 movement in the reservoir. The programme consists of ambient condition tests using centrifuge, unsteady state displacements, together with reservoir condition measurements using supercritical CO_2. For reservoir condition testing, all measurements were made at a reservoir temperature of 57°C and a reservoir (pore) pressure of 2030 psig (140barg). Analytical grade CO_2 was used as the injection gas. An outline of the SCAL programme is given in Figure 4.13. Brief descriptions of each element of the SCAL programme and the associated results are outlined as follows:

Figure 4.13: SCAL Experimental Process Description

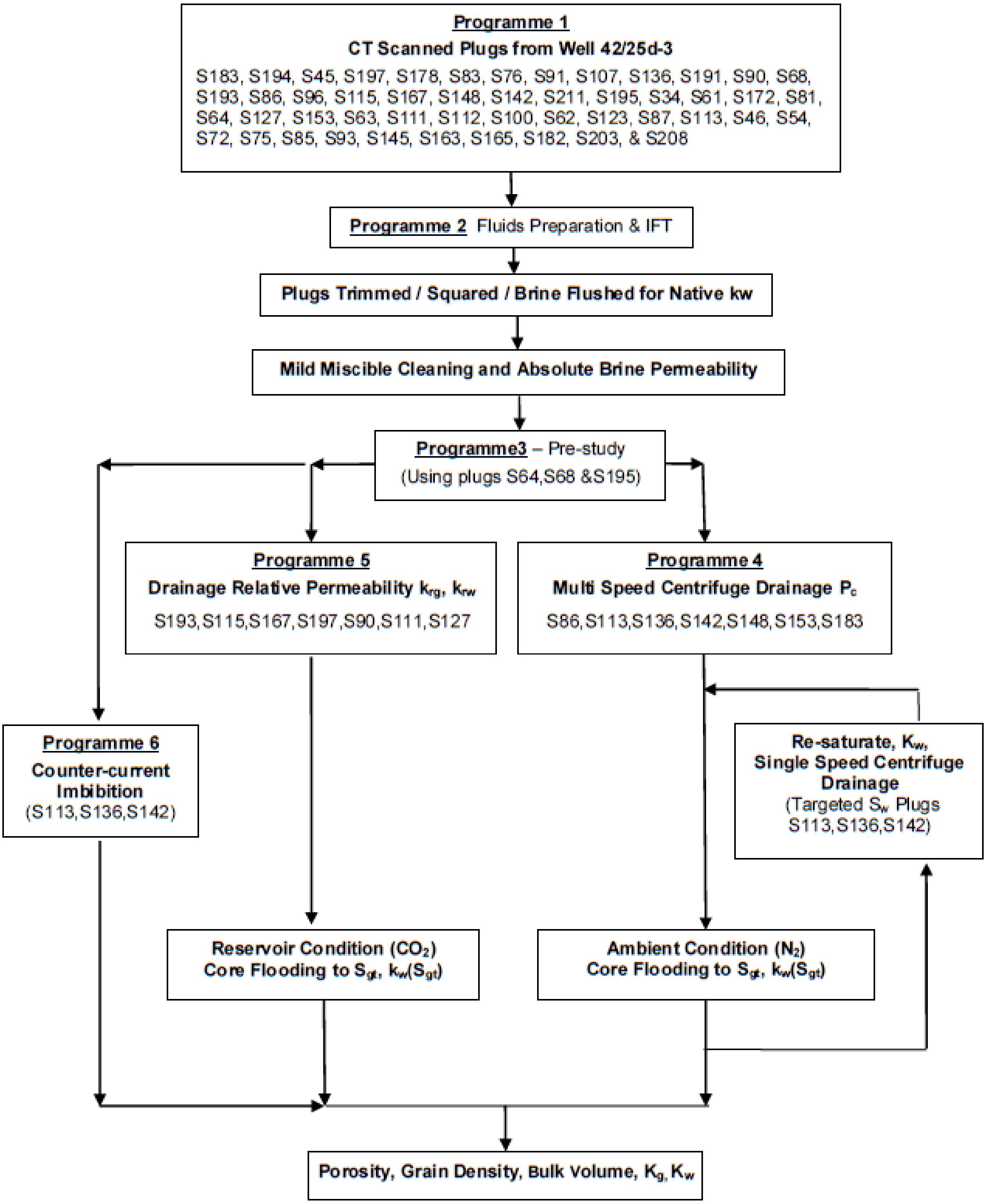

4.1.2.1 *Programme 1 – Plug selection*

Plug selection involved:

- Plug CT scanning: 12 of the original 49 samples disqualified after X-ray CT scanning, leaving 37 plugs going forward;
- Native State (as-received) Brine Permeability: Brine permeability was measured for all remaining 37 samples using synthetic formation brine (also known as synthetic formation water) and under a confining back pressure of 145 psig (10barg);
- Sample Cleaning & Routine Core Analysis: Sample cleaning was performed following the procedure described in the cleaning pre-study (Section 4.1.1.1). The results of the RCA have already been presented in Section 4.1.1;
- Brine Permeability: dry samples were formation brine saturated, degassed and absolute brine permeability (Kw) measured using a back-pressure of 145 psig (10barg); and
- Mercury Injection Capillary Pressure (MICP): MICP was measured on 36 samples and has already been discussed in Section 4.1.1.9.

4.1.2.2 *Programme 2 - Fluid Preparation*

Synthetic Formation Brine a laboratory filtered (0.45µm) and degassed synthetic formation brine was prepared according to the salts given in Table 4.2. Data in the table corresponds to SFW density of 1.24 g/cc and salinity of 248, 000 ppm. For measurements using in-situ saturation monitoring, approximately 0.25 mole of CsCl dopant (Molar mass 168.36 g/mol) was used to replace 0.25 mole NaCl (Molar mass 58.44 g/mol). The doped synthetic brine composition is given in Table 4.3 for reference. The measured density of the doped brine was 1.26 g/cc corresponding to a brine salinity of about 264,300 ppm.

Reservoir Fluids: both an impure CO_2 mixture and pure (analytical grade) CO_2 were used at reservoir conditions (57°C at 141bar). The CO_2 mixture was measured to have a density of 0.577 g/cm^3 (at 57 °C at 141bar). The CO_2 -brine interfacial tension (IFT) was measured to be 36.8 ± 0.7 mN/m. This compared to a measured (analytical grade) CO_2 density of 0.596 g/cm^3 and CO_2-brine IFT of 39.5 ± 0.8 mN/m at the same test conditions.

Table 4.2: Synthetic Formation Brine

Heading Left	Heading Right
NCl	258.13
$CaCl_2.2H_2O$	40.09
$MgCl_2.6H_2O$	31.05
KCl	3.48
$SrCl.6H_2O$	0.42

Table 4.3: Doped Formation Brine

Salt	g/L
NCl	244.24
CsCl	40.00
$CaCl_2.2H_2O$	40.09
$MgCl_2.6H_2O$	31.05

KCl	3.48
$SrCl.6H_2O$	0.42

4.1.2.3 Programme 3 - Pre-Study

Three plugs (S64, S68, S195) were selected for pre-study testing which includes Critical Velocity tests and Acid Brine Sensitivity test. Critical velocity tests were aimed at identifying the potential for fines movement within the plug and its threshold value. The acid brine sensitivity test was to see if the pore matrix was affected by brine that will become acidified when in contact with CO_2 in the reservoir. The results of the critical velicity test was inconclusive whilst for the Acid Brine Sensitivity test, a small reduction in grain volume (0.64 cm^3 to 1.14 cm^3) was observed for each plug as a result of acid brine flooding; this corresponds to an increase in porosity of about 2% to 6%. Klinkenberg CO_2 permeability was also observed to increase post-flooding (approximately 10% for S64 & S68 and over 20 % for S195).

4.1.2.4 Scanning Electron Microscopy (SEM)

Scanning Electron Microscopy (SEM) of native pre-test and post-acidified brine flood end-trims were undertaken to determine if there is evidence for pore structural change following exposure to acidified brine. The most notable and common difference between the pre-test and post-test samples was the absence of halite in the post-test samples. No evidence for change in pore structure was observed.

4.1.2.5 Programme 4 – Ambient Temperature Tests

All measurements were performed at a laboratory temperature of 22°C with a pore (back) pressure of around 145 psig (10barg). Analytical grade nitrogen (N2) was used as the injection gas. Primary drainage (air displacing brine) to target Swi was performed by unconfined multi-speed centrifuge tests.

Primary drainage gas-water capillary pressure (P_c) was measured on seven core plugs covering the rock types and permeability ranges for the Bunter sandstone. These data are shown in Figure 4.14. Plotting of J-function curves showed only samples S153 and S142 of the seven tested plugs as being from the same rock type. Plug S148 was chosen to constrain reservoir condition Pc modelling (discussed in Section 4.1.2.6) since the base parameters (K, phi) were the closest match available to the composite parameters (S193, S115, S167).

Each plug at Swi was brine flooded to acquire trapped gas saturation and end point brine relative permeability. In-situ saturation monitoring was utilised to quantify both the initial gas saturation and trapped gas saturation. Imbibition end-point data are summarised in Figure 4.15. End-point trapped gas saturation was verified independently using volumetric gas production data and sample (post-study) pore volume measurements.

Targeted brine saturations of 0.30, 0.70 and 0.80 were established on individual plugs (S113, S136 & S142) using the single speed centrifuge method. These plugs were also brine flooded to trapped gas saturation for the measurement of krw at Sgt. The relationship Sgt versus Sgi correlated as expected (see Figure 4.15, targeted S_w data points) but it was clear from ISSM that the saturation distributions were very non-uniform (Figure 4.16 is an exemplar). Because of the non-uniformity in brine saturation, it is unlikely that measured krw is representative. This ambient condition work showed that uniform brine saturation profiles cannot be acquired at high values of brine saturation from centrifugation.

Post-study plug characterisation data show that grain volume change was less than 0.1cm^3 for all samples. Significant gas permeability loss was observed for sample S136 but remaining samples were within +/-10% of original values. This was not true for absolute brine permeability which was found to decline by 10% to 30%.

Figure 4.14: Primary Drainage Capillary Pressure, Combined Plot

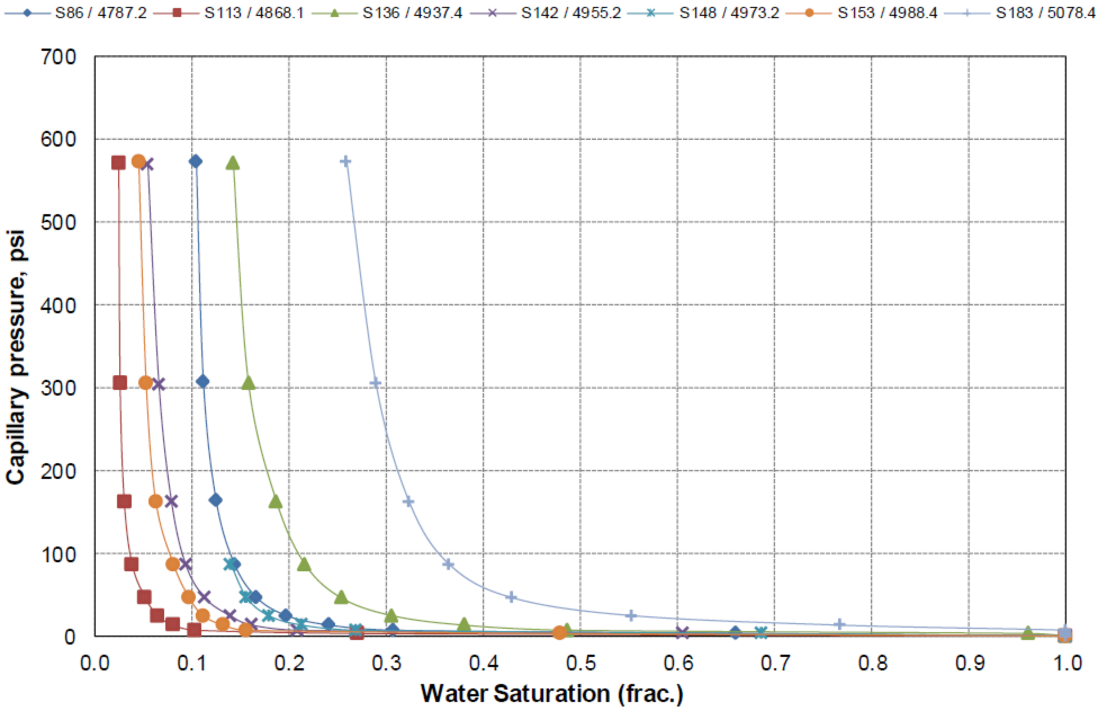

Figure 4.15: Trapped Gas Saturation versus Initial Gas Saturation

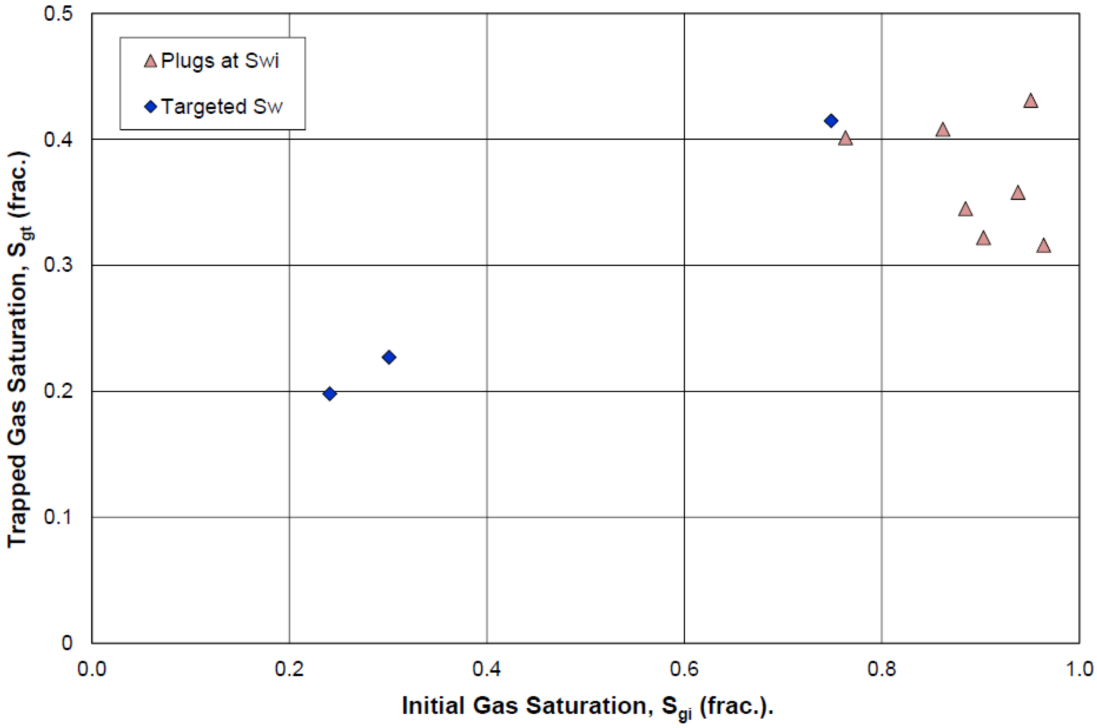

Figure 4.16: Saturation Distribution Targeted Swi 0.3 (Plug S113)

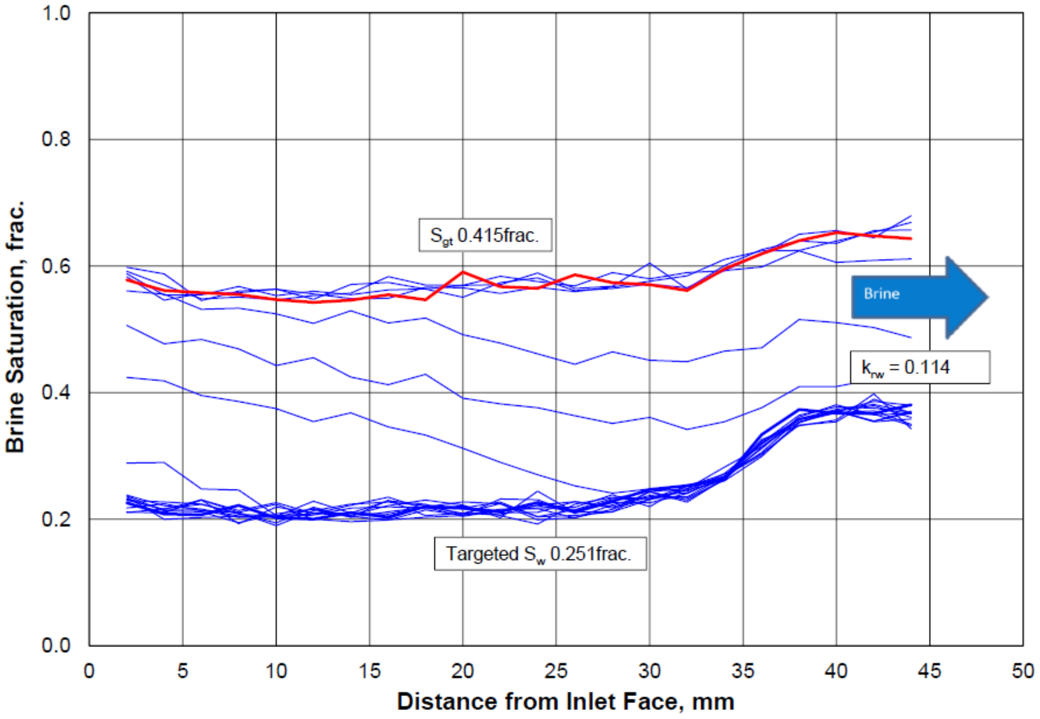

4.1.2.6 Programme 5 - Reservoir Condition Gas-Water Kr

Unsteady-state primary drainage gas-water relative permeability was measured using two composites and two single plugs. All measurements were performed at a reservoir temperature of 57°C with a reservoir (pore) pressure of 2,030 psig (140barg), using analytical grade carbon dioxide (CO_2) as the injection gas. The first test used a three plug composite core (Composite S193, S115, S167) with a measured absolute brine permeability of 115.7mD (porosity 0.253). The brine saturation distribution was influenced by the component plug individual properties and plug butting (see Figure 4.17). Subsequent tests were therefore performed with single plugs, plug S197 (11.6mD, porosity of 0.152frac) and plug S90 (77.5mD, porosity of 0.267). The final test however reverted back to a composite core (Composite S111, S127) since the rock type was of high permeability. The measured absolute brine permeability for this composite was 1324mD (porosity 0.272).

Measured CO_2 relative permeability was similar for plug S90 and composite S111, S127 (krg 0.158 and krg 0.184 respectively at Sg 0.560 and 0.556). Higher CO_2 relative permeability was observed for composite S167, S115, S193 and plug S197. The measured analytical end-point CO_2-water relative permeability data for these floods are shown in Figure 4.18.

Imbibition brine flooding to trapped CO_2 saturation was also performed starting from low initial CO_2 saturations (1-Swr). Initial CO_2 saturations ranged from $0.424 < Sgi < 0.579$ resulting in trapped CO_2 saturation (Sgt) ranging from $0.255 < S_{gt} < 0.387$. All trapped CO_2 saturation data including ambient and reservoir condition flooding is summarised in Figure 4.19 which also show the correlations of Spiteri et al. (2008) and that of Land. The alternative data provided on this plot came from counter-current imbibition (CCI) experiments (Programme 6), where the initial saturation is controlled using toluene- CO_2 saturation and imbibition experiments are undertaken under purely spontaneous processes, allowing toluene to imbibe into the sample under capillary forces. The corresponding brine relative permeability (krw) at Sgt is shown plotted in Figure 4.20.

As Figure 4.17 shows, coreflood drainage experiments are strongly affected by capillary end effects leading to non-uniformity in saturation distribution along the core length. One way of minimising this effect is by performing experiments at high injection rates. For this study, CO_2 injection rate ranged between $4cm^3/h$ (corresponding to a reservoir advance rate of 1.2ft/day) to $400cm^3/h$. However, high flow rates are known to induce instabilities at the flood front that are unrepresentative of displacement conditions deep in the reservoir.

To reconcile time and spatially dependent experimental data and generate relative permeability data that is corrected for the effects of laboratory scale capillary pressure, core flood simulation was performed using *Sendra*^{TM}. *Sendra*^{TM} is a proprietary simulator based on a two phase 1-D black oil simulation model together with an automated history matching routine. The simulator recreates the balance of forces in the core experiment, taking as input the capillary pressure and relative permeability data, to match measured experimental production and pressure data. Once a satisfactory match has been obtained, a characteristic reservoir relative permeability is then generated that corrects for the laboratory capillary artefacts.

To improve confidence in simulated relative permeability data, it is usually better to employ capillary pressure data from samples within the same rock type. In the case of Bunter data (except for sample S90), this proved difficult and it became necessary to use an analytical capillary pressure model as an input, where the simulator was given some flexibility to estimate parameters of the capillary pressure model. The model employed is due to Skjaeveland et al (2000) and is as stated in Equation 4.1, recast in terms of water and gas phases. Comparison of Pc generated with the Skjaeveland model and those generated from two laboratory tests – the multi-speed centrifuge capillary pressure (LabPc) and the corrected Mercury Injection Capillary Pressure (MICP) – are shown in Figure 4.21 through Figure 4.23.

Equation 4.1 $Pc = \frac{c_w}{\left(\frac{S_w - S_{wR}}{1 - S_{wR}}\right)^{a_w}} + \frac{c_g}{\left(\frac{S_g - S_{gR}}{1 - S_{gR}}\right)^{a_g}}$

where c and a are constants defining the capillary entry pressure (threshold pressure) and curvature exponent, respectively for water and oil (as denoted by subscripts 'w' and 'o', respectively).

Although this model was designed to allow for mixed-wet capillary pressure data in imbibition and secondary drainage processes, it may still be used for strongly wetting systems in primary drainage, by either negating the gas term or by using cg = 0. Table 4.4 lists the Skjaeveland parameters used as input for each coreflood simulation.

Table 4.4 lists the end points used as input to the simulation model. K_L and K_w represents the Klinkenberg and water permeability respectively. Water permeability was lower than the Klinkenberg permeability and also exhibited a decreasing trend as shown in Figure 4.24. This is uncommon in clean sandstone materials and the anomaly creates unusual CO_2 relative permeability when relative permeability is based on water permeability as the absolute – i.e. the effective CO_2 permeability at initial water saturation (Swi) become greater than specific water permeability at 100% water saturation, and hence the relative permeability to CO_2 at Swi would be greater than 1.

Although this phenomenon is apparently counter to conventional hydrocarbon system relative permeability behaviour, as referenced in reservoir engineering literature, there are a number of experimental studies reporting similar observed behaviour. These papers incorporate two different potential hypotheses for the phenomenon. The first theory is that clay minerals may become swollen in the presence of formation water, and that the fresher the water, the more pronounced the effect. The second theory suggests that turbulent flow may be occurring in a water-filled system due to water flowing over and through tight, rough surfaces – postulating that at irreducible water saturation the gas (or oil) path is free from such turbulence since water continues to fill the rough, clay rich surfaces. The dominance of Illite in the Bunter clay mineralogy would underpin the first hypothesised mechanism. Illite swells in the presence of brine and can thus reduce the permeability to this phase whilst in the presence of CO_2 the clays will shrink and allow an enhanced permeability. The second hypothesis has also been described in terms of non-wetting lubrication. Since the CO_2 occupies the largest pores, it is speculated that the CO_2 then sees a reduced drag or surface friction because it is in contact with smoother surfaces. The Bunter sandstone is considered (strongly) water-wet and both mechanisms could therefore be complementing one another in the Endurance matrix.

Simulated relative permeability curves were defined using the Corey model which for water relative permeability is defined as:

Equation 4.2 $K_{rw} = K_{rw_{max}} \cdot S_{wn}{}^{Nw}$

where K_{rw} is the relative permeability to water, $K_{rw_{max}}$ is the maximum relative permeability to water, Nw is the Corey exponent for water, and S_{wn} is normalised water saturation – given as, $S_{wn} = (S_w - S_{wi})/(1 - S_{wi})$, for a primary drainage process.

The Corey model for relative permeability to gas (in a gas-water system) is defined as:

Equation 4.3 $$K_{rg} = K_{rg_{max}} \cdot (1 - S_{wn})^{Ng}$$

where K_{rg} is the relative permeability to gas, $K_{rg_{max}}$ is the maximum relative permeability to gas and Ng is the Corey exponent for gas.

The Corey exponent for water (Nw) ranged from 4.7 to 6.0, and for gas (Ng) the range was from 2.5 to 3.0. The curves derived from these parameters are presented in Figure 4.25 on Cartesian and semi-log axes (left and right-side, respectively). The curves are also presented as a function of normalised water saturation in Figure 4.26. Figure 4.27 and Figure 4.28 show production and saturation profiles history match for the composite sample S111/S127 using Corey exponents of Nw=4.7 and Ng = 2.7. They show good matches in production, differential pressure and saturation profiles.

Figure 4.17: Primary Drainage In-situ Brine Saturation S115 S167 S193

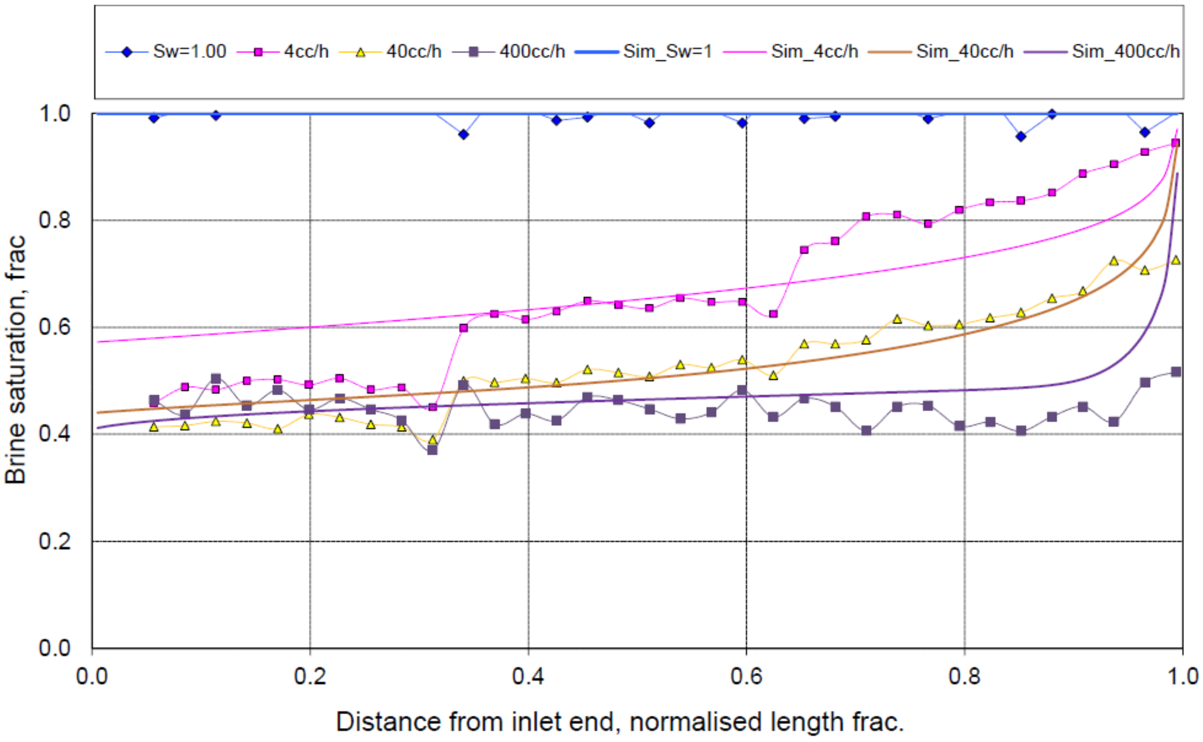

Figure 4.18: Analytical (End-point) Gas Relative Permeability (Programme 5)

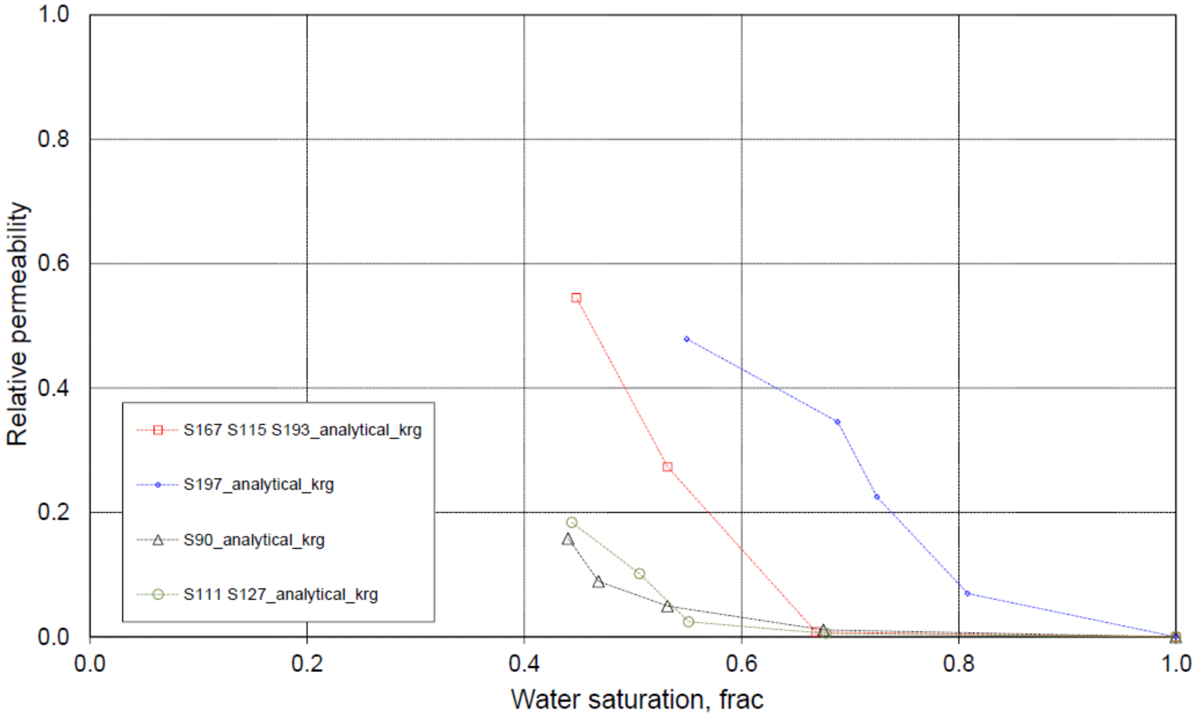

Figure 4.19: Trapped gas saturation (Sgt) as a function of initial gas saturation (Sgi) – all methods

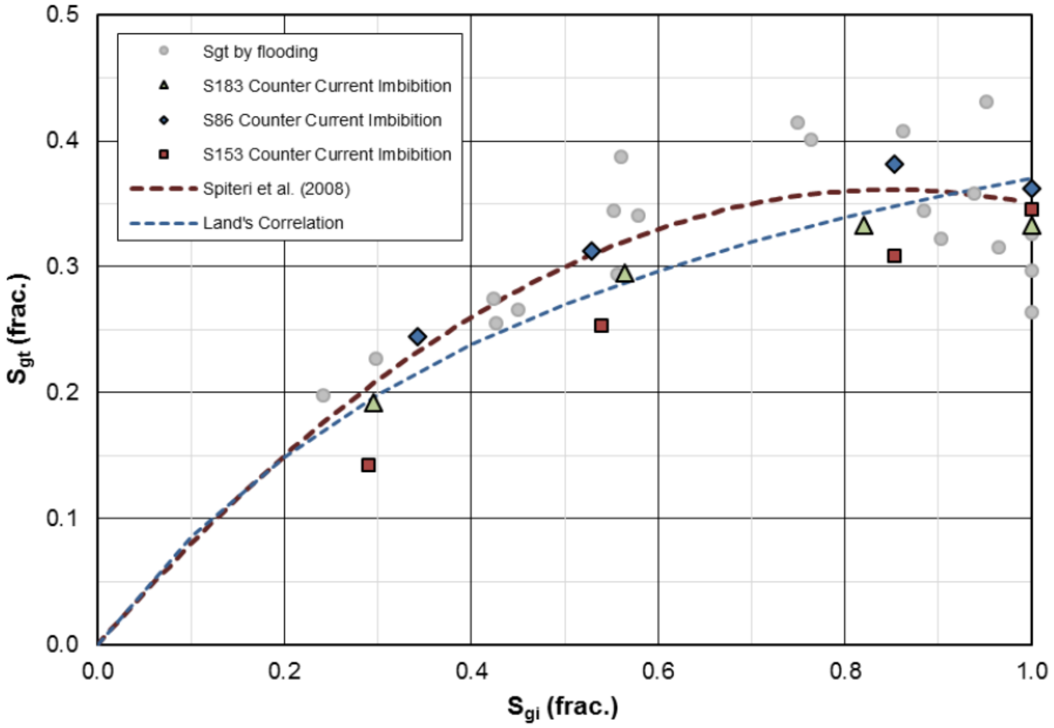

Figure 4.20: Brine Relative Permeability versus Sw_max (Programme 5)

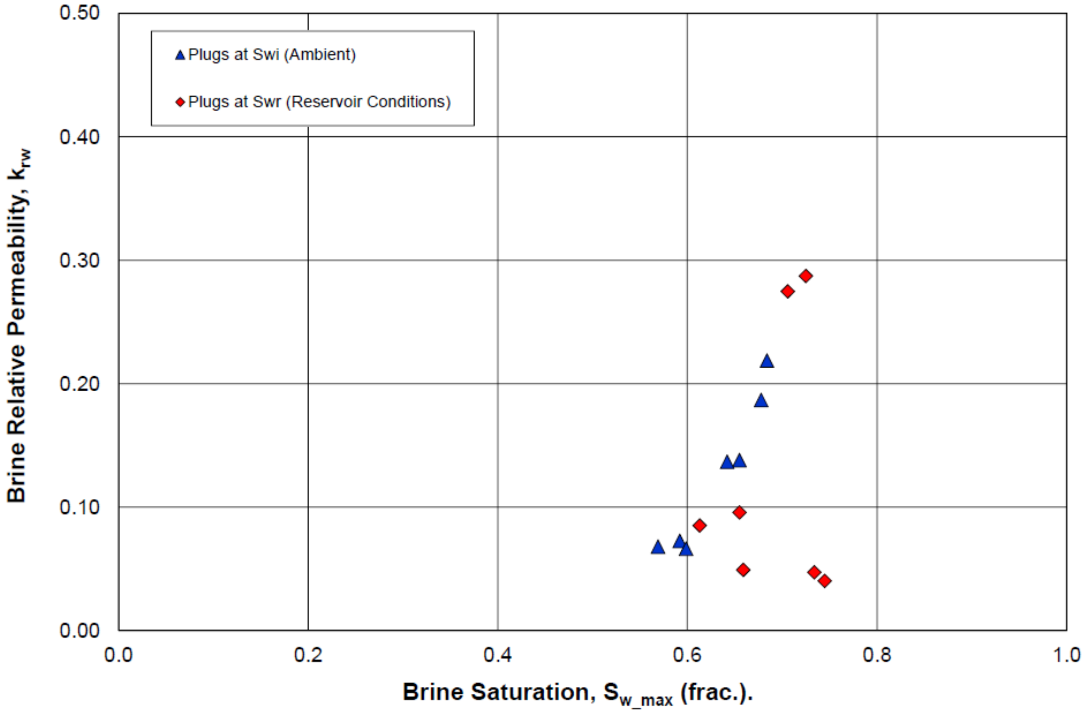

Figure 4.21: Good correlation of centrifuge Pc (lab Pc) and MICP data (S113 & S153)

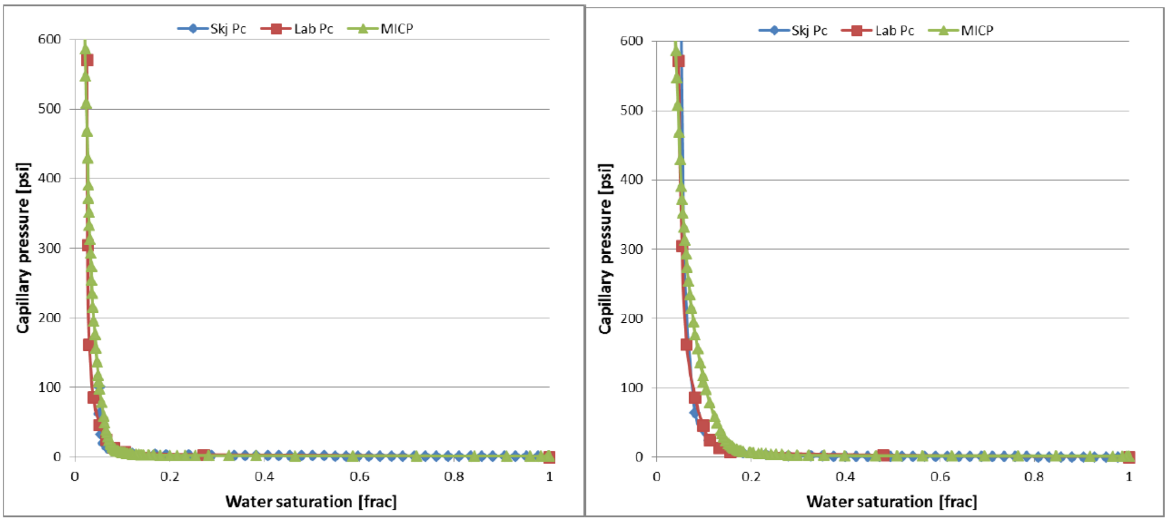

Figure 4.22: Reasonable correlation between centrifuge Pc (lab Pc) and MICP data (S86, S142 & S148)

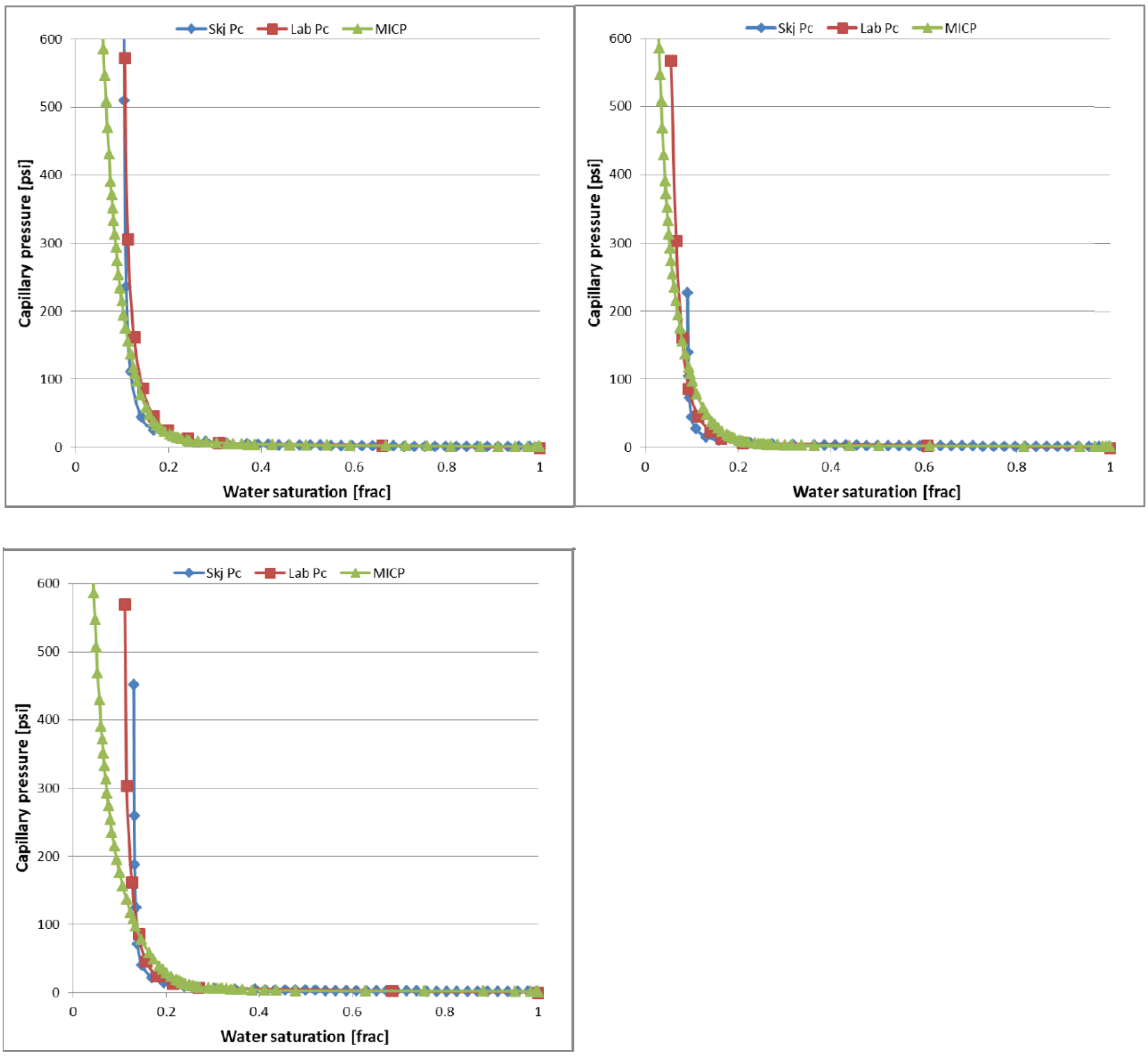

Figure 4.23: Poor correlation between centrifuge Pc (Lab Pc) and MICP (S136 & S183)

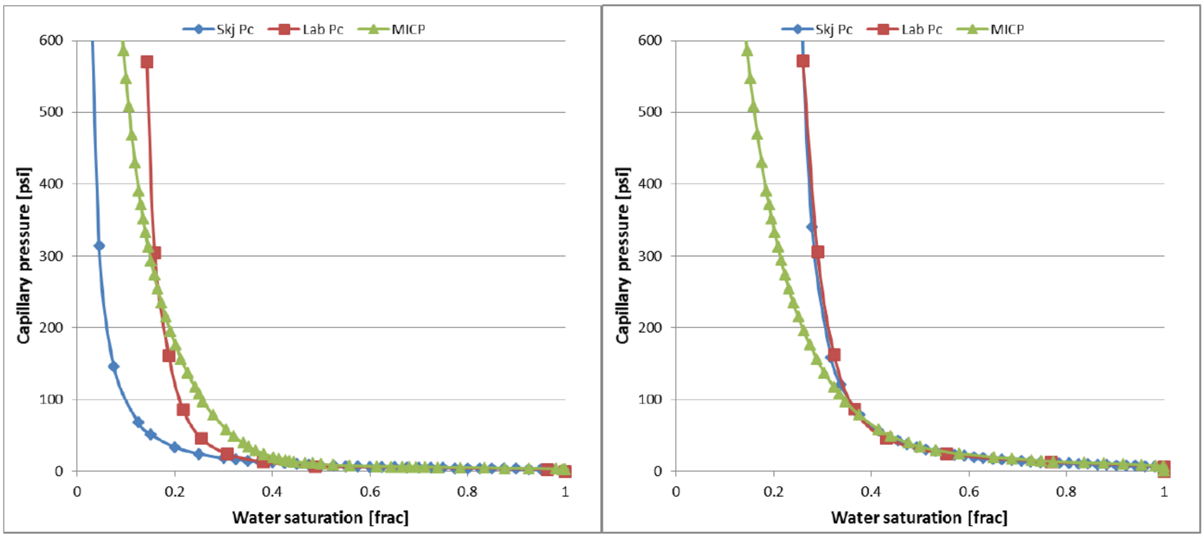

Table 4.4: Endpoint Simulation Inputs

Sample	KL	Kw	Krw_max	Kg@max	Krg_max
S115/S167/S193	275	171	0.620	275	1.000
S197	14	6.75	0.482	14	1.000
S90	173	103	0.596	173	1.000
S111/S127	1583	1136	0.718	1583	1.000

Table 4.5: Skjaeveland Pc Model Parameters

Sample	cw	aw	Swi
S115/S167/S193	1.7	0.2	0.080
S197	4.5	0.2	0.190
S90	-	-	-
S111/S127	0.7	0.5	0.030

Figure 4.24: Water permeability (Kw) versus Klinkenberg gas permeability (KL)

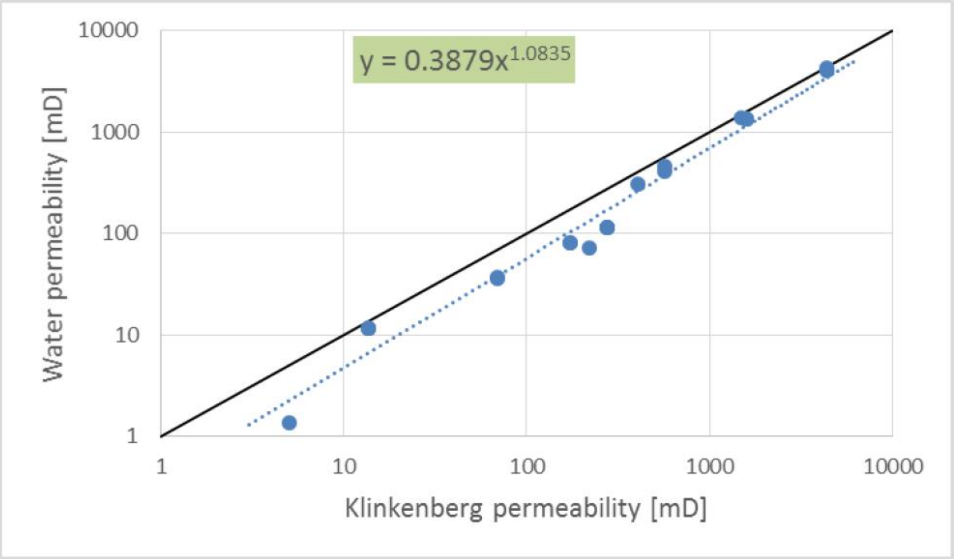

Figure 4.25: Simulated relative permeability curves – indicating the observed exponent variance

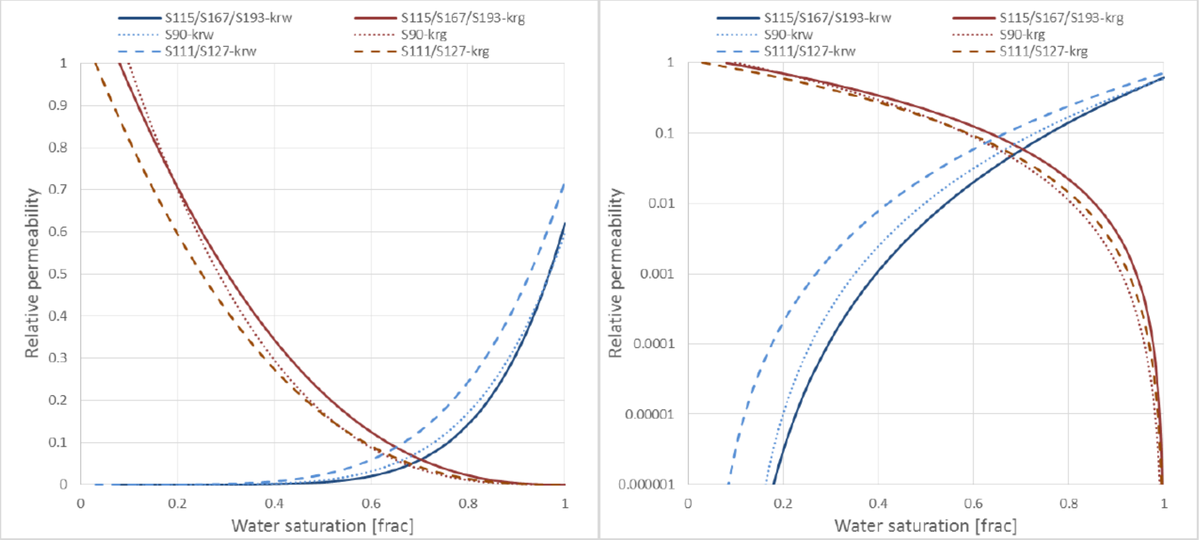

Figure 4.26: Simulated relative permeability curves versus normalised water saturation

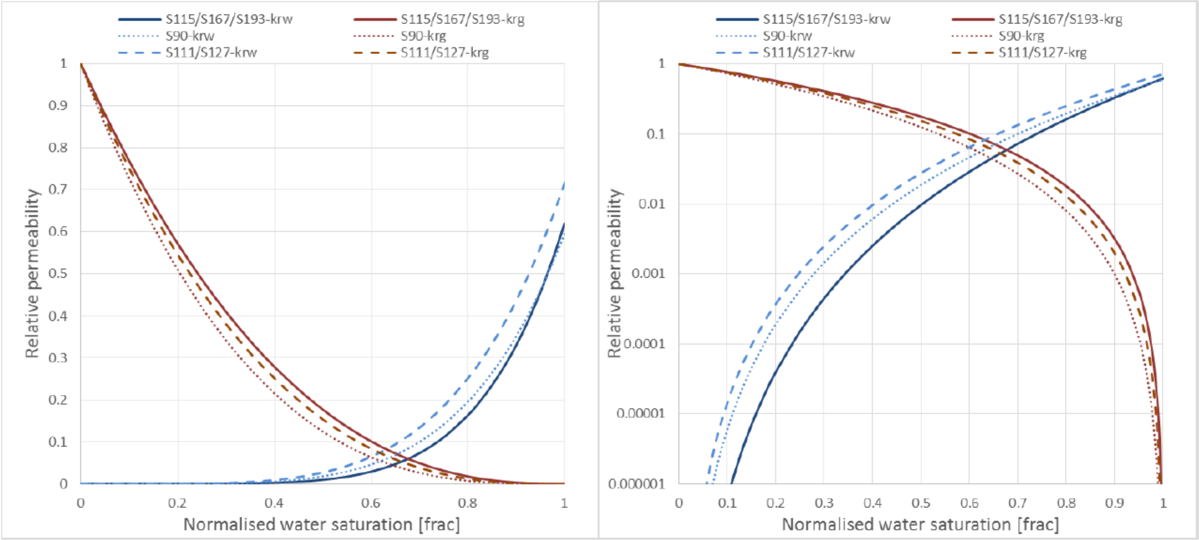

Figure 4.27: Production history match for S111/S127

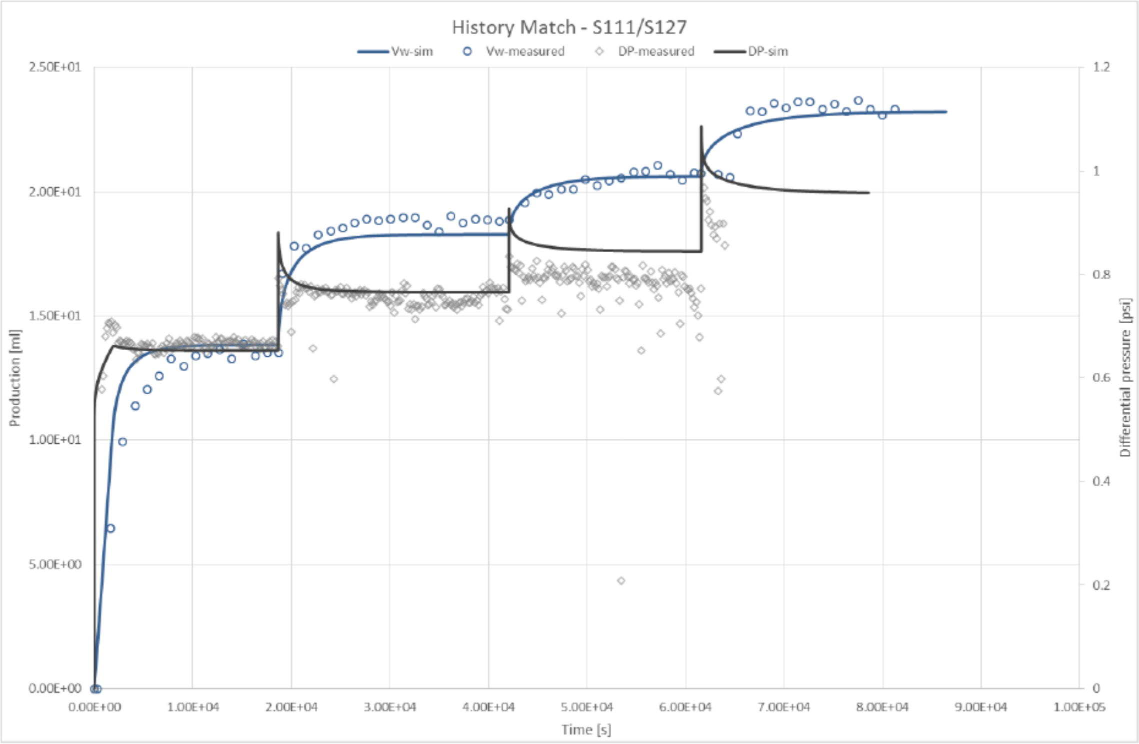

Figure 4.28: Saturation Profiles – S111/S127

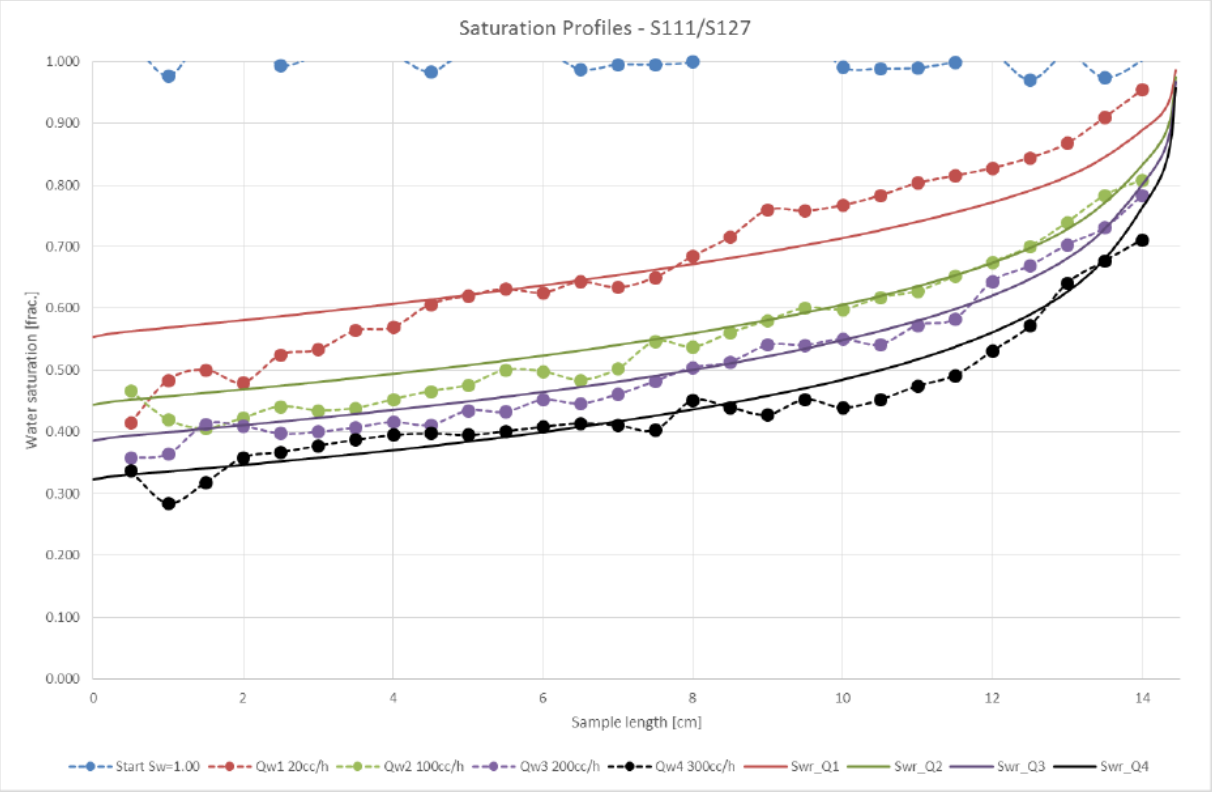

4.2 PVT and Phase Behaviour of Injected CO_2

Pure CO_2 is a gas with a density of around 1.98 kg/m^3, which is about 1.67 times that of air, at standard ambient temperature and pressure conditions (25°C and 1barg). Figure 4.29 shows the phase diagram of CO_2 and illustrates the temperature and pressure conditions under which it can exist as a gas, a liquid, a solid or a dense (supercritical) phase. The compositional specification of CO_2 that will be injected into the Endurance Storage Site, as listed in Table 4.6**,** characterises it as near-pure CO_2 stream which will exhibit a phase behaviour very similar to that of pure CO_2. Details of the CO_2 pipeline transportation system entry requirements are provided in Appendix A.

To be able to meet the design injection capacity of 2.68MTPA, pipeline pressure and temperature are selected such that CO_2 is transported in a liquid state. Table 4.6 gives the specified CO_2 platform arrival properties for the White Rose CO_2: the variations in minimum and maximum arrival temperatures are due to seasonal variations in the temperature of the sea and thus of the 90km segment of the pipeline along the sea bed. Given the design temperature range, Figure 4.29 shows that CO_2 can be kept in the liquid state as long as the pipeline pressure is above 50barg; this is much lower than the pipeline minimum operating pressure of 90barg (Table 4.6**).**

As CO_2 leaves the pipeline and enters the well, its pressure will be controlled during both start-up and normal operating conditions to inhibit transition into gaseous phase due to the inherent operational cooling and heating effects: Joule-Thomson cooling across the choke, geothermal heating coupled with an increasing hydrostatic pressure in its descent through the well. This is to reduce flow instabilities associated with density fluctuations.

CO_2 will exist as a dense phase under in situ Endurance Storage Site conditions (Figure 4.29): the injected CO_2 will be liquid phase at the well perforations and initially within the formation during injection due to the temperature being substantially below critical point (Figure 4.29). Once in the reservoir, or as injection is stopped, CO_2 will move into dense phase as its temperature increases.

Figure 4.29: Phase Diagram of pure CO_2

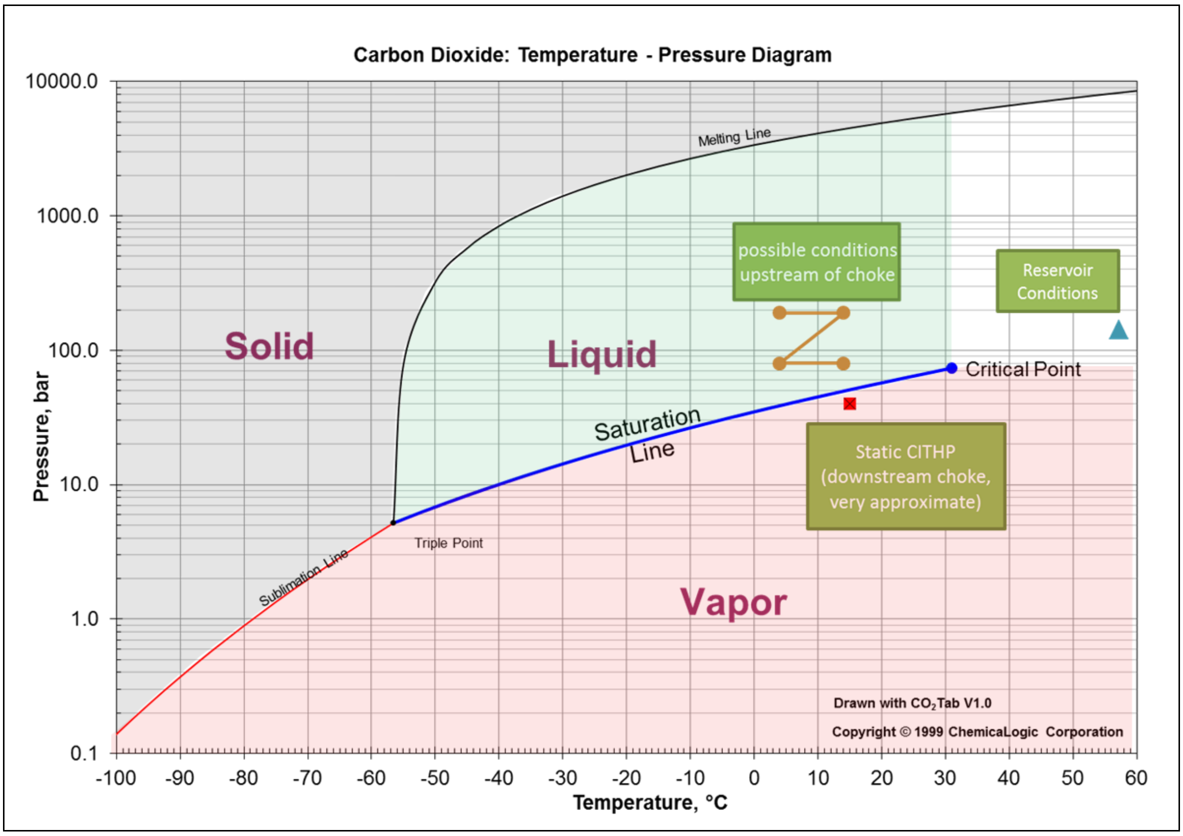

Table 4.6: CO_2 Arrival Properties

Property		value	unit	Notes
Max Arrival Rate	Max	2.68	MTPA	White Rose only (139.6 MMscf/day)
Min Arrival Rate	Min	0.58	MTPA	White Rose only (30.4 MMscf/day)
Max Arrival Pressure	Max	182	barg	Design pressure =200barg
Min Arrival Pressure	Min	90	barg	
Max purity	Max	99.7	%	0.3% N_2+Ar, 10 ppmv O_2
Typical Purity White Rose		99.7	%	
Typical (generic) Purity		97.4	%	2% N_2, 0.6% Ar, 10 ppmv O_2
Min purity	Min	96	%	4% N_2+O_2+H_2 + CH_4 + Ar
Max arrival Temperature	Max	16 / 24	C	
Min arrival Temperature	Min	3 / -7	C	

4.3 Well Testing and Vertical Interference Test Results

4.3.1 Well Test Results

As part of the data gathering programme in the 42/25d-3 appraisal well, a well test was completed over the interval 1396.3 - 1414.3 mTVDSS to achieve the following:

1. establish key reservoir parameters; permeability, thickness & skin;
2. determine the influence of nearby boundaries and/or heterogeneities within the volume of the reservoir investigated by the test;
3. investigate vertical connectivity and estimate K_v/K_h (vertical/horizontal) permeability ratio over the tested interval;
4. secure good quality formation water samples for chemical & biological analysis and electrical properties;
5. carry out a step rate injection test to prove injectivity of the best practicable analogue to supercritical CO_2 (filtered seawater); and
6. investigate (injection) rate dependent skin including any plugging, fraccing or dissolution effects seen during testing.

The testing programme consisted of a production period of approximately 24 hours at a rate of 5000 stb/d (795 m^3/day) using an Electrical Submersible Pump (ESP), followed by a shut-in and pressure build-up for 48 hours. Subsequently a multi-rate injection test using filtered seawater (CO_2 was not used due to safety concerns over handling the fluid in its super-critical state and sourcing a sufficient volume of CO_2) was performed at rates of 5000, 10000 & 15000 stb/d (795, 1590, 2385 sm^3/day), followed by a 12 hour pressure fall-off test. The key results calculated from the test include:

- an average permeability of 271 mD based on a test interval of 230.4 m. This is an excellent match with reservoir properties derived from porosity-permeability trends;
- a negative skin of -1.1;
- no evidence of boundaries in the volume investigated by the test, which was calculated to extend to a radius of 1.2km;
- a vertical to horizontal permeability ratio (K_v/K_h) of 2.19×10^{-4}, which is considerably lower than that seen on the scales investigated by the Vertical Interference Tests (VIT) (discussed below); this was attributed to the test taking place within a laterally extensive high permeability zone which flows preferentially. K_v/K_h ratio calculated from VIT was used for reservoir simulation;
- multi-rate injection tests generated unexpected results, most likely caused by mechanical blockage of the perforations by debris from the surface equipment;
- a maximum rate-dependent skin of 80; and
- the injection test demonstrated that injection at the specified rates would be possible over the perforated interval despite what was thought to be significant mechanical blockages in the completion.

4.3.2 Vertical Interference Test (VIT)

As part of the wireline programme of the 42/25d-3 appraisal well, three VITs were undertaken at depths of 1580.4, 1522.8 and 1429.8 m MD to determine formation permeability and quantify vertical to horizontal permeability ratio (K_v/K_h) to a depth of investigation deeper than would be seen using formation pretests (mini-DST). VIT was also used to identify any barriers to vertical flow over the interval tested.

Each test was planned to use four different pump rates of approximately 30 minutes each, followed by a build-up period of one hour. The VITs were interpreted using Transient Pressure Analysis (PTA) and reservoir simulation.

The mini-DST result for the first station (1429.8 m MD) was successful and recorded a formation permeability of 24 mD from the PTA and 18 mD from the numerical simulation, with a high degree of confidence. Stations two and three (1522.8 and 1580.4 m MD, respectively) could not be taken with similar confidence due to operational reasons; however the estimated results were within the range expected from the porosity-permeability trend. No barriers to vertical flow over the intervals tested could be detected. K_v/K_h ratios were determined from all three stations, ranging from 0.10 to 0.36. This range has informed the choice of the K_v/K_h range of 0.10 to 0.15 for reservoir simulation purposes.

4.4 Information from Analogous Reservoirs

The best reservoir analogues to the Endurance Storage Site are gas fields developed within the BSF in the SNS. Production performance of these fields have been analysed in the context of their geological characteristics to enable a better understanding of the future dynamic performance of Endurance and the underlying Greater Bunter aquifer.

A review of the depletion characteristics of the Caister gas field to the east of Endurance and the Esmond Complex (comprising Esmond, Forbes, and Gordon gas fields) to the north, indicates that primary depositional and diagenetic characteristics provide the main control on production performance. Pressure and geological data from Caister suggests that internal barriers to vertical flow (siltstones and cemented sands) confine pressure communication to individual layers within the gas accumulation. This is to be contrasted with the more homogeneous Esmond reservoir which records a uniform pressure distribution. Comparison of the gross gamma ray log character in the appraisal well 43/21-1 on the crest of Endurance with those in wells at Caister and Esmond field suggests a greater similarity in reservoir properties between Endurance and Esmond (which in turn suggests similar dynamic performance) than with Caister.

Review of Esmond production performance also suggests a good hydraulic connection to a regional aquifer volume in the lower part of the Bunter reservoir with an effective permeability of around 16 mD (based on 98 m sand thickness) and a radius of at least 15km with no limit to the maximum size.

Analysis of gas production data from the Forbes and Gordon reservoirs which are part of the Esmond complex showed a similar influence of significant water influx from a large regional aquifer. This information has been used to constrain the aquifer properties in the reservoir simulation models of CO_2 injection into Endurance.

Pressure data from Esmond indicates that a thin, 6m interval of Röt Clay, is capable of holding back a differential pressure of at least 110barg. This provides a useful analogue for the Endurance structure, where the Röt Clay is approximately twice as thick.

Direct seismic identification of hydrocarbon saturation or rock property variations (e.g. differential cementation) as a result of hydrocarbon displacement, has been extensively used in both the Esmond Complex and Caister Bunter reservoirs and suggests that seismic techniques are likely to be effective in monitoring CO_2 migration within the Endurance Storage Complex. Another important analogue in this respect is the Sleipner CCS project, which has injected approximately 0.9MTPA of CO_2 into the saline

Utsira Formation which overlies the Sleipner West and East gas fields. Around 15 MT has been sequestered since inception of the project in the mid-1990s. As well as being the first such project in the world, it is probably best known for the quality of the 4D seismic that has been gathered to track the development of the CO_2 plume as shown in Figure 4.30.

Before measurements of Routine Core Analysis (RCA) and Special Core Analysis (SCAL) on the core recovered from the 42/25d-3 appraisal well were completed, preliminary dynamic reservoir simulations of CO_2 injection into the Endurance Storage Site utilised published CO_2/brine relative permeability (Kr) data derived from a Canadian Viking sandstone sample as well as relative permeability data from a Ketzin core recovered from the Stuttgart formation in the late Triassic Keuper age rocks that overlie the early Triassic Buntsandstein (Endurance Bunter equivalent) formation. Details of how this analogue information has been implemented in the reservoir models can be found in Section 4.6.4. Subsequent to the receipt and use in dynamic modelling of relative permeability data from the SCAL studies done on core from appraisal well 42/25d-3 drilled on the Endurance structure, the relative permeabilities used previously can be considered as sensitivities on relative permeability with respect to the dynamic modelling of Endurance.

Of interest to this project are the efforts that have been made to history match the plume development. According to Chadwick, the absolute permeability has to be increased by about an order of magnitude to match to migratory speed of the CO_2. Measured Endurance petrophysical data suggests that the relative permeability of the CO_2, and hence the effective permeability of CO_2 is somewhat higher than previously considered likely, see Section 4.6.4.1.

Figure 4.30: 4D Seismic of CO_2 Plume Development in Sleipner CCS Project (see Ref 10)

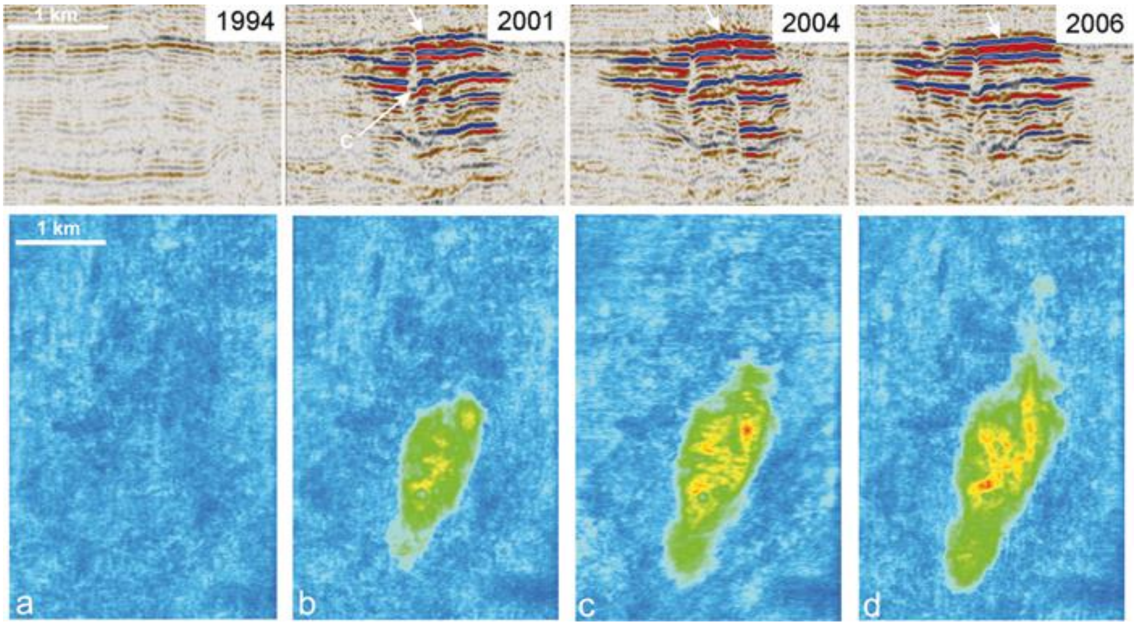

4.5 Extent and Effective Hydraulic Communication of the Aquifer

Two separate reviews, one looking at the geology of the BSF in the UK SNS within a regional Area of Interest (rAOI) that includes the Endurance Storage Complex (Figure 4.31), and the other looking at the historical pressure behaviour at Endurance and the nearby Esmond gas field, suggest that it could be in hydraulic communication with an area approximately 20,000km^2 to 23,000km^2.

A triangle drawn to approximate the area of the BSF bounded by faults to the west (the Dowsing Fault Zone), north and north-east, and the thinning to the east across the Base Cretaceous Unconformity on the Cleaver Bank High in the Dutch sector of the SNS (see Figure 4.31), was shown to extend to a width of 160km and a height of 240km, giving an area of about 20,000km^2.

Comparison of pressure gradient measurements in the 42/25-1 appraisal well drilled in 1990 and the 42/25d-3 appraisal well drilled in 2013 shows that pressure in Endurance has fallen by 0.7bar in 23 years. This was probably caused by gas offtake from the Esmond field about 50km north-east of Endurance and the subsequent expansion of the aquifer to replace this void space. A material balance calculation estimated an aquifer with an area of 23,000km^2 to be required to result in the observed pressure decrease. If production from other gas fields in the Esmond Complex (Forbes and Gordon) were taken into account then an aquifer of twice the estimated size or compressibility would be required. It is therefore highly probable that Endurance is connected to a large regional aquifer which can help to limit the pressure increase associated with White Rose CO_2 injection and ensures that the sealing integrity of the cap rock is preserved.

Figure 4.31: Extent of the regional area of interest (rAOI) bounded by faults in the BSF of the SNS (original figure from Ref 8)

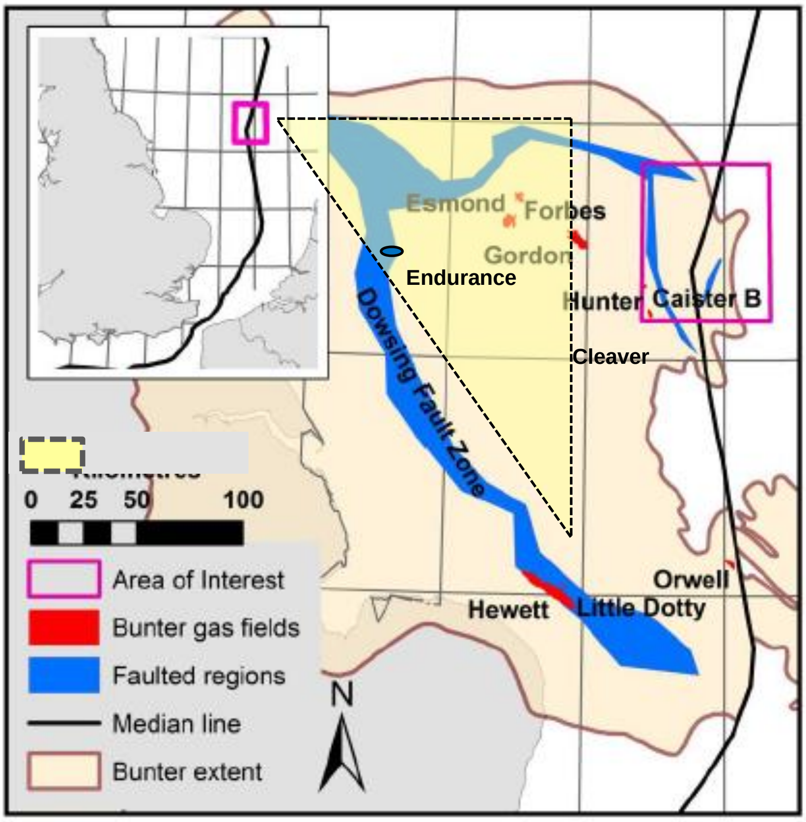

4.6 Dynamic Simulation Models

Dynamic modelling has been performed using the Blackoil ECLIPSE 100 simulator (E100) from Schlumberger. Two classes of simulation models have been built: (a) the Base or Sub-regional simulation model which was used to address issues surrounding general plume development, storage capacity and pressure profile predictions; and (b) Simplified models consisting of the Simplified AOI simulation model and the Simplified injection model which were developed for the purposes of undertaking various sensitivities in an expeditious manner including the impact of reservoir properties on CO_2 migration and pressure profiles and the impact of completion strategy on CO_2 injectivity. The Sub-regional model is next described in detail.

4.6.1 Sub-regional simulation model

The dynamic model for simulation covers an area spanning about 42km by 11km, and thereby encompasses and extends beyond the Endurance anticline which measures about 25km long by 8km wide along the 1500mTVDSS contour close to the depth of the most likely spill. The outcrop to the east southeast of the Endurance structure has been included in the simulation model to enable the assessment of the effects of potential hydro-dynamic communication between Endurance Structure and the outcrop during CO_2 injection. A Top Bunter depth map view of the resulting grid is shown in Figure 4.32.

Figure 4.32: Grid Model Using 200/400m Cells of Endurance Area of Interest

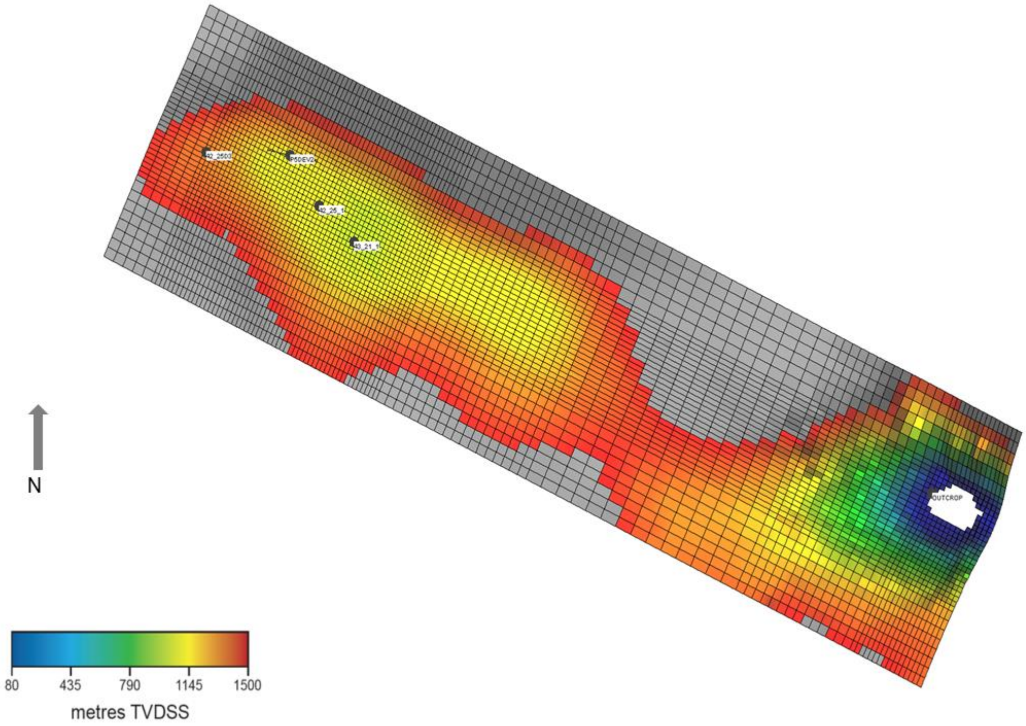

The Bunter sandstone thickness in the AOI varies between 250m and 300m. The vertical grid cell resolution has been maintained regardless of which aerial resolution was adopted to adequately capture the buoyancy driven migration of injected CO_2. The average vertical grid cell size is about 2m.

4.6.2 Upscaling for Reservoir Simulation

4.6.2.1 Simulation and Grid Design

A total of 125 cells in the vertical direction (Nz = 125) were used to model the whole Endurance structure volume (an average vertical cell size of 2m over a 250m interval). Total grid size therefore increases very rapidly once X- and Y-direction grid cells (Nx and Ny) are accounted for. A 200m by 200m X and Y-directions cells would imply Nxyz ≈ 1.4 million cells. It was decided to use relatively fine grids only in the area between the injection points and the crest of the structure to adequately resolve buoyancy-driven CO_2 migration. Control lines have therefore been drawn parallel and perpendicular to the main axis of Endurance to bound the core area of the model and also the outcrop (Figure 4.33).

Figure 4.33: AOI and Control Lines for Hybrid Gridding

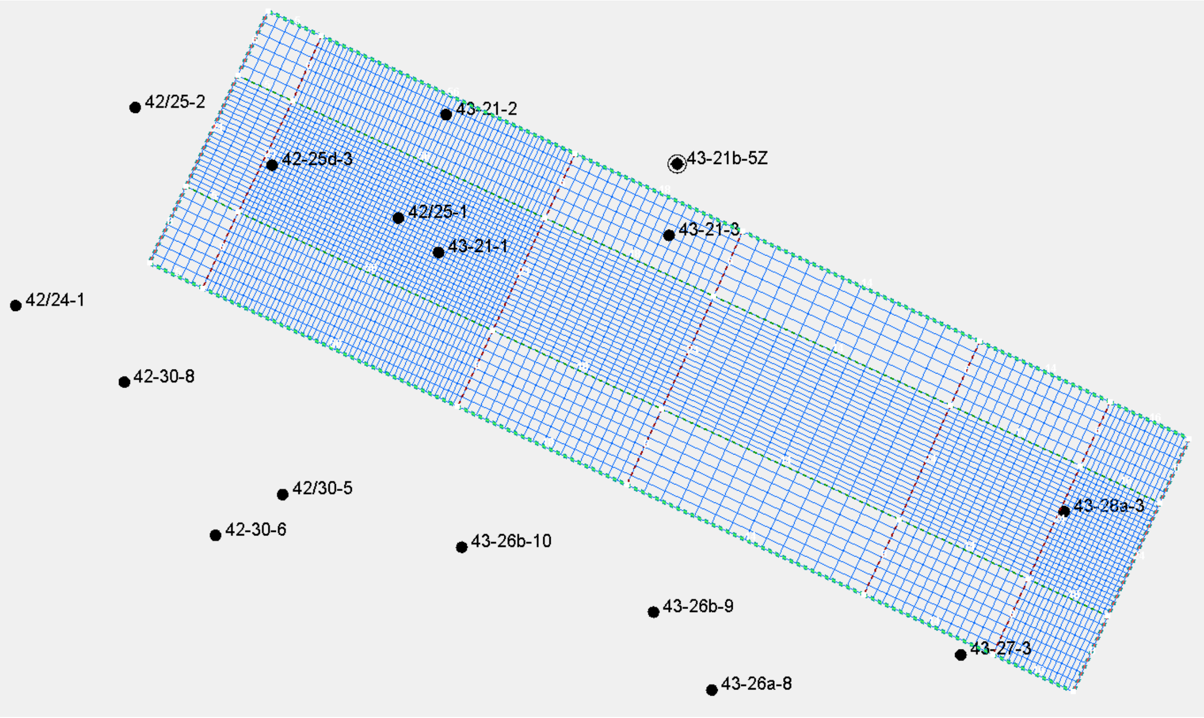

Using these control lines, a hybrid gridding scheme was developed that minimises the overall cell count whilst maximising detail where required. In the core area (and over the outcrop) the finest cell sizes have been implemented, these being:

- 100m by 100m (Fine);
- 200m by 200m (Intermediate); and
- 400m by 400m (Coarse).

Stepping away from the core area in a given direction (X or Y) beyond the control lines, the cell size is allowed to increase by a factor up to two (to minimise material balance errors due to finite difference gradient approximation).

The net result is the total number of grid cells is reduced from $N_{xyz} \approx 1.4$ million to about $N_{xyz} \approx 1.0$ million cells. Whilst this is only a 29% saving in total cells, the reduction in computing time is approximately 80 to 100%. The actual grid dimensions for the three scales considered are shown in Table 4.7.

Table 4.7: Grid Sizes and Dimensions

Case	Core Δ/[m]	(N_x, N_y, N_z)	$N_x N_y N_z$	N_{active}
Fine	100	(258, 82, 228)	4,823,568	2,880,734
Intermediate	200	(129, 41, 228)	1,205,892	734,353
Coarse	400	(66, 21, 226)	313,216	194,896

Comparison of simulated CO_2 breakthrough times (the time for CO_2 to reach the 43/21-1 well at Top Bunter) and peak pressure responses between reservoir models incorporating the three grid sizes showed minor differences. Preference has therefore been given to the coarse or intermediate models for the reservoir engineering modelling runs since they run much quicker (Table 4.8). Where appropriate, verification runs have been done using the fine scale model.

Table 4.8: CO_2 Time to Crest and CPU Time by Grid Size

Model	Break-Through Time [yr]	CPU Time to 2100 [hr]
Coarse	3.5	0.17
Intermediate	3.9	0.53
Fine	4.2	4.05

4.6.2.2 Up-Scaled Parameters

The key parameters required by the simulation model are the NTG ratio, porosity and permeability. NTG and porosity have been upscaled from a fine scale geological model to a coarser scale simulation model using simple pore volume weighted arithmetic averaging. The NTG array depends on the minimum porosity or porosity cut-off below which a volume of rock is considered non-reservoir or non-net. The dynamic effects of porosity cut off was tested on the intermediate grid using the values of minimum porosity shown in Table 4.9 which also shows the resulting average porosity and Water Initially in Place (WIIP).

Table 4.9: Average Porosity and Water Initially in Place versus Porosity Cut-Off

Minimum Porosity/[fraction]	Average Porosity/[fraction]	WIIP 10^9 m^3
0.04	0.189	20.8
0.07	0.192	20.5
0.12	0.202	18.6

As the minimum porosity is increased, the resulting average porosity increases but the WIIP decreases as more of the Gross Rock Volume (GRV) is moved from reservoir to non-reservoir. The dynamic pressure profile shows the peak and asymptotic shut-in pressures increasing as WIIP decreased with increase in cut off (Figure 4.34).

Figure 4.34: Sensitivity of Crestal Pressure to Porosity Cut-Off

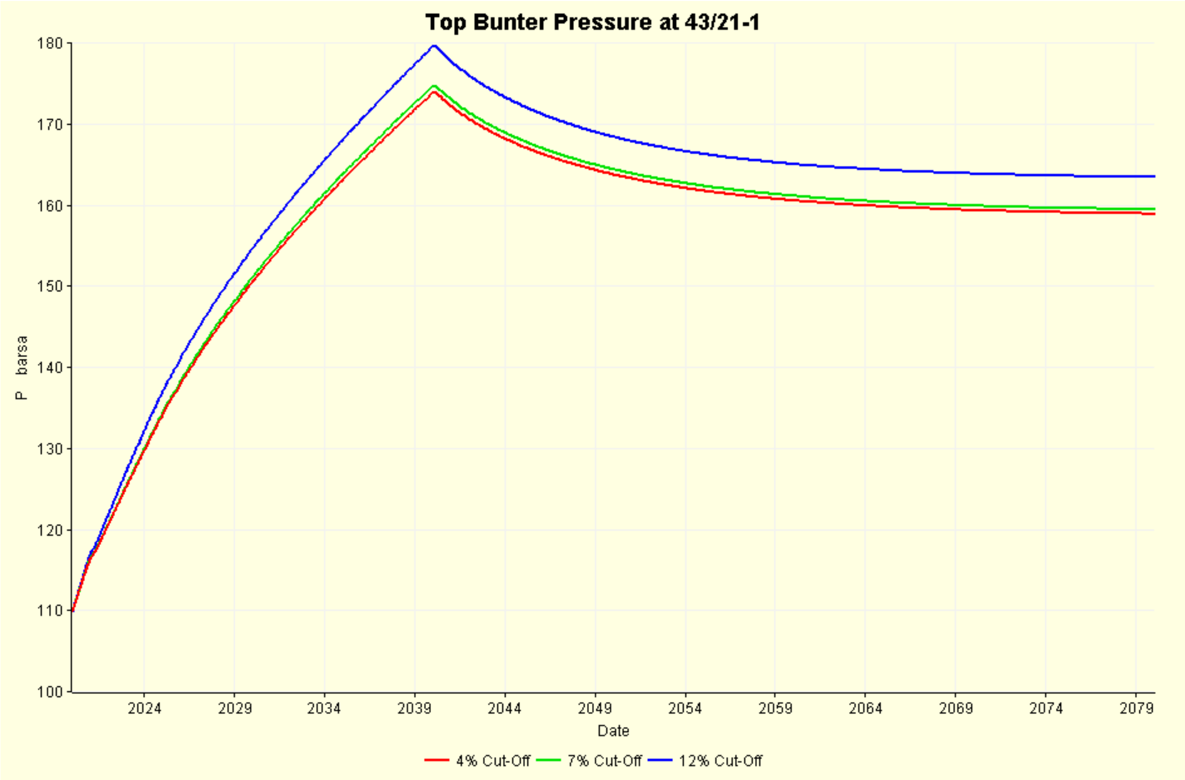

The mid-case porosity cut-off of 0.07 was selected for use in the modelling work.

The Top Bunter porosity map corresponding to that shown in Figure 4.32 is shown in Figure 4.35. Note the minimum porosity here was set to 0.10 and any cells with values less than that are coloured grey. The outline of the seismic phase reversal is clearly visible.

Permeability was distributed based on the upscaled porosity distribution according to Equation 4.4. Regardless of the grid size and permeability upscaling algorithm used, the permeability was multiplied by a factor such that the (arithmetic) average will be close to 271 mD for the pore volume within Endurance above 1500mTVDSS. The Top Bunter X-direction permeability distribution corresponding to that shown in Figure 4.32 is shown in Figure 4.36; note a logarithmic distribution has been used [0.3 to 3000.0mD]. It is assumed that areally permeability is homogeneous, i.e. Y-direction permeability equals X-direction permeability. The average K_V/K_H was taken to be 0.15 as indicated by the VIT run in well 42/25d-3.

Equation 4.4 $$\log_{10} K = 15.6\phi - 0.9$$

Figure 4.35: Top Bunter Porosity Distribution

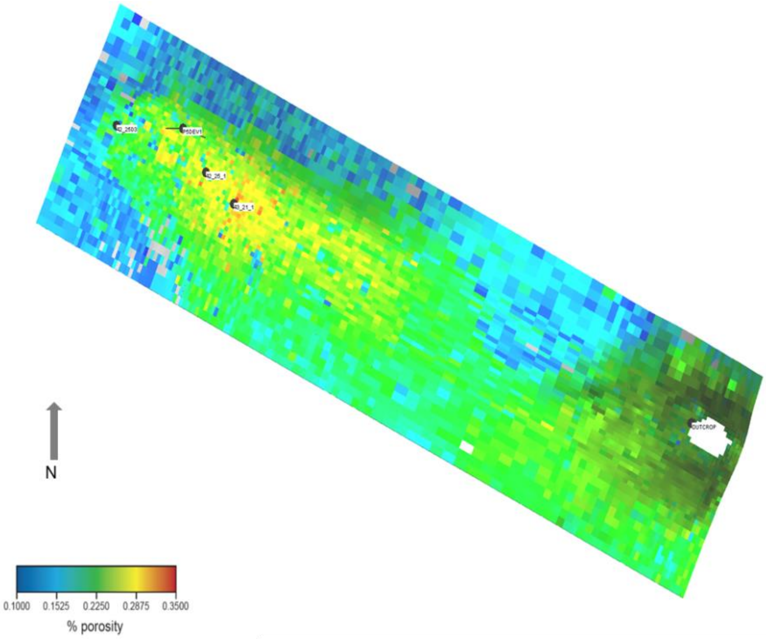

Figure 4.36: Top Bunter Permeability Distribution

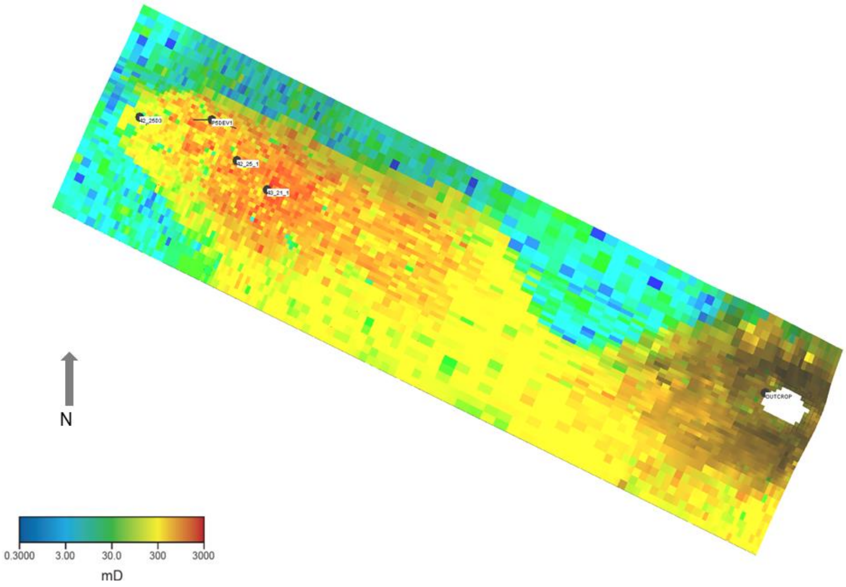

4.6.3 Fluid Properties

All simulations have generally been performed at constant reservoir temperature, assuming immiscible CO_2 and brine with no solid phase. The localised (near well bore) cooling of the reservoir from the injection of cold CO_2 was studied using a simple model (see Section 4.6.15). The possible implications of CO_2 dissolution and solid precipitation on CO_2 storage security have been considered separately in Sections 4.7 using somewhat different dynamic modelling methodologies and software other than Eclipse 100. The details of how fluid properties have been modelled under these conditions will be reported accordingly.

4.6.3.1 CO_2

The CO_2 stream composition used in the reservoir simulation model is a typical composition notionally indicative of the commingled stream from multiple prospective CO_2 emitters (i.e. power stations). This composition is given in Table 4.10 and conforms to the National Grid Safe Pipeline Transportation Specification for CO_2 Mixtures.

Table 4.10: Notional CO_2 Stream Composition

Component	Mnemonic	Mole Percent
Carbon Dioxide	CO_2	96.0
Argon	Ar	0.6
Nitrogen	N_2	2.0
Hydrogen	H_2	0.6
Oxygen	O_2	0.8

In terms of phase behaviour within the reservoir, the main effect of the impurities is to increase the effective critical pressure and critical temperature of pure CO_2 which are 73.9bar and 31.1°C. As long as the pressure in the system stays above 85.0bar, the mixture will be in its super-critical state.

4.6.3.2 Brine

Brine has been modelled using data derived from brine samples taken in wells 42/25-1 and 42/25d-3. An in situ brine density of 1169.2 kg/m^3 was determined from the RFT (repeat formation tester) pressure gradient measurement of 0.1147bar/m in well 42/25-1. In situ brine salinity was estimated as 243,000mg/kg using the Rowe and Chou correlation, an oil and gas industry standard, which takes in density, pressure and temperature as input. The salinity trend observed from the MDT measurements in 42/25d-3 have also been incorporated into the brine model.

The concentration of anions and cations from the three MDT samples along with the sample depths, pressures and temperatures are shown in Table 4.11.

Table 4.11: Concentration of Anions/Cations from MDT Samples

	unit	MDT Water Samples		
Sample		1.04	1.09	1.13
MD	ft	5167.5	4722.0	4634.0
MD	m	1575.1	1439.3	1412.4
Pressure	bar	171.48	155.75	152.65

	unit	MDT Water Samples		
Temperature	C	64.35	60.21	59.39
TDS	mg/kg	253426	242549	241832
pH		6.84	6.61	6.54
Sulphate	mg/kg	296	359	385
Chloride	mg/kg	154146	148780	148164
Fluoride	mg/kg	0.15	0.12	0.10
Bromide	mg/kg	473	460	444
Total BiCarb	mg/kg	51	43	34
Sodium	mg/kg	85512	79664	79953
Potassium	mg/kg	1400	1469	1483
Calcium	mg/kg	8858	8610	8037
Magnesium	mg/kg	2543	3014	3192

4.6.4 Relative Permeability and Capillary Pressure functions

Both analogue and measured Endurance CO_2-brine relative permeability (Kr) and capillary pressure data were used at different stages in the assessment of the likely dynamic behaviour of the Endurance Storage Site.

4.6.4.1 Measured Endurance Data

The program of experiments that has been used to generate relative permeability from core taken from well 42/25d-3 has already been summarised in Section 4.1.2.6of this document. As Figure 4.24 shows the Klinkenberg permeability was found to be always greater that measured effective water permeability and this led to the choice of Klinkenberg permeability as the base permeability for calculating the relative permeability in order to avoid the peculiar situation of having CO_2 relative permeability at irreducible waster saturation being greater than 1.0. However, the Endurance Storage Site is currently brine filled, i.e. $S_w = 1$. Therefore, the effective water permeability must be taken to be the absolute permeability K_{abs}, since this is the permeability measured from the dynamic tests undertaken on the 42/25d-3 appraisal well, which include the production well test, the VITs and even the MDT pressure measurements. Because $K_w = K_{abs}$, it means $K_{rw}(S_w=1) = 1$. Selecting (effective) water permeability as the base (absolute) permeability in relation to which relative permeability is defined means the data generated in the SCAL analysis had to be re-based. In Figure 4.37 the re-based relative permeability is compared to the originally generated curve from SCAL laboratory analysis.

Figure 4.37: (a) SCAL Analysis- Water/ CO_2 Relative Permeability Curves and (b) Re-Based Water/ CO_2 Relative Permeability Curves. Note the dashed lines refer to the logarithmic axis shown as the right-hand y-axis

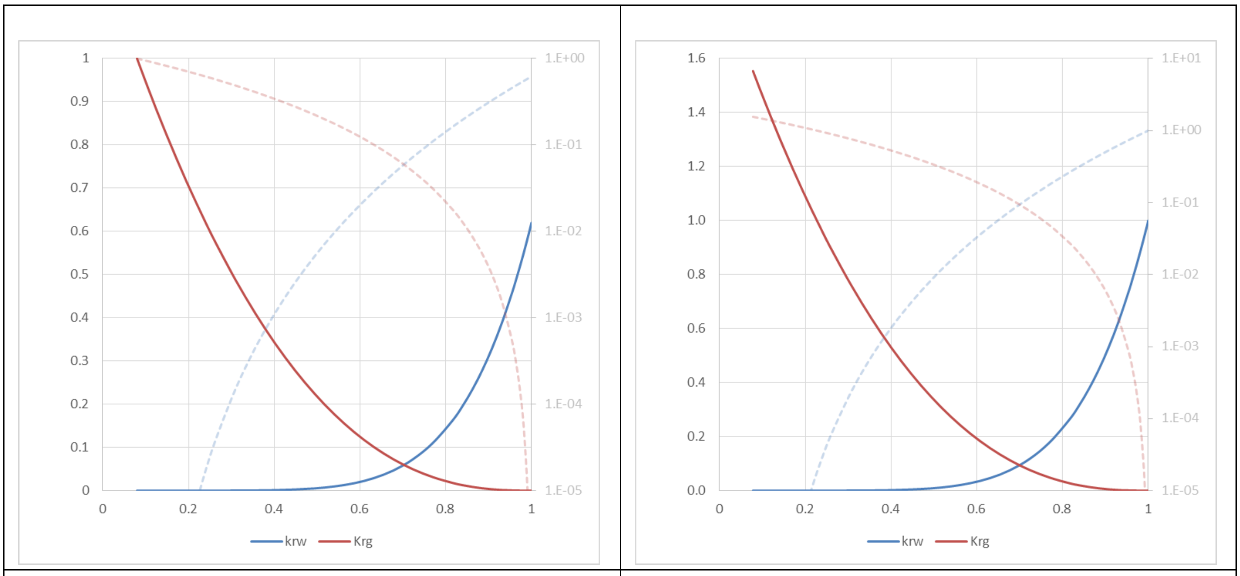

a

b

The Corey exponents and the irreducible water saturation were found to be functions of the Klinkenberg permeability, the Corey exponents being weakly so as Table 4.12 and Figure 4.38 show respectively. The trapped gas saturation S_{gt} is shown in Figure 4.19 to be a function of S_{wi} i.e. $S_{gi} = 1 - S_{wi}$. The Land model of S_{gi} vs S_{gt} in Figure 4.19 was preferred to the Spiteri model because of the tendency of the Spiteri model to generate a maximum at $S_{gi} < 1$ (giving two values of S_{gi} for a single value of S_{gt}) which could cause numerical problems.

4.6.4.2 Capillary Pressure

Mercury Injection Capillary Pressure (MICP) and centrifuge methods were used to measure capillary pressure. It was found that the MICP data was best for determining the entry pressure, i.e. $P_c(S_w=1) > 0$ whereas the centrifuge data was best at describing the behaviour at low (water) saturation. The final capillary pressure behaviour was generated from a Skjaeveland model:

Equation 4.5 $$P_c = \frac{C_w}{\left(\frac{S_w - S_{wi}}{1 - S_{wi}}\right)^{a_w}}$$

Here the coefficients were determined to be $(C_w, a_w) = (1.7, 0.2)$.

Understanding and quantifying the non-zero entry pressure $P_c(S_w=1)$ was a critical step in determining the relative permeability data shown in Figure 4.37 as in practical terms this data was generated using a core flood simulator called SENDRA using the measured capillary pressure data as one of its sets of input data.

Figure 4.39 shows the drainage and imbibition “base” relative permeability data for CO_2 and brine as well as the capillary pressure curve as implemented in ECLIPSE. Note that the values of the key Corey end-points and exponents have been indicated on the figure. The imbibition water relative permeability follows the drainage curve except that the maximum water saturation is now $1 – S_{gt}$. The imbibition CO_2 relative permeability curve starts at $[S_{wi}, K_{rg}(S_{wi})]$ and terminates at S_{gt}. These dependencies have been modelled using the ECLIPSE End-Point-Scaling functionality (EPS).

Table 4.12: Variation in Endurance Corey Water (Nw) and Gas (Ng) Exponents

Sample	K_L/[mD]	N_w	N_g
S193, S115, S167	276.0	6.0	2.5
S197 *	13.6	4.8	2.4
S90	173.0	5.0	3.0
S111, S127	1583.0	4.7	2.7

* Sample S197 was disqualified based on QC-analysis.

Figure 4.38: Irreducible Water Saturation versus Klinkenberg Permeability

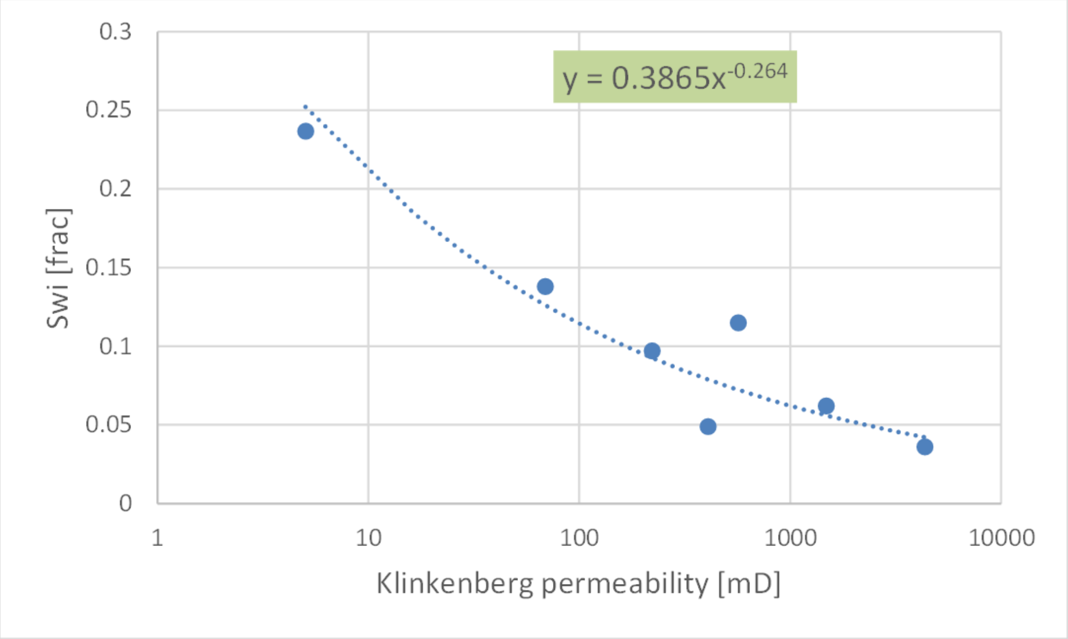

Figure 4.39: Drainage/Imbibition Gas/Water Relative Permeability Data for Endurance

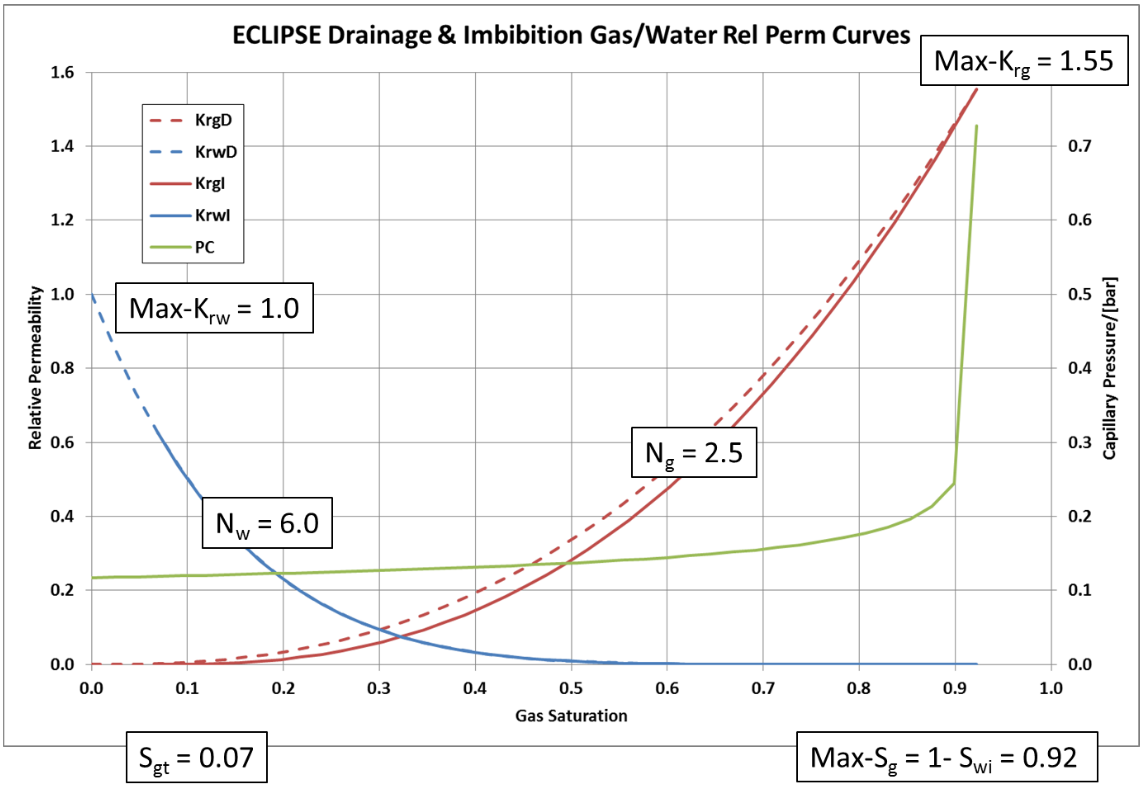

4.6.4.3 Endurance Relative Permeability Analogues

Whilst awaiting Endurance SCAL (special core analysis) results, a literature survey was conducted to assess the suitability of published CO_2/brine relative permeability (Kr) and capillary pressure data for use in the reservoir model. The CO_2-brine Kr data determined using a Viking sandstone reservoir sample as as reported in Ref 11 and reproduced in Figure 4.40, is a commonly used analogue data for simulation of CO_2 storage in sandstone formations. There is however significant differences between the physical properties of the Viking sandstone formation compared to the Endurance Bunter sandstone. The Viking sandstone sample was taken from a depth of 1343 m where the pressure and temperature are 86bar and 35°C with an average porosity and permeability of 0.195 and 21.7 mD and a brine salinity of 28,300mg/kg. The Endurance Bunter sandstone formation on the other hand has average porosity, permeability and salinity of 0.192 (7% cut-off), 271 mD (well test), and 250, 000mg/kg, respectively.

A closer analogue to the Endurance Bunter sandstone was found in the Ketzin core Kr measurements as shown in Figure 4.41 (reproduced from Ref 12). The Ketzin core was recovered from the Stuttgart formation in the late Triassic Keuper age rocks that overlie the early Triassic Buntsandstein (Endurance Bunter equivalent) formation. In flow tests, the permeability was measured to be between 50m and 100mD whilst tests on core showed values range between 500 and 1000mD. The brine salinity was reported as 220,000mg/kg. The values of the Corey coefficients are reproduced in Table 4.13. Results obtained from these analogue data have been interpreted as model sensitivities on Kr behaviour.

Figure 4.40: Viking Relative Permeability and Capillary Pressure Data

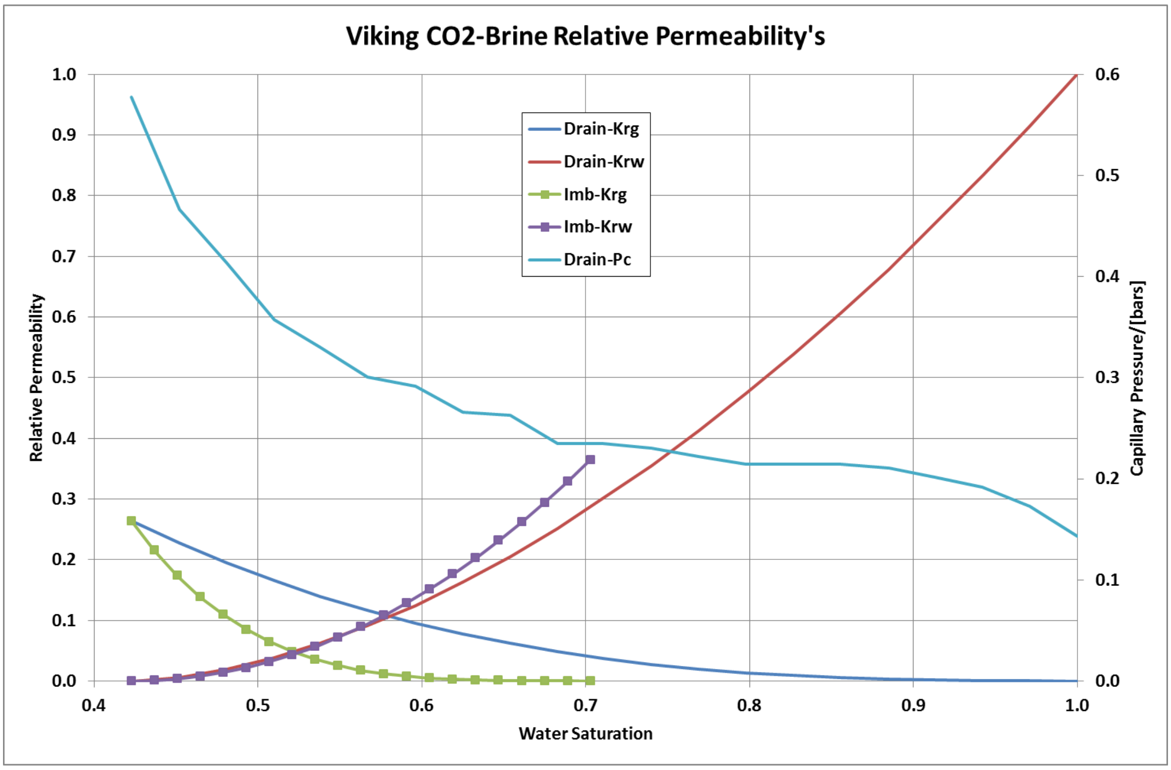

Table 4.13: Ketzin Corey Relative Permeability Coefficients

Parameter	CO_2	Brine
Exponent	1.50	5.50
Drainage-Residual	0.05	0.15
Imbibition-Residual	0.30	0.15

Figure 4.41: – Ketzin Relative Permeability and Capillary Pressure Curves

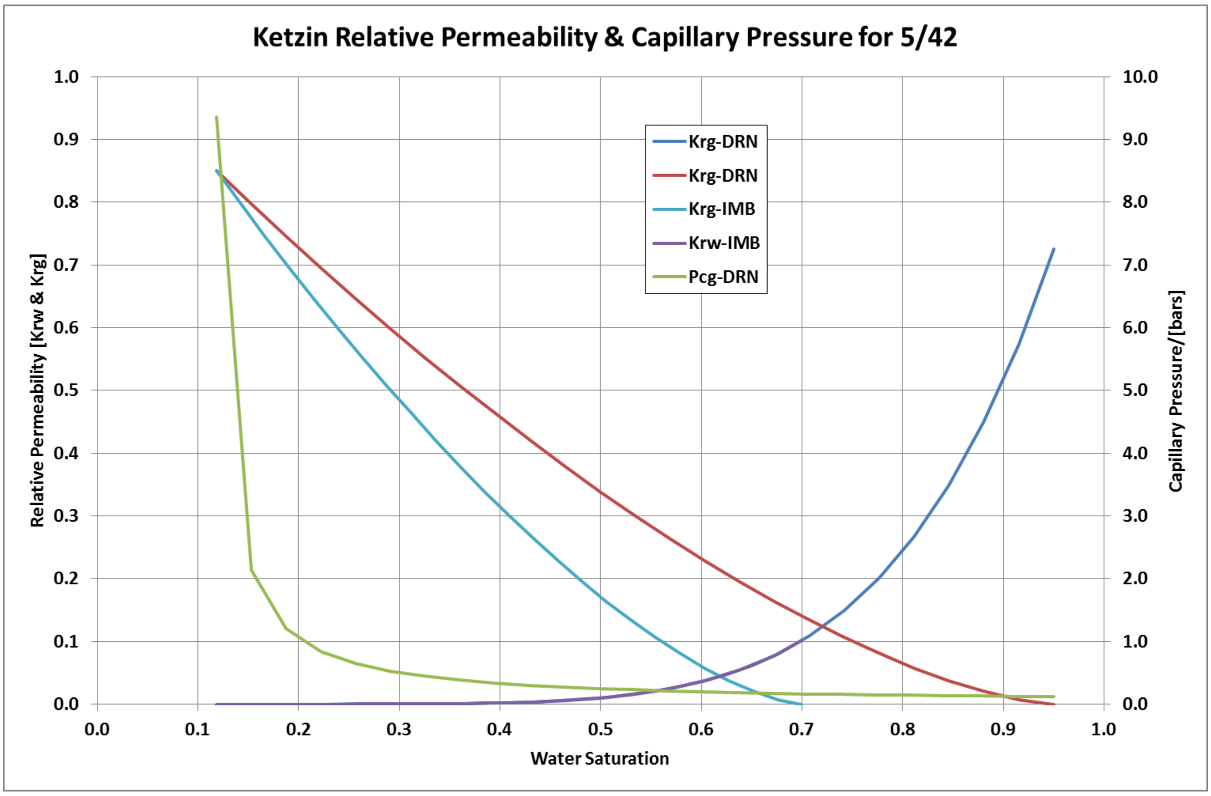

The capillary pressure function is given by:

Equation 4.6

$$P_c = \left(\frac{S_w - S_{wi}}{a} \right)^m$$

where a = 0.096 and m = -0.989. Of course Equation 4.6 becomes infinite as $S_w \to S_{wi}$ so a small offset is introduced to keep P_c finite.

Note the maximum gas (CO_2) relative permeability in Figure 4.41 of $K_{rg}^M = 0.85$ is 3.2 times larger than the corresponding value in the Viking data (Figure 4.40) and so the CO_2 will move proportionally faster towards the crest of the structure.

4.6.5 Initialisation

Pressure, temperature and salinity (via collection of brine samples) measurements were taken from the 42/25d-3 appraisal well.

4.6.6 Pressure Variation

The model uses a datum pressure of 140.0bar at a reference depth of 1300mTVDSS and the pressure gradient is taken to be 0.115bar/m. These values have been derived from the combined interpretation of RFT and MDT pressure measurements in wells 42/25-1 and 42/25d-3 respectively (see Section 3.7.4).

4.6.6.1 Temperature Variation

Analysis of the temperature data gathered from the 42/25d-3 appraisal well has been summarised in Section 3.7.4. A reference temperature of 55.9°C at 1300mTVDSS was calculated from a temperature gradient of 0.0305°C/m which was determined from the MDT long duration tests, i.e. pressure points and brine sampling.

The CO_2 injected into Endurance will be somewhat cooler than the reservoir given that it will have travelled along a 90km pipeline and the seabed temperature in this part of the UK SNS is known to vary between 5 and 15°C winter to summer. The CO_2 will heat as it travels down the injection wells into the reservoir and this has been estimated to be about 10°C although this will of course depend critically on the flow rate. It has been assumed that the minimum temperature of the CO_2 at the perforations is 15°C (in winter). The injection of CO_2 which is cooler than the reservoir temperature is likely to cause thermal fracturing. For this reason the perforation strategy prescribes the perforation of the deeper sections of the injection wells. A 185 m perforation interval across the L1 zone of the Bunter sandstone has been shown to support the White Rose maximum design CO_2 injection rate of 2.68MTPA whilst allowing for ample distance between the Röt Clay caprock and any potential thermally induced fractures in order to provide for future perforating should existing perforations become plugged or collapse, or the near wellbore becomes damaged.

4.6.7 Salinity Variation

Analysis of the MDT brine samples suggests that there is a variation of salinity with depth as shown in Figure 4.42.

Re-arranging the Equation of the fitted trendline gives a Total Dissolved Solids (TDS) (mg/kg) = 74.6 (TVDSS (m) + 1808) so that at the seabed location of the outcrop where TVDSS = 65 m, then TDS $\approx$ 135,000mg/kg.

It is uncertain whether the outcrop could maintain such a linear gradient in salinity and have a TDS at seabed of around 135,000mg/kg (whilst sea-water salinity is around 35,000mg/kg). Petrographic analysis of cuttings in well 43/28a-3 that passes through the western side of the outcrop suggests flow of meteoric water in the past and also that the high quality Bunter and more recent Quaternary sands are open to flow. The outcrop is by default open to flow and a sensitivity analysis has been performed in which it is considered closed to better characterise its dynamics during and post CO_2 injection.

Figure 4.42: TDS variation with depth from 42/25d-3 MDT samples

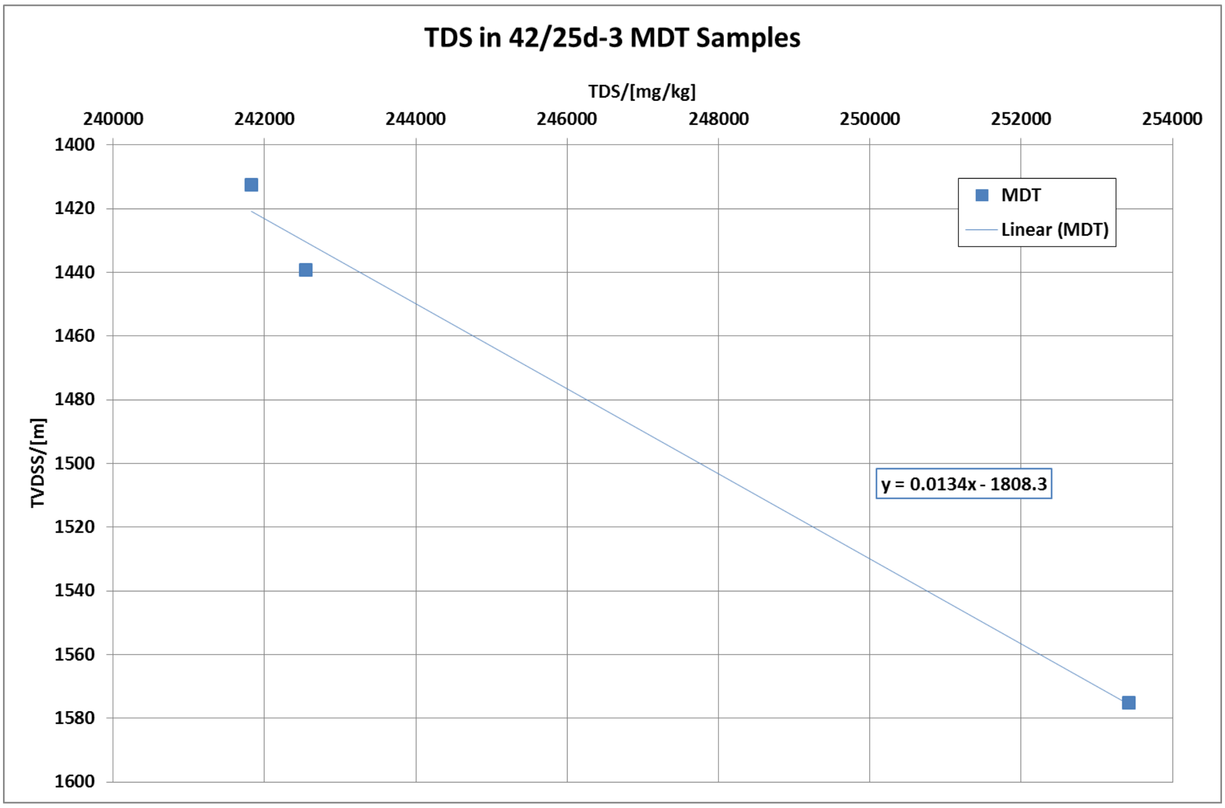

4.6.8 Greater Bunter Size and Properties

Even though an area of about 460km^2 is being considered with a pore volume of around 20.0x10^9 m^3 (the Endurance pore volume measured to the most likely spill is about 4.8x10^9 m^3), it is considered most likely that Endurance is connected to a much larger volume of the BSF, see Section 4.5 for a summary of the arguments.

To avoid the prohibitive simulation CPU requirement, the greater Bunter was not modelled explicitly. Instead, the Carter-Tracy aquifer model in Eclipse has been used. The two parameters which define the model are the time constant τ (with dimensions of time) and the aquifer influx coefficient β (with dimensions of total influx per unit pressure change). These parameters are defined by:

Equation 4.7
$$\frac{1}{\tau} = c_1 \frac{K_A}{\mu_w \phi_A c_T r_o^2}$$

Equation 4.8
$$\beta = c_2 H f \phi_A c_T r_o^2$$

The variables in Equation 4.7 and Equation 4.8 are defined in Table 4.14 along with values where appropriate. Some of the variables are explained by use of the schematic diagrams shown in Figure 4.43.

Figure 4.43: Schematic of the Carter-Tracy Aquifer Model

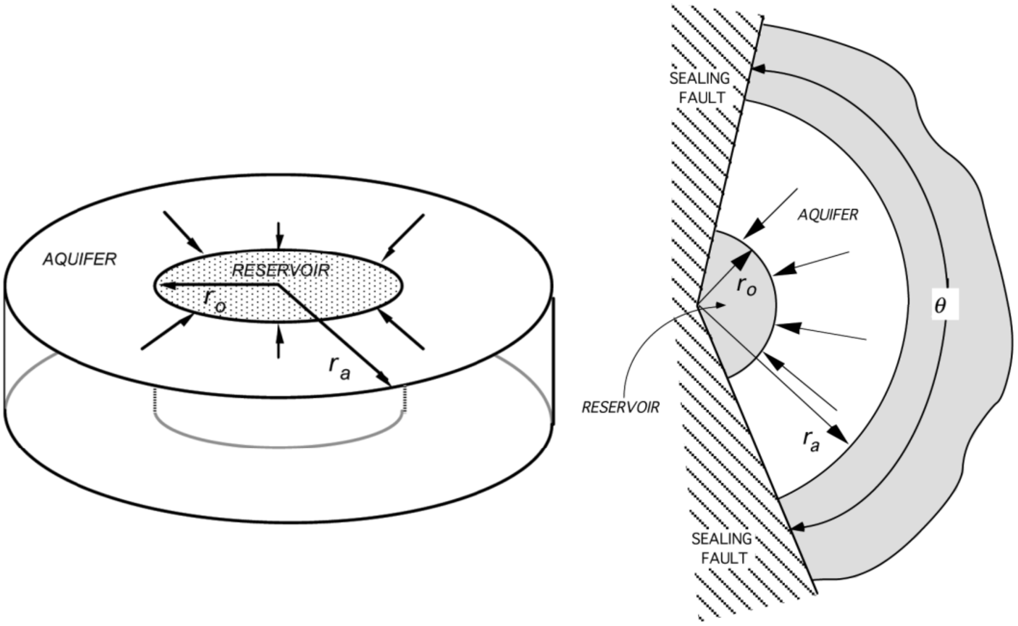

Table 4.14: Parameters in the Carter-Tracy Aquifer Model

Symbol	Parameter	Default Value
K_A	Aquifer Permeability	mD
μ_W	Aquifer Brine Viscosity	1 cP
ϕ_A	Aquifer Porosity	
c_T	Total (Rock and Brine) Compressibility	85x10^{-6} /bar
r_o	Reservoir Radius	11,000m
H	Aquifer Thickness	250m
f	Fraction of Angle Subtended	

For the application of the Carter-Tracy model, rather than a rectangular AOI whose major and minor axes are 40km and 10km, the AOI is considered to be a circle with a radius of 11km, i.e. equivalent area (hence the value of r_o shown in Table 4.14). It has been argued that the aquifer attached to 5/4 extends to an area in excess of 20,000km^2. This implies a pore volume of about 1 x 10^{12} m^3, assuming an average thickness of 250m and porosity of 0.19. Sensitivity of Endurance dynamic pressure to aquifer property is presented in Section 4.6.12.2.

4.6.9 The Outcrop

The AOI for the dynamic model has been chosen to explicitly include the outcrop so that sensitivity to whether it is connected to Endurance and open to flow or not can be studied. The geological interpretation of the outcrop bathymetry is shown in Figure 4.44 whilst Figure 4.45 shows the map and sides views of the out crop in the simulation model. Note the area of Bunter Sandstone thought to be exposed at the seabed is around 1.4km^2. Even if only a fraction of this area is open to flow, it is likely to have significant production for minimal pressure increase, i.e. a very large Productivity Index (PI).

Allowing the outcrop to flow to the sea if the whole system is pressured up is achieved by defining a super-well at the edge of outcrop within the ring of modelled cells with a transmissibility that is 100 times greater than that of a typical well in order to capture the expected high PI.

Figure 4.44: Geological Interpretation of Outcrop Seabed Bathymetry

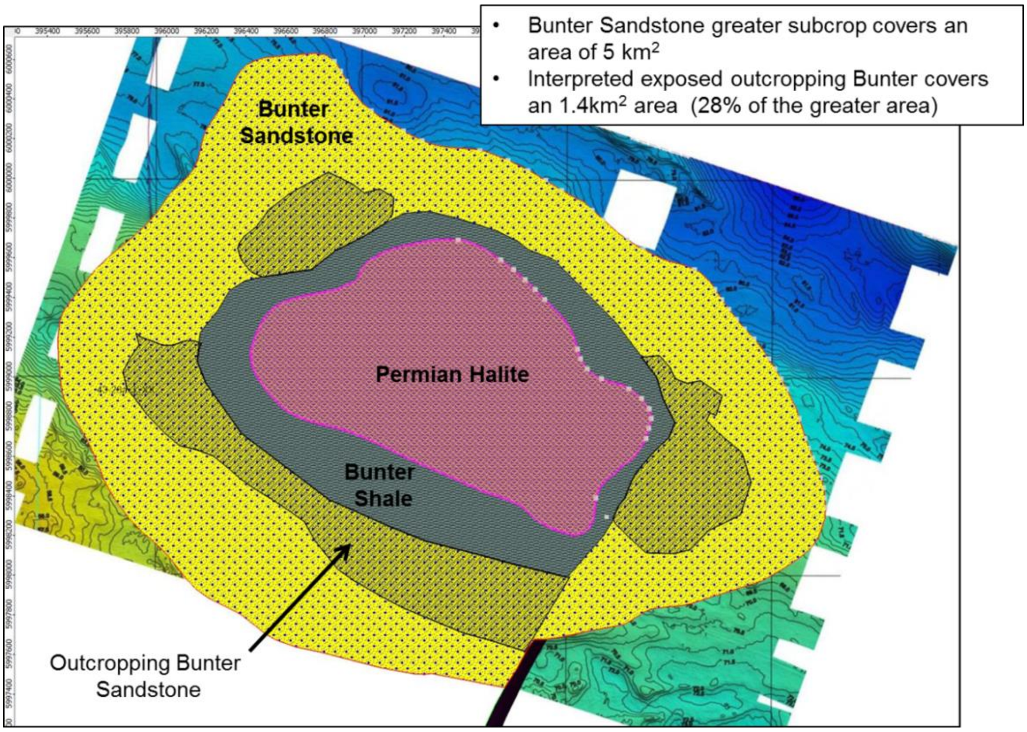

- Bunter Sandstone greater subcrop covers an area of 5 km^2
- Interpreted exposed outcropping Bunter covers an 1.4km^2 area (28% of the greater area)

Figure 4.45: Map and Side-Views of the Outcrop in the Simulation Model

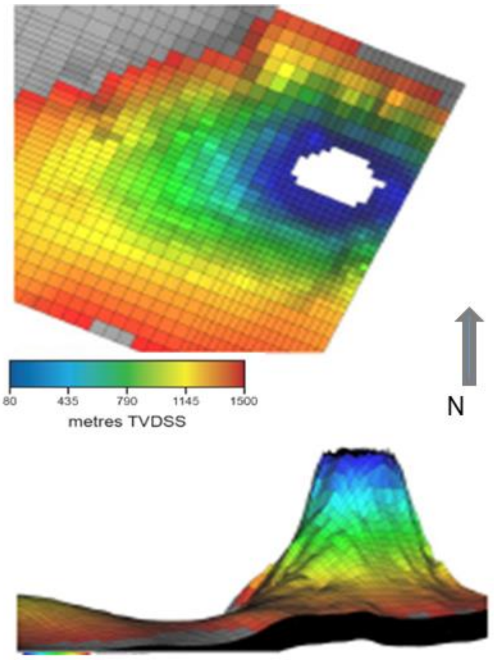

4.6.10 Simplified AOI Simulation Model

To allow more sensitivity runs to be made, a simplified simulation model has been constructed which incorporates the key features of the detailed model. Firstly the model is about 50km long, 12km wide and 250m thick. Porosity is made a linear function of depth with 0.28 at Top Bunter and 0.12 at Bottom Bunter. Horizontal permeability is a function of porosity as per Equation 4.4 and vertical permeability is set using $K_V/K_H = 0.15$. The pore volume of the model is adjusted such that the total volume is about the same as the detailed model of 1.9×10^{10} m^3. Vertical grid cell resolution is 2 m throughout the 125 layers (to make a total thickness of 250m). The areal grid resolution varies as shown in Figure 4.46.

Figure 4.46: Top Bunter Depth of Simplified Model

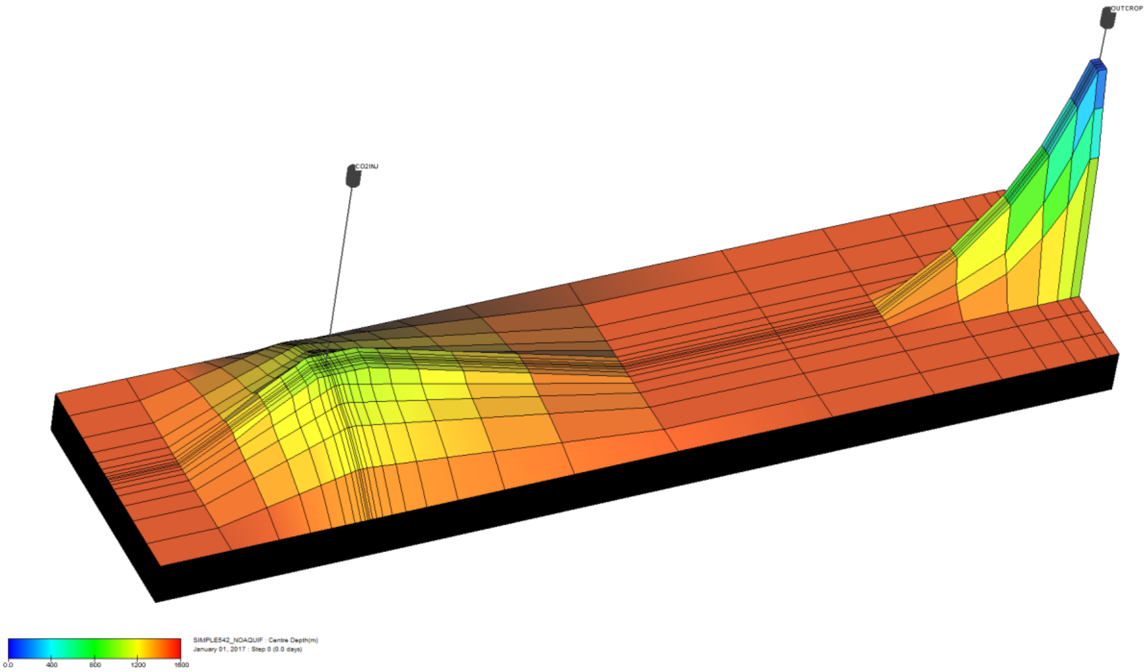

4.6.10.1 Simplified Injection Model

Even the fine scale grid considered in Section 4.6.2.1 was too coarse for looking at issues surrounding injectivity which are dominated by near well bore effects. Therefore the type of grid developed in the previous section has been modified to study sensitivities around injectivity as discussed in Section 4.6.14.

This model has been developed to study injectivity issues by adding finer grid cells to a core area whose extent has been defined by the horizontal departure of a well drilled through the Bunter sand at 50 to 60^o orientation from the vertical. A grid size of $(\Delta X, \Delta Y) = (50m, 50m)$ has been adopted with $(N_x', N_y') = (21, 21)$ cells for this core area. Outside this area, the grid cells are increased by a factor of 1.5 until an area comparable to that of the Greater Bunter in the UK SNS has been covered. A map view of the grid showing the ΔX-values is shown in Figure 4.47 and a cross section in Figure 4.48.

Both Röt Halite and Röt Clay have been included in this model to permit quantification of the conductive cooling created from injecting cold CO_2 through the wells. Porosity and permeability of the halite layers are set to 0.001 and 1 μD whilst the values in the clay are set to 0.005 and 10 μD. The porosity in the Bunter sandstone is made a linear function of depth with a value of 0.27 at Top Bunter and 0.14 at Bottom Bunter. Permeability of the Bunter sandstone is calculated using Equation 4.4.

Figure 4.47: Simplified Grid to Study Injection Issues

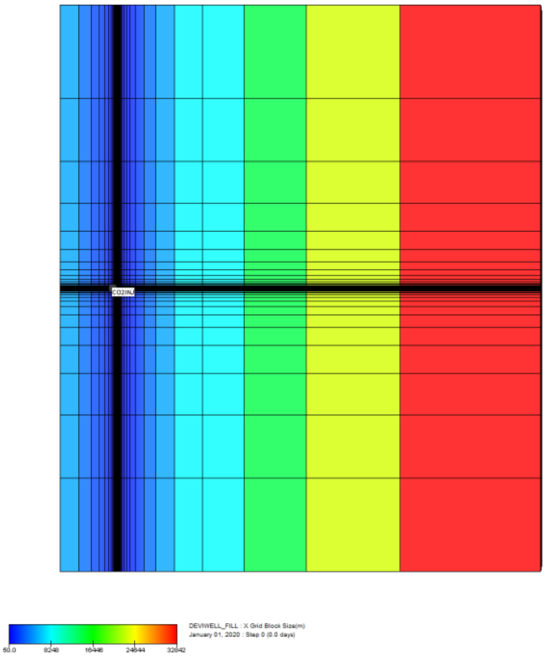

Figure 4.48: West-East Porosity Cross-Section through Injection Model

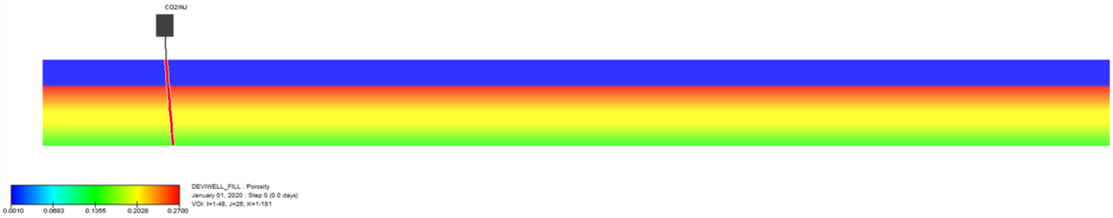

4.6.11 Wells

The injection wells have been designed to ensure ease of access during potential well interventions: wellheads will be located on a platform and a maximum well trajectory of less than 60º has been adopted to ensure operations can be undertaken via wireline. Since all wells will be set on a single platform it is important to perforate as deep as possible to maximise the separation of the plumes generated from each well whilst ensuring the injected CO_2 remains within the confines of the structure defined by the shallowest possible spill point.

Injecting the CO_2 as deep as possible has other advantages, namely:

- maximises the offset from the cap rock, i.e. delays the CO_2 arrival time to the crest of the structure;
- maximises opportunity for residual and dissolution trapping; and
- minimises risk of thermal fracturing of the cap rock.

4.6.11.1 Well Locations and Trajectories

The location chosen for the platform is at 366882 m Easting's and 6012790m Northing's in UTM Zone 31 on the ED50 datum.

The deviation of the three specified CO_2 injection wells (55º to 60º from the vertical) is shown in Figure 4.49. The red and purple images in the map overlay are overburden faults. Avoidance of overburden faults was one of the criteria which dictated the well placement.

4.6.11.2 Perforation Interval

As stated above, the perforation strategy is to perforate the wells as deep as possible. Whilst the relative buoyancy guarantees that CO_2 will migrate upwards, a decision has been made to set the deepest perforation 30m above the shallowest possible spill point of the structure. It is assumed that the topmost perforation will be set in the middle of the L2-Bunter Sandstone.

Figure 4.49: Well Trajectories from P5 Platform Location

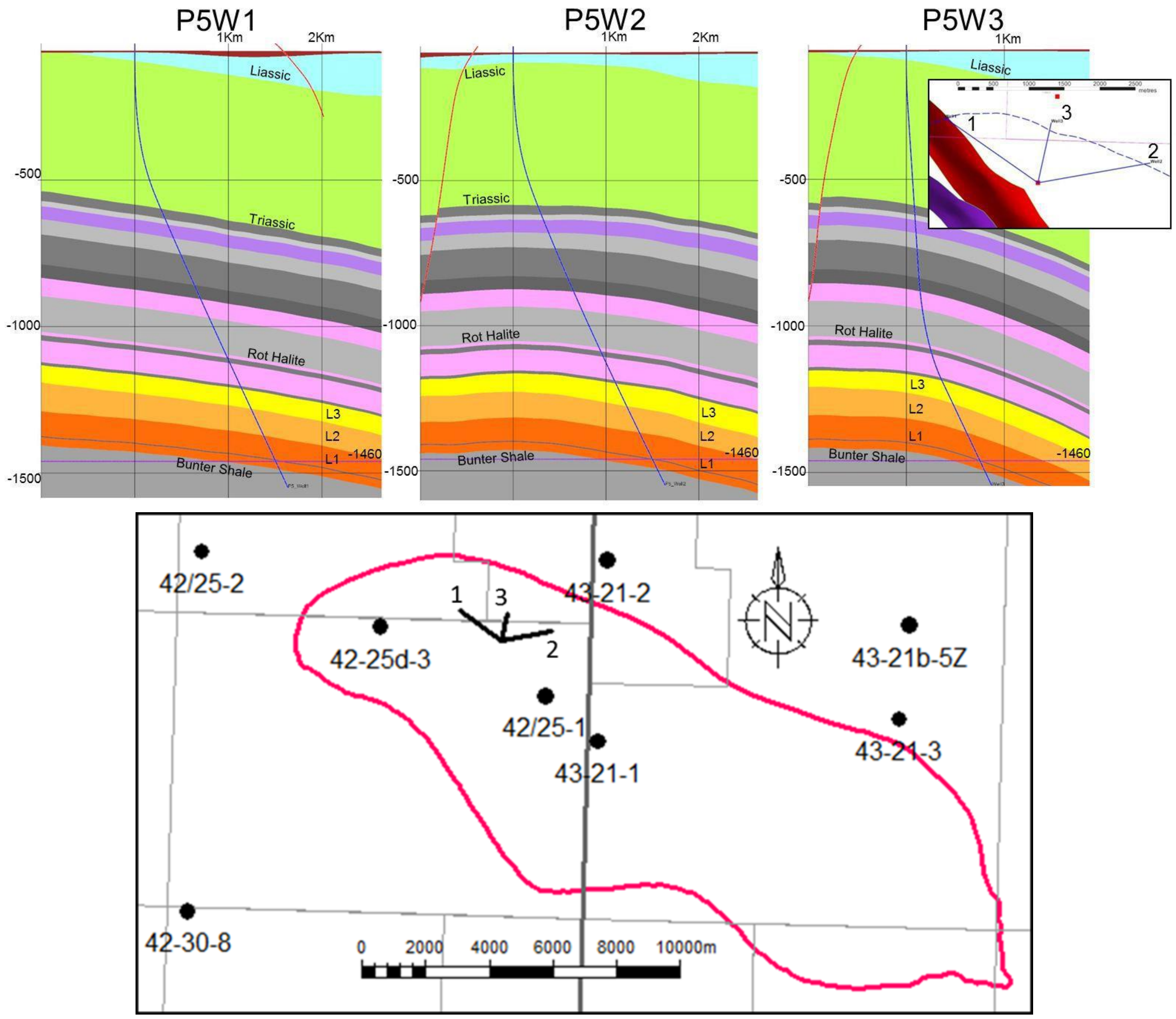

4.6.11.3 *Well Switching*

Considering the three injection wells discussed above, the standard operating strategy that has been adopted in the dynamic simulations is to split the maximum injection rate of 2.68MTPA between two of the three wells, i.e. 1.34MTPA/well and then to cycle between the set of wells every six months so that any given well is injecting for 12 out of every 18 months.

4.6.12 CO_2 Storage Volumes and Reservoir Pressure Profiles

The mid-case pore volume quoted in Section 3.8.1 was 4.6 Bm^3. So assuming an average irreducible water saturation of 0.15, the mid-case static volume that could be accessible by CO_2 would be 3.9 Bm^3. The density of supercritical CO_2 in Endurance will vary between 600 and 800 kg/m^3; so an average value of 700 kg/m^3 can be used for the purposes of estimation. This means if all the moveable brine could be replaced with CO_2, a mass of $(3.9x10^9)x(700) = 2.7x10^{12}$ kg or 2700 Million tonnes (MT) could be stored. By comparison the maximum Phase-I loading is 2.68MTPA for 20 years or 53.6 MT in total; again assuming an average CO_2 density (in the reservoir) of 700 kg/m^3 this corresponds to a downhole volume of 77 Mm^3. Therefore the White Rose injection volumes will be less than 2% of the static volume of the Endurance structure.

The 53.6 MT (maximum White Rose injection mass) will occupy about 76 Mm^3 at reservoir conditions. The compressibility of rock and brine is about $85x10^{-6}$ /bar giving rise to a (maximum) increase of pressure of $\Delta P \approx (76.6x10^6)/[(4.6x10^9)(86x10^{-6})] = 194$bar which is probably sufficient to fracture the reservoir and cap rock whose fracture closure pressure has been estimated as 264bar at 1362.8 mTVDSS. But this estimate doesn't take account of the additional volume of Bunter Sandstone connected to Endurance, nor does it consider that the outcrop to the ESE of Endurance is probably open to flow to the seabed. Thus the first two sensitivities that will be considered are:

- whether the seabed outcrop is connected to Endurance and open to flow; and
- what is the size and strength of the Greater Bunter attached to Endurance?

The assumption of whether the outcrop is open or closed needs to be addressed first as having the outcrop open will obscure questions concerning the aquifer size and strength.

4.6.12.1 *Outcrop Open/Closed*

CO_2 at a rate of 2.68MTPA is injected for 20 years, i.e. 53.6 MT in total, followed by a 20 year shut-in period. Initially the model is limited to the AOI (no additional aquifer volume) to include Endurance and the outcrop so that the (7% porosity cut-off) pore volume is $20.5x10^9$ m^3 compared with the most likely Endurance fill-to-spill volume of $4.6x10^9$ m^3 quoted above. The pressure calculated at the crest of Endurance which corresponds to the location of the 43/21-1 well is shown in Figure 4.50 when the outcrop is closed and open along with the brine production rate in the latter case.

Figure 4.50: Pressure Change at Endurance Crest when Outcrop Closed/Open and Water Production

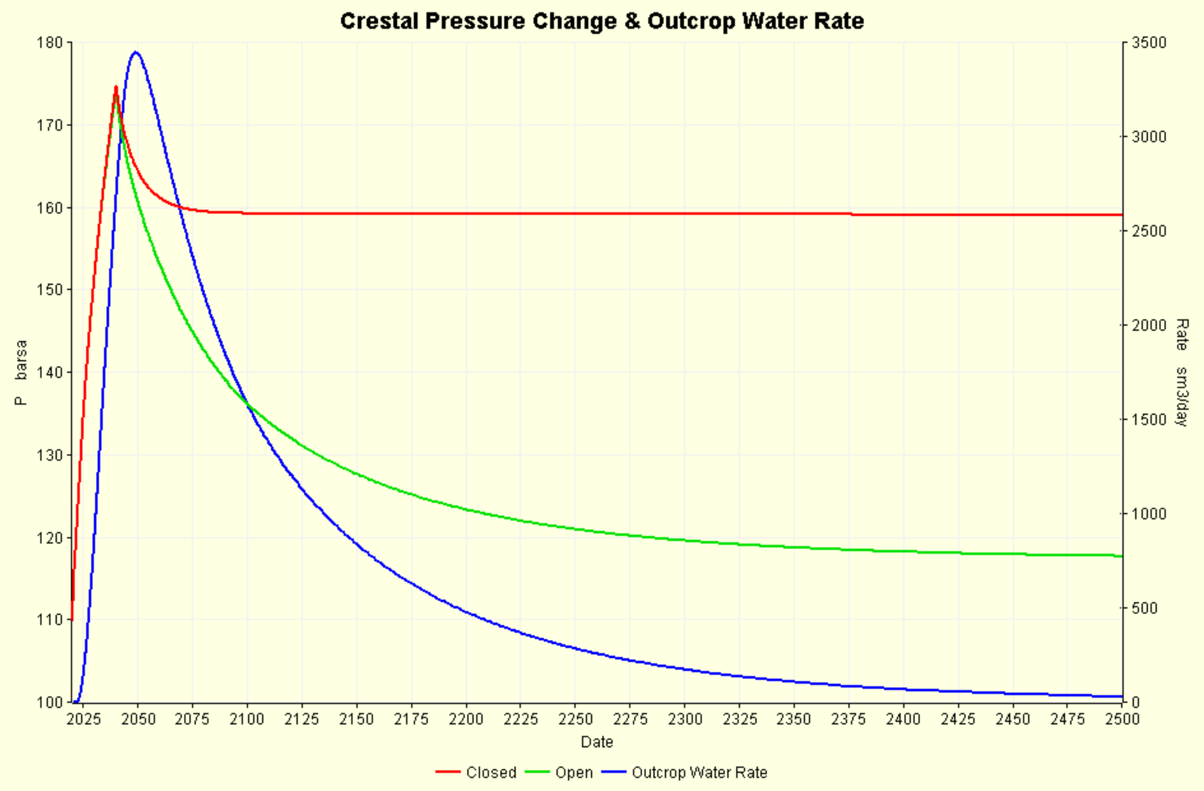

A relevant form of the conservation of mass derived from the definition of (microscopic) compressibility may be stated here as

Equation 4.9 $$\Delta V \approx cV\Delta P$$

In which ΔV is the volume of fluid measured at reservoir conditions injected into a closed box of volume V and average compressibility c which as a result of the injection sees an increase of pressure of ΔP.

When the outcrop is closed the maximum pressure increase is 64.8bar at the end of injection which drops to 49.2bar after shut-in. The reservoir volume occupied by the 53.6 MT of injected CO_2 is $80x10^6$ m^3 so with a total compressibility (of rock and brine) of $85x10^{-6}$ /bar the pressure change predicted from Equation 4.9is $(80x10^6)/[(85x10^{-6})(20.5x10^9)]$ = 45.9bar showing good agreement between this simple model and the simulation.

With the outcrop open, the maximum pressure at the end of injection is only 0.9bar lower than the closed case but the pressure then continues to drop as the excess pressure causes flow from the outcrop to continue during the shut-in period. By the year 2500, 460 years after shut-in, the pressure is just 7.8bar over initial pressure.

Brine production starts 2.5 years after the start of CO_2 injection (when the pressure at the outcrop is 0.1bar above its initial pressure), it peaks around $3500m^3$/d about nine years after shut-in and is still over $3000m^3$/d twenty years after cessation of injection. By 2500 the production rate is still more than $30m^3$/d.

Generally, it will be assumed that the outcrop is open unless a specific case when it is closed is being investigated and discussed.

At least as far as the Endurance Phase I development is concerned, whether the outcrop is open or closed seems to have little effect on the maximum pressure increase during the injection phase.

4.6.12.2 Greater Aquifer

An argument is presented in Section 4.5 which strongly suggests that Endurance is in hydrodynamic communication with a much larger volume than itself, perhaps 50 to 100 times larger. This has the potential to greatly reduce the pressure increase associated with White Rose CO_2 injection. However, because of the distance between the injection point(s) and the additional volume, there will be a time-lag in pressure response and the reduction in peak pressure within Endurance will not be proportional to the amount of additional volume increase. Further, the nature of the time-lag is dependent on the strength of the coupling between the greater Bunter and Endurance. However, whilst there appears to be good evidence over the size of the greater Bunter, the strength by which it couples to Endurance is less clear.

Aquifer Size: if the Greater Bunter attached to Endurance has an area in excess of 20,000km^2, then this is 100 times the area of the Endurance structure anticline (assuming a spill at 1500mTVDSS = 25 x 8 = 200km^2) and 43.5 times the area of the simulation model.

To test a range of additional volumes a finite radial aquifer of variable r_{eD} ($r_{eD} = r_a/r_o$, i.e.ratio of aquifer radius to reservoir radius or the dimensional radius) has been attached to all the edge cells of the simulation model, comprising just under 29,000 connections for the Intermediate grid model. The thickness has been set to 250m and an average porosity of 0.192 was used (corresponding to the average porosity in the 7% cut-off model shown in Table 4.9). Using Equation 4.4, the applied porosity yields an aquifer permeability of 125 mD. The angle subtended by the aquifer is assumed to be 360^o, i.e. full circle, the total compressibility of the rock and brine is 85x10^{-6} /bar, the brine has a salt concentration of 250,000mg/kg and the area of the simulation model converts to a circle of radius 11km. The set of r_{eD} investigated is shown in Table 4.15 along with the resulting area (with respect to the AOI) and the total PV of the AOI and attached aquifer. Note that the first row in the table with $r_{eD} = 1.0$ means no additional volume attached, i.e. the green line in Figure 4.50. The pressure response reported at the crestal location is shown in Figure 4.51. Note that at $r_{eD} = 5.0$, the total area of the AOI and aquifer system is only 25 times that of AOI alone, somewhat less than the previously speculated size of the Greater Bunter attached to Endurance.

It can be seen once $r_{eD} > 2.0$ the peak increase in pressure at the crest is not significantly reduced from its value of 38.0bar at $r_{eD} = 2.0$. Clearly the asymptotic behaviour during shut-in is changed but some of this change is due to the water production rate from the outcrop which has been open to flow in all these cases; the outcrop production rate versus aquifer size is shown in Figure 4.52. As the attached aquifer becomes larger, it can take-up more of the pressure increases caused by injection meaning less pressure at the outcrop and hence less brine production.

It takes 10-12 years to differentiate between the $r_{eD} = 2$ and $r_{eD} > 2$ cases. It would appear to be nearly impossible to differentiate between the $r_{eD} > 2$ cases though this may be easier if porosity and permeability are less than the 0.192 and 125 mD assumed here. This is studied in the next section.

Going forward the r_{eD} = 3.6 aquifer size will be assumed unless notified otherwise.

Table 4.15: Size of Aquifer and Resulting Model Area and Pore Volume

r_{eD}	Area wrt Model Area	Total PVX 10^9 m^3
1.0	1.00	20.5
1.5	2.25	46.1
2.0	4.00	82.0
3.6	12.96	265.7
5.0	25.00	512.5

Figure 4.51: Sensitivity of Crestal Pressure Increase to Aquifer Size

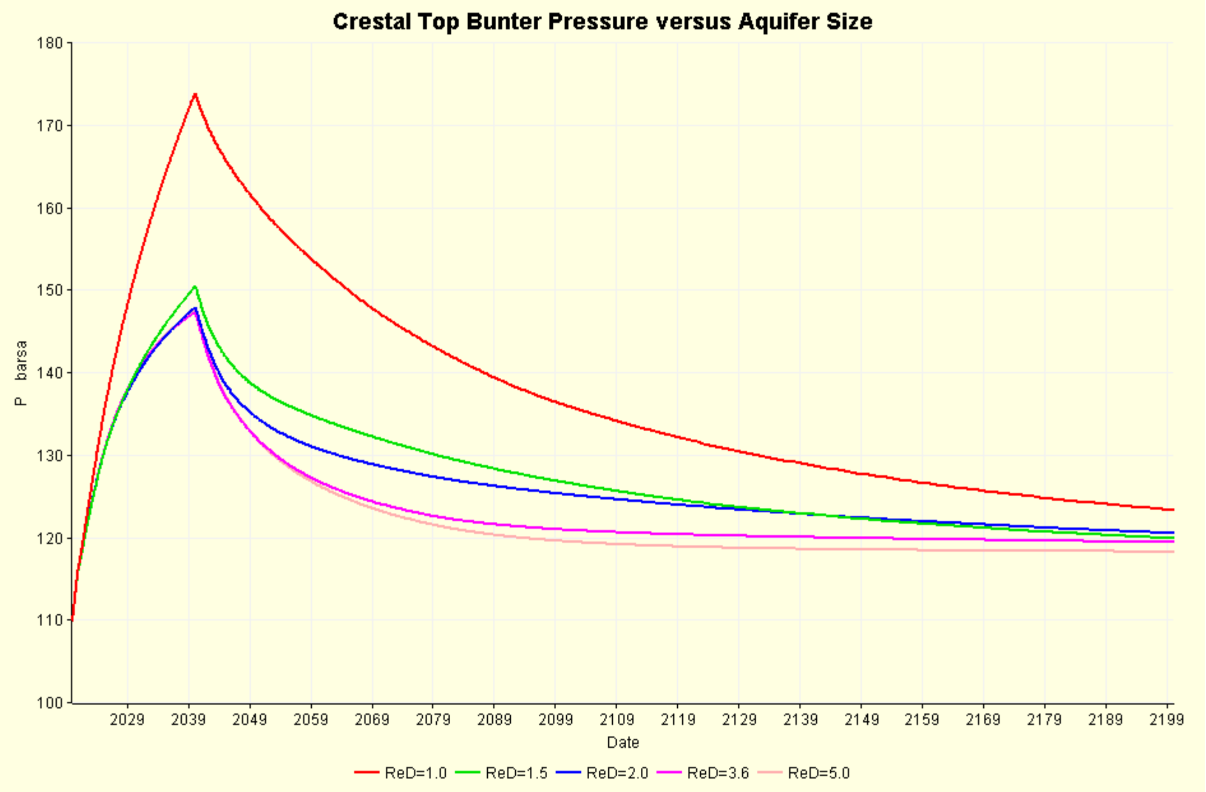

Figure 4.52: Outcrop Production Rate versus Aquifer Size

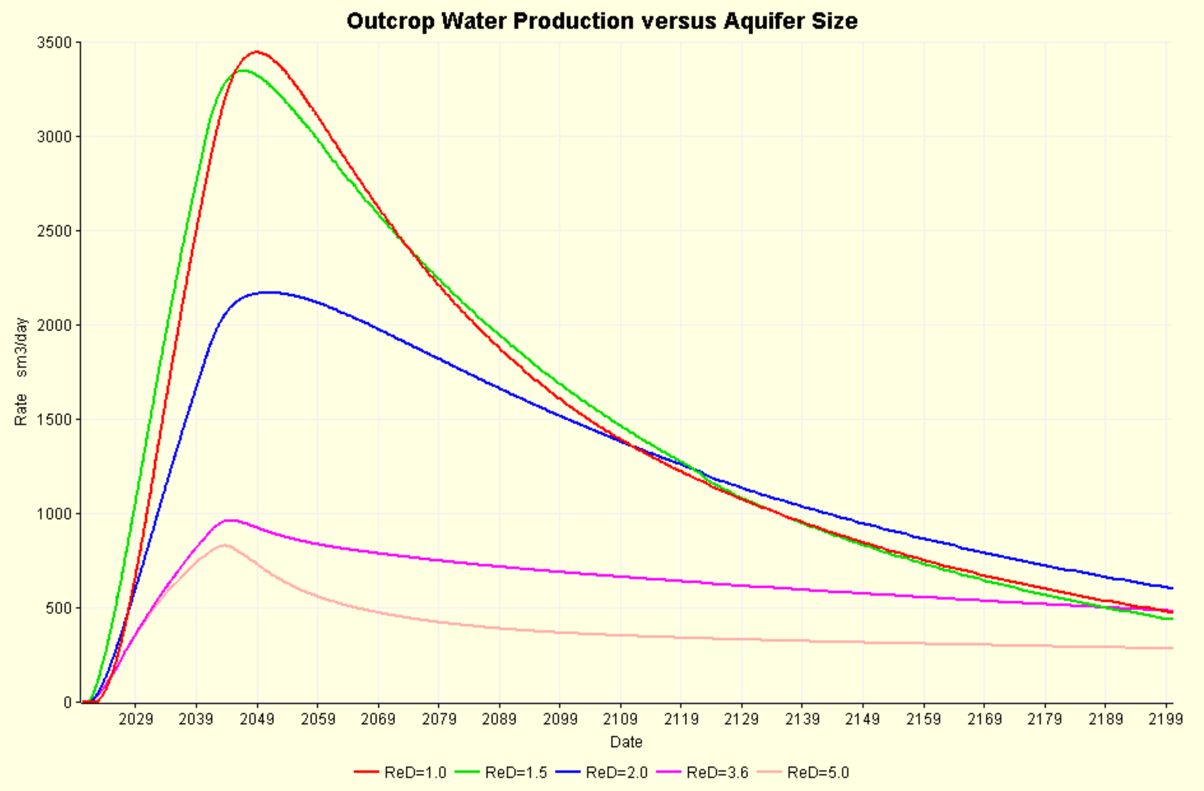

Aquifer strength: the properties of the attached aquifer, in particular the related (through Equation 4.4) porosity and permeability are clearly unknown. Previous generic studies of the Bunter aquifer have used permeability values that ranged from less than 1 mD to 250mD.

As stated above, the r_{eD} = 3.6 aquifer size has been used but the porosity and permeability of the Carter-Tracy aquifer are as defined in Table 4.16.

Table 4.16: Porosity and Permeability Used in Aquifer Strength Sensitivity

Porosity [fraction]	Permeability [mD]
0.06	1.25
0.13	12.50
0.19	125.00
0.26	1250.00

The results of this sensitivity are shown Figure 4.53. Reducing the quality of the attached aquifer clearly has a detrimental effect on the injection scheme by increasing the crestal pressure seen at the Top Bunter 43/21-1 location. In particular, relative to the K = 125 mD case, reducing the permeability to 12.5 mD and 1.25 mD causes the peak pressure to increase from 37bar to 47bar and 58bar, respectively.

Figure 4.53: Crestal Pressure Increase versus Aquifer Properties

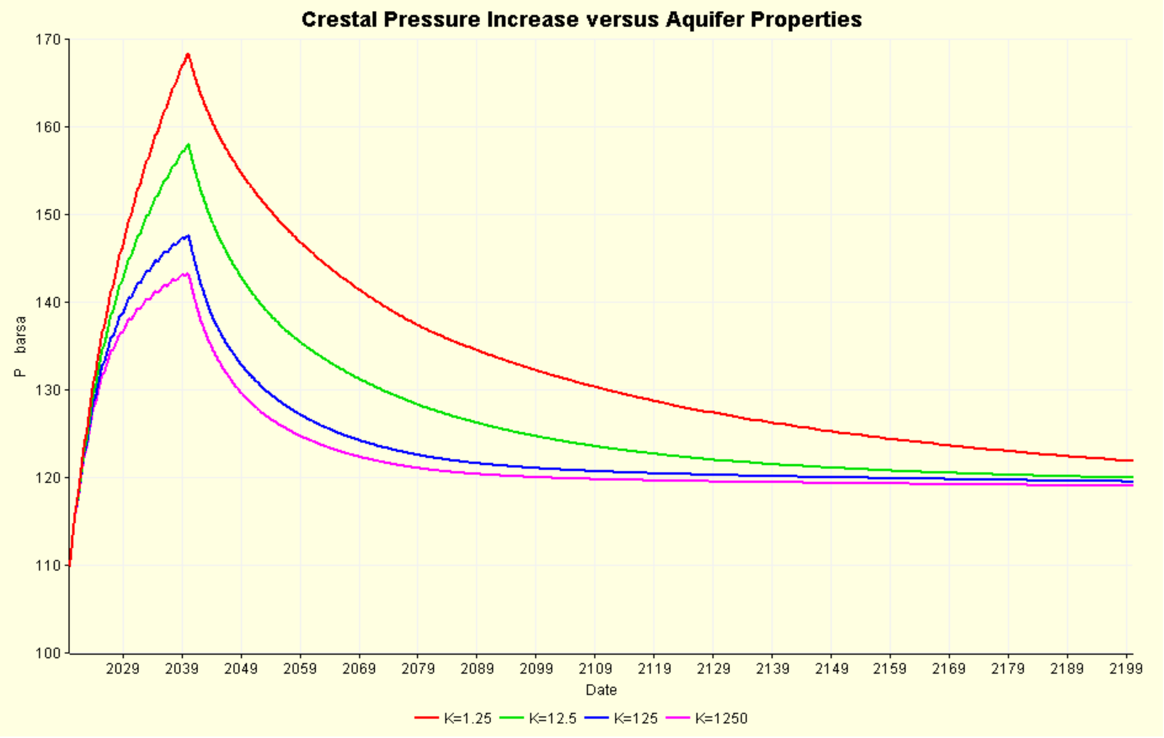

Figure 4.54: Crestal Pressure Increase versus Aquifer Properties for the Injection Period (first 20 years)

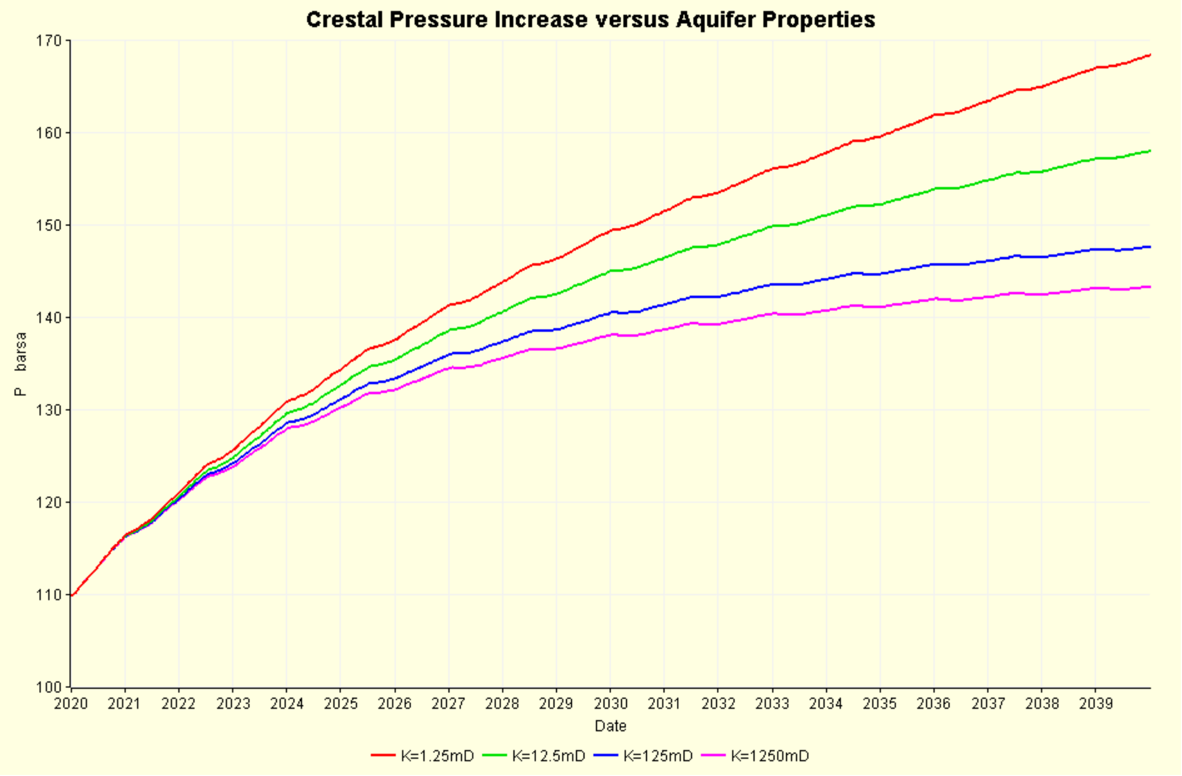

Figure 4.54 is a " zoomed-in" version of Figure 4.53 shows just the 20-year injection period to demonstrates that the impact of different aquifer properties only start to show after third year of injection.

Regarding the most representative aquifer properties, at the Esmond field 45km North East of Endurance, a Greater Bunter aquifer average permeability of 16 mD was estimated from material balance calculations that used actual production performance and post shut-in pressure build up data. However, much wider range of values has been estimated by a number of authors. Ref 6 reported average porosity and permeability for the Greater Bunter of 0.18 and 250mD whilst in Ref 8 the values were 0.20 and 100mD, respectively. Ref 13 estimates the average well porosity for wells in the UK SNS Bunter as 0.187 (from 603 core plugs) – although a great variability of porosity within individual wells was observed; from 0.024 in well 42/10a-1 to 0.22 in well 42/25-1. For the 42/25d-3 appraisal well, the average porosity is approximately 0.20 – 0.27 at the top and 0.14 at the base.

There is therefore considerable uncertainty around Greater Bunter aquifer properties. Nevertheless, a Greater Bunter permeability of125 mD has been used in simulations from here onward unless explicitly stated otherwise as this is consistent with a porosity of 0.19 from the poro-perm function in Equation 4.4.

4.6.13 Plume Development

The change in pressure caused by CO_2 injection has been shown to depend mainly on the size and strength of Greater Bunter attached to Endurance. Once the effect of the near wellbore over-pressure required to cause inflow has dissipated, the dense CO_2 will migrate upwards and because of the density difference between it and the native brine, until a seal is encountered. Thereafter CO_2 will flow upwards along the Top Bunter until it pools at the crest of the structure.

The impact of a number of parameters on plume development has been considered and is outlined in the sections that follow.

4.6.13.1 Horizontal Permeability

As with the sensitivity of the aquifer properties analysed in Section 4.6.12.2, varying the horizontal permeability of the Endurance rock will change the crestal pressure increase as shown in Figure 4.55. In varying the horizontal permeability, the earlier constraint on average model permeability imposed by the upscaling method has been temporarily relaxed to permit the use of low (135 mD) and high (540mD) case permeability values. The 271 mD from 42/25d-3 production well test is taken as the mid case. Note the maximum pressure increase follows the differences seen in Figure 4.53 and Figure 4.54.

Figure 4.55: Crestal Pressure Increase versus Endurance Horizontal Permeability

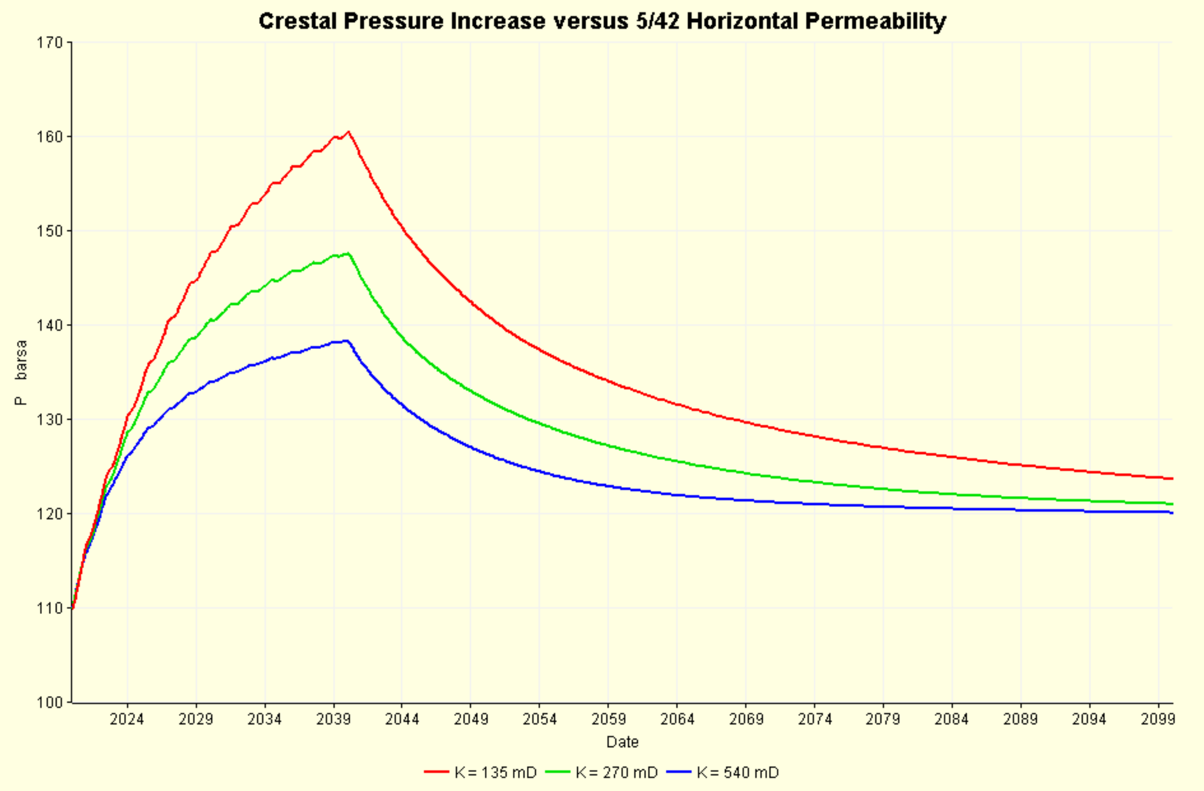

Part of the increase (for K = 135 mD) and decrease (for K = 540mD) in crestal pressure is because of the reduced and increased well injectivity, respectively.

The main effect under study here is the frontal advance of the CO_2 plume because of the reduced/ increased K_H and this is shown in Figure 4.56; the break through time (first CO_2) is listed in Table 4.17.

Table 4.17: Time to First CO_2 at Crest of Endurance versus Permeability

KH/[mD]	First CO_2/[yr]
135	5.5
270	3.3
540	1.8

A semi-transparent map view of the Top Bunter depth is shown in Figure 4.57 on which a line can be seen from WNW to ESE across the crest of the structure. This line denotes the set of cross-section displays that follow. The line includes the DEV1 (NW) well as well as the 42/25-1 and 43/21-1 wells. The CO_2 saturations in this mid-case (271 mD) cross-section at 6 months after the start of injection, 5 years after, 20 years after (the end of injection) and a further 60 years of shut-in are shown in Figure 4.58, Figure 4.59, Figure 4.60, and Figure 4.61respectively.

Figure 4.56: CO$_2$ Saturation at Top Bunter 43/21-1 Location

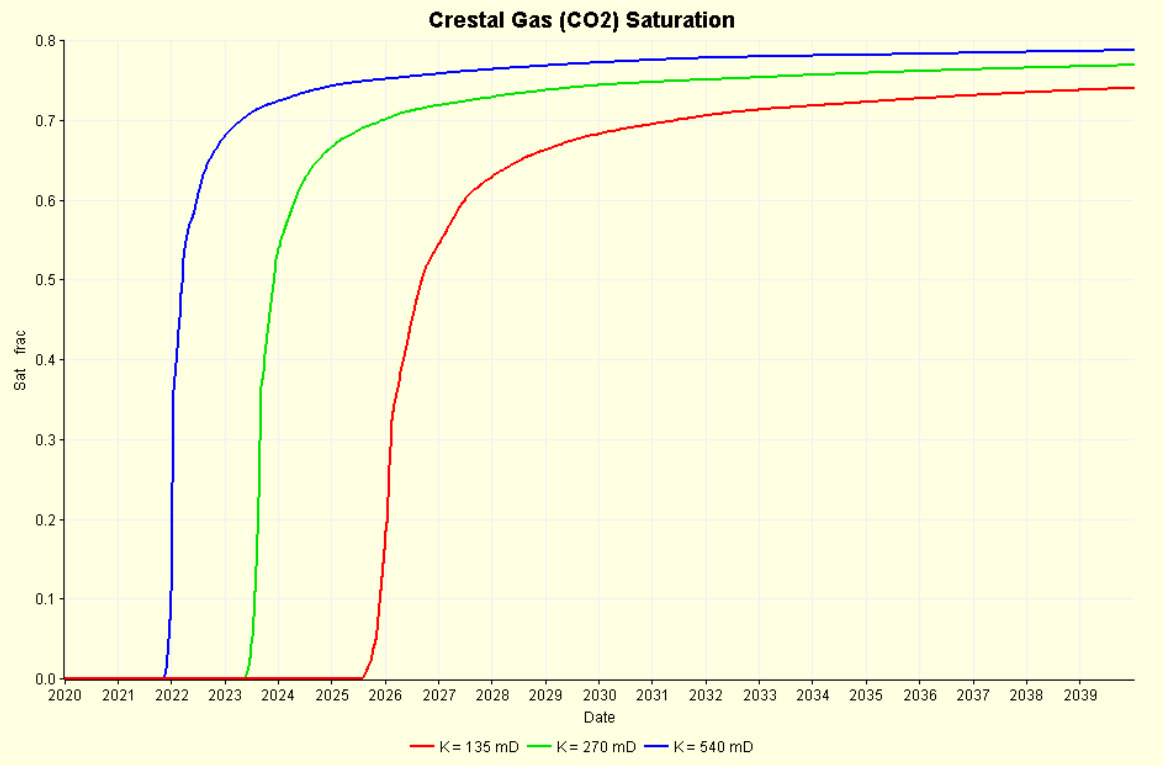

Figure 4.57: Cross-Section through DEV1, 42/25-1 and 43/21-1

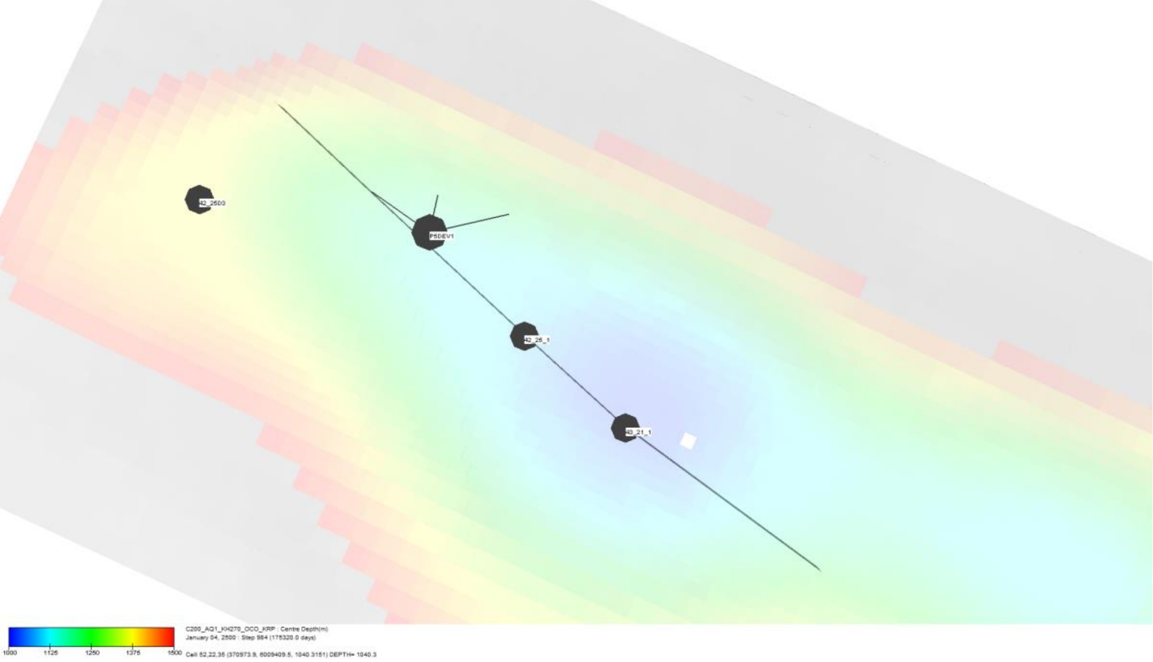

Figure 4.58: CO₂ Distribution after 6 Months of Injection

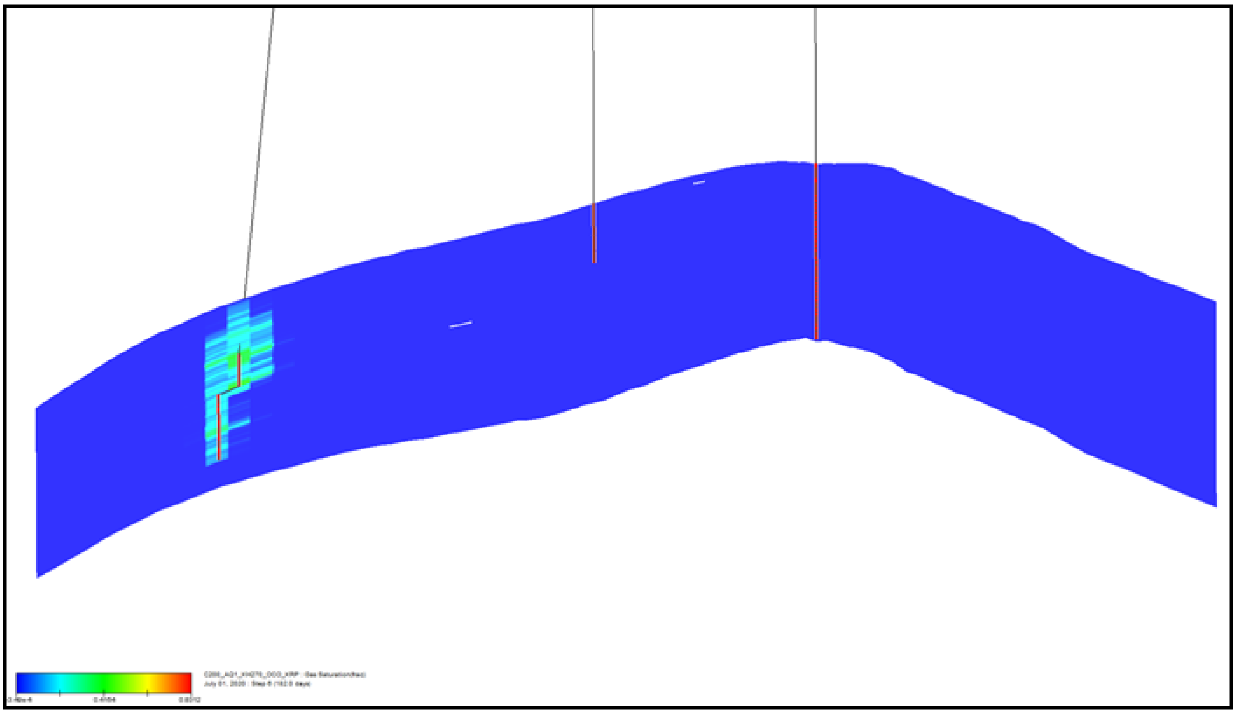

Figure 4.59: CO₂ Distribution after 5 Years of Injection

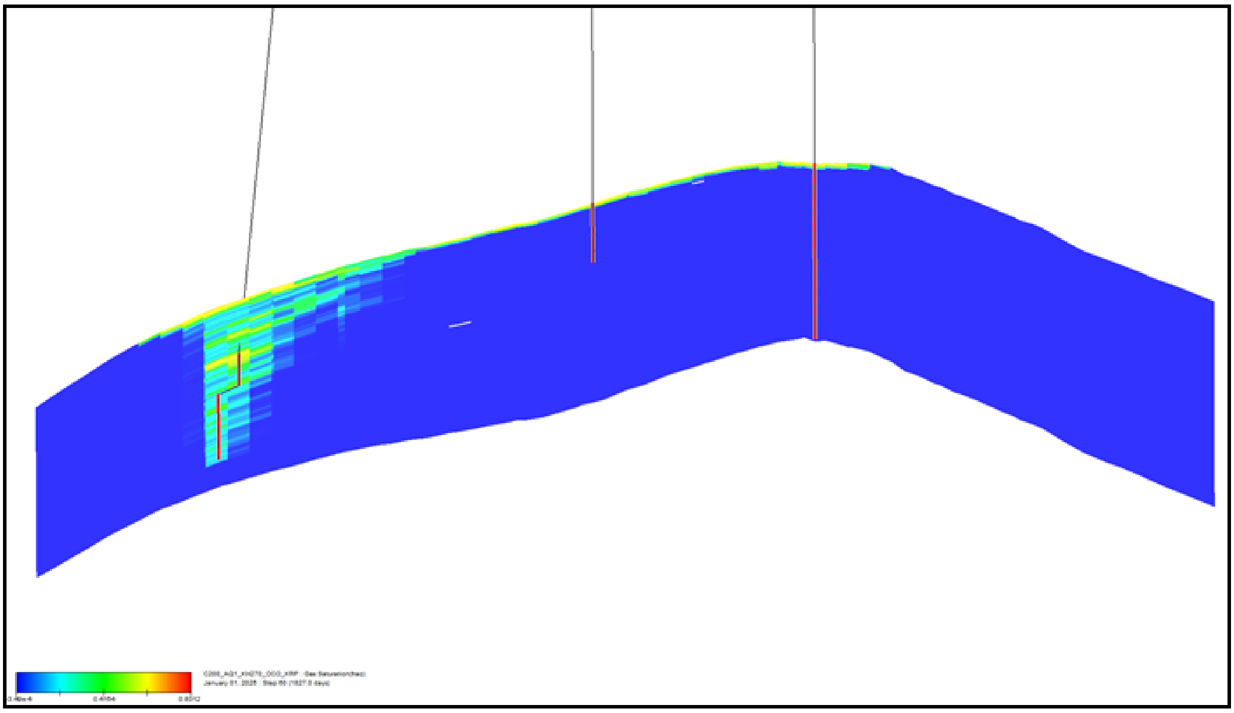

Figure 4.60: CO_2 Distribution after 20 Years of Injection

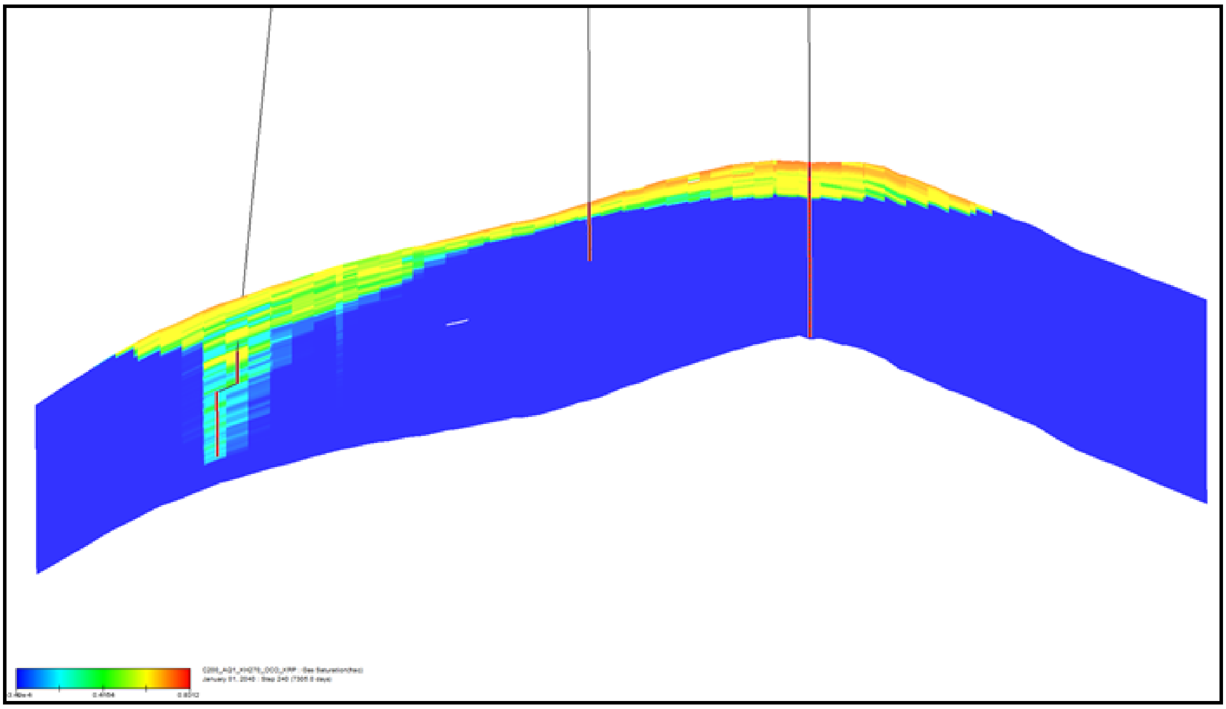

Figure 4.61: CO_2 Distribution after 20 Years of Injection and 60 Years of Shut-In

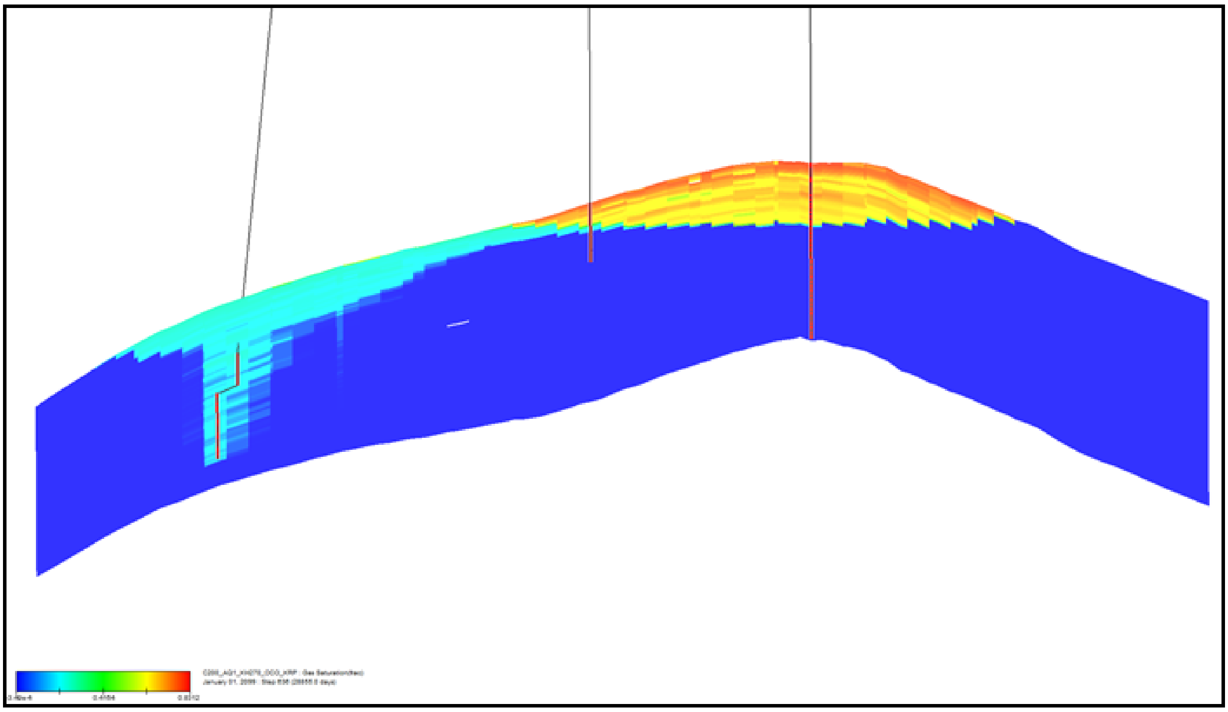

Even though CO_2 is being injected in the lower half of the Bunter sandstone, it reaches the cap rock in just over 6 months, Figure 4.58. After 5 years, Figure 4.59, the CO_2 cap is starting to become established at the crest of the structure. At the end of injection, Figure 4.60, the area above the DEV1 well shows predominantly green and yellow coloured cells indicating saturations in the range 0.4 to 0.6, i.e. well above the imbibition critical gas saturation S_{gt} = 0.3. After shut-in, the mobile CO_2 continues to migrate upward to the cap rock and on to the crest whilst fresh brine imbibes into the area surrounding the well trapping CO_2 at this 0.30 saturation limit as seen in Figure 4.61. The free CO_2 at the crest now approaches its limiting saturation of $S_g = 1 – S_{wc} \approx 0.90$, coloured red in this figure. Running this model onto 01 Jan 2500, 460 years after shut-in, produces the distribution shown in Figure 4.62. Essentially all the CO_2 is now free at the crest or residually trapped elsewhere.

Figure 4.62: CO_2 Distribution after 20 Years of Injection and 460 Years of Shut-In

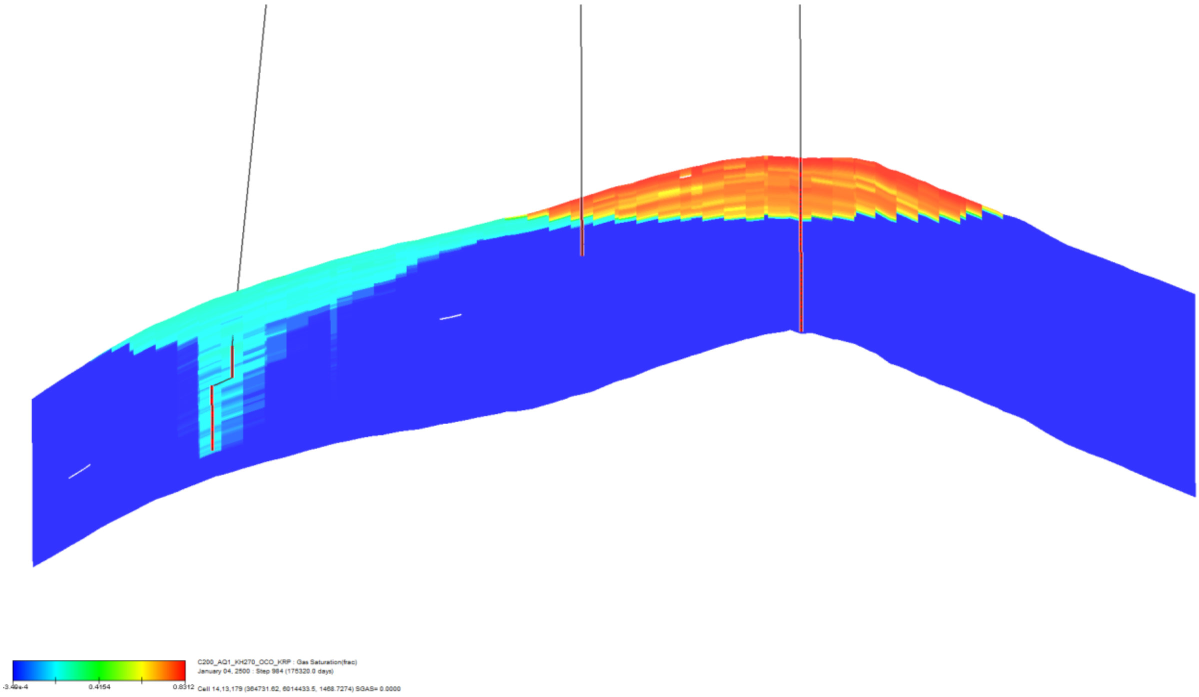

It is important to remember some of the limitations of this model, namely:

- no CO_2 dissolution in the brine;
- no temperature effects;
- no diffusive flow; and
- no geochemical effects.

Dissolution effects are discussed in Section 4.7 whilst temperature effects are addressed in Section 4.6.15. In particular, diffusion is thought to be the mechanism by which free CO_2 which has pooled at the crest of the structure can dissolve in the underlying fresh brine generating saturated brine which is slightly denser than fresh brine. ujThis density difference (which will be 0.1 to 0.2% in a 250,000mg/kg brine) can then generate Rayleigh-Taylor instability in which the saturated brine flows down while fresh brine flows up to act as the recipient for additional free CO_2 from the crestal pool. This process in conjunction with long term geochemical reactions between the saturated brine and the rock fabric leading to potential mineralisation of the CO_2 has been suggested by many academic researchers investigating the ultimate fate of the sequestered CO_2. However, all of the experimental research that has been reported has tended to focus on idealised scenarios that use unrepresentative rock matrix and on timescales of days to months rather than thousands of years as is more appropriate for CO_2 sequestration. Whilst modelling and simulation could be used to overcome some of the limitations there is still a great deal of uncertainty as to the accuracy of the results since even the most advanced models are able to account for only a small fraction of the potential geochemical interactions. The approach for investigating the likely dissolution-convection-mineralisation processes as a result of White Rose CO_2 injection into Endurance has been to use 2D sector models to investigate limit cases using proven databases. The results are presented in Section 3.9.2 and Section 4.7.

4.6.13.2 Vertical/Horizontal Permeability Ratio

Generally vertical permeability K_V is calculated via a multiplier applied to the horizontal permeability K_H; the multiplier is the ratio of K_V/K_H. The mid-case value of K_V/K_H has been presented as 0.15 in Section 4.6.2.2; low and high values for K_V/K_H have been derived as 0.10 and 0.36 respectively from vertical interference test (Section 4.3.2).

The result of this sensitivity had no material effect on the pressure change measured at the crest of the structure. Varying the ratio did not change the horizontal permeability and it was K_H that was used to calculate well injectivity.

The speed at which the CO_2 plume moves is clearly affected by K_V/K_H as shown in Figure 4.63

Figure 4.63: Crestal CO_2 Saturation versus KV/KH

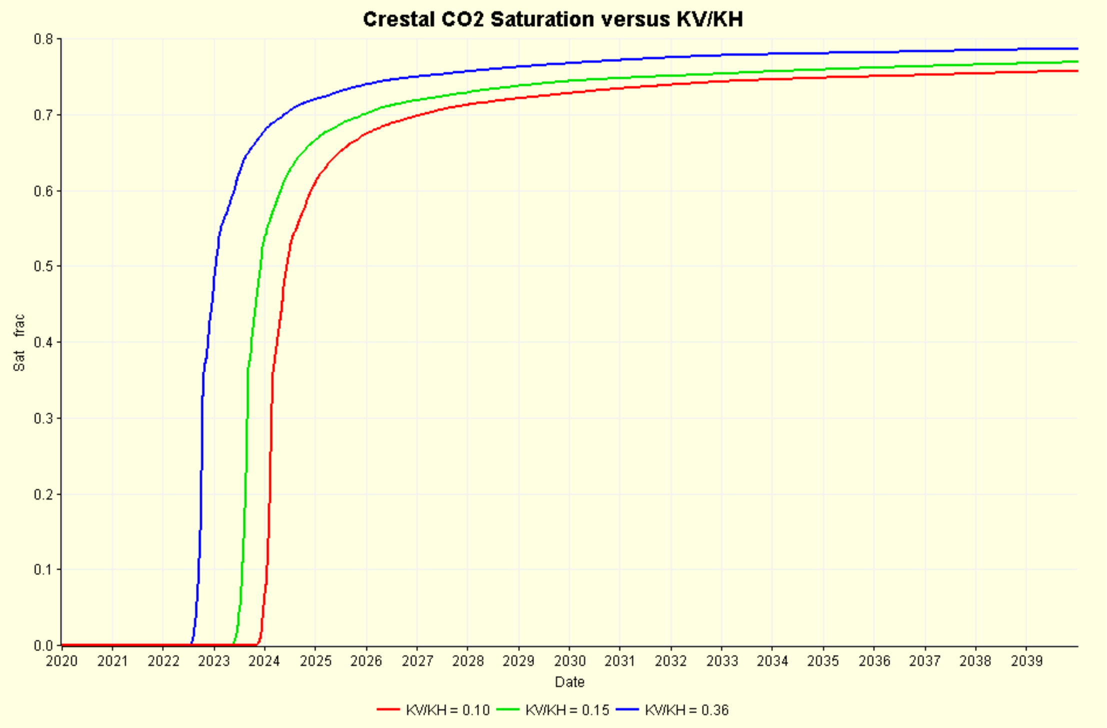

More than doubling the mid-case value from 0.15 to 0.36 does not half the crestal arrival time of the CO_2 but reduced it by around 10 months.

4.6.13.3 Sub-Seismic Baffling

There is no evidence for baffles in any of the three well penetrations nor can faults be seen on seismic within Endurance. This does not preclude the existence of such features being present within the structure.

Therefore, to test the effect of baffles and barriers a simple set of modifications have been employed. First, 1% of the total cells in the intermediate model (representing 7000 cells) were randomly assigned vertical cell-to-cell transmissibility *Tz* of zero. Cells in the intermediate grid have 200m aerial grid spacing over the core of Endurance. The difference between the case without the barriers and that with the 7000 flow barriers is small, with only a slight delay in the arrival time of the CO_2 at the crest of the structure (Figure 4.64).

Two further cases were constructed where the size and then the orientation of the barrier was changed, the results of which (crestal pressure change and CO_2 saturation) are shown in Figure 4.65. Firstly, the set of 7000 horizontal barriers (as applied through a vertical transmissibility multiplier) studied previously were all extended in size. Rather than being the cross-sectional area of a single grid block (200m by 200m), the barriers were made three blocks by three blocks, i.e. 600m by 600m. These values are shown as the pair of blue lines (solid line for CO_2 saturation and dashed line for pressure) in Figure 4.65. The green pair of lines shown on the same figure is for a case where the barriers are vertical in their orientation.

Figure 4.64: Crestal Pressure Change & CO_2 Saturation Without & With Horizontal Barriers

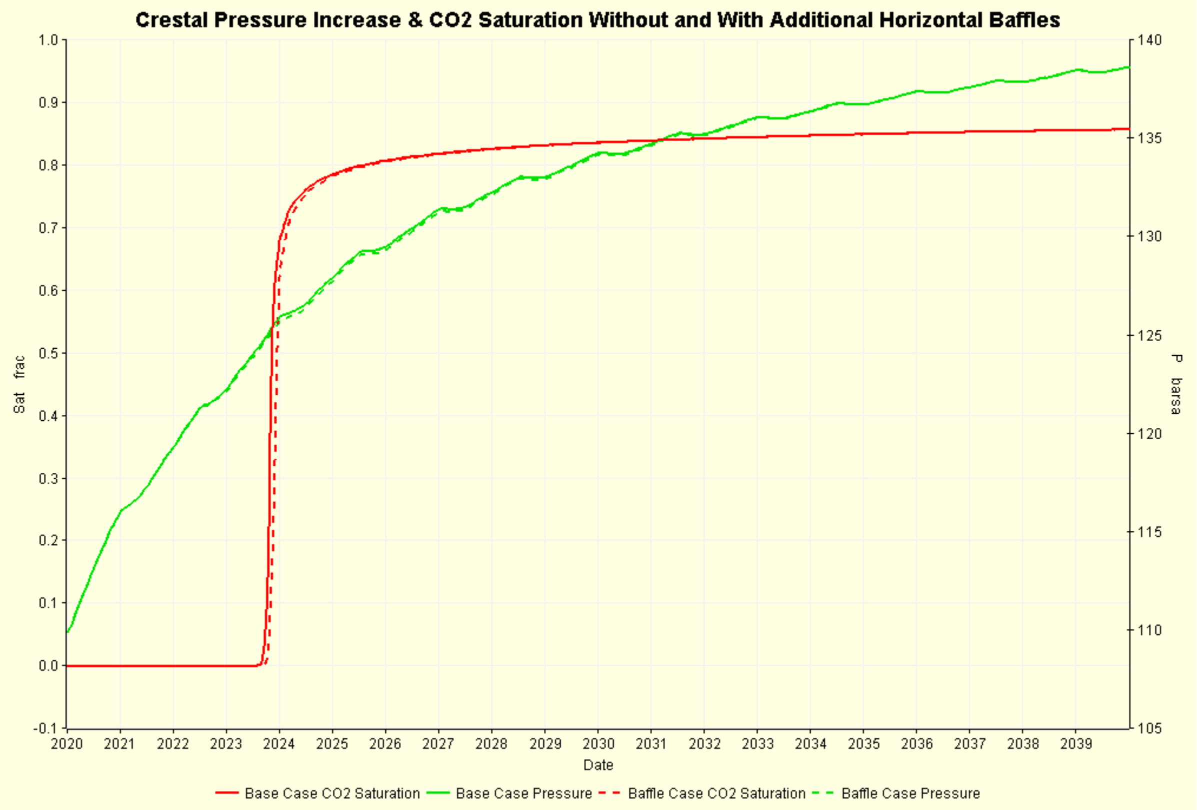

Figure 4.65: Crestal Pressure Change & CO_2 Saturation versus Different Barriers

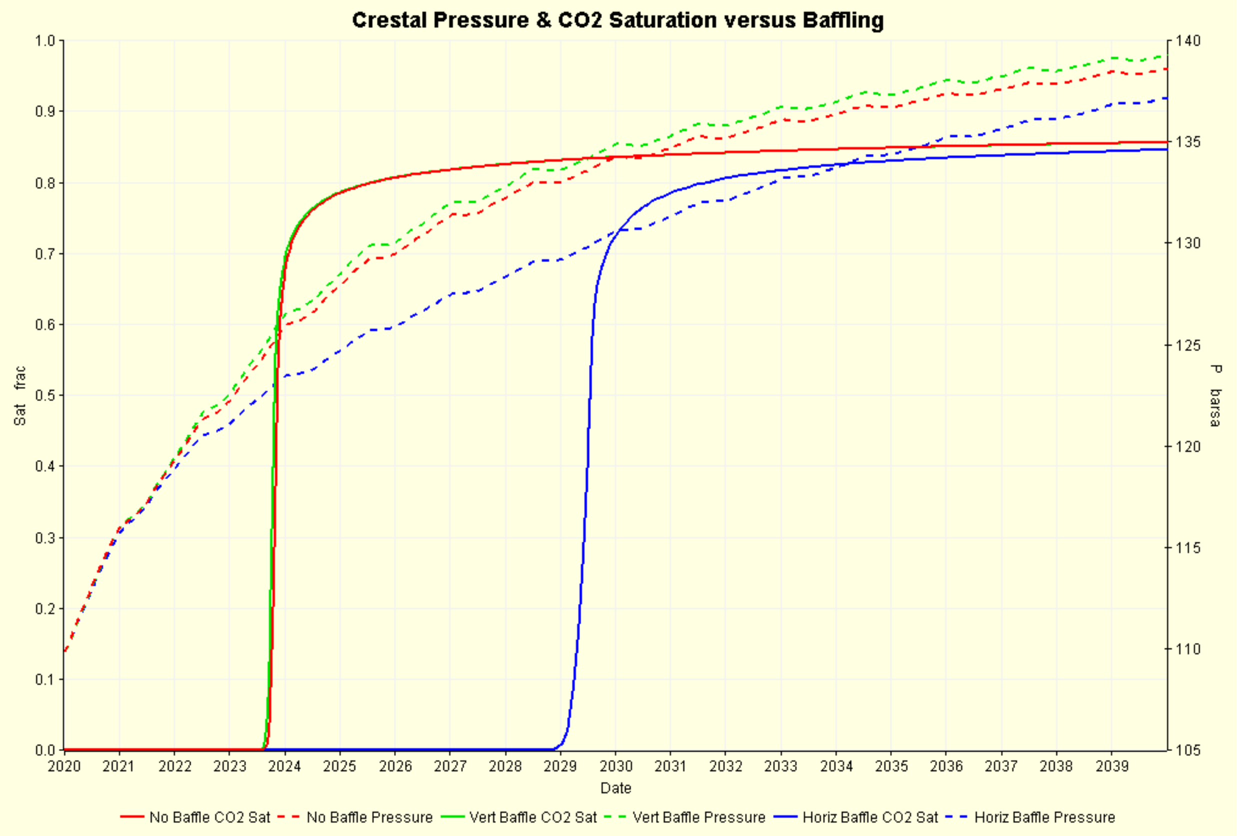

The vertical barriers are three grid blocks wide, i.e. 600m and five grid blocks high, i.e. 10m. The height is considered to be less than that resolvable on seismic, which is typically 20m. It is noticeable from Figure 4.65 that the vertical barriers (in green) have little impact on the progress of the CO_2.

The effect of larger horizontal barriers (shown in blue) is much more pronounced (also see Figure 4.66 and Figure 4.67). The arrival time of the CO_2 at the crest has been increased from 3.5 years to over 9.0 years whilst the increase in pressure is also reduced although this difference is gets smaller toward the end of the 20 year injection period.

Figure 4.66: No Baffle CO_2 Cross-Section after 9 years

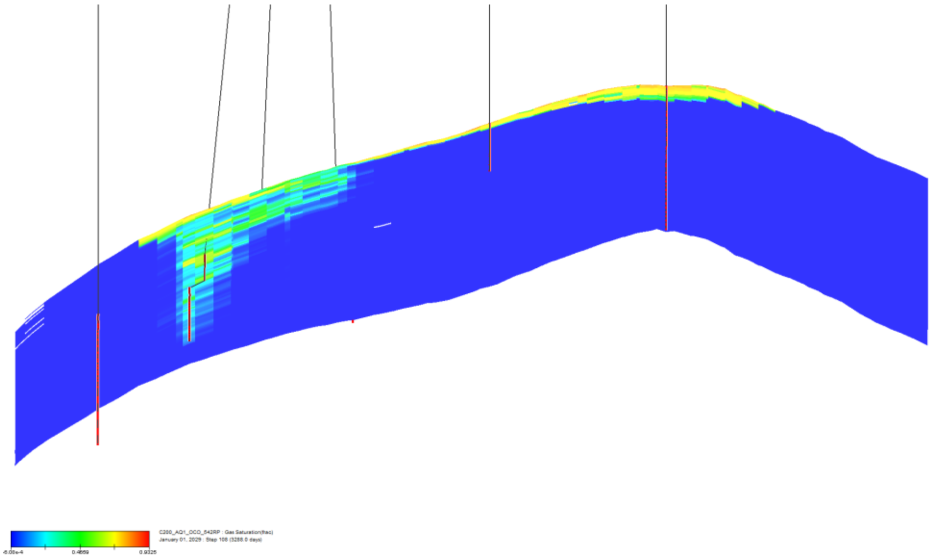

Figure 4.67: Vertical Baffle CO_2 Cross-Section after 9 years

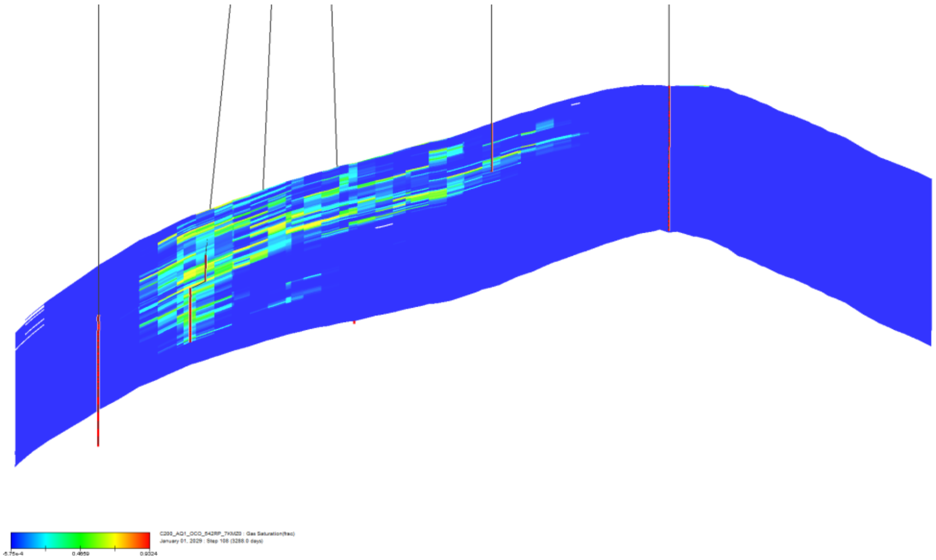

It must be stressed there is little geological evidence for either of the barrier cases presented here, horizontal or vertical; there is evidence for barriers in the Caister Bunter field. That said, most reservoirs are usually found (late in the field life) to be more heterogeneous than first thought.

4.6.13.4 Impact of Relative Permeability data on Model Behaviour

The behaviour of the mid-case Ketzin data (dashed lines) is compared with that of the Endurance relative permeability data (solid lines) in Figure 4.68, which shows the CO_2 saturation and pressure at the crest of the structure. The difference in the pressure response was predicted to be minimal. The asymptotic value of CO_2 saturation was higher for the Endurance data because of the low irreducible water saturation for Endurance at the crest of the structure where the CO_2 is pooling.

One of the interesting results is the delayed arrival of CO_2 at the crest (by 3 months) when using the measured Endurance data set compared to the Ketzin data set. This has been attributed to the CO_2 Corey exponent for the Endurance data ($N_g = 2.5$) being higher than that used in the Ketzin data ($N_g = 1.5$). The Corey exponents control the curvature of the relative permeability curve and comparing Figure 4.41 for the Ketzin data and Figure 4.39 for the Endurance data the CO_2 relative permeability can be observed to be lower for the Endurance data when the CO_2 saturation is less than 50% because of the increased curvature.

Figure 4.68: Crestal CO_2 Saturation & Pressure versus Relative Permeability Set

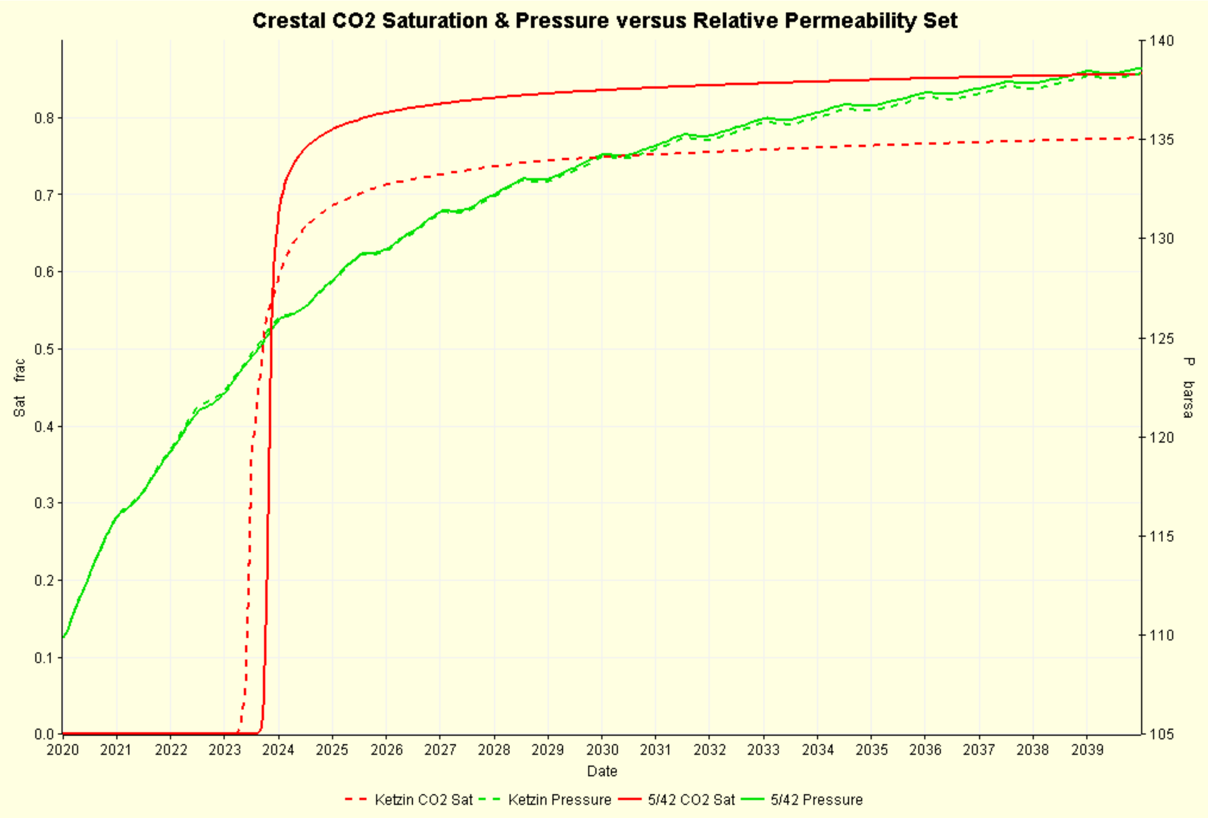

The CO_2 saturation after 20 years of shut-in (following 20 years of injection) along the WNW-ESE cross-section is shown in Figure 4.69 using the Ketzin data and in Figure 4.70 using the Endurance data; note both figures use the same range of 0.01 to 0.85 hence most cells are greyed-out, i.e. zero CO_2 saturation.

Figure 4.69: CO₂ Saturation Cross-Section after 20 years of Shut-In: Ketzin Rel Perm

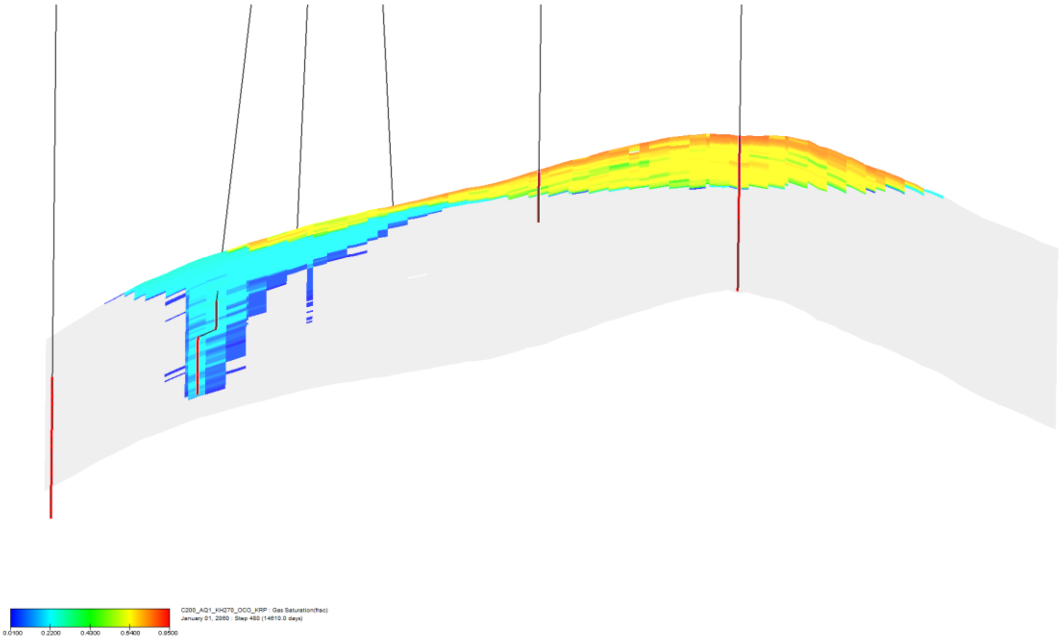

Figure 4.70: CO₂ Saturation Cross-Section after 20 years of Shut-In: Endurance Rel Perm

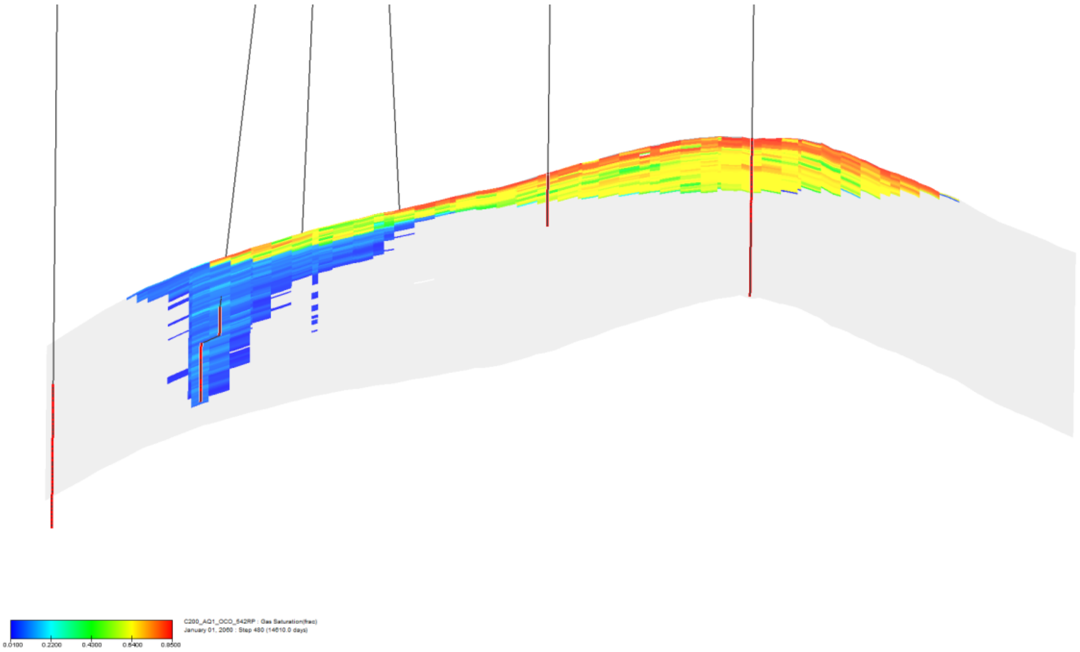

Note the shape of the plume is very similar. What differs of course is the trapped gas saturation which is lower using the Endurance data as shown by the darker blue colours in the vicinity of the injection wells. Whilst there appears to be significant differences between the analogue Ketzin and measured Endurance relative permeability data, in terms of the overall model performance there is little difference between the two.

4.6.13.5 Maximum Gas Relative Permeability

In Figure 4.51 the maximum gas relative permeability is shown as being K_{rg}^{M} = 0.85; this has been taken as the mid-case value. Low and high values have been set to 0.5 and 1.0, respectively, and the resulting crestal CO_2 saturations are shown in Figure 4.71. The effect is as expected and it replicates the changes seen by varying K_H and K_V/K_H.

Figure 4.71: Crestal CO_2 Saturation versus Maximum-Krg

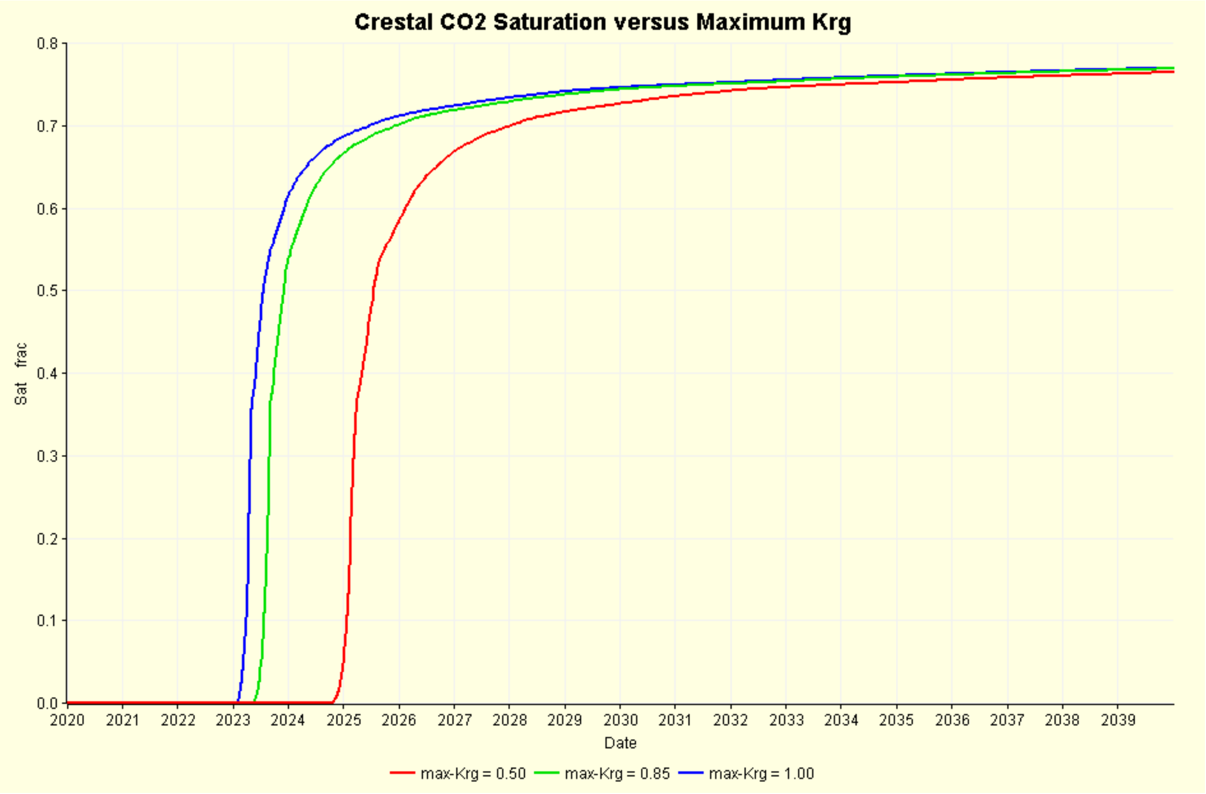

There is a change in the maximum pressure increase seen at the crest but the difference between the 0.50 and the 0.85 and 1.00 cases is less than 2.0bar.

4.6.13.6 Drainage Critical Gas Saturation

The default (mid-case) drainage critical gas saturation S_{gc} has been set to 0.05 from Table 4.13. For a low case S_{gc} = 0.0 and a high case S_{gc} = 0.1. The resulting crestal CO_2 saturation profiles are shown in Figure 4.72. Clearly setting S_{gc} = 0.0 means the CO_2 does not have to wait in a grid cell for its saturation to rise before it is free to move onto the next grid cell. This sensitivity has no discernible effect on the maximum pressure increase.

Figure 4.72: Crestal CO_2 Saturation versus Drainage Critical Gas Saturation

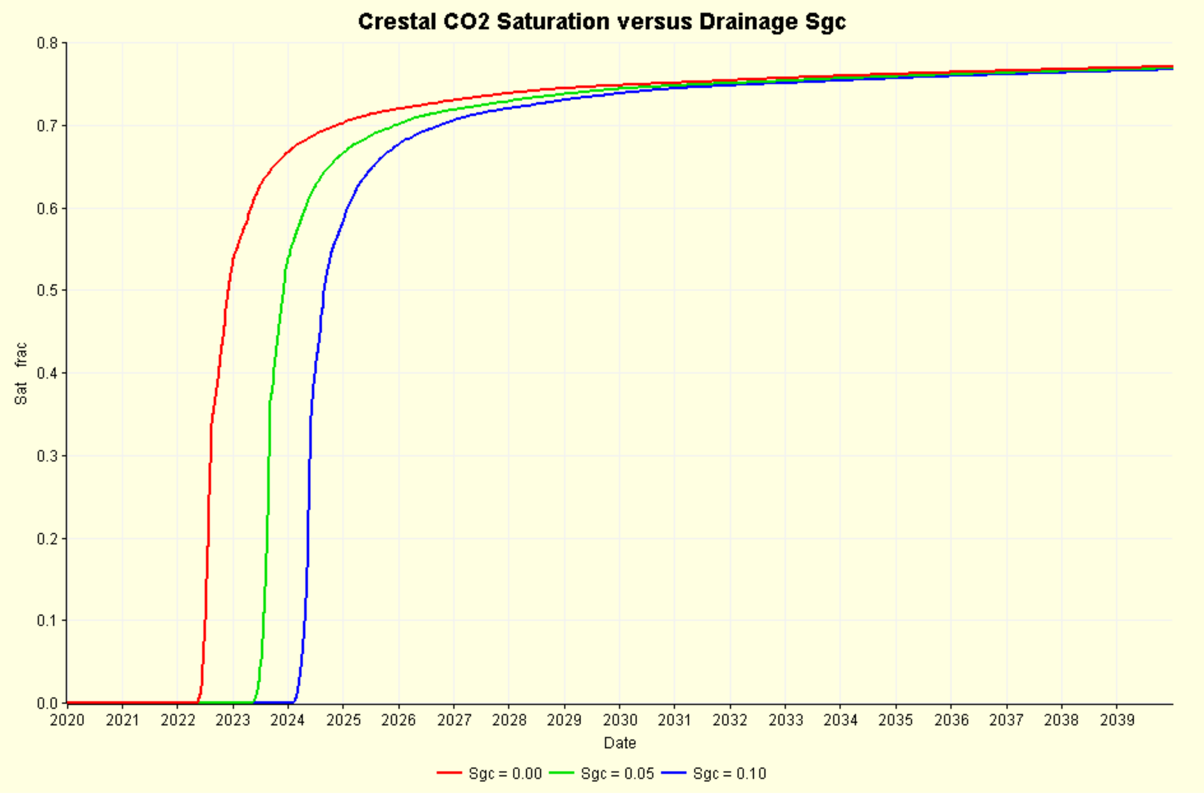

4.6.13.7 Imbibition Critical Gas Saturation

The mid-case value adopted in Table 4.13 has been S_{gt} = 0.30; low and high case values were 0.20 and 0.40 respectively. There was no discernible difference in crestal pressure increase or CO_2 arrival time as a result of this sensitivity.

4.6.13.8 Critical Water Saturation

The drainage (and imbibition) critical water saturation S_{wc} quoted in Table 4.13 was 0.15. For sensitivity to critical water saturation the mid-case S_{wc} used was 0.118. Low and high case values of 0.05 and 0.20 were selected and the resulting crestal CO_2 saturation profiles are shown in Figure 4.73.

Varying this parameter does not affect the time at which the CO_2 reaches the crest, rather it changes the maximum saturation $S_g = 1 - S_{wc}$. There is no effect on the pressure change from this sensitivity.

Figure 4.73: Crestal CO_2 Saturation versus Critical Water Saturation

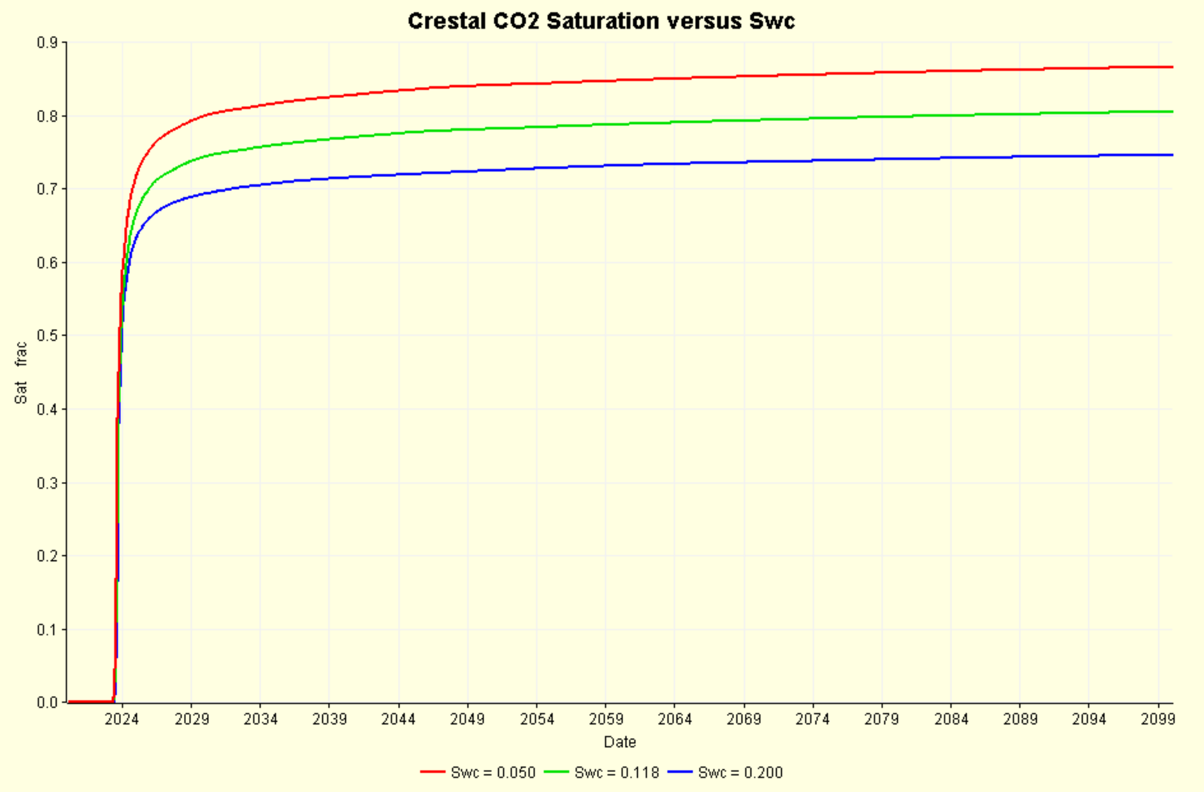

4.6.13.9 Reservoir Location of White Rose CO_2

The downhole (reservoir) volume occupied by the White Rose CO_2 mass of 53.6 MT of CO_2 (being 2.68MTPA for 20 years) is predicted to be 84.9×10^6 m^3 from the mid case model. Assuming no dissolution or residual trapping and a critical water saturation of $S_{wi} \approx 0.15$, the pore volume required to store this volume is about 100×10^6 m^3.

Figure 4.74: WNW-ESE Depth Cross-Section through the core of Endurance

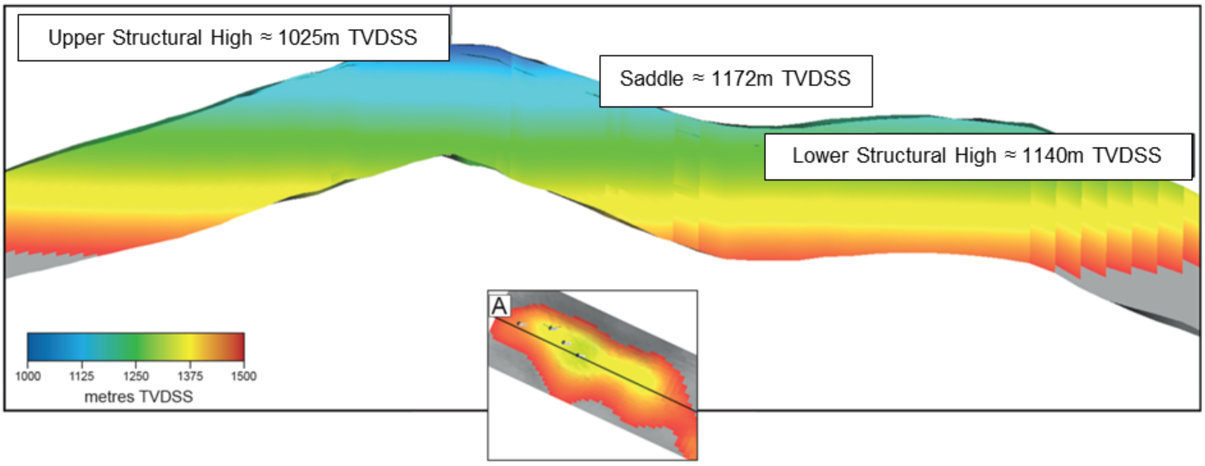

Figure 4.74 shows a cross-sectional depth display along the spine of Endurance. Note the depth of the upper peak (corresponding to the location of the 43/21-1 exploration well), the depth of the lower peak and the saddle between them. The pore volume contained in the upper peak to the spill at the saddle depth of 1172 mTVDSS is 362x10^6 m^3, i.e. 3.6x larger than the White Rose volume. So, consideration is given here to whether there is any way CO_2 can get to any part of Endurance other than the upper peak given the current injection locations to the NW of the structure.

It is pertinent here to consider Darcy's Law applied in the vertical direction:

Equation 4.10

$$v_z = \frac{K_V K_{rC}}{\mu_C} \frac{dP}{dZ}$$

Here the effect of capillary pressure and gravity head has been ignored, v_Z is the vertical velocity (in m/s), K_V is the vertical permeability (in m^2), K_{rC} is the CO_2 relative permeability, μ_C is the CO_2 viscosity and dP/dZ is the vertical pressure gradient.

The pressure gradient is driven by the density difference between the native brine of $\rho_B \approx 1170$ kg/m^3 and the CO_2 density in the reservoir which varies between $600 \leq \rho_C \leq 800$ kg/m^3; a mid-case density of $\rho_C \approx 700$ kg/m^3 is assumed here to give a density gradient of $dP/dZ \approx (\rho_B - \rho_C).g = (1170 – 700)$ (9.81) = 4610 Pa/m (0.0461bar/m).

The average vertical permeability can be estimated from $K_V = K_H (K_V/K_H) = (271) (0.15) (10^{-15}) = 41 \times 10^{-15}$ m^2, where $K_V/K_H \approx 0.15$, $K_H \approx 271$ mD, and 1 mD $\approx 1 \times 10^{-15}$ m. At typical reservoir conditions the CO_2 viscosity $\mu_C \approx 0.06 \times 10^{-3}$ Pa.s.

The vertical velocity of CO_2 can then be estimated to be $v_Z = 3.15 \times 10^{-6} K_{rC}$ m/s, where K_{rC} is the maximum CO_2 relative permeability which when set to 0.85 gives $v_Z = 2.68 \times 10^{-6}$ m/s. The injection rate of 2.68MTPA is equivalent to a reservoir conditions volumetric rate of 11,500m^3/d or $Q = 0.133$ m^3/s. Therefore the horizontal velocity will be $v_H = Q/(2\pi RH)$ where R is the radial distance from the well where the velocity is being calculated and H is the perforated length through which the fluid is being injected. With the injection wells being deviated 60^o from the vertical, the perforated length in the reservoir is about 250m so that $v_H \approx Q/(1500\ R) = 90 \times 10^{-6}/R$ m/s. Therefore, at around 30m from the injection wellbore the (near-constant) vertical velocity will always exceed the falling horizontal velocity so even if one or more of the wells intersected an extremely high permeability streak, the CO_2 cannot avoid its ultimate fate of pooling under the upper peak. A further reinforcing consideration is that the injection rate of 2.68MTPA is a maximum value (of flow from the power station) unlikely to be reached in practice for any extended period of time.

4.6.14 Injectivity

One of the key objectives of the flow test performed on 42/25d-3 appraisal well was to assess injectivity. The test (summarised in Section 4.3.1) demonstrate that injection at the specified rates would be possible over the perforated interval although the large pressure spike observed about 1200 s after the start of injection give cause for caution. The timing is significant as it corresponds to the time required for the sea-water from the surface to reach the perforations (at 795 m^3/d) given the Internal Diameter (ID) of the well tubing.

The pressure spike is thought to have been caused by some contamination carried with the injected sea water. The pressure spiked until a fracture was created and as the injection test continued, and the rate was increased in two further increments, the effect of the blockage was gradually reduced. There is a possibility that the blockage was caused by an interaction between the native brine and the sea-water or as a temperature effect.

4.6.14.1 CO_2 Injection Wells Injectivity

To maximise the opportunity for residual trapping as well as keep colder CO_2 away from the cap rock it is proposed to perforate the lower half of the three injection wells drilled from the P5 platform location. One downside of the lower half perforation strategy is the quality of the BSF degrades with depth so that while porosity at the top of the Bunter often exceeds 0.25, at the bottom of the Bunter it can be less than 0.15, with consequent effect on permeability via Equation 4.4. This has been investigated using the simplified injection model developed in Section 4.6.10.

Equation 4.11 $$Q = I_I \Delta P$$

In Equation 4.11 ΔP is the (depth corrected) pressure difference between the BHP and (average) reservoir pressure into which the (total) rate Q is being injected and I_I is the Injectivity Index.

To assess injectivity two simulations were performed with one having the well shown in Figure 4.68 perforated through the whole of the Bunter sandstone and the other having the well just in the lower half. The resulting well Injectivity Index for the two cases is shown in Figure 4.75.

The units for II in Figure 4.75 are m^3/day/bar which E100 does not append to the outputted property. After the transient (pressure and saturation) changes have declined, the pseudo-steady-state II is over three times lower for the case where the whole well has been perforated.

The variation of BHP however needs to be considered in conjunction with the differences in Injectivity Index. In Figure 4.76 the BHP variations for the three CO_2 injection wells are shown for the mid-case model. Note the cyclic nature of the wells which are injecting half the total rate of 2.68MTPA for 12 months out of every 18 months (see Section 4.6.11.3 for summary of well switching scheme).

The transient spike in BHP at the start of each well’s 12-months of injection is a relative permeability effect. In the grid cells containing the well completions, the CO_2 saturation and hence the CO_2 relative permeability is low initially. This in turn means the mobility is small and a high pressure difference is required to achieve the desired flow rate. The transient spike is almost the same on the first injection cycle for all three wells. All the wells see an increase in the transient pressure on the second cycle of injection. Thereafter the transient pressure for P5DEV2 is greater than P5DEV3 which is greater than P5DEV1.

Figure 4.75: Well Injectivity Index in Simplified Model

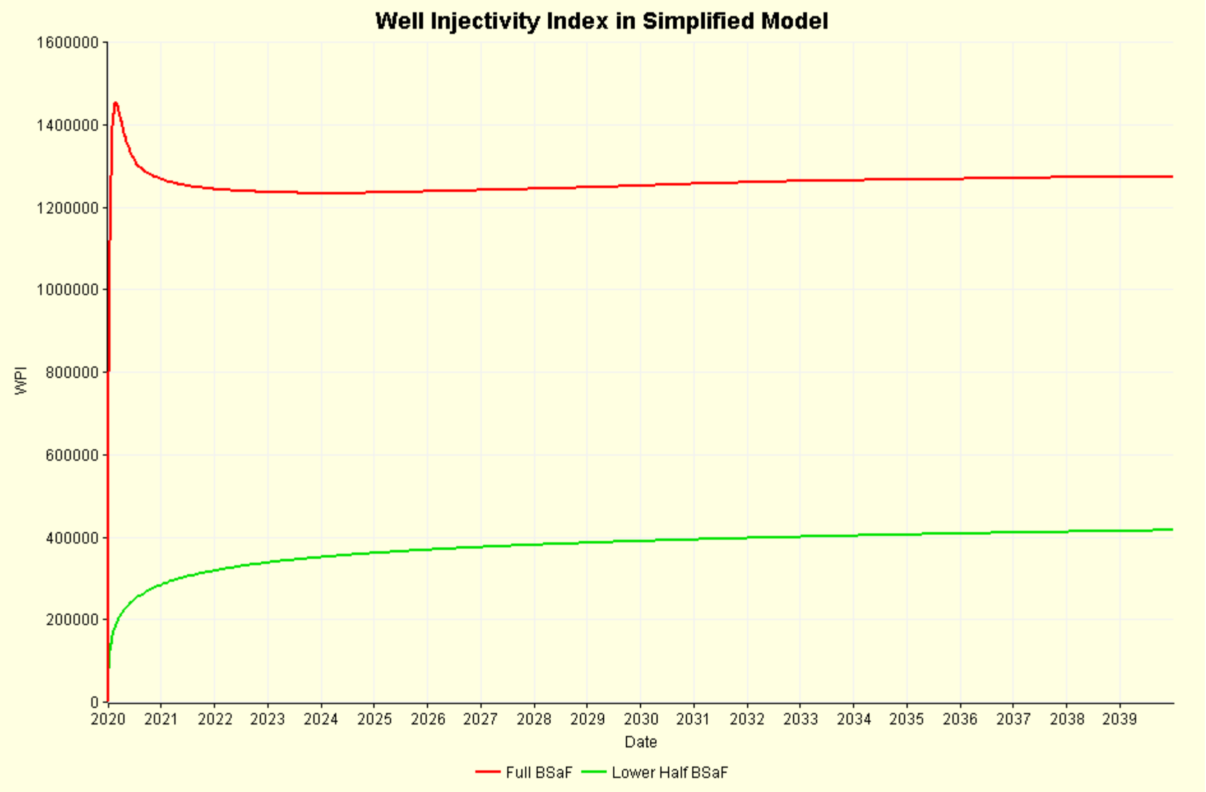

The jump in the transient pressure spike between the first and second cycles of injection was because in the six months period that the well is shut-in, the buoyant CO_2 migrates up-structure and fresh brine imbibes into the vicinity of the shut-in well, trapping CO_2 at a saturation of about $S_{gt} = 0.30$. When CO_2 injection resumes, a new drainage (of the brine) phase begins but with a lower effective CO_2 relative permeability and hence the need for a larger BHP to achieve the required flow rate. After the third and fourth cycles the pattern settles down. Note that the Ketzin Kr data (Figure 4.41) which incorporates the extreme limit of S_{gt} was used for this simulation. In contrast the measured Endurance Kr data (Figure 4.39) has in contrast S_{gt} ~ 0.10 which would likely cause a smaller change in CO_2 mobility after fresh brine imbibition and hence reduce the pressure spikes predicted in Figure 4.75.

The differences between the BHP responses of the three wells are due to their relative locations and the way in which CO_2 and brine move during the 12-month injection period and 6-month shut-in period of each well. CO_2 injected in P5DEV1 and P5DEV3 migrates upward in the plane of the wells before heading toward the crest, thereby leaving higher CO_2 saturation behind, whereas the CO_2 injected in P5DEV2 move tangentially away from this well's trajectory toward the crest (Figure 4.75 and Figure 4.78).

Figure 4.76: BHP Variations from Mid-Case Model

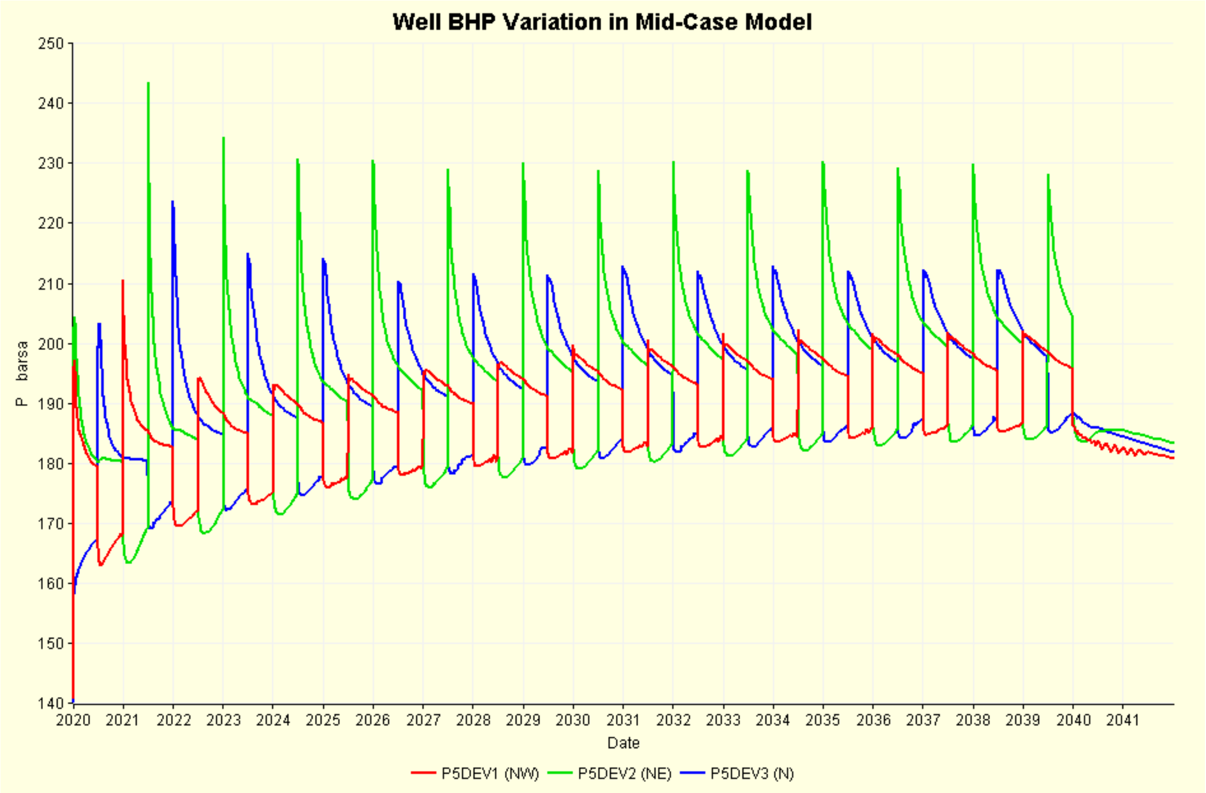

Figure 4.77: Line of Cross-Section through Injection Wells

Figure 4.78: – CO_2 Relative injectivity shown on Cross-Section Defined in Figure 4.77

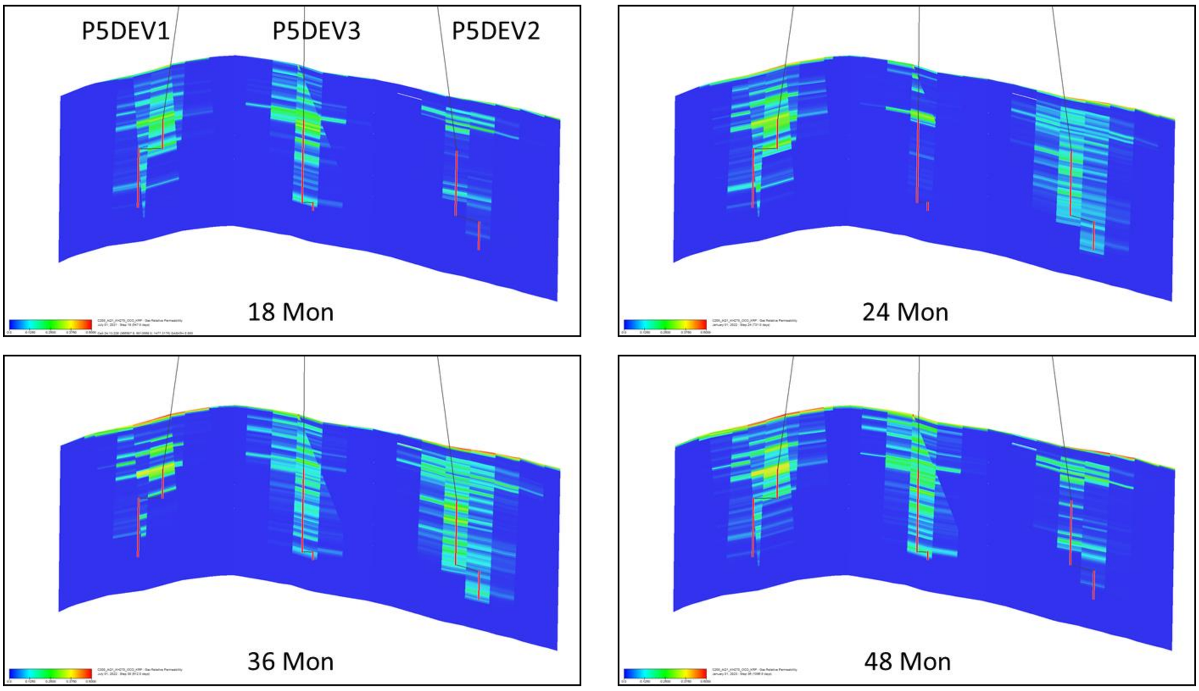

4.6.14.2 Skin Factor

The default skin applied to all the wells is zero. There is a case to suggest that the skin in the actual wells could be negative as a result of thermal fracturing caused by relatively cold CO_2 cooling the rock in the near wellbore – note that the perforation strategy will prevent any thermal fracturing near the Röt Clay caprock by confining perforations to the deeper zones of the Bunter formation. Alternatively, positive skin may result due to mechanical blockage as was seen in the injection phase of the 42/25d-3 well test. For the purposes of understanding the range of possible effects a beneficial case has been simulated using a skin of S = -2 applied to all perforations whereas a detrimental case has been simulated using S = +5; the mid-case being S = 0.

There is no effect of changes in skin (of the range of magnitudes investigated) in terms of the crestal pressure increase or the time taken for the CO_2 to reach the crest of the structure. Skin clearly has an effect on well BHP and the difference is shown in Figure 4.79 for the P5DEV1 only. The other two wells show a similar response.

The beneficial effect of the negative skin (red line) is relatively modest but again it must be stressed the value of S = -2 has been assessed based on experience of realistic negative skins rather than detailed modelling.

The detrimental effect of the positive skin (blue line) is potentially of more concern as the assessed value of S = +5 is not considered particularly high and yet the second cycle transient response is close to the maximum pressure that would be tolerated to avoid hydraulic fracturing.

Figure 4.79: P5DEV1 BHP versus Skin-Factor

4.6.15 Temperature Effects

The simplified injection model was used to examine how temperature profiles within Endurance might change as a result of injection of cold CO_2.

The CO_2 will be transported to Endurance via a 90km 24” pipeline and so will cool to the seabed temperature which will vary between 5°C and 15°C winter to summer. Using the steady-state Prosper modelling, it is estimated that the CO_2 will heat by about 10°C between wellhead and the perforations meaning the lowest sandface temperature is estimated to be 15°C compared with a reservoir temperature of about 55°C, see Figure 3.53 (the specified CO_2 injection wells are up-structure of 42/25d-3).

Two cases of the simplified injection model have been considered here. The first considers the whole Bunter interval is perforated so see the effect of putting cold CO_2 against the cap rock, see Figure 4.80. The second case is thought to be more likely as only the lower half of the well has been perforated, see Figure 4.81.

Figure 4.80: Temperature Cross-Section after 20 years, All Bunter Perforated

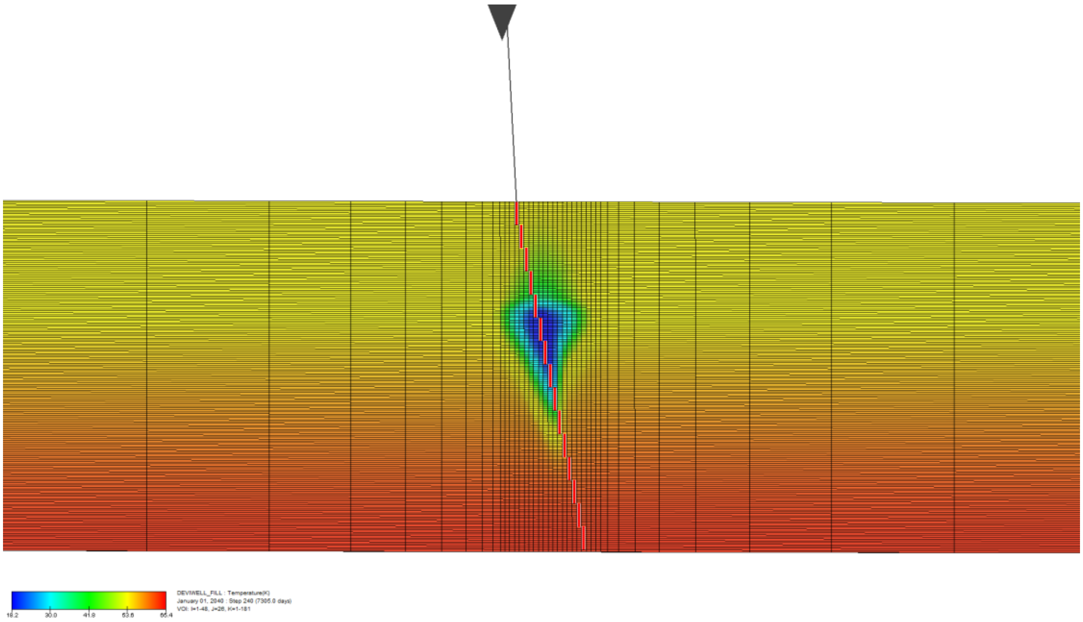

Figure 4.81: Temperature Cross-Section after 20 years, Lower Bunter Perforated

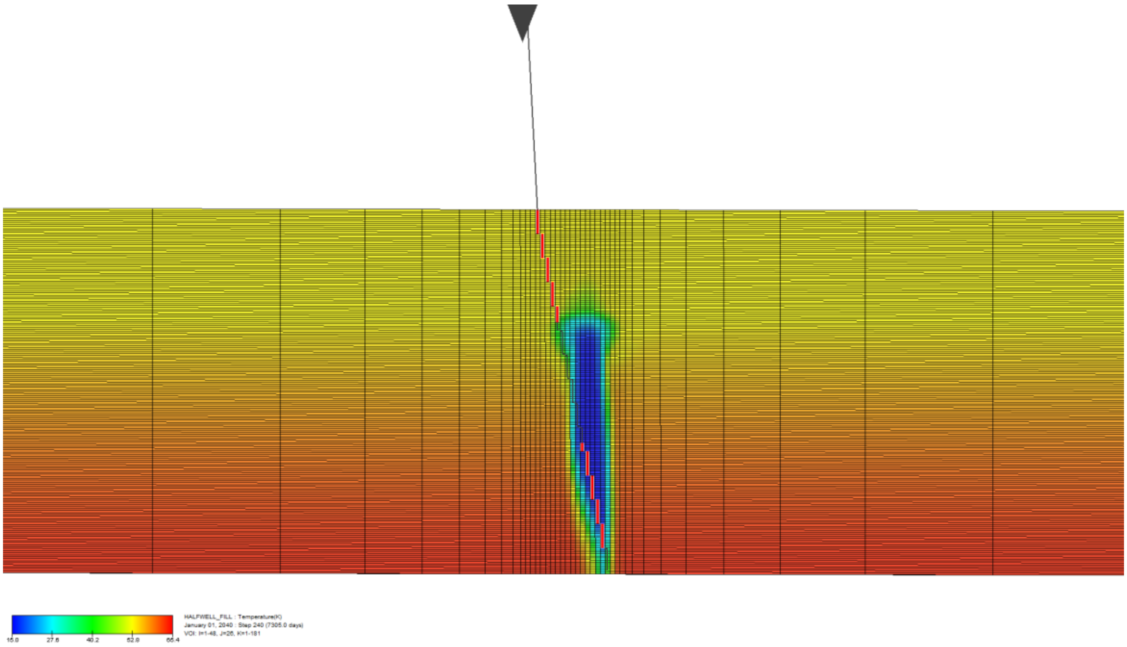

The convective cooling effect of placing cold CO_2 against the cap rock is felt immediately if the top of Bunter sandstone is perforated as is seen in Figure 4.80. This should be compared with the gradual cooling that would be achieved by injecting deeper in the Bunter sandstone. With reference to the detailed simulation models it is noted that the CO_2 takes between 6 to 12 months to flow from top perforation to the cap rock. Therefore the 20 year profile shown in Figure 4.81 would take many months to develop in practice.

4.7 Simulation of the Diffusion-Dissolution-Convection (DDC) process

The four main CO_2 trapping mechanisms during CO_2 sequestration include:

- structural trapping in which CO_2 accumulates beneath an impermeable caprock;
- residual trapping in which part of the migrating CO_2 plume gets detached and ultimately trapped by capillary forces;
- solubility trapping in which both structurally and residually trapped CO_2 dissolves in the brine via diffusion and convective processes; and
- mineral trapping in which the dissolved CO_2 reacts with the brine and the host rock to produce solid minerals.

Section 4.6 has already dealt with structural and residual trapping and Section 3.9.2 with mineral trapping. Only the characterisation of solubility trapping has not been presented so far.

The full field simulation approach used in the prediction of CO_2 plume development, specifically the use of analytical aquifer models, does not permit direct modelling of the dissolution of CO_2 in brine under dynamic flow conditions. An alternative scheme that uses a 2D XZ sector model of Endurance has therefore been used to quantify solubility trapping and thereby gain a better insight into the long term fate of White Rose CO_2.

4.7.1 DDC Process Overview and Simulation Model Set Up

CO_2 dissolution in brine occurs by molecular diffusion across the CO_2-brine interface and this process would take place wherever a CO_2-brine interface exists i.e. both CO_2 trapped by capillary forces and CO_2 trapped under the cap rock will undergo dissolution over time. Since the Endurance relative permeability measurement suggests that less than 10 % of White Rose CO_2 is likely to be trapped in residual form, the DDC modelling has focused on dissolution of the CO_2 cap at the crest of the Endurance structure.

Dissolution of CO_2 increases the brine density (by approximately 2.5 kg/m^3), creating a denser brine layer below the plume. This layer eventually becomes gravitationally unstable so that fingers of dense CO_2-rich brine propagate downward and transport the aqueous CO_2 away from the interface. This density-driven convection increases the rate of mass transport from the free CO_2 phase into the brine phase and is typically orders of magnitude faster than pure diffusion.

The E100 black oil simulator with the diffusion option has been used for modelling the DDC process. The grid is a 2D XZ sector model of Endurance, 2500m × 200m across and consisting of 100, 000 cells (Figure 4.82). The central portion (500m) of the model is assumed to capture the extent of the CO_2 plume predicted by the full field model (Figure 4.82a). The left and right hand sides are for the reservoir section outside the CO_2 plume footprint area. The simulation model is given a dip angle of 2.3^o by varying the depth of cells on the left and right hand sides at the top layer as shown in Figure 4.82. The key parameters for this model are:

- Cell number (N_x, N_y, N_z) = (500, 1, 200);
- $\Delta X = 5$ m;
- $\Delta Y = 3000$m; and
- $\Delta Z = 1$ m.

The top layer of the model is used to represent the CO_2 plume in the crest of the reservoir structure at a depth of 1299 mTVDSS. Using a pore volume multiplier of 20, the top layer has a free CO_2 initially in place of 2.24 billion sm^3, which is about 1/10th of the CO_2 at the crest of Endurance at the end of injection. The 2D sector model is therefore considered scalable to the CO_2 storage in Endurance.

Porosity and permeability were distributed across the model in the manner described in Section 4.6.2.2. Firstly porosity was defined as a linear function of depth with a value of 0.27 at the top and 0.14 at the base. Then horizontal permeability was defined from Equation 4.4 with an approximate value of 2020mD at the top and 19 mD at the base of the model. Additionally, a small random variation in permeability is applied to initiate the development of the dense brine fingers. Fluid and rock properties pertinent to the simulation are listed in Table 4.18. The PVT inputs (viscosity, solubility, etc) are generated based on the correlations found in the technical literature.

Figure 4.82: Construction of the DDC model

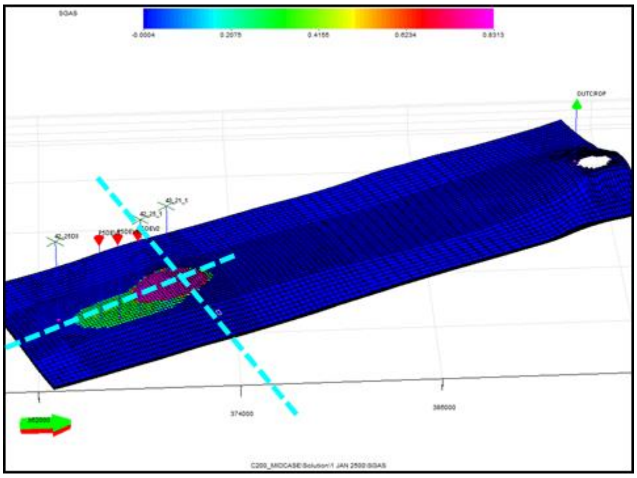

(a) Full Field Model

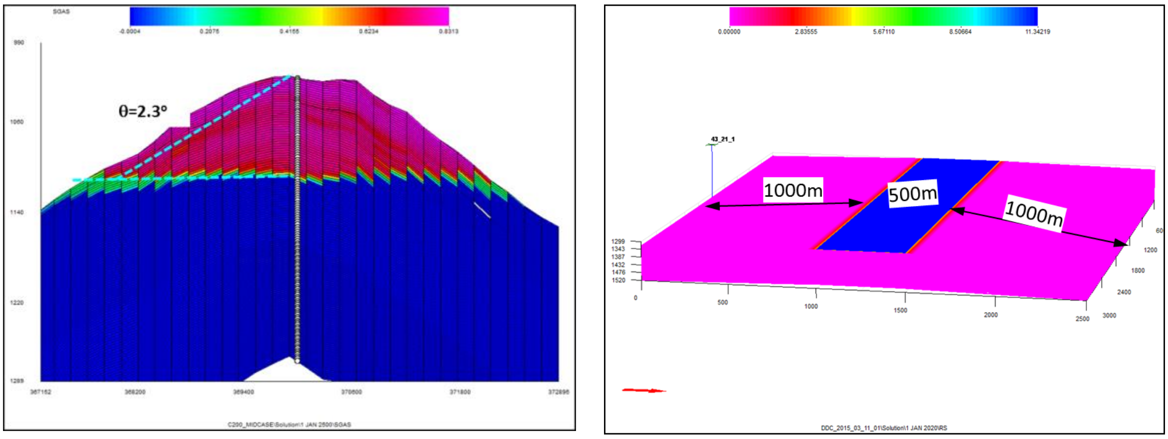

(b) 2D Slice, X-Direction

c) Full DDC model

Table 4.18: Critical Parameters of DDC Using Typical Bunter Properties

Parameter/Attribute		unit	
Temperature	56	C	
Reservoir pressure	141	Bar	
Salinity	250, 0000	Mg/kg	
Viscosity	$9.0x10^{-4}$	Pa.s (kg/s/m)	0.9 cP
Diffusion coefficient	$2.0x10^{-9}$	m^2/s	
K_V/K_H	0.15		

4.7.2 DDC Simulation Results

The CO_2-in-Brine concentration (in m^3 of CO_2 per m^3 of brine, both at standard conditions) is shown in Figure 4.83. The eight cross-sections are shown at 01/January/YYYY where YYYY is the year shown.

The onset of convective fingers is discernable 100 years post injection. The process starts out with multiple fingers which then broaden and coalesce as CO_2-laden brine propagate downward whilst the lighter brine flows upward, a phenomenon that has been widely reported by several researchers.

The plume of saturated brine does not reach the base of the model until 01/Jan/12000, i.e. about 10,000 years after the cessation of injection, at which time about 25% of the initial CO_2 in place had dissolved.

Figure 4.83: CO_2-in-Brine Distribution at Stated Years

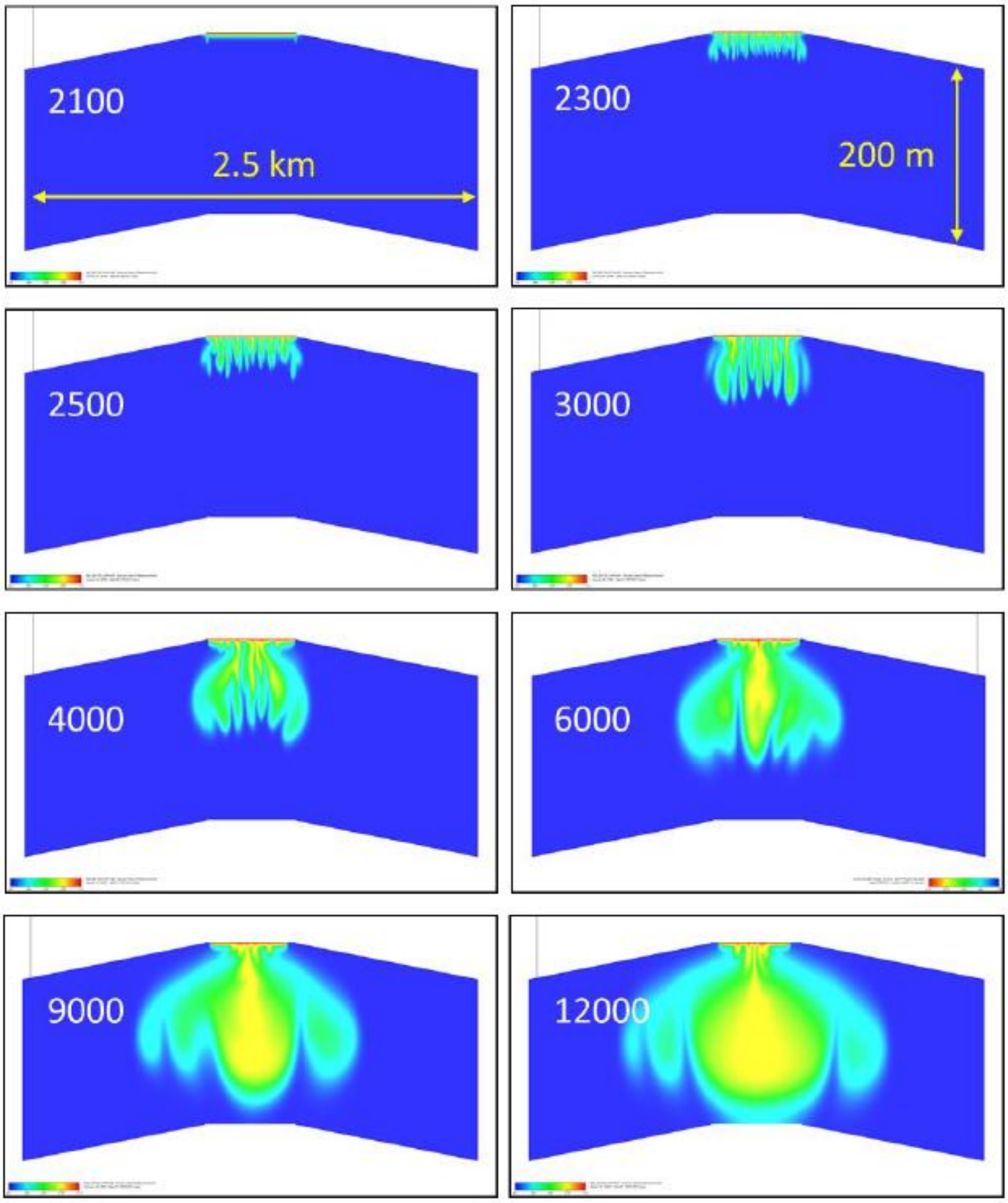

4.8 Possible Influence and Effects on Regional Hydrocarbon Developments

Hydrocarbon developments in the SNS that are likely to be influenced by CO_2 injection into Endurance are fields producing (or that previously have produced) gas from the BSF. Table 4.19 shows the production data from the eight gas fields within the potential regional area of influence around Endurance and Figure 4.31 their locations. As gas is produced from a gas reservoir and the reservoir depressurizes, water encroaches from the underlying aquifer into the reservoir to provide pressure support. Any process that increases the pressure of the underlying aquifer such as CO_2 injection will increase this pressure support. Although the gas fields listed in Table 4.19 produce wholly or partly from the BSF, only a subset (Esmond, Caister-Bunter, Forbes & Gordon) show evidence of hydraulic connectivity to a shared aquifer with Endurance and close enough to receive any significant transient pressure support from CO_2 injection into Endurance.

The Hewett field is the dominant producer but only 35% of its production comes from the BSF (the rest is from Hewett Sandstone and Zechstein Carbonates). Moreover, water influx into the Hewett BSF interval has been shown to be limited due to local faulting in this area and this applies also to the Little Dotty reservoir. Both Hewett and Dotty are therefore probably not in hydraulic communication with Endurance.

Figure 4.31 shows that Orwell is located just south of the Cleaver Bank Zone where the Bunter Sandstone is partially eroded; thus limiting any potential pressure communication with Endurance. Data on the dynamic behaviour of the Hunter field is not available and would probably be of little value in properly assessing its hydraulic connectivity to Endurance given the insignificant production from this field relative to other fields within the regional area of influence.

To summarise, the influence of CO_2 injection into the Endurance Storage Site upon regional hydrocarbon developments is likely to be non-existent or immeasurably small. The gas fields that share a common aquifer with Endurance have either ceased producing or have too weak hydraulic connectivity to the sector of the Bunter aquifer within the potential regional area of influence to receive any measureable pressure communication with Endurance.

Table 4.19: Cumulative Production from Bunter Gas Fields

Field	Cumulative Gas Production to 2013 Msm^3	Date Production Ceased
Caister-Bunter	3,202	-
Esmond	8866	Mar 1995
Forbes	1473	Feb 1993
Gordon	3994	Feb 1995
Hewett[1]	122,378	Still Flowing
Hunter	41	-
Little Dotty[2]		
Orwell	8618	Jan 2000

Hewett Field has reservoirs in Upper Bunter (BSF), Lower Bunter or Hewett Sandstone and Zechstein Carbonates. Little Dotty production is via Hewett 48/29-A platform.

5 Geomechanical and Fracture Pressure Analysis

This section summarises the modelling workflow used to build the Geomechanical Model (GM) of the Endurance Storage Complex and this models use to assess the effect of dynamic pressure and temperature responses on the stress, deformation, and failure properties and behaviour of the Endurance Storage Complex during and at the cessation of White Rose CO_2 injection. It also summarises the methodology and results contained in the full geomechanical modelling report and some of the stress measurement data presented in the initial geomechanical data report.

5.1 Geomechanical Modelling Summary

Geomechanical modelling has been performed to assess the geomechanical integrity of the Endurance structure during and after the injection of White Rose CO_2. The modelling utilised the Petrel Geomechanics / Visage software. A grid over the structure was generated with layering from the underlying Zechstein salt up to the seabed and was populated with properties derived from log and geomechanical core test data some of which has been modified based on other published sources. The key issues investigated include:

The modelling incorporated simplified pressure increases based on the White Rose CO_2 injection scheme of 2.68MTPA (as a maximum) for 20 years.

The potential for fault related failure was addressed by modelling the mapped overburden faults with three different sets of fault properties (Strong, Weak and Very Weak). In addition one crestal fault was extended (i.e. shifted downwards) so that it intersected the upper Bunter Sandstone layers to simulate the possibility of a sub-seismic fault intersecting the Bunter. It should be noted this scenario is not a situation which has been seen on seismic but has been run as a potential worst case scenario.

For each case, the geomechanical model in-situ stress system was modelled in stages with three optimisation runs; two to match the 42/25d-3 Röt Clay and Bunter Sandstone minifrac data and a third run to optimise isotropic lithostatic salt stresses. These three separate property sets were combined into concatenated total stress models for use in the main modelling cases.

For the White Rose CO_2 the main conclusion is that there is little risk of significant strain and/or failure of the Röt Clay and Röt Halite seals as a consequence of Endurance structure being subject to the predicted pressure and temperature changes.

In order to assess worst case conditions, two cases were created to check the point at which the model would indicate noticeable strain or yield failure.

1. Weak and Very Weak faultrocks with a fault extended into the upper part of the Bunter Sandstone resulted in minor increased strain and localised displacement in the overburden and in the upper Bunter Sandstone layers. Extended faults have not been mapped from seismic and the Very Weak faultrock is regarded as highly unlikely; and
2. cooling of the Röt Clay and Röt Halite above a simplistic CO_2 plume leads to tensile failure (fracturing) of some Röt Halite cells immediately above the plume. The Röt Clay and clay rich Röt Halite however do not show this tensile failure. To reiterate, the degree of cooling modelled is very unlikely and the slower process of conduction would dominate over convection unless there is already a leak pathway.

5.2 Geomechanical Modelling Description

The structural models and the rock mechanics test results from the 42/25d-3 appraisal well have been used as input. The modelling was large scale in that the grid had 200m x 200m cells and covered the whole structure from Zechstein halite to seabed with some additional side volumes for geomechanical boundary condition compliance. The key issues investigated were as follows:

1. investigation of optimal rock properties for modelling incorporating previous NGC work plus recent FracTech core test results from the Röt Halite, Röt Clay and Bunter Sandstone in 42/25d-3;
2. stress initialisation in the Röt Halite, Röt Clay and Bunter Sandstone at virgin pressure conditions calibrated to the 42/25d-3 Röt Clay and Bunter Sandstone minifrac data;
3. overburden uplift during and at the end of injection using one way coupled runs from four pressure steps (initial, +5 years, +10 years, +20 years);
4. impact of cooling at the injection site on the stresses and strains; and
5. Potential tensile fracturing, shear fracturing and fault reactivation in the Röt Clay and shallower levels.

Fully coupled (Visage-Eclipse) simulations that would modify the reservoir and overburden permeabilities due to decompaction, tensile fracturing or fault reactivation have not been performed as they have a relatively low probability of occurrence with the First Load (White Rose) injection rates and associated pressures.

5.3 42/25d-3 Formation Integrity Test (FIT) and Minifrac Data Analysis

These data were acquired from three intervals and are summarised in Table 5.1 below:

Table 5.1: 42/25d-3 FIT and minifrac data

Unit	Depth mTVDss	Sh bar	Sh bar/m	Sh psi/ft	Regional SH/Sh	Type
Röt Halite 1	-1339	214	0.160	0.727	-	FIT
Röt Clay	-1363	264	0.194	0.856	1.20	Minifrac
Bunter Sandstone	-1520	262	0.172	0.762	1.15	Minifrac

The Röt Halite FIT showed no indications of leak-off or fracturing and the actual stresses are likely to be closer to lithostatic within the purer halite layers (~0.24bar/m). The minifrac data from the Röt Clay and Bunter Sandstone (Figure 5.1and Figure 5.2) are high quality measurements based on five cycles of breakdown, pump-in and shut-in. The closure stresses (i.e. Shmin stresses) calculated on the last three iterations of these tests are consistent and regarded as accurate estimates of Shmin at the 42/25d-3 location. Note that the 13 $^3/_8$" casing shoe XLOT attempt in the Liassic Shales at 2447 ft BRT achieved a pressure of 0.195bar/m, which is very similar to the Röt Clay minfrac values. This implies good sealing potential in the shallow section clays in the absence of pre-existing weaknesses.

Figure 5.1: Röt Clay minifrac data from Schlumberger fracturing report

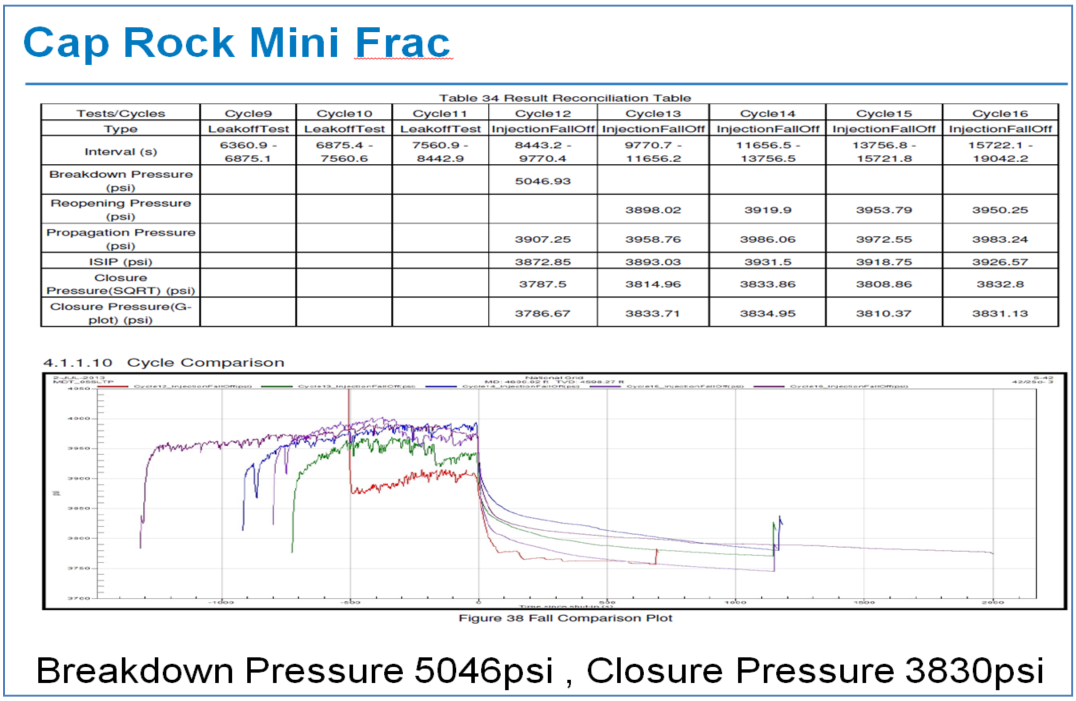

Cap Rock Mini Frac

Table 34 Result Reconciliation Table

Tests/Cycles	Cycle9	Cycle10	Cycle11	Cycle12	Cycle13	Cycle14	Cycle15	Cycle16
Type	LeakoffTest	LeakoffTest	LeakoffTest	InjectionFallOff	InjectionFallOff	InjectionFallOff	InjectionFallOff	InjectionFallOff
Interval (s)	6360.9 - 6875.1	6875.4 - 7560.6	7560.9 - 8442.9	8443.2 - 9770.4	9770.7 - 11656.2	11656.5 - 13756.5	13756.8 - 15721.8	15722.1 - 19042.2
Breakdown Pressure (psi)				5046.93				
Reopening Pressure (psi)					3898.02	3919.9	3953.79	3950.25
Propagation Pressure (psi)				3907.25	3958.76	3986.06	3972.55	3983.24
ISIP (psi)				3872.85	3893.03	3931.5	3918.75	3926.57
Closure Pressure(SQRT) (psi)				3787.5	3814.96	3833.86	3808.86	3832.8
Closure Pressure(G-plot) (psi)				3786.67	3833.71	3834.95	3810.37	3831.13

4.1.1.10 Cycle Comparison

Figure 38 Fall Comparison Plot

Breakdown Pressure 5046psi , Closure Pressure 3830psi

Figure 5.2: Bunter Sandstone minifrac data from Schlumberger fracturing report

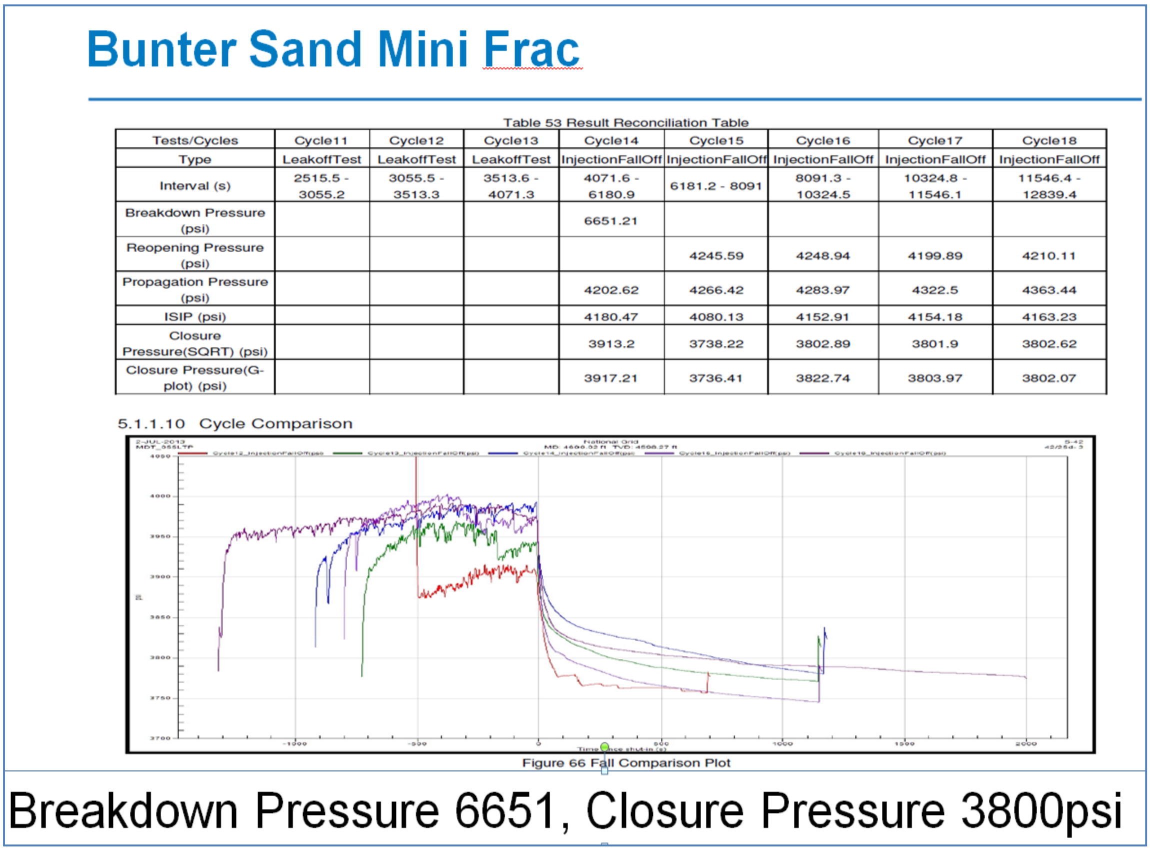

Bunter Sand Mini Frac

Table 53 Result Reconciliation Table

Tests/Cycles	Cycle11	Cycle12	Cycle13	Cycle14	Cycle15	Cycle16	Cycle17	Cycle18
Type	LeakoffTest	LeakoffTest	LeakoffTest	InjectionFallOff	InjectionFallOff	InjectionFallOff	InjectionFallOff	InjectionFallOff
Interval (s)	2515.5 - 3055.2	3055.5 - 3513.3	3513.6 - 4071.3	4071.6 - 6180.9	6181.2 - 8091	8091.3 - 10324.5	10324.8 - 11546.1	11546.4 - 12839.4
Breakdown Pressure (psi)				6651.21				
Reopening Pressure (psi)					4245.59	4248.94	4199.89	4210.11
Propagation Pressure (psi)				4202.62	4266.42	4283.97	4322.5	4363.44
ISIP (psi)				4180.47	4080.13	4152.91	4154.18	4163.23
Closure Pressure(SQRT) (psi)				3913.2	3738.22	3802.89	3801.9	3802.62
Closure Pressure(G-plot) (psi)				3917.21	3736.41	3822.74	3803.97	3802.07

5.1.1.10 Cycle Comparison

Figure 66 Fall Comparison Plot

Breakdown Pressure 6651, Closure Pressure 3800psi

5.4 Geomechanical Properties

The geometrical properties geomechanical core test programme are summarised below. The key properties modelled relate to the elastic responses for linear elastic simulations and the failure criteria for non-linear or plastic responses. The key difference being that elastic simulations produce recoverable strain up to the point of failure whereas non-linear or plastic simulations do not.

The various properties can be defined from dynamic measurements (based on compressive sonic, shear sonic and density logs) or static measurements (based on core plug tests). The two usually have different values due to a variety of factors:

- measurement timescale – very fast for dynamic and slower for static;
- applied loads – low for dynamic, high for static; and
- pore pressure conditions - undrained for dynamic and generally drained for static.

The available compressional and shear sonic slowness logs (µs/ft) were converted to velocity logs (m/s) and upscaled along with the density logs. Shear sonic was calculated from compressional sonic where the latter was not available; this usually provides an adequate estimate. The logs were distributed with conditioning to the matrix porosity as the applied rock property model was one of a relatively sharp increase in cementation with increasing depth within the Bunter and when moving from the crest of the structure to the flanks. A variety of standard equations were then used to convert these log values into the geomechanical parameters which are listed below:

▪ Shear Modulus (G)	calculated from density and shear velocity;
▪ Bulk Modulus (K)	calculated from density, compressional velocity and G;
▪ Young's Modulus of elasticity (E)	calculated from G and K; and
▪ Poisson's Ratio (□)	calculated from G and K.

For the VISAGE geomechanical modelling the E and □ values were modified to scale these to the core data results.

Failure Criteria:

- Unconfined Compressive Strength (UCS);
- Friction Angle (F);
- Dilation Angle (D); and
- Tensile Strength (T).

For the VISAGE geomechanical modelling the UCS and F and D values were checked and modified where necessary to scale them to the core data results.

Additional properties obtained from core measurements only or published data are:

- Linear Thermal Expansion Coefficient (LTEC);
- Salt creep responses (not used in the modelling); and
- Biot's Elastic Constant (α), which was assumed to be one in all units.

5.5 Geomechanical Modelling Process

The Petrel Reservoir Geomechanics package was used to model the Endurance structure Bunter Sandstone injection response. This package incorporates the VISAGE finite element geomechanical modelling simulator which can be fully coupled to ECLIPSE runs if required (albeit not used here). The VISAGE runs were run as one way coupled runs that used simple pressure and temperature properties at five different time steps (including pre-injection) to capture the geomechanical impact. Petrel Reservoir Geomechanics was run in a series of steps:

5.5.1 Make/edit geomechanical grid

Select an existing grid (the AOI) and add sideburden and underburden volumes plus stiff plates on the outer layer to properly initialise stresses within the AOI.

5.5.2 Material modelling

Define a library of rock materials with predefined geomechanical properties. These can be modified or added to.

5.5.3 Populate properties

Create regions within the grid with geomechanical properties selected from the library of rock materials. The properties can also be overwritten by properties within the grid which was done here so that the log / core derived geomechanical properties could be used. The log derived, core modified properties described in Section 5.4 was used in the models. Two variants were created:

1. Reference Case with a higher Young’s Modulus and lower Poisson’s Ratio in the Röt and Zechstein halites to match published halite rock experiments (i.e. a relatively stiff rock); and
2. Weak Halite case with a low Youngs Modulus and high Poisson’s Ratio in the Röt and Zechstein halites to simulate the weaker longer term behaviour that could occur in these units.

To some extent this second option is compensating in linear elastic failure modes for the fact that halite deforms by plastic creep over the months to years timescale when responding to load changes such as the presence of a wellbore or changes in reservoir pressure.

5.5.4 Discontinuity modelling

Faults and/or fractures were added to the grid as properties where they intersect the cells. This allowed computation of potential discontinuity related strain or reactivation via tensile or shear modes. Faults were encountered in the overburden only and these were modelled including a variant where one on the crest was moved partially into the Bunter Sandstone to simulate a sub-seismic fault in this unit. No fractures were modelled as few are believed to exist in this sequence. The faults were modelled with three main property variants as listed in Table 5.2.

Note NS = Normal Stiffness in bar/m and SS = Shear stiffness in bar/m.

Table 5.2: Fault Property Variants

Imported Fault material	Weak	NS: 500	SS: 200
Imported Fault material [1]	Very weak	NS: 50	SS: 20
Default Fault	Strong (VISAGE default)	NS: 40,000	SS: 15,000

5.5.5 Define Pressure/Temperature/Saturation conditions

Define simple linear gradients / functions or couple the model to ECLIPSE output properties in the grid. One way coupling was used here where pre-existing pressure and temperature step properties were read in at the required times during the simulation (Pre-injection = 2020, 2025, 2030 and 2040). The pressure properties were depth related linear functions calibrated to the ECLIPSE outputs for the mid case (moderate aquifer) pressure response in the Endurance structure. These extend all over the model and are regarded as somewhat pessimistic as the pressure is likely to drop in the flanks of the structure. In the final thermal plume variant, the temperatures were defined from a depth related linear gradient with a simple CO_2 plume modelled around the upper Bunter Sandstone injection site in CO_2 injector Well 3 (deviated 55° azimuth of 012°). Maximal cooling is to 16°C in the upper three Bunter Sandstone layer cells intersected by the injector. In the surrounding cells below the injection perforation interval more moderate cooling of 19°C to 45°C in each cell with increasing depth is seen. Cooling to 48°C to 50°C in the Röt Clay and Röt Halite 1 immediately above the plume occurs. The geothermal gradient at these depths is 54°C to 65°C from the Röt Halite 1 to Bunter Sandstone L1a respectively.

5.5.6 Define boundary conditions

Vertical stress was calculated from the density property. Also setup was a horizontal stress gradient and a maximum horizontal stress (SH) / minimum horizontal stress (Sh) ratio. This approach doesn’t always fully account for differences in stress from different material properties so an explicit initialisation as a set of properties was used here after optimising the stress gradients (calibrated to the 42/25d-3 data) in the Röt Halite, Röt Clay and Bunter Sandstone.

5.5.7 Define RG simulation case

Select the required properties, pressure, temperature and stress conditions and run in linear (elastic) or non-linear (plastic) failure modes. The option with four core parallel processing was used here. Note that non-linear runs often take a long time to converge so only a few selected cases were run in this mode.

5.5.8 Stress charting

The VISAGE results need to be loaded into Petrel in the same way as ECLIPSE simulation cases and some or all of the outputs can then be converted into grid properties. This process also allows interrogation of the results on a cell by cell basis to assess Mohr circles and stress paths. It also allows the creation of additional properties such as the principal stress magnitudes and orientations.

5.6 Geomechanical Modelling Results

The key results from the modelling are summarised in Table 5.3. The basic conclusion is that with the Phase 1 CO_2 load of 2.68MTPA (as a maximum over 20 years), the Endurance structure when modelled with reasonable properties shows only minor uplift of 9 cm at the crest, associated with CO_2 injection over 20 years (Figure 5.3). In reality cumulative injection of the first load over 20 years will be less than the maximum possible aggregate of 53.6MTPA.

Figure 5.3: Vertical displacement property and vectors for the linear Reference case (LIN_EEATRWH_PRESPLUMECOOLV2_BCEXPLRWH_F); Crestal EW section, W on left. Vertical exaggeration x3.

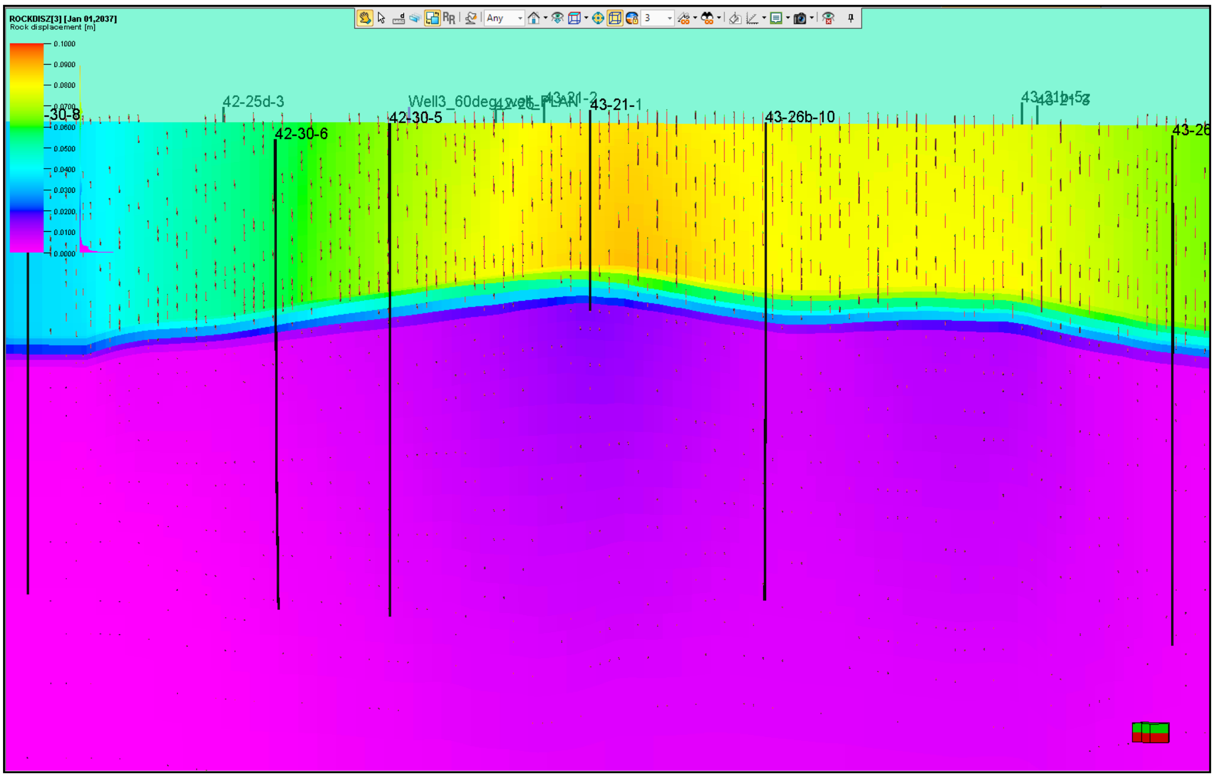

Table 5.3: Summary of key VISAGE runs for the Endurance structure

VISAGE Run Name	Notes
LIN_EEATRWH_PRESCOOL_BCEXPLRWH_NOF	**Initial Case** - No faults, weak halite, explicit stress initialisation, simple CO_2 cooling at perforations, Tensile failure in Rot Halite 1 from cooling above injection.
LINEEATRWH_PRESPLMCOOL_BCEXPLRWH_WKF	**Pessimistic Limit Case** - Very weak faults, one overburden fault extended into Bunter Sandstone, weak halite, explicit stress initialisation, V1 of CO_2 plume cooling above Well 3 (affects halite). Some failure seen in Bunter fault and in cooled Rot Halite. All faults failing in upper cells - (Jurassic). Quarternary also failing but this interval is very weak in the model and probably not realistic.
NONLIN_EEATRWH_PRESPLMCOOL_BCEXPLRWH_WKEXF	**Pessimistic Limit Case** - Non-linear run of LINEEATRWH_PRESPLMCOOL_BCEXPLRWH_WKF. Some differences to linear case, especially in increased elastic strains around faults.
LIN_EEATRWH_PRESPLMCOOL_BCEXPLRWH_EXF	**Limit Case** - Weak faults, one overburden fault extended into Bunter Sandstone, weak halite, explicit

VISAGE Run Name	Notes
	stress initialisation, V1 of CO_2 plume cooling around Well 3. Some failure in upper 1-2 layers (spurious?). Also failure in the two halite cells above plume.
LIN_EEATREF_PRESPLMCOOL_BCEXPLRRH_EXF	**Limit Case** - Weak faults, one overburden fault extended into Bunter Sandstone, reference (strong) halite, explicit stress initialisation, V1 of CO_2 plume cooling around Well 3. Some failure in upper 1-2 layers (spurious?). Also failure in the 3-4 halite cells above plume. Greater likelihood of cooling related tensile failure in salt with higher Young's Modulus and lower Poisson's Ratio compared to weak halite.
LIN_EEATRWH_PRESPLMCOOL_BCEXPLRWH_STEXF	**Optimistic Limit Case** - Strong faults (VISAGE default), one overburden fault extended into Bunter Sandstone, weak halite, explicit stress initialisation, V1 of CO_2 plume cooling around Well 3. Some minor failure in upper layers on Endurance crest (spurious?). Also tensile failure in 2 cells in halite above the plume. No obvious changes in stresses around faults.
LIN_EEATRWH_PRESPLUMECOOLV2_BCEXPLRWH_F	**Reference Case** - Weak faults, no fault extension, weak halite, explicit stress initialisation, V2 of plume cooling around Well 3. Some minor failure in upper layers on Endurance crest (spurious?). Some minor stress changes and strain around OB faults but no thermal or fault related yielding below layer 10. No significant failure modelled.
NONLIN_EEATRWH_PRESPLUMECOOLV2_BCEXPLRWH_F	**Reference Case** - non-linear run. Very similar results to linear case (LIN_EEATRWH_PRESPLUMECOOLV2_BCEXPLRWH_F).

The results in Table 5.3 include a number of ‘limit’ cases where the fault locations, fault strength and degree of cooling were pushed up to or possibly beyond realistic ranges to get some failure. Even in these cases the increased strain or failure appears to be minor and localised and is not likely to create a significant leak pathway. Note that little difference was generally observed between the linear and non-linear runs. These results are summarised below:

Shifted one crestal fault into the Bunter Sandstone, applied very weak shear and normal stiffness values. The shear and normal stiffnesses were reduced to values just above zero to simulate cohesionless faults. At the end of simulation this localised the increase in displacement to 16 cm around the shifted fault hanging-wall (see Figure 5.4). Additional localised increases in shear and tensile strain on faults in the overburden were also observed (compared to the faults with stiffer properties). Most cases with the very weak faults displayed strains even at the initialisation step which indicates the values are probably too low. Even if that strain is possible, it is probably not enough to create a connected leak pathway. Some increase in elastic strain occurred around overburden faults in the non-linear case compared to the linear case.

Figure 5.4: Vertical rock displacement (ROCKDISZZ) indicating the amount of uplift in the very weak shifted faults case (LINEEATRWH_PRESPLMCOOL_BCEXPLRWH_WKF)

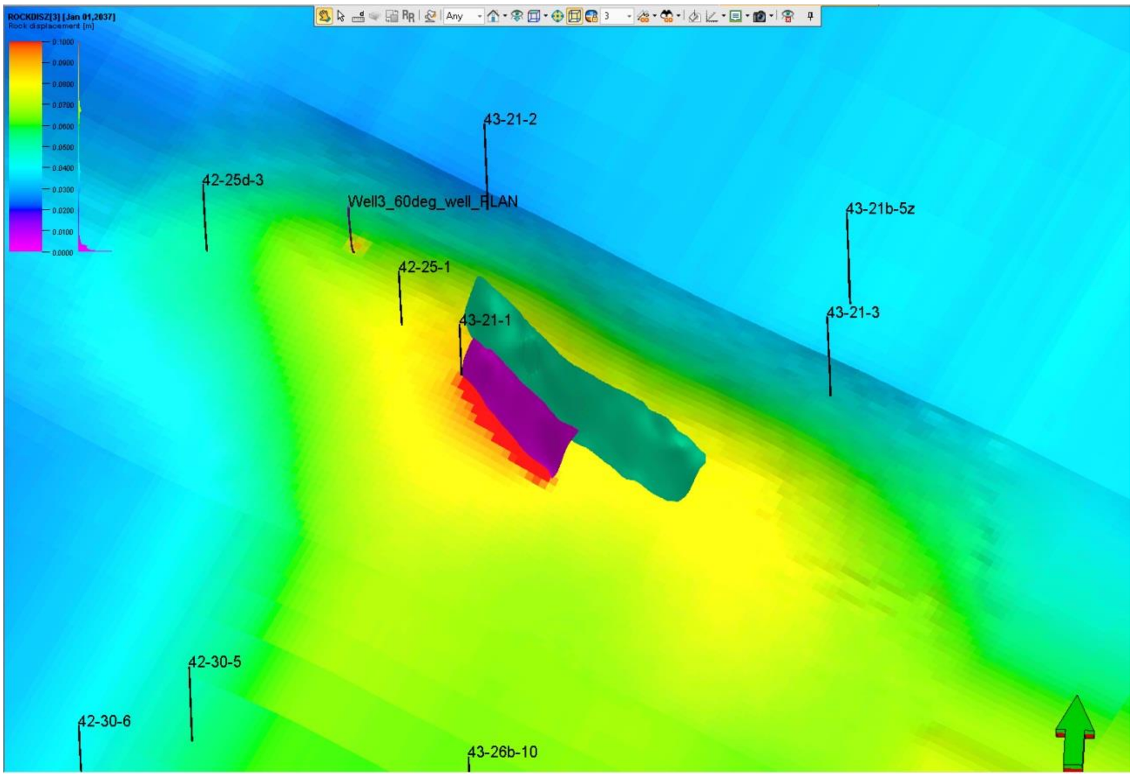

Aggressive plume cooling around and above the Well 3 injector. The cooling in the Röt Halite and Röt Clay cells above the perforations was to 22°C which is higher than from conduction alone. Localised failure of a few Röt Halite 1 and Röt Halite 3 cells occurred via tensile fracturing. This tensile failure occurs over a few more Röt Halite 1 cells in the lateral direction when the Reference Case Halite properties are used.

6 Summary of Chapter 3 to 7 and Conclusions Drawn

Interpretation of a wide range of geophysical and well data, and the results of log and core analysis have shown the Endurance structure to be a large anticlinal structure with excellent porosity and permeability and overlain by a 10m thick Röt Clay of proven sealing quality. The Röt Clay is in turn overlain by a 75 m Röt Halite within the 900m thick Triassic Haisborough Group which also includes the Muscelkalk halite, Keuper anhydrite, and a number of shale layers that provide secondary sealing capability.

Various calculations performed using both analytical and numerical simulation methods indicate that the maximum White Rose Project CO_2 volume of 53.6 MT will occupy less than 2 % of the static volume of the Endurance Storage Site which has a most likely net pore volume of 4.6 Bm^3. The associated aquifer pressure increase during and after CO_2 injection is estimated to be substantially lower than the fracture gradient of the caprock, with only minor uplift of 9 cm predicted at the crest of the structure.

Initially, the majority of the injected CO_2 is predicted to form a 25 m thick CO_2 gas cap at the crest of the structure because of the buoyancy of the CO_2 relative to the native brine. The amount of CO_2 trapped by capillary forces between the injection wells and the crest of the structure is considered to be relatively small, less than 5 % of the total injected volume because of the high reservoir quality. In the longer term, over thousands of years, structurally trapped CO_2 gas cap will diffuse and dissolve into the underlying brine creating a CO_2-rich denser brine phase which will then initiate a convection process that gradually depletes the CO_2 cap and thereby enhances dissolution trapping. Simulation indicates, that CO_2-rich brine will reach the base of the structure in about 10,000 years (assuming no temperature anomalies and no reactivity of the dissolved CO_2 with the formation) when approximately 25 % of total White Rose CO_2 is predicted to be dissolved.

The main geochemical reactions resulting from a decrease in brine pH due to CO_2 dissolution will involve dissolution of dolomite and precipitation of halite and calcite minerals. Since dolomite occurs within the formation as isolated nodules, no impact on rock mechanical properties is considered likely from dissolution reactions whilst precipitation reactions are predicted to contribute to sequestering less than 1 % of total injected CO_2 in the first 10,000 years.

One of the primary objectives of the MMV Plan is to confirm the conformation of the various geoscience models to actual behaviour of the Storage Complex and an annual update would provide a revision of these conclusions regarding the characterisation of the Endurance structure.

7 Drilling of the Wells

7.1 CO_2 Injection Wells

The design of the White Rose CO_2 injection wells takes into account, in addition to requirements of the Wells Basis of Design document , the following main considerations:

- The thermodynamic characteristics and physical properties of the specific composition of the CO_2 to be injected;
- The robustness, reliability and safety of the well design for injection of CO_2 and for its isolation and repair in the event of failure during the injection phase;
- The ability to reliably, permanently and safely seal the wells for the secure storage of CO_2
- That three wells are required to provide the reliability and to meet the system availability criteria of the transport and storage system.

The main drivers for the moderate deviation (less than 60°) well design were:

- to optimise the reservoir placement and particularly to maximise the separation between the injection points;
- so that the wells are accessible for wireline intervention; and
- to limit wellbore instability issues during drilling.

7.1.1 Wells Location and Trajectory

The Endurance platform location (42/25d-P5) and therefore the coordinates from which the wells will be drilled is provided in Table 7.1.

Table 7.1: Platform Location

Location System	Coordinate	Ordinate
UTM Coordinates:	6 012 790.00m N	366 882.00m E
Latitude / Longitude:	54^0 14' 40.496" N	00^0 57' 25.810" E
Geodetic System:	International 1924 Spheroid, European 1950 (ED50) Datum, UTM Zone 31	

The injection wells are designated P5W1; P5W2 and P5W3 from the choice of the 5th platform location and the drilling sequence number. The designations are often shortened to W1; W2 and W3. The coordinates are the target locations and depths are based upon the penetration at the top of Bunter Sandstone. The positional tolerance for each well is a 100m x 150m rectangle oriented with the long side east to west (see Table 7.2).

Table 7.2: Target Well Locations

Quality	Coordinate	Ordinate
W1 UTM Coordinates:	6 013 395.42 m N	366 017.37 m E
Latitude / Longitude:	54^0 14' 59.259" N	00^0 56' 37.103" E
Depth:	1,214 mTVDSS	
W2 UTM Coordinates:	6 012 967.42mN	367 888.19mE
Latitude / Longitude:	54^0 14' 47.170" N	00^0 58' 21.078" E
Depth:	1,199 mTVDSS	
W3 UTM Coordinates:	6 013 755.54mN	367 096.05mE
Latitude / Longitude:	54^0 15' 11.915" N	00^0 57' 36.087" E

Quality	Coordinate	Ordinate
Depth:	1,187mTVDSS	

The 3 injection wells will be drilled directionally increasing to a 55° tangent angle in the 17½” hole section. This angle will be maintained through the 12¼” and 8½” hole sections and on to a TD at ± 2300m MDBRT in the Bunter Shale. Figure 7.1 shows the plan and section of the three wells.

Figure 7.1: Three injection wells in Plan and Section

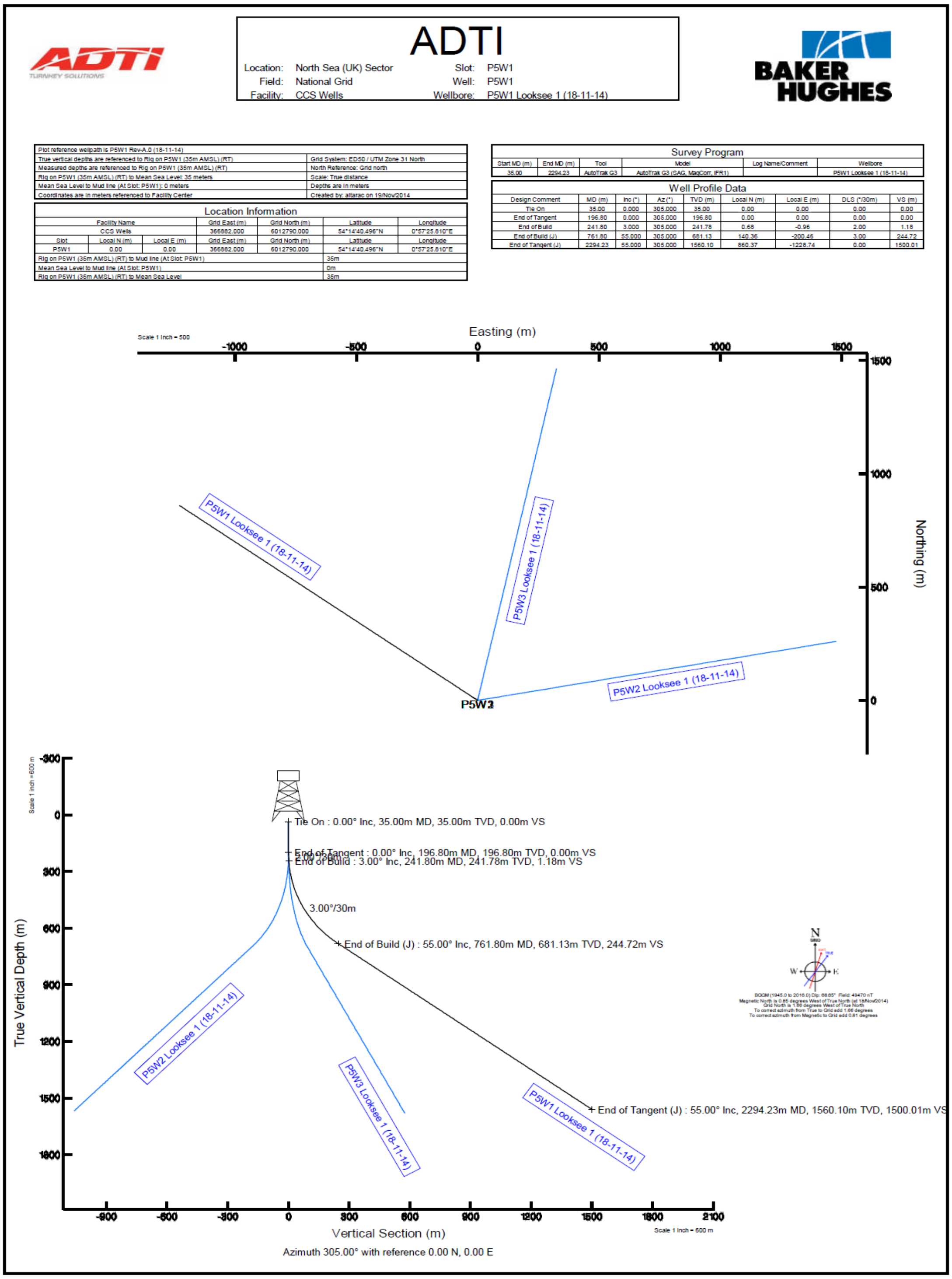

ADTI

Location: North Sea (UK) Sector
Field: National Grid
Facility: CCS Wells
Slot: P5W1
Well: P5W1
Wellbore: P5W1 Looksee 1 (18-11-14)

Plot reference wellpath is P5W1 Rev-A.0 (18-11-14)	
True vertical depths are referenced to Rig on P5W1 (35m AMSL) (RT)	Grid System: ED50 / UTM Zone 31 North
Measured depths are referenced to Rig on P5W1 (35m AMSL) (RT)	North Reference: Grid north
Rig on P5W1 (35m AMSL) (RT) to Mean Sea Level: 35 meters	Scale: True distance
Mean Sea Level to Mud line (At Slot: P5W1): 0 meters	Depths are in meters
Coordinates are in meters referenced to Facility Center	Created by: altarac on 19/Nov/2014

Location Information

Facility Name			Grid East (m)	Grid North (m)	Latitude	Longitude
CCS Wells			366882.000	6012790.000	54°14'40.496"N	0°57'25.810"E
Slot	Local N (m)	Local E (m)	Grid East (m)	Grid North (m)	Latitude	Longitude
P5W1	0.00	0.00	366882.000	6012790.000	54°14'40.496"N	0°57'25.810"E
Rig on P5W1 (35m AMSL) (RT) to Mud line (At Slot: P5W1)					35m	
Mean Sea Level to Mud line (At Slot: P5W1)					0m	
Rig on P5W1 (35m AMSL) (RT) to Mean Sea Level					35m	

Survey Program

Start MD (m)	End MD (m)	Tool	Model	Log Name/Comment	Wellbore
35.00	2294.23	AutoTrak G3	AutoTrak G3 (SAG, MagCorr, IFR1)		P5W1 Looksee 1 (18-11-14)

Well Profile Data

Design Comment	MD (m)	Inc (°)	Az (°)	TVD (m)	Local N (m)	Local E (m)	DLS (°/30m)	VS (m)
Tie On	35.00	0.000	305.000	35.00	0.00	0.00	0.00	0.00
End of Tangent	196.80	0.000	305.000	196.80	0.00	0.00	0.00	0.00
End of Build	241.80	3.000	305.000	241.78	0.68	-0.96	2.00	1.18
End of Build (J)	761.80	55.000	305.000	681.13	140.36	-200.46	3.00	244.72
End of Tangent (J)	2294.23	55.000	305.000	1560.10	860.37	-1228.74	0.00	1500.01

Tie On : 0.00° Inc, 35.00m MD, 35.00m TVD, 0.00m VS
End of Tangent : 0.00° Inc, 196.80m MD, 196.80m TVD, 0.00m VS
2.00°/30m
End of Build : 3.00° Inc, 241.80m MD, 241.78m TVD, 1.18m VS
3.00°/30m
End of Build (J) : 55.00° Inc, 761.80m MD, 681.13m TVD, 244.72m VS
End of Tangent (J) : 55.00° Inc, 2294.23m MD, 1560.10m TVD, 1500.01m VS

BGGM (1945.0 to 2016.0) Dip: 68.65° Field: 49470 nT
Magnetic North is 0.85 degrees West of True North (at 18/Nov/2014)
Grid North is 1.66 degrees West of True North
To correct azimuth from True to Grid add 1.66 degrees
To correct azimuth from Magnetic to Grid add 0.81 degrees

Azimuth 305.00° with reference 0.00 N, 0.00 E

7.1.2 Drilling Plan and Casing Design

The outline drilling programme is as listed below.

1. Mobilise rig to 42/25d-P5 surface location and interface with the White Rose platform.
2. Skid drilling package over selected slot.
3. Spud well and drill 36” x 26” section with sea water and sweeps to ±172 m MDBRT; displace section to 10.0 ppg (1.2 SG) bentonite mud.
4. Run 30” x 20” conductor to ±171 m MDBRT (Top Lias) and cement to seabed. The 30” conductor shoe joints will be swedged down to 20” to allow them to be drilled out with a 17½” bit without the requirement to perform a dedicated cleanout run in a larger bit size.
5. Nipple up overshot and diverter.
6. Drill 17½” section with 9.5 ppg (1.14 SG) KCl polymer mud to ±671 m MDBRT.
7. Run 13⅜” casing to ±670m MDBRT in the Lower Lias and cement to ±457 m.
8. Pressure test 13⅜” casing to 1700 psi on plug bump (conservative pressure based upon pore pressure plus a hydrocarbon gas column to surface).
9. Install surface wellhead & 13⅝” BOP. Pressure test BOP and wellhead connector to 2000 psi.
10. Drill out 13⅜” casing shoe and perform LOT (leak-off test).
11. Drill 12¼” hole to ±1646 m MDBRT with 11.0 ppg (1.32 SG) LTOBM (low toxicity oil based mud).
12. Run wireline logs (wireline logs are assumed although options for LWD will be assessed during detailed design).
13. Run 9⅝” casing to 1646 m MDBRT (in the Rot Halite) and cement back to ±914 m MDBRT.
14. Pressure test 9⅝” casing to 5,000 psi (actual pressure to be based on completion requirements) on plug bump.
15. Drill out 9⅝” casing shoe and perform LOT. Drill ahead to core point.
16. Core part of the Rot Halite, Rot Claystone and an amount of the Bunter Sandstone (requirement for coring to be confirmed on a well by well basis, but notionally 2 x 27 m cores to be cut).
17. Drill remainder of 8½” section to TD (±2286 m MDBRT) with 10.0-10.5 ppg (1.2-1.26 SG) LTOBM.
18. Run wireline logs (wireline logs are assumed although options for LWD will be assessed during detailed design).
19. Run 7” liner to ±2286 m MDBRT and cement back to TOL (top of liner) at ±1494 m MDBRT.
20. Pressure test 7” liner to 5,000 psi (Test Pressure to be confirmed based upon completion requirements).

Casing Seat Selection and Casing Design Figure 7.2 shows the casing configuration for a generic injection well design and Table 7.3 gives the casing schedule. The following outlines the design considerations behind the selection of each casing seat.

7.1.2.1 30” x 20” Conductor

The conductor string with 6 joints below the seabed will be set on depth, based on the length of conductor joints, at ±172 m MDBRT. The bottom of the conductor will be swedged to 20” OD, in line with the slim hole design of this well. It is planned to cement the conductor back to the mudline with 300% excess cement. A riser analysis will be carried out on the 310 lb/ft 30” OD conductor during the detailed design phase to ensure the suitability of the planned conductor string which may result in a reduction of the OD of the 30” conductor to 26”.

7.1.2.2 13 3/8” Surface Casing

The 13⅜", 68 lb/ft, L80 DINO VAM surface casing is planned to be set at ±594 mTVDSS (±671 m MDBRT) in the Lias formation. This will isolate most of the reactive Lias formation. The casing setting point will be set on depth. The 13 ⅝” BOP stack will be installed after running the casing, allowing the mud system to be swapped to LTOBM and the mud weight to be increased to drill the deeper formations.

7.1.2.3 9 5/8” Intermediate Casing

A 9⅝", 53.5 lb/ft, L80, VAM TOP production casing string will be run and set +/- 20m above the Rot Clay cap rock in the Rot Halite formation at ±1173 mTVDSS (±1646 m MDBRT). The 9 ⅝" will cover most of the potential mobile salt sections allowing the Rot Halite, Rot Clay and Bunter Sandstone to be cored. It will also provide a production conduit with sufficient burst, collapse and tensional strength to withstand the pressure experienced during the CO_2 injection phase. The casing setting depth can be moved higher up the well, in the Rot Hailite, if future abandonment requirements (for improved store integrity to CO_2 leakage) dictate the need for a larger cement plug above the Rot Clay cap rock.

7.1.2.4 7” Production Liner

A 7", 29 lb/ft, SM25CRW-125, Super Duplex VAM TOP HT production liner will be run and set off bottom at ±1570mTVDSS (±2301 m MDBRT). A liner top overlap of +/- 150m will be incorporated and the string cemented to top liner hanger with CO_2 resistant cement. The VAM TOP HT connection is being specified so that the liner can be rotated during the cement job whilst the 25 Chrome Super Duplex liner is being specified for its inert nature and CO_2 resistant properties. Further work in the detail design phase will be required to select the ideal metallurgy, and this may involve confirmation testing of the material.

Figure 7.2: Schematic of casing setting depths in a generic injection well

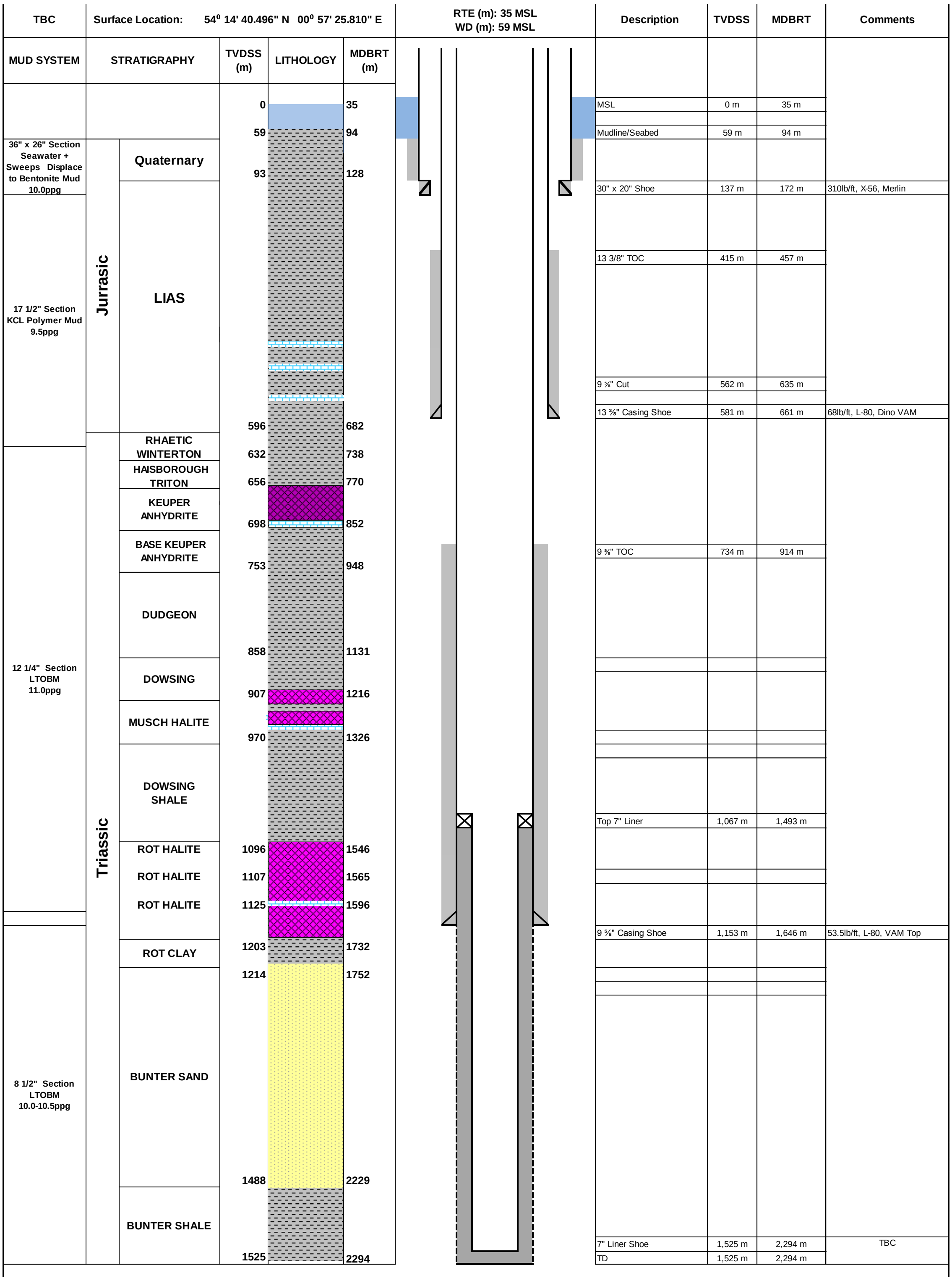

Description	TVDSS	MDBRT	Comments
MSL	0 m	35 m	
Mudline/Seabed	59 m	94 m	
30" x 20" Shoe	137 m	172 m	310lb/ft, X-56, Merlin
13 3/8" TOC	415 m	457 m	
9 ⅝" Cut	562 m	635 m	
13 ⅜" Casing Shoe	581 m	661 m	68lb/ft, L-80, Dino VAM
9 ⅝" TOC	734 m	914 m	
Top 7" Liner	1,067 m	1,493 m	
9 ⅝" Casing Shoe	1,153 m	1,646 m	53.5lb/ft, L-80, VAM Top
7" Liner Shoe	1,525 m	2,294 m	TBC
TD	1,525 m	2,294 m	

Table 7.3: Casing Schedule for proposed Endurance injection wells

Casing Function	Casing OD	Casing Grade	Casing Weight (lb/ft)	Connection Type	Burst (psi)	Collapse (psi)	Tensile (klb)
Conductor	30”	X-56	310	Merlin	3,267	1,681	5,102
	20”	X-56	133	Welded Swedge	3,060	1,450	2,130
Surface Intermediate	13⅜”	L80	68	DINO VAM	5,024	2,263	1,555
Production	9⅝”	L80	53.5	VAM TOP	7,930	6,620	1,244
Production Liner	7”	SM25CR W-125	29	VAM TOP HT	13,110	9,110	1,056

Minimum Casing Design Safety Factors Table 7.4 gives is a summary of the casing design results. It highlights the minimum safety factors calculated for the anticipated load cases during the life cycle of the well. The generic load cases adopted often represent the most extreme conditions anticipated in the well. Buckling and compression loading has been run in Stress Check with no problems noted.

Table 7.4: Minimum safety factors for generic injection well casing design

		Minimum Design Factors			
Casing	**Size**	**Burst**	**Collapse**	***Axial***	***Triaxial***
Conductor	30” x 20”	N/A	3.81	N/A	2.58
Surface	13⅜”	2.89	2.25	3.26	2.69
Production	9⅝”	1.33	2.97	2.29	1.39
Production Liner	7”	2.13	3.25	5.48	2.27
Minimum Design Factors		**1.2**	**1.0**	**1.5 (Premium Conns) 1.8 (Non-premium Conns)**	**1.25**

7.1.3 Drilling Rig Selection Criteria

The minimum required rig specification has been reviewed for the specific purpose of drilling and completing the CO_2 injection wells for the White Rose project.

Various scenarios were reviewed, including drilling the wells before the platform installation. As potential long term well integrity issues were envisaged with the extra potential leak paths associated with this option, the main study work was based upon the premise that the wells will be drilled after the installation of the platform, and therefore the drilling is restricted to the use of a jack-up type rig.

The rig will be required to be jacked up to a suitable air gap to allow sufficient space between the platform weather deck and the rigs cantilever deck and the drilling package will be skidded out to an appropriate distance over the platform. These interface requirements, will have an impact on the rig selection process as the dimensions and operating air gap of the rig chosen may limit the selection of rigs that allow interface with the proposed platform. Water depth at the platform has been assumed to be 59m (referenced to mean sea level – MSL) and the rotary table elevation to be 34.7 m above MSL. Rig selection criteria also needs to consider numerous other factors such as deck space, personnel, pit space requirements, and a rigs recent safety and environmental track record.

Other considerations for drilling rig selection include drilling and completion operations based on the outline programme of the CO_2 wells which recognised some key features one of which is the rig depth rating. Other considerations include derrick load capacity, crown block and travelling block capacity, drilling line size and pulling force, for which calculations were performed to ensure rig capacity would be adequate for the wells.

Additional rig related capacities to be checked include variable deck load (VDL – 2000 to 5000 T is typical and adequate for White Rose operations), POB (Personnel on Board, preference is for a minimum of 100 personnel capacity) mud pump capacity (3 x 12-P-160 1600 hydraulic horsepower pumps are adequate), mud storage requirements, rig power requirements (4500 kW power capacity is adequate for the maximum drilling load envisaged for the White Rose wells), well control equipment rating (maximum surface pressure envisaged is 1650 psi but the likely rating of the equipment accompanying a standard jack-up rig is 135/8” 10,000 psi or 15,000 psi, which far exceeds the requirement).

To illustrate the issues associate with interfacing a jack-up rig with the Endurance platform, the water depth, rig elevation requirements and adequate space to cantilever out over the platform, Figure 7.3 illustrates the rig, platform and relevant dimensions that need to be considered.

Figure 7.3: Schematic of the Interface between a Jack-up Rig and the Endurance Platform

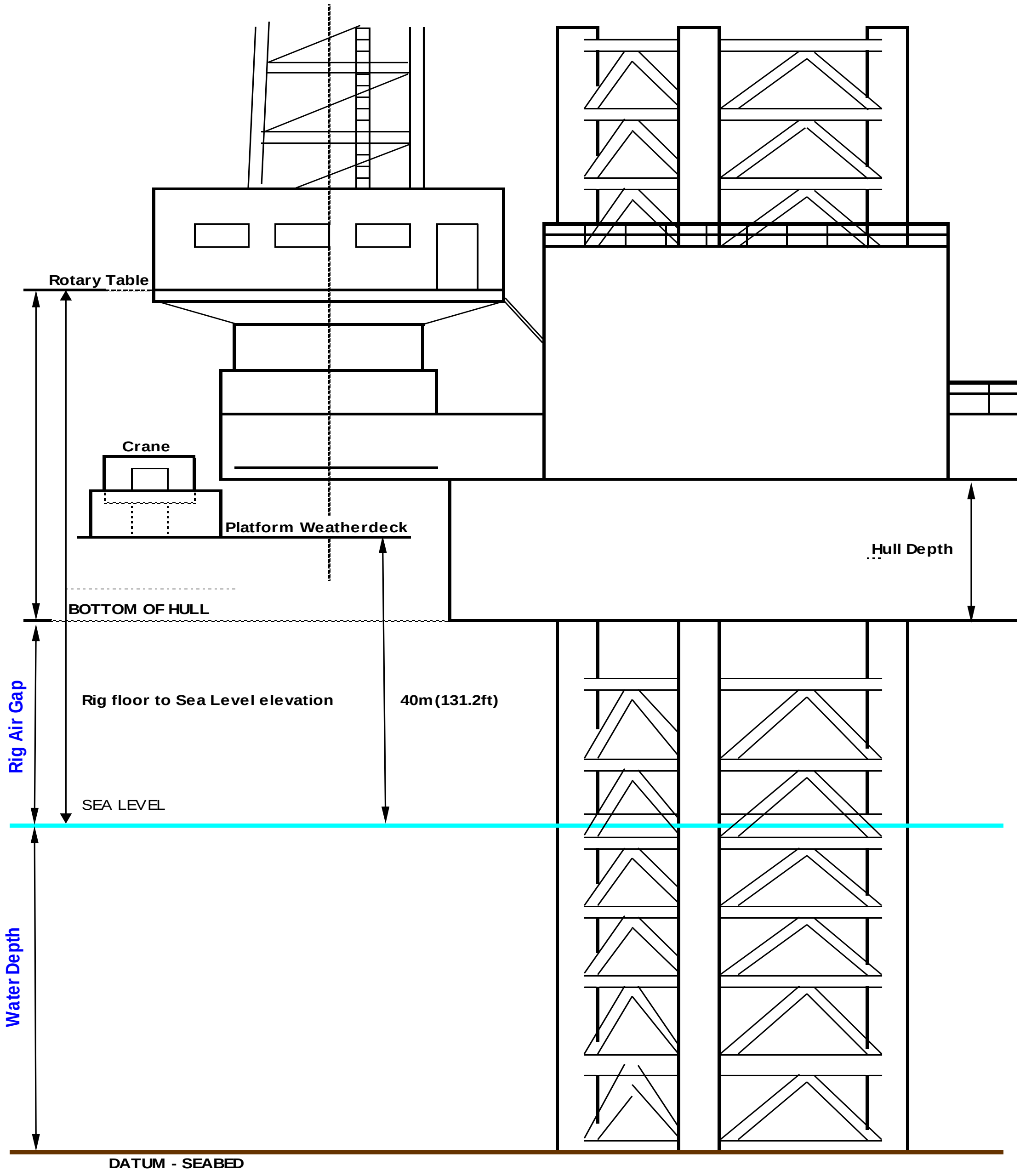

To interface successfully with the Endurance platform, a rig will be required to have sufficient cantilever envelope to drill the first load wells within the specified slots of the platform and allow access to additional slots for contingency for any re-spud requirements.

It is not known at this time the minimum distance of the rig from the platform. This will be dependent upon the dimensions of the platform jacket, the cantilever operating envelope, the dimensions of the rig spud cans and the condition of the seabed. The cantilever must be capable of skidding far enough aft to cover this distance and position the rotary table over the specified slots. As several wells will be drilled at a single visit then the rig positioning is critical to ensure that sufficient cantilever loading is available for each of the slots. The slots have been designed to be less than 7m from the edge of the platform with a 2.5m slot spacing, allowing any standard jack-up rig to successfully access the drilling slots. It is anticipated that the well loads should be well within the cantilever load capabilities of the vast majority of the jack-up rigs used in the SNS but this must be verified during the rig selection process.

7.1.4 Formation Evaluation and Sampling

Open hole wireline operations will be undertaken in the wells to provide information on the formations, particularly the Bunter Sandstone and the seal formations. The precise tools to be used will be finalised in the detailed design phase but logs of formation resistivity, magnetic resonance, P & S wave sonic, gamma ray spectroscopy (for mineralogy and lithology) will be acquired. Additional optional wireline logging using ultrasonic borehole imagers, and to test formation pressure and perform micro-frac tests may be used.

For surveying requirements, a Gyro While Drilling (GWD) tool will be included in the 17½” BHA for directional work down to the depth where magnetic interference from the casing of other wells persists. Below that, an MWD directional tool using SAG and Magnetic correction is adequate to intercept the drilling target.

Mudlogging sample intervals and other operational requirements will be specified during the detailed design phase.

7.2 Completion, Wellheads and Production Trees

7.2.1 Completion Design

The objective of the CO_2 injection wells is to facilitate safe, reliable, and efficient construction, and subsequent use for the injection of CO_2 into the Endurance Storage Site for a period of 20 years. The wells are expected to cater for a range of injection rates ranging from a minimum equivalent to 0.61MTPA to a maximum equivalent to 2.68MTPA. The wells will be designed with due consideration to the short-term CO_2 injection and for the permanent store integrity with the need to monitor and verify this integrity in the post closure phase.

Figure 7.4 shows a schematic of a generic completion design for the CO_2 injection wells. Downhole, the sand-face of the well will be completed with a 7” cemented and perforated liner.

A 5-1/2” upper completion will be run comprising a seal mandrel, permanent packer, a permanent downhole pressure and temperature gauge system, completion tubing, and tubing retrievable safety valve.

Perforations will be in the lower (deeper) 50% of the Bunter Sandstone interval.

The well and completion design including material selection will be adequate for the expected minimum potential temperature of -20°C to -30°C associated with J-T cooling due to the surface CO_2 injection choke.

The completion and casing will be tested to a maximum of 5000 psi (345bar). This is in excess of both the anticipated final reservoir pressure (circa 200bar) and the pipeline design pressure of 200bar. The pressure testing requirement is due to the maximum expected pressures associated with well operations including tasks such as packer setting or perforating and are currently anticipated to be up to 4500 psi (310bar).

The completion design will allow for the corrosion potential of the periodic water wash treatments that maybe required to treat halite deposits that may occur in the near wellbore region of the storage reservoir due to ‘drying-out’ caused by the injected CO_2.

Hydrate management, possibly required during well start-up after a long duration shut-in or after a water wash treatment, will be by the use of Mono-Ethylene Glycol (MEG).

Figure 7.4: Generic Well Completion Design Schematic for CO_2 Injection Wells

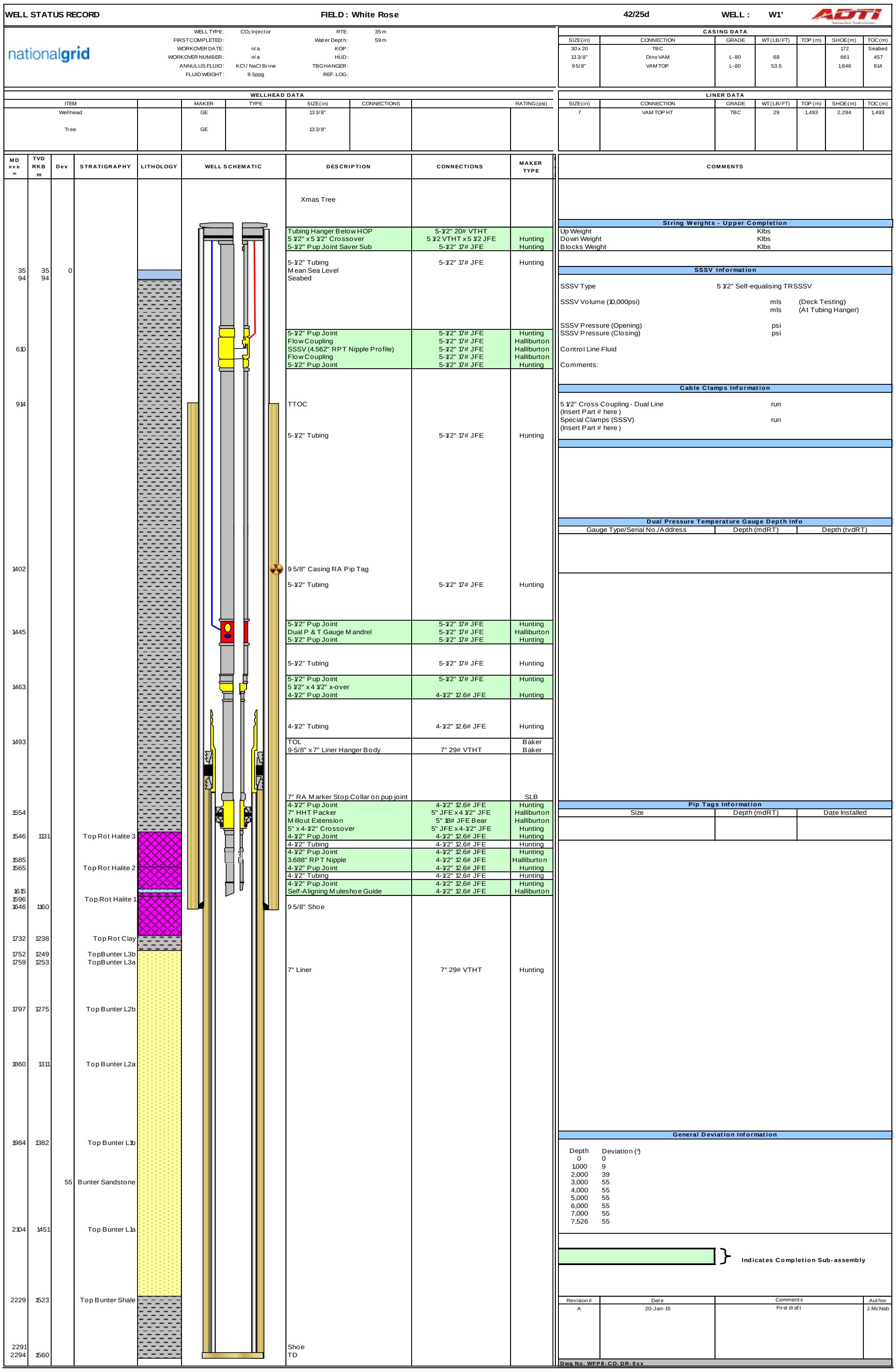

WELL STATUS RECORD FIELD : White Rose 42/25d WELL : W1'

WELL TYPE : CO_2 Injector
FIRST COMPLETED :
WORKOVER DATE : n/a
WORKOVER NUMBER : n/a
ANNULUS FLUID : KCl / NaCl Brine
FLUID WEIGHT : 9.5ppg
RTE : 35 m
Water Depth : 59 m
KOP :
HUD :
TBG HANGER :
REF. LOG :

CASING DATA

SIZE (in)	CONNECTION	GRADE	WT (LB/FT)	TOP (m)	SHOE (m)	TOC (m)
30 x 20	TBC				172	Seabed
13 3/8"	Dino VAM	L-80	68		661	457
9 5/8"	VAM TOP	L-80	53.5		1,646	914

WELLHEAD DATA

ITEM		MAKER	TYPE	SIZE (in)	CONNECTIONS		RATING (psi)
Wellhead		GE		13 3/8"			
Tree		GE		13 3/8"			

LINER DATA

SIZE (in)	CONNECTION	GRADE	WT (LB/FT)	TOP (m)	SHOE (m)	TOC (m)
7	VAM TOP HT	TBC	29	1,493	2,294	1,493

MD RKB m	TVD RKB m	Dev	STRATIGRAPHY	LITHOLOGY	WELL SCHEMATIC	DESCRIPTION	CONNECTIONS	MAKER TYPE
						Xmas Tree		
						Tubing Hanger Below HOP	5-1/2" 20# VTHT	
						5 1/2" x 5 1/2" Crossover	5 1/2 VTHT x 5 1/2 JFE	Hunting
						5-1/2" Pup Joint Saver Sub	5-1/2" 17# JFE	Hunting
						5-1/2" Tubing	5-1/2" 17# JFE	Hunting
35	35	0				Mean Sea Level		
94	94					Seabed		
						5-1/2" Pup Joint	5-1/2" 17# JFE	Hunting
						Flow Coupling	5-1/2" 17# JFE	Halliburton
610						SSSV (4.562" RPT Nipple Profile)	5-1/2" 17# JFE	Halliburton
						Flow Coupling	5-1/2" 17# JFE	Halliburton
						5-1/2" Pup Joint	5-1/2" 17# JFE	Hunting
914						TTOC		
						5-1/2" Tubing	5-1/2" 17# JFE	Hunting
1402						9 5/8" Casing RA Pip Tag		
						5-1/2" Tubing	5-1/2" 17# JFE	Hunting
						5-1/2" Pup Joint	5-1/2" 17# JFE	Hunting
1445						Dual P & T Gauge Mandrel	5-1/2" 17# JFE	Halliburton
						5-1/2" Pup Joint	5-1/2" 17# JFE	Hunting
						5-1/2" Tubing	5-1/2" 17# JFE	Hunting
						5-1/2" Pup Joint	5-1/2" 17# JFE	Hunting
1463						5 1/2" x 4 1/2" x-over		
						4-1/2" Pup Joint	4-1/2" 12.6# JFE	Hunting
						4-1/2" Tubing	4-1/2" 12.6# JFE	Hunting
1493						TOL		Baker
						9-5/8" x 7" Liner Hanger Body	7" 29# VTHT	Baker
						7" RA Marker Stop Collar on pup joint		SLB
						4-1/2" Pup Joint	4-1/2" 12.6# JFE	Hunting
1554						7" HHT Packer	5" JFE x 4 1/2" JFE	Halliburton
						Millout Extension	5" 18# JFE Bear	Halliburton
						5" x 4-1/2" Crossover	5" JFE x 4-1/2" JFE	Hunting
1546	1131		Top Rot Halite 3			4-1/2" Pup Joint	4-1/2" 12.6# JFE	Hunting
						4-1/2" Tubing	4-1/2" 12.6# JFE	Hunting
						4-1/2" Pup Joint	4-1/2" 12.6# JFE	Hunting
1585						3.688" RPT Nipple	4-1/2" 12.6# JFE	Halliburton
1565			Top Rot Halite 2			4-1/2" Pup Joint	4-1/2" 12.6# JFE	Hunting
						4-1/2" Tubing	4-1/2" 12.6# JFE	Hunting
						4-1/2" Pup Joint	4-1/2" 12.6# JFE	Hunting
1615						Self-Aligning Muleshoe Guide	4-1/2" 12.6# JFE	Halliburton
1596			Top Rot Halite 1					
1646	1160					9 5/8" Shoe		
1732	1238		Top Rot Clay					
1752	1249		TopBunter L3b					
1759	1253		TopBunter L3a					
						7" Liner	7" 29# VTHT	Hunting
1797	1275		Top Bunter L2b					
1860	1311		Top Bunter L2a					
1984	1382		Top Bunter L1b					
		55	Bunter Sandstone					
2104	1451		Top Bunter L1a					
2229	1523		Top Bunter Shale					
2291						Shoe		
2294	1560					TD		

COMMENTS

String Weights - Upper Completion

Up Weight	Klbs
Down Weight	Klbs
Blocks Weight	Klbs

SSSV Information

SSSV Type	5 1/2" Self-equalising TRSSSV	
SSSV Volume (10,000psi)	mls	(Deck Testing)
	mls	(At Tubing Hanger)
SSSV Pressure (Opening)	psi	
SSSV Pressure (Closing)	psi	
Control Line Fluid		
Comments:		

Cable Clamps Information

5 1/2" Cross Coupling - Dual Line (Insert Part # here)	run
Special Clamps (SSSV) (Insert Part # here)	run

Dual Pressure Temperature Gauge Depth Info

Gauge Type/Serial No./Address	Depth (mdRT)	Depth (tvdRT)

Pip Tags Information

Size	Depth (mdRT)	Date Installed

General Deviation Information

Depth	Deviation (°)
0	0
1,000	9
2,000	39
3,000	55
4,000	55
5,000	55
6,000	55
7,000	55
7,526	55

🟩 } Indicates Completion Sub-assembly

Revision #	Date	Comments	Author
A	20-Jan-15	First draft	J.McNab

Dwg No. WFP8-CO-DR-0xx

7.2.1.1 Wellhead

A standard design compact wellhead rated for 5,000 psi maximum working pressure in “slim-hole” configuration will be used for the injection wells – see Figure 7.5 for illustration.

Figure 7.5: Schematic of A Typical Compact Wellhead and Injection Tree

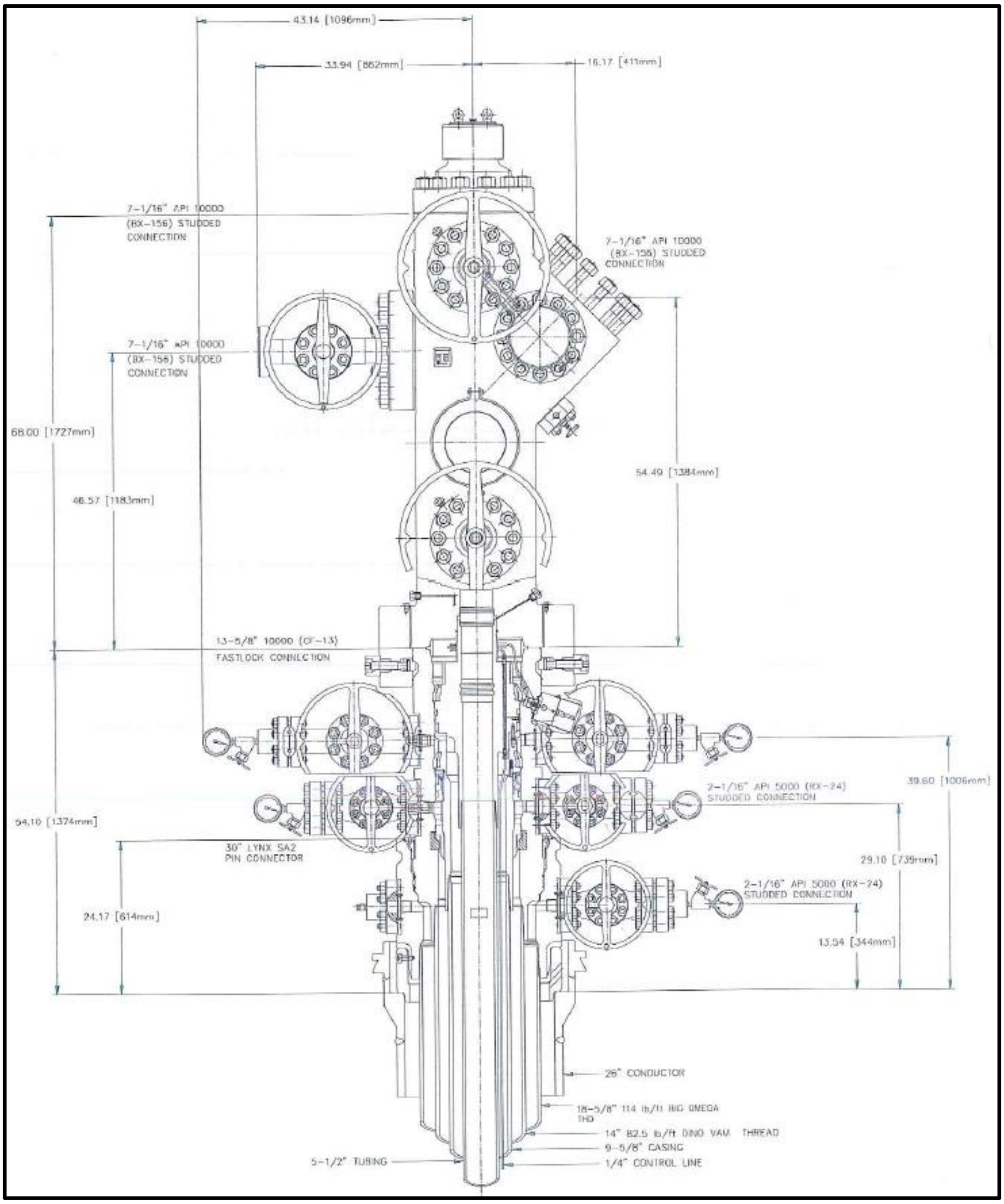

7.2.1.2 Christmas Tree

A 5⅛" 5,000psi working pressure conventional surface tree with standard valve configuration will be mounted after the upper completion has been installed.

The 5⅛" bore is compatible with 5 ½" tubing. The tubing hanger and wellhead would be ported for between four and six downhole feed-throughs which can be allocated for hydraulic, electrical or fibre-optic functions, as necessary. Redundant ports can be blank if not required. A conventional wireline plug profile would be machined into the tubing hanger bore and the premium tubing connection below. Wetted surfaces and other internal seal surfaces will be clad in CRA to mitigate corrosion potential due to water from water wash treatments.

Standard valve configuration will be used with manual lower master valve, remote actuated upper master, manual swab, remote actuated production wing and manual kill valve.

The temperature rating for the tree will be API "L" (-46°C) or API "K" (-60°C). The technical difference being that the lower temperature "K" rated tree and tubing hanger would use metal-to-metal seals whereas the "L" tree and tubing hanger may use a combination of metal-to-metal and non-elastomeric seals. Flow assurance and transient flow studies indicated that the minimum wellhead temperature will be approximately -20°C.

The worst case exposure with respect to corrosion is expected at the base of the well where the provisional recommendation is for use of high chromium material (25% Cr) with a PREN greater than 40.

7.2.2 MMV Plan Instrumentation

Some sensors required for the Measurement, Monitoring and Verification (MMV) Plan will be installed in the wells.

7.2.2.1 Monitoring of Surface Pressure and Temperature

Sensors for pressure and temperature measurements will be incorporated at the wellhead to provide monitoring of the tubing and annuli. Monitoring of the 'A' annulus pressures will indicate if there are any integrity failures of the 'A' annulus envelope which is comprised of the completion packer, tubing hanger, upper completion tubing, and individual upper completion assemblies. Monitoring for pressure in the 'B' annulus can provide an indication of migration of CO_2 through cement or indicate casing integrity issues.

These sensors will be connected to the platform information bus, will be powered by platform supplies and will provide semi-continuous high accuracy data. For redundancy, multiple sensors will be deployed as replacement of sensors would require a rig workover.

7.2.2.2 Downhole Pressure and Temperature Gauges

Pressure and temperature gauges installed downhole in each of the injection wells will provide an accurate measure of downhole injection and annulus pressure during the injection phase.

As with the surface sensors, these gauges will be connected to the platform information bus, will be powered by platform supplies and will provide semi-continuous high accuracy data. For redundancy, multiple sensors will be deployed as replacement of sensors would require a rig workover.

7.2.2.3 Injection Allocation Meters

Allocation meters will be installed to measure the volumes of CO_2 injected into each well. These meters will be installed upstream of the well chokes and therefore can be relatively easily repaired or replaced if they fail.

7.2.3 Well Interventions and Workovers

The following workover and intervention requirements are considered to be necessary during the injection phase of the project, and the platform is sized and configured adequately for these intervention and workover requirements:

- water washes, to mitigate any consequences of halite precipitation, will be accomplished by bullheading wash water (flow rate diversion) down the wells; and
- slickline or electric line surveys for production logging and for the measurement of any corrosion or erosion.

Provision has also been made for interventions that may also be required via wireline or slickline for the following reasons:

- downhole gauge failures;
- injectivity reduction requiring additional perforations;
- TRSSSV failure requiring repair using an insert WRSSV;
- coil tubing cleanout of an obstruction; and
- coiled tubing to perform planned water wash treatment if bullhead method proves ineffective.

Unplanned non-wireline interventions using a rig to workover may also be required in the event that:

- failure of TRSSSV where WRSSV repair is unsuccessful or not applicable; and
- completion tubing or packer failure.

7.2.4 Closure and Abandonment of CO_2 injection Wells

During the post-closure, pre-transfer period, wells and other infrastructure will be abandoned to reinstate the long-term integrity of the storage site; monitoring of the store and complex will continue to confirm the reliability of the sealing of the store.

Figure 7.6 shows a well abandonment diagram illustrating the proposed abandonment plan for the reinstatement of a CO_2 injection well for the long term integrity.

The following assumptions have been made for the injection well:

- the completion string has been removed from the well;
- a surface wellhead have been utilised;
- no pressure monitoring system has been installed in the well;

- no temporary suspension in the wellbore; and
- casing integrity already checked and confirmed.

Figure 7.6: Abandonment Scheme for CO₂ Injection Well

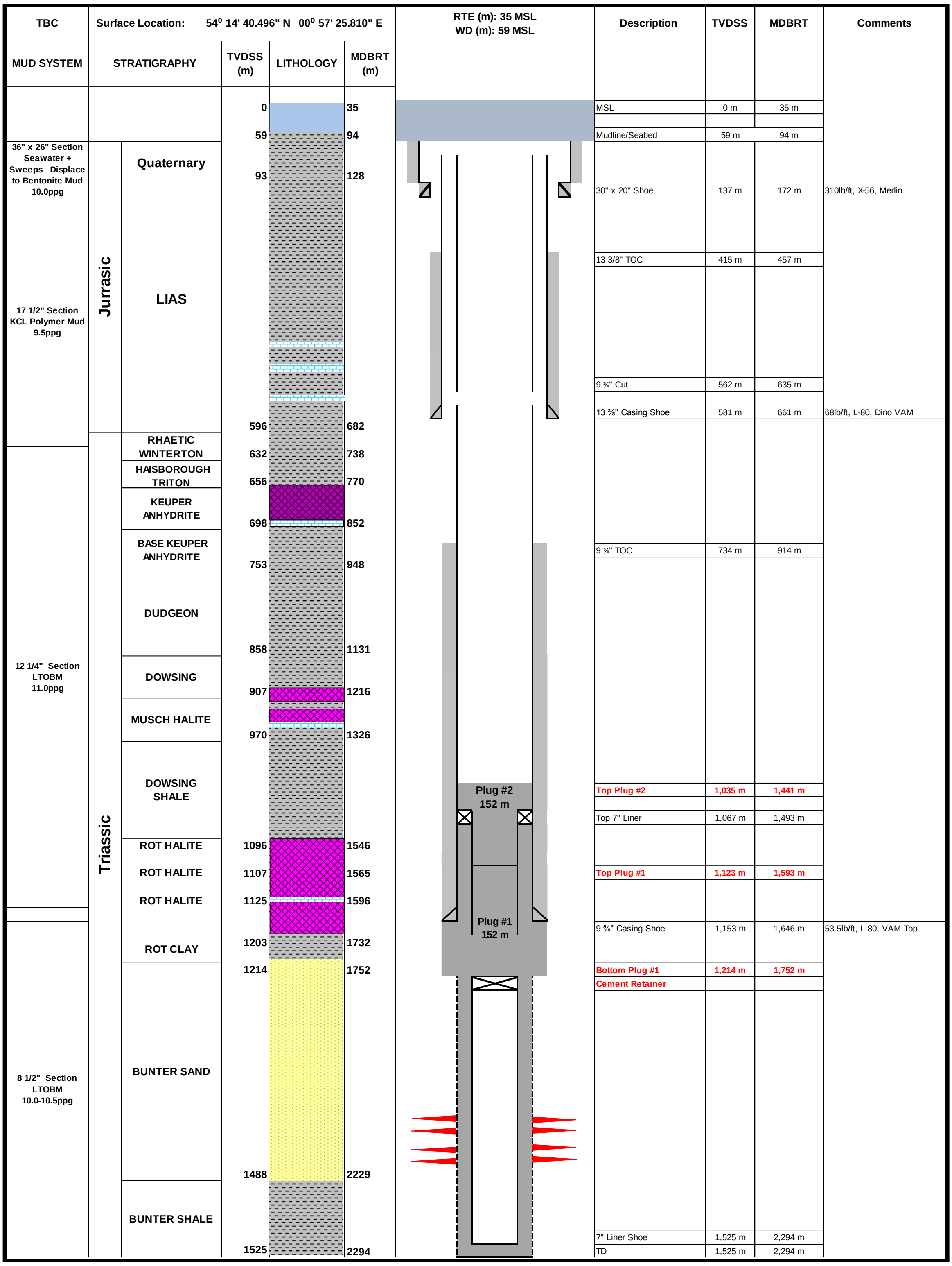

Description	TVDSS	MDBRT	Comments
MSL	0 m	35 m	
Mudline/Seabed	59 m	94 m	
30" x 20" Shoe	137 m	172 m	310lb/ft, X-56, Merlin
13 3/8" TOC	415 m	457 m	
9 ⅝" Cut	562 m	635 m	
13 ⅜" Casing Shoe	581 m	661 m	68lb/ft, L-80, Dino VAM
9 ⅝" TOC	734 m	914 m	
Top Plug #2	**1,035 m**	**1,441 m**	
Top 7" Liner	1,067 m	1,493 m	
Top Plug #1	**1,123 m**	**1,593 m**	
9 ⅝" Casing Shoe	1,153 m	1,646 m	53.5lb/ft, L-80, VAM Top
Bottom Plug #1	**1,214 m**	**1,752 m**	
Cement Retainer			
7" Liner Shoe	1,525 m	2,294 m	
TD	1,525 m	2,294 m	

The operations required for the abandonment of the well are as follows:

7.2.4.1 Mill Section #1

Mill 88 m of 7” liner from ± 1751 m to 1691 m MDBRT. It is critical that the section of 7” liner located at the primary seal Rot Clay from 1751 m to 1732 m is milled. Due to CO_2 resistant cement having been placed behind the 7” liner, it is unlikely that this cement would be required to be milled, but in the event that there is an insufficient bond between plug #1 and formation wall, it would be advised to mill the cement.

7.2.4.2 Plug #1 1751 m – 1593 m (Pancake Plug)

A 16.0 ppg CO_2 resistant cement plug will be set from 1751 m to 1593 m (length 158 m) to act as the primary barrier to the Bunter sand. This plug will restore the cap rock and seal across the naturally sealing formations in the Rot Clay and Rot Halite. Note that it is an option to mill the casing window a little higher in order to use the Rot Halite as the primary barrier.

The plug will be verified with a 15 klb tag, and be pressure tested to 500psi above the maximum injection pressure of the Bunter Sandstone.

7.2.4.3 Plug #2 1593 m – 1441 m

A 158 m, 16.0ppg Class G cement plug will be set on top of Plug #1, to act as a secondary barrier for the Bunter sand. The plug will be verified with a 15 klb tag.

Should it be thought that an additional Pancake Plug type barrier is preferred, another option is to mill a window across the Muschelkalk Halite and set Plug #2 across this interval.

7.3 Abandoned Exploration Wells

Two wells have been drilled into the crestal part of the Endurance structure. They were drilled as hydrocarbon exploration wells and were designed to test for the presence of gas in the Bunter Sandstone structure. The wells are located in the part of the structure where the CO_2 will repose once the plume has migrated to its final static position. When no hydrocarbon gas was shown to be present the wells were abandoned according to the standards and regulations at that time.

Although they were drilled twenty years apart in 1970 and 1990, the configuration of the wells and their abandonment is remarkably similar. Most importantly, although abandonment was not undertaken with long-term CO_2 storage in mind, the abandonment methodology, which followed standard practise and satisfies the regulations prevalent at that time, provides adequate containment for White Rose CO_2.

The wells are 43/21-1, drilled in 1990 by British Petroleum plc, and 42/25-1, drilled in 1970 by Mobil North Sea Limited and both wells were remarkably similar in their design and implementation and most importantly, in both cases the shallowest section of Rot Halite 2 was left uncased and uncemented. The latest research and industry recommendations (although not included in the regulations) advocate the use of uncased and uncemented salt as being the safest and most reliable abandonment method when CO_2 storage is proposed . In summary, salt, even at moderate depths, behave like a fluid (more precisely as a rheid) and ‘creeps’ to seal any voids or fractures.

The configuration of the two wells, the geological formations drilled and their abandonments are as shown in Figure 7.7.

The information for both wells has been collated from the summary drilling reports and their composite well logs. These reports are those available from the Common Database Access (CDA) maintained by DECC.

The wells were drilled and abandoned as follows:

1. 30” conductor run in 36” hole to just over 124m in 43/21-1 and to 160m in 42/25-1;
2. 13-3/8” casing run and cemented in 17-1/2” hole; casing shoe set at 548m in 43/21-1 and 557m in 42/25-1 in both cases just below the Keuper Anhydrite in the Triton Shales and in both cases the casing was cemented up to the seabed;
3. Formation Integrity Test (FIT) of 13 ppg (1.56 SG) at 13-3/8” shoe in Triton Shale in 42/21-1; Leak-Off Test (LOT) of 14.3 ppg (1.72 SG) in Triton Shale in 43/25-1; other nearby formation tests are shown in Table 7.5;
4. drilled 12-1/4” hole to Bunter Sandstone. Cores were taken in the Bunter Sandstone in the 43/25-1 well; no cores were taken in the 43/21-1 well;
5. 43/21-1 was drilled to the Bunter Shale below the Bunter Sandstone; 43/25-1 was TD in the Bunter Sandstones;
6. wireline logs were run in both wells;
7. in the 43/21-1 well, the first abandonment plug was run off bottom with 53 m of cement in the Bunter Sandstone, through the Rot Clay and approximately 40m into the 56 m thick Rot Halite 2 (a further 1 0m of halite is present in the shallower Rot Halite 1); In the 42/25-1 well, the first abandonment plug was set at TD with 80m of cement in the Bunter Sandstone, through the Rot Clay and approximately 58 m in to the 70m thick Rot Halite. In neither well was this first plug weight nor pressure tested. In 43/21-1 the cement plug was placed at TD, in 42/25-1, the plug was set off bottom and the depth of the cement top is based on pipe depth when the plug was placed and slurry volumes;
8. in both wells the second abandonment plug was set across the 13-3/8” shoe open hole against the Triton/Dudgeon Shales and in the cemented casing up to the Keuper Anhydrite; in both wells the plugs were pressure tested; in 43/21-1 the plug was also tagged with 30 klb;
9. in both wells the third abandonment plug was set in 13-3/8” casing from below the depth of the 30” shoe to approximately 20m below the seabed;
10. in both wells both the 30” and 13-3/8” casings were cut a few meters below the seabed.
11. the location of both wells was confirmed by magnetometer survey in 2012; and
12. cement use in 43/21-1 for casing cementation and for the abandonment plugs conformed to API 10A Class ‘B’; cement used in 42/25-1 for casing cementation and for the abandonment plugs conformed to API 10A Class ‘G. Volumes and slurry compositions are shown in Table 7.6.

Table 7.5: Nearby Formations Tests at Surface Casing Shoe

Formation	*Fracture Pressure (SG)*	Fracture Pressure (ppg)	*Depth TVDSS (m)*	*LOT / FIT*	*Well*
Lias	1.97	16.4	500	LOT	42/30-8
Triton	1.56	13.0	522	FIT	43/21-1
Triton	1.72	14.3	529	LOT	42/25-1
Lias	1.88	15.7	569	LOT	43/21a-4
Lias	1.62	13.5	579	FIT	43/21-2
Lias	1.91	15.89	715	FIT	42/25d-3

Formation	***Fracture Pressure (SG)***	**Fracture Pressure (ppg)**	***Depth TVDSS (m)***	***LOT / FIT***	***Well***
Lias	1.73	14.4	869	FIT	43/21b-5
Lias	1.56	13.0	885	FIT	42-24-1
Lias	1.79	14.9	973	LOT	42/25-2
Rot Halite	1.68	14.0	1,342	FIT	42/25d-3

Table 7.6: Abandonment Plugs Cementation

	43/21-1 (drilled 1970)		**42/25-1 (drilled 1990)**	
Casing Cementation	Design	Mix	Design	Mix
30” Casing	To surface	500 sx Class ‘B’ With 2% $CaCl_2$	To surface	Class ‘G’ Neat
13-3/8” Casing	To 305’ RKB	a. 800 sx Class ‘B’ With 8% gel b. 500 sx Class ‘B’ Neat	To surface	Class ‘G’ Neat
Abandonment Plug 1	Base 1,111 m Top 1,006 m	250 sx Class ‘B’ Salt saturated	Base 1,195 m Top 1,045 m	11.5 cu.m Class ‘G’ Neat
Abandonment Plug 2	Base 598 m Top 462 m	374 sx Class ‘B’ Salt saturated Weight test 30klb	Base 607 m Top 508 m	11.6 cu.m Class ‘G’ Neat Weight test 15klb Pressure test 1k psi
Abandonment Plug 3	Base 200m Top 113 m		Top 180m Base 125m	4.5 cu.m Class ‘G’ Neat

Figure 7.7: Abandonment Scheme for CO_2 Injection Well

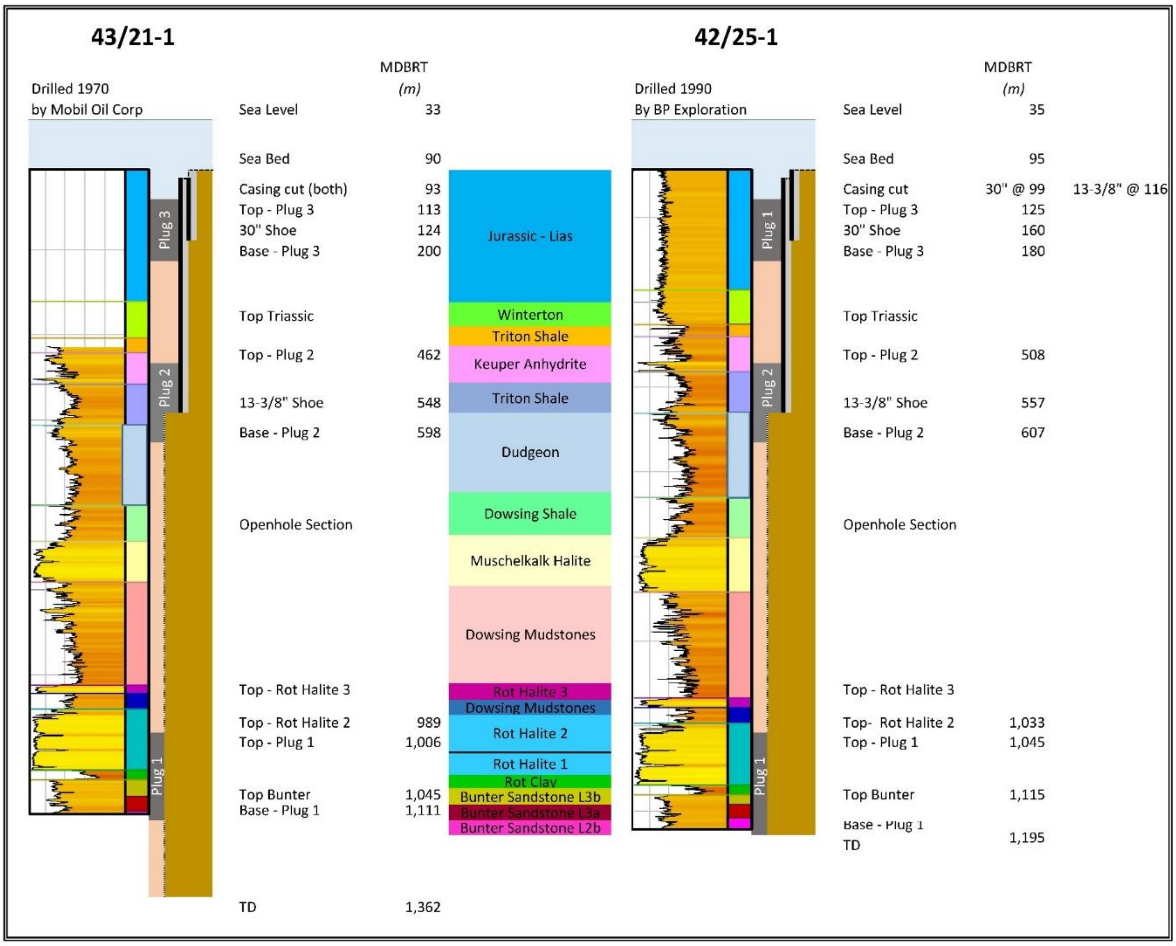

In order for stored CO_2 to leak from the storage site via the two legacy wells there will need to be multiple independent failure of sealing barriers that have been shown to be capable of containing the CO_2 both from geochemical reactivity and pressure integrity points of view. Although they were drilled and abandoned before the concept of CO_2 storage in saline aquifers such as the Endurance structure were considered, the abandonment procedure is, mainly by virtue of the uncased salt sections, is adequate for the long term security for the storage of White Rose CO_2 volumes.

Geochemical simulations of the mixtures of CO_2 with both the fabric of the reservoir and caprock do not raise any concerns as to either the short term or long term exposure and the review of CO_2 interactions with cement used in the abandonment of the wells although indicating the presence of geochemical reactions, as there is no flow past the plugs that these reactions will slow and eventually stop as the reactivity of the CO_2 is buffered by the reaction products.

Overall, there is a high confidence that the legacy wells that were drilled and abandoned on the crest of the Endurance structure will not cause any problem for the permanent secure storage of White Rose CO_2.

8 Asset Management

8.1 Reservoir Management Plan

8.1.1 Scope of the WRM Plan

The Well and Reservoir Management (WRM) Plan would be developed as the guidelines to govern the operation of the Endurance structure and the operation of the injection wells for White Rose Project.

Preliminary drafting of the plan would start once the detail design of the wells has been finalised and the procurement of materials, equipment and services is on-going. However, the finalisation of the first operational version of the WRM Plan would be completed only after the wells have been drilled and perforation intervals for each have been chosen. This first version, the Commissioning WRM Plan would be for use during the commissioning of the full chain. Once commissioning activities were completed and the system is operating in a stable condition, injectivity testing of each of the wells across their full operating range would take place. These injectivity results would then be used to prepare the operational phase WRM Plan. It is envisaged that this plan would be updated on an annual basis during the main operational phase of injection however more frequent revisions may be required during the initial years of operation.

In addition to acting as the operational guide, the WRM Plan would form an essential part of the suite of planning and operating documentation that make up the asset management procedures: Asset Reference Plan (ARP) and the Measurement, Monitoring and Verification (MMV) Plan and NGCL’s Asset Management Policy.

8.1.2 WRM Plan Preparation and Structure

The WRM Plan would contain the operational criteria for the wells and would interface with the full chain control mechanisms. It would also be the primary reference that considers well integrity and well’s operational safety and would interface to the project’s HSE and operational policies and procedures which would be developed and adopted during the detailed design phase.

To enable the plan to evolve from the Commissioning WRM Plan to the operation phase version, it would access and integrate the appropriate MMV Plan data streams but would also require injectivity testing routines to characterise well and reservoir response across the full range of operating scenarios.

The primary controls for well operations are the injection chokes on each well and the selection of which wells to use for injection. The near real-time monitoring data available for each well includes individual well flowrates, surface and downhole pressures and temperatures.

It is anticipated that under a stable operating regime that long periods of steady injection (typically three months or so) would provide for optimum system performance. It is further anticipated that two of the three wells would have adequate injectivity for the maximum production rate of the power plant and the third well, whilst not used for injection, would provide a downhole pressure monitoring point. The nature of the reservoir formation indicates that it would take of the order of 10 days for bottomhole pressures to re-stabilise after a well is shut-in following a period of injection. These stabilised pressures are essential for the estimation of key reservoir parameters particularly the scale and degree of connectivity of the aquifer.

Once a stable operational regime has been established, the effect of formation desiccation and salt precipitation would be closely monitored. Should significant degradation of injectivity performance be quantified, water washing of the near wellbore formation may be scheduled. The WRM Plan would specify the conditions and procedures for these near well bore water washes. The platform facilities design includes equipment for this work. Of critical importance to prevent damage and operational problems is the effective use of hydrate inhibition and to closely adhere to the re-start procedures for the wells which are designed to avoid excessively low temperatures and extended periods of two phase flow in the upper completion assemblies.

Under the auspices of the MMV Plan, occasional production logging is scheduled. The production logging is primarily to characterise the injection profiles for each well and this information would be used to upgrade the WRM Plan.

The WRM Plan would contain inspection, testing and maintenance schedules and would implement the system operating strategies and philosophies.

8.2 Asset Reference Plan

8.2.1 Scope of the ARP

The Asset Reference Plan (ARP) would be developed to provide a forward looking life cycle view of the Storage Site and Storage Complex. The ARP is intended to act as a driver for future optimal operation of the Store and consequently to maximise the value of the assets.

The Asset Reference Plan as a part of the asset management procedure is governed by NGCL’s Policy for Asset Management. The Asset Management System Policy is consistent with other policies adopted by NGCL for Health, Safety and Environment and takes account of the requirements set out in the British Standards Institute’s publically available specification PAS 55-1:2008 *Asset Management Specification for the Optimised Management of Physical Assets.*

The ARP:

- is an integral part of the planning process and specifically the work programme and budget;
- details asset strategies;
- summarises the economic modelling of the asset; and
- integrates key data, activities and processes and all resources allocated to them.

8.2.2 ARP Preparation and Structure

The process of developing the ARP is a part of the overall planning process. It sets out the long term strategy to optimise the storage site and captures the activities that occur during the project life cycle from detailed design and build, through the operational phase (injection), the post injection, post closure and to the transfer of responsibility to the Competent Authority.

Three stages would be considered in the development of the ARP, namely planning, activity based cost modelling and documentation. Subsequently, the regular updates would reflect any changes in the internal or external environment, legislation or regulatory affairs and would take into account the histories and forecasts from the MMV Plan outputs and other factors that would affect or influence the costs, revenues and overall economics.

The up-to-date ARP then would form a key part of the preparation of the annual work programme and budget. For this purpose, there would be consistency imposed between the activities based cost model and budgetary cost codes.

The base-case ARP would utilise detailed design documentation, along with the Basis of Design and Operations Philosophies that have been finalised during the front end engineering design (FEED) phase of the project.

9 Field Development Plan

9.1 Storage Permit Application

This Field Development Plan (FDP) reflects the content of the larger part of the Storage Permit Application that will be submitted to the UK Competent Authorities for the CS001 Carbon Storage and Appraisal License in the Southern North Sea.

Consent is sought to develop the Endurance Structure as a Carbon Capture and Storage Complex and commence the injection of CO_2 in to it.

The application is made in line with the UK legislation (The Storage of Carbon Dioxide (Licensing etc.) Regulations 2010 and The Storage of Carbon Dioxide (Termination of Licences) Regulations 2011) and EU CCS Directive on Geological Storage of Carbon Dioxide (Directive 2009/31/EC).

In November 2012, the UK's first CO_2 Appraisal and Storage Licence (CS001) was awarded nand in February 2013 the Crown Estate awarded an Agreement for Lease to NG29 for the Endurance Storage Site.

The work undertaken by NGCL for the appraisal and characterisation of the site and for the design of the infrastructure was co-funded by both the European Economic Programme for Recovery (EEPR) grant agreement, Energy Technologies Institute (ETI) and DECC's UK CCS Commercialisation Programme.

9.2 Key Technological Aspect

For the offshore sections of the White Rose CCS Project, there are a number of key technological aspects and decisions that have led to this plan for the implementation of the project.

Extensive research, analysis and studies of the available geological, geophysical and well data culminated in the drilling of the 42/25d-3 appraisal well in 2013. The objectives and the design of the evaluation programme for this appraisal well was to gather additional information to assist in characterising the Endurance Storage Complex. Subsequent to the drilling of the well, there was a comprehensive programme of testing and analysis and particularly the work on the core continued for over 20months. The results and data from this post-appraisal work programme have been included in the suite of geological, reservoir and geomechanical models that have been used to characterise and predict the behaviour of the Endurance Storage Complex.

Both in the characterisation of the Storage Site and in the plan for the development of the Storage Complex, technology and techniques proven in the hydrocarbon exploration and production industry have predominantly been used. Where the specialist requirements for the permanent storage of CO_2 exceed the capabilities or experience of the oil and gas industry, know-how, research and peer review from the CO_2 storage and enhanced oil recovery industries has been incorporated to inform the project design and implementation.

As the White Rose CCS Project plans to use in 20 years less than 2% of the estimated static storage capacity of the Endurance structure, if the behaviour of the Storage Site conforms to expectations after injection has commenced, an application for the expansion of the project may be considered. Measurement of the pressure response to injection of CO_2 for a few years will be required to fine tune the dynamic modelling of the Storage Site and provide additional information for any expansion plan.

However, some of the White Rose infrastructure, particularly the pipeline and transport assets have been designed to have spare capacity for a possible future upscaling of the storage volume and to provide a hub for transmission of CO_2 to other nearby storage sites.

Since National Grid's work on CCS commenced over six years ago, the evolution of the project has considered many options and has made some fundamental decisions that have led to the current proposal for the transport and storage infrastructure for CO_2 capture and storage. Having considered both depleted gas fields and saline aquifer structures in the southern part of the North Sea, saline aquifers were prioritised for the first CO_2 store for the Humber area for a number of reasons including:

- availability – most of the gas fields will still be producing at the time the CO_2 store is planned to be developed;
- capacity – The storage capacity of the aquifer structures is generally larger than the volume of the gas fields;
- storage integrity: it is anticipated that wells drilled for hydrocarbon exploration and development present the greatest risk for the long term security of the CO_2 Storage Complex and as there are significantly fewer wells drilled through the saline aquifer structures, long term Storage Complex security will be superior and containment risks will be minimised.

9.2.1 Use of Dense Phase CO_2 Pipeline:

CO_2 can be transported either in gaseous phase or in dense phase. For longer pipelines in excess of a few kilometres, despite the higher pressure requirements, the advantages of dense phase CO_2 transportation far outweigh the disadvantages:

- higher flow capacity per unit cost; increased capacity outweighs additional cost of increased pressure requirement;
- lower pressure drop per unit mass of CO_2;
- ease of operation and benefits of the use of pumps rather than compressors;
- the use of dense phase also precludes the necessity for the provision of injection compressors on the offshore platform since booster pumps can be located onshore; and
- the dense phase pipeline is to be constructed from carbon steel (rather than high cost chrome/nickel alloy steel) and CO_2 purity is tightly controlled and dehydrated to less than 50 ppm to preclude any corrosion or hydrogen embrittlement issues.

9.2.2 Oversizing of the pipeline for future expansion:

The transportation assets from the Camblesforth Multi-junction to the Endurance platform location have been sized to be able to transport a maximum of 17MTPA of CO_2 compared to the White Rose requirement of up to 2.68MTPA. Should the pressure response of the storage site be satisfactory, it is envisaged that future emitters will connect into the Camblesforth Multi-junction to benefit from the security and cost benefits of shared CO_2 transportation. These additional loads may then be stored in the Endurance Storage Site (if approved via a new Storage Permit application) or alternatively passed to other future storage sites that might be developed nearby.

9.2.3 Use of injection platform instead of a subsea installation:

The decision to use an offshore platform rather than sub-sea facilities was based on operability concerns associated with a ‘first-of-a-kind’ project. Although the characterisation of the Storage Site and Storage Complex is comprehensive, there is limited experience of CO_2 injection in offshore saline reservoirs and a platform allows for a substantially more flexible operating mode and provides enhanced capability for monitoring and measurement of key parameters. The reasons for choosing offshore platform over a purely subsea installation include:

- dry trees with their benefit of accessibility;
- workover capabilities from the platform without the need for a well intervention vessel for electric line or slickline interventions or water wash for salt precipitation in the near wellbore region;
- active control of injection pressures and flowrates between wells;
- accurate individual well metering for the allocation of CO_2 volumes between wells;
- filtration of the CO_2 stream before injection;
- data handling for MMV Plan equipment – high data transmission requirements are needed for the seabed micro-seismic array and the downhole pressure and temperature sensors; and
- provision for expansion, including water production risers, spare well slots, CO_2 export risers.

9.2.4 CO_2 storage volume

From the estimation of the NPV of the Endurance Structure and even considering the accuracy and sensitivities of these estimations, the White Rose volumes of up to 2.68MTPA for a period of 20 years (54 MT) is approximately 2% of the mean 2,600mT static capacity indicated by the 4.6 Bm^3 (most likely geological model – P64) NPV.

The dynamic capacity depends on the maximum allowable excess pressure (above hydrostatic) to which the Storage Site will be subjected. The excess pressure is a function of the injection rate as well as the connectivity and extent of the aquifer that is attached to the Endurance Structure. Although modelling indicates that pressure relief via water production is not necessary for White Rose volumes, the various relevant factors cannot be definitively determined until injection has commenced and the pressure response of the system has been measured. The evidence that the Esmond gas field, some 60km to the north, is in pressure communication with the Endurance Storage Site provides a positive indication of the connectivity to the Greater Bunter although quantification is still required.

9.2.5 Storage mechanisms for CO_2

There are four commonly recognised storage or trapping mechanisms for the CO_2 that is injected into underground reservoirs. For each individual reservoir the proportion of the total CO_2 subject to each mechanism is dependent on the type and structural configuration of the rock, the composition of the formation brines, the fill ratio of the Storage Site and the timing. To a lesser extent, the proportions of the CO_2 trapped by each mechanism at each time-step are dependent on the ambient pressure and temperature. Geochemical modelling combined with reservoir simulation results provide the best determination of the magnitude of the proportion attributable to each mechanism during the evolution of the store. The four trapping mechanisms are:

1. Structural/Hydrodynamic Trapping – This is the most dominant of the trapping mechanisms at early time. The super-critical CO_2 is more buoyant than the formation brine and will therefore flow up through the sandstone until it meets the caprock and then will continue laterally until it reaches the crest of the structure.
2. Residual Trapping – As the CO_2 percolates through the reservoir from the injection wells it forms a plume that migrates vertically under the influence of buoyancy forces, displacing formation brine. Upward migration of CO_2 continues after injection ceases and as the brine returns to the pore volume previously occupied by the plume, an amount of CO_2 equivalent to the critical gas saturation remains trapped within the rock matrix. The volumes trapped by this mechanism depends on the location of the injection wells compared to the crest of the structure, the depth and extent of the CO_2- brine contact and the depth and profile of the injection perforations
3. Solubility Trapping – This process is caused by the CO_2 being dissolved in the formation brine. It is driven by the diffusion of CO_2 in to the formation brine and therefore occurs in the area of the plume and immediately under the CO_2-brine contact. This process continues for thousands of years. Also, as the brine with CO_2 dissolved in it is denser than the brine itself it consequently initiates convection and downward movement of the CO_2-rich brine. In the very long-term all the structural/hydrodynamically trapped CO_2 will diffuse into the brine.
4. Mineral Trapping – A range of geochemical reactions occur between the CO_2 and the CO_2-rich brine both with the reservoir rock and to a much lesser extent with the caprock. These reactions have been modelled by geochemical simulation.

9.2.6 Geological modelling of the Storage Site and Storage Complex:

For the response and performance of the Storage Site and Storage Complex under operating conditions, extensive use of simulation and modelling is required in order to reliably predict the outcomes of the complicated and inter-related effects. The modelling uses separate platforms for the different sections and each subsequent platform uses the output of preceding stages. The order of precedence of the models used for the Endurance Storage Site and Storage Complex is as follows:

1. Static geological modelling of the Storage Site and Storage Complex – This model uses as its inputs the seismic interpretation of the structure, the under and overburden. It uses the logs from local and regional wells in order to specify the stratigraphy. For the Storage Site, it uses the log and core analyses to specify the facies for each subdivision and to interpolate and extrapolate the primary rock properties across the structure. The mineralogy and porosity of the reservoir intervals are the key outputs to the next stage, the Reservoir Simulation;
2. Reservoir Simulation is the dynamic modelling of the reservoir. Taking the static modelling results and adding permeabilities, relative permeabilities, fluid characteristics and wells, the movement of CO_2 from the injection wells to its final static location are predicted. Additional data comes from the analysis of core and well testing and is significantly upscaled from the limited local results right across the reservoir structure. For these tasks, the information gained from the appraisal well namely; routine and special core analysis results, advanced vertical interference tests and conventional production and injection test interpretation results have been most important. The outputs of the reservoir simulation provided both the expected CO_2 plume migration plus the pressures and temperatures across the structure – key inputs to the geomechanical modelling.
3. Geochemical Modelling – the geochemical modelling assesses the reactions of the Mineral Trapping mechanism over a 10,000 year time-frame. The most significant outputs to be carried over to the geomechanical modelling below are any predicted changes to the mechanical properties of the

reservoir and the cap rock and consequently any long-term changes to the trapping and seal integrity of the Storage Complex.

4. Geomechanical Modelling – This model is based on the original static geological model but uses mechanical properties across the structure to predict movement and stress changes based on the pressure and temperature responses from the dynamic simulation of CO_2 injection. The modelling process is more fully described in Section 5.5 and uses confining blocks to establish boundary constraints both laterally and below the underburden. Specific inputs are derived from logs and from mechanical properties testing of core samples.

9.2.7 Multiple injection wells for maximum system availability

In order to maximise the injected volumes of the CO_2 generated by the White Rose OPP, high system reliability is required from the transport and storage assets. For this reason, three wells will be drilled so that during any interventions that may be required on the wells, the system can continue to operate with one well in a shut-in condition whilst the other two are available to inject at the full production rate of the power plant.

9.3 Additional Components of the field Development Plan

9.3.1 Measurement, Monitoring and Verification Plan

Proposes equipment and methodologies to assess the conformance of the Storage Complex compared to its predicted response and to monitor its confinement of the stored CO_2. It provides routine and regulatory reporting of storage volumes and regularly updates and revises performance predictions. It is divided over the phases of the project when different requirements for the verification of conformance and confinement are in effect.

9.3.2 Corrective Measures Plan

Describes the measures and actions taken to correct significant irregularities or to close leakages in order to prevent, mitigate or stop the release of CO_2 from the Storage Complex. A significant irregularity detected implies the risk of a leakage or a risk to the environment or to human health. The corrective measures plan acts, in order of priority:

- to prevent risks to human health;
- to prevent risks to the environment; and
- to prevent leakage from the storage complex.

9.3.3 Storage Site and Storage Complex Risk Assessment

Independent scientific and mathematical consultants have conducted a quantitative risk assessment of the Storage Complex.

Determines the risks associated with the underground aspects of CO_2 storage throughout the lifecycle of the White Rose CCS Project and identifies any risks that might call into question the long-term safety, integrity or the effectiveness of the Storage Complex and any risk to human health and the environment.

The results of the risk assessment provide a high level of confidence that long-term containment of the CO_2 planned to be stored will be achieved and the system will evolve to long-term stability. Risks to human health or environmental receptors associated with loss of containment (in the unlikely event that it occurs), the displacement of brine via the outcrop and deformation at the seabed are either low or very low.

9.3.4 Project Environmental Statement

Project Environmental Statement documents the results of the EIA process, highlighting environmental sensitivities, identifying potential hazards, assessing/predicting risks to the environment and identifying practical mitigation and monitoring measures. The Environmental Assessment process was initiated at an early stage in project planning and relevant information was collected relating to the natural environment and other users of the sea at or within a distance from the proposed pipeline route and surface facilities where interactions were deemed possible. It also considers, as far as possible at this time, the decommissioning of the offshore infrastructure.

10 Technology Maturation Plan

10.1 Technology Maturation Plan (TMP) Scope

At the present time, there are no technologies planned or proposed for use in the development of the Endurance Storage Complex that require maturation in order to implement the project. If, after detailed design has been completed and the various systems and components that will be used in the project have been fully specified, technologies are required that have not been proven, a technology maturation plan will be required to make those technologies ready for application during the execution phase.

Both in the characterisation of the Storage Site and in the plan for the development of the Storage Complex, technology and techniques that have been proposed by FEED have been selected because they are mature, proven and already in common use, predominantly in the oil and gas industry. If modification of equipment, applications or procedures in order to adapt mature hydrocarbon based solutions are required for their use in the White Rose Project for carbon capture and storage purposes, these requirements are expected to be very limited. Already, where the specialist requirements for the permanent storage of CO_2 exceed the capabilities or experience of the oil and gas industry's know-how, research and peer review from the CO_2 storage and enhanced oil recovery industries has been incorporated to inform the project design and implementation.

10.2 TMP Process

A TMP will use a Technology Readiness Assessment (TRA) for every element of the project that has not previously been used under the full range of expected operational conditions. A TRA is a systematic, metric based evaluation of how far a technology has developed in terms of its suitability for its purpose and applicability for its use in the project. Once the TRAs are complete, any additional input, research or development required for an element is quantified for scope schedule and costs will be compiled into the TMP.

11 References

1. Glennie, K. W. and Boergner, P. L. E.. Sole Pit Inversion Techtonics. In Illing, L.V., and Hobson, D.G., eds., Petroleum Geology of the Continental Shelf of North-west Europe: Special Publication, Institute of Petroleum, London, p. 110-120.1981.
2. Appelo, C. A. J. & Postma, D.: Geochemistry, Groundwater and Pollution, ninth ed. Balkema, Rotterdam, 2013
3. Grude, S., J. Dvorkin, A. Clark, T. Vanorio, and M. Landrø. “Pressure Effects Caused by CO_2 Injection in the Snøhvit Field.” First Break 31, no. 12 (Dec 2013).
4. Nermanrud C., Eiken O., Hensen O.R., Statoil, Bolas H.M.N., Simmenes T.H., Teige G.M.G., Hansen H., Johansen, S.: Importance of Pressure Management in CO_2 Storage, OTC23961, Offshore Technology Conference held in Houston, Texas, USA, 6-9 May 2013.
5. Bolourinejad B., and Herber R : Experimental and Modeling Study of Salt Precipitation During Injection of CO_2 Contaminated with H_2S into Depleted Gas Fields in the Northeast of Netherlands, SPE 164932, 2014.
6. Heinemann, N., Wilkinson, M., Pickup, G.E., Haszeldine, R.S. and Cutler, N.A., “CO_2 storage in the offshore UK Bunter Sandstone Formation”, International Journal of Greenhouse Gas Control, 6, pp. 210-219, (2012).
7. NORTH SEA GEOLOGY, Technical report produced for Strategic Environmental Assessment – SEA2, TR_008, BGS, Edited by Peter Balson, Andrew Butcher, Richard Holmes, Howard Johnson, Melinda Lewis, Roger Musson Drafting: Paul Henni, Sheila Jones, Paul Leppage, Jim Rayner, Graham Tuggey. Aug 2001.
8. Noy, D.J., Holloway, S., Chadwick, R.A., Williams, J.D.O., Hannis, S.A. and Lahann, R.W., “Modelling large-scale carbon dioxide injection into the Bunter Sandstone in the UK Southern North Sea”, International Journal of Greenhouse Gas Control, 9, pp. 220-233, (2012).
9. Johnson, H, Warrington, G., and Stoker, S. J.: Lithostratigraphic nomenclature of the UK North Sea, 6. Permian and Triassic of the Southern North Sea, BGS, 1994.
10. http://www.bgs.ac.uk/science/CO2/home.html
11. Bennion, D.B., and Bachu, S.: “Supercritical CO_2 and H_2S – Brine Drainage and Imbibition Relative Permeability Relationships for Intergranular Sandstones and Carbonate Formations”, SPE Paper Number 99326, 2006.
12. Wiese, B., Nimitz, M., Klatt, M. and Kühn, M., “Sensitivities of injection rates for single well CO_2 injection into saline aquifers”, Chemie der Erde – Geochemistry, 70, Suppl. 3, pp. 165-172, (2010)
13. Brook, M., Shaw, K., Vincent, C., and Holloway, S., “Gestco case study 2a-1: Storage Potential of the Bunter Sandstone in the UK sector of the southern North Sea and the adjacent area of Eastern England”, British Geological Survey commissioned report CR/03/154N, Keyworth, Nottingham, 2003.

12 Glossary

Term or Capitalisation	Meaning
AOI	Area of Interest
API	American Petroleum Institute (generally with reference to material and equipment specifications)
AUV	Autonomous underwater vehicle (free swimming submersible)
Ba	Barium
bar	Absolute Pressure
barg	Gauge Pressure
BCU	Abbreviation for Base Cretaceous Unconformity
Be	Berylium
BHP	Bottom Hole Pressure
BHT	Bottom Hole Temperature
BGS	British Geological Survey
BOP	Blow-out preventers for well control
CCS	Carbon Capture and Storage (carbon sequestration)
Ce	Cerium
Co	Cobalt
CPL	Capture Power Limited
CRA	Corrosion Resistant Alloy
CsCl	Caesium chloride
CT	Computed Tomography
CWC	Concrete Weight Coating (for offshore pipelines)
DCO	Developments Consents Order
DINO VAM	Vallourec proprietary casing connection type
Dual Packer Mini Frac Test	The Dual Packer Mini Frac Test is a pressure test using a formation tester such as a MDT to fracture the formation between two inflatable packers that isolate a small area of the formation in a well bore. The data is collected for geomechanical properties.
DVHM	Diffuse Vertical Hardground Model
E100	Blackoil ECLIPSE 100 simulator
E300	Compositional ECLIPSE 300 simulator
Electro Facies	Facies that have been generated on either raw or processed wireline logs data. Such facies are often based on reservoir quality and may not be related to sedimentological facies that have been logged from core.
EOR	Enhanced Oil Recovery
ESP	Electrical Submersible Pump
Facies	A body of rock with specified characteristics that could relate to the process of sedimentation or reservoir quality, or both.
FEED	Front End Engineering Design (a part of the competition contract)
FEP	Features, Events and Processes. A Feature that represents a component of a storage system or an Event or Process relevant to its evolution. The term includes ‘external’ FEPs or EFEPs that are part of the global system but external to the storage system; the EFEPs may however act upon the system to alter its evolution (e.g. seismic effects). Together, the FEPs of the system describe conceptual models that may be related to scenarios for system evolution
FIT	Formation Integrity Test
Forewind	Offshore wind farm operator

Term or Capitalisation	Meaning
GASSCO	Langeled pipeline operator
GEM-GHG^{TM}	A reservoir simulation by Computer Modelling Group Limited specifically designed for simulating CO_2 sequestration processes.
GM	Geomechanical models
GRV	Gross rock volume
GWC	Gas Water Contact
GR	Gamma ray
H_2S	Hydrogen Sulphide
Hardground	In the context of this application the term hardground refers to sandstone that has been cemented by pore filling cements. The reservoir quality of the hardground sandstone is very poor and it generates an acoustically faster response on sonic logs and can be recognised on seismic data.
Heterolithic	A compound facies type that comprises a range of poorer reservoir quality facies that are commonly seen together. They usually include fine-grained sandstones, silts and shales.
HMI	Human machine interface
HVDC	High voltage direct current (for offshore subsea electric power lines)
Langeled	UK – Norway gas pipeline interconnector
Lithostratigraphy	The description, definition and naming of rock units
ICP-MS	inductively-coupled plasma - mass spectrometry
ICP-OES	inductively-coupled plasma - optical emission spectrometry
IFT	Interfacial Tension
IID	Internal inspection device (intelligent pig)
II	Injectivity Index
Isochore	Depth thickness (vertical in this context)
Isochron	TWT thickness (vertical in this context)
ISSM	gamma-ray In-Situ Saturation Monitoring
KCl	Sodium Chloride (salt)
KP	Kilometre point (for the offshore pipeline)
La	Lanthanum
LAT	Lowest astronomical tide level
Layers	The intervals that subdivide a zone
LER	Local equipment room (platform)
LOT	Leak-off test
LPSA	Laser Particle Size Analysis
LTOBM	Low toxicity oil based mud (for well drilliing)
LWD	Logging while drilling equipment
MEG	Monoethylene glycol (for hydrate inhibition)
MDBRT	measured depth below rotary table (well depth reference)
MDT	The Modular Formation Dynamic Tester (MDT) is a Schlumberger wireline tool used for measuring formation pressure and collecting reservoir fluid samples.
MICP	Mercury Injection Capillary Pressure
Mis-tie	In seismic interpretation, mis-tie refers to the absolute error, in terms of two way travel time, between an interpreted seismic horizon and its associated geological pick at a well location containing a velocity function allowing depth to time transforms.
MMV plan	Measurement, Monitoring and Verification plan

Term or Capitalisation	Meaning
MSL	mean sea level
MW	Mega Watts
MT	Million tonnes
MTPA	Million tonnes per annum
Mudline	seabed (at water depth)
MWD	measurement while drilling equipment
NACE	National Association of Corrosion Engineers
NCP	Net Confining Pressure
NDE	Non-destructive testing (typically ultrasound, eddy current and radiography)
NGCL	National Grid Carbon Limited
NPV	Net pore volume
NRV	Net Rock Volume
NUI	Normally unmanned installation (offshore platform)
OBC	Ocean Bottom Cable
OD	Outside diameter (pipelines and casing)
Ooid	Small (up to 2 mm in diameter), spheroidal, layered sedimentary grains, usually composed of calcium carbonate and usually formed in shallow tropical seas.
OPP	Oxyfuel power plant
Overburden	Stratigraphic interval above the top of the reservoir.
Pc	Capillary Pressure
PD8010 Parts 1 & 2	British Standard for steel pipelines onshore and subsea
PGS	plane grating spectrometer
pH	The negative log of the activity of the hydrogen ion in an aqueous solution. Solutions with a pH less than 7 are said to be acidic and solutions with a pH greater than 7 are basic or alkaline. Pure water has a pH of 7.
Phase	The angle or lag/lead of a sine wave with respect to a reference or time zero.
PHREEQC	A computer program written in the C programming language that is designed to perform a wide variety of low-temperature aqueous geochemical calculations.
PI	Productivity Index
Polarity	If a seismic amplitude arises from a geological layer that produces an increase in acoustic impedance across it, the polarity is a function of how that seismic amplitude is displayed. By convention, positive polarity is displayed as a peak for an increase in acoustic impedance. If the signal arises from a reflection that indicates a decrease in acoustic impedance, the polarity is termed negative and is displayed as a trough.
ppg	pounds per gallon (for mud density)
PREN	Pitting resistance equivalent number (in respect of alloy quality)
PV	Pore Volume
Pr	Praseo
PRP	Phase reversal polygon is a boundary clearly seen on seismic that separates clean Bunter sandstones (within) from sands strongly affected by halite cementation (outwith). A possible explanation for this boundary is the thermo-haline convection theory that may result in salt dissolution within a limited rock volume.
PTA	Pressure Transient Analysis
rAOI	regional Area of Interest
RCA	Routine Core Analysis

Term or Capitalisation	Meaning
RFT	Repeat Formation Tool
ROV	Remotely operated vehicle (submersible).
RSFM	Regional Structural Framework Model.
SAG correction	Sag correction: a method for the determination of the effects of variable sag of a supporting element of a support system on an image of a slice of a subject.
SCAL	Special Core Analysis.
SD	Standard deviation.
SFW	Synthetic Formation Water.
SG	specific gravity.
S-Lay	Offshore pipeline installation method.
SM25CRW	Super duplex stainless steel material to specification API 5CT / ISO 11960.
SmartWind	Offshore wind farm operator.
SNS	Southern North Sea.
T&S System	Transport and storage assets of the White Rose Project.
Tartan Grid	A model grid that has a fine scale cell lateral dimensions in a rectangular core area, which become progressively coarser on the margins of that area. Visualised in plan view the grid has a tartan like appearance.
TDS	Total Dissolved Solid
THP	Tubing Head Pressure
TMP	Technology Maturation Plan
TOL	Top of liner (7" production liner)
TWT	Two way traveltime
TVDSS	Total vertical depth referenced to the depth below the MSL for wells
Underburden	Stratigraphic interval below the base of the reservoir.
UTM	Universal Transverse Mercator
UXO	Unexploded ordinance
VAM TOP (HT)	Vallourec proprietary casing connection type (high temperature rated)
Variogram	A variogram is a function that defines how data varies spatially with distance. Variograms can be isotropic, showing the same relationship in all directions, or anisotropic, where the relationship varies in the X, Y and Z directions, respectively.
Vertical Interference Test (VIT)	A vertical interference test or VIT is method of monitoring a pressure pulse created by drawdown from formation tester such as a MDT across a small interval of formation (2-11m) in a well.
V0k	A linear with depth function that that takes the form of the equation of a straight line as in Vi=V0+k(z). This equation states that the instantaneous velocity (Vi) increases linearly with depth (z) where V0 is a constant related to the velocity at the start of a particular layer in the velocity model and k is an acceleration term that describes the compaction of the rock interval depth.
WD	Water depth
WIIP	Water Initially in Place
WHT	Wireline Head Thermometer
WWII	The Second World War (1939-1945)
Xline	(cross-line) a seismic line within a 3D survey orthogonal to the direction in which the data was acquired
Zone	The thickness interval between stratigraphically defined horizons

13 Appendix A

13.1 CO_2 COMPOSITION SPECIFICATION

13.1.1 Entry Requirements

The CO_2 pipeline transportation system entry requirements have been defined by NGCL and are set out in the NGCL Specification for Carbon Dioxide Quality Requirements for Pipeline Transportation NGC/SP/PIP/25. The composition Safe Operating Limit (SOL) is a saturation pressure for the CO_2 rich mixture of no more than 80barg along with the individual maximum allowable component levels defined in NGC/SP/PIP/25. A summary of the specification is shown in Table 13.1 for information. The entry specification provides the permitted limits for each component relative to safety design, integrity design and hydraulic efficiency criteria.

Table 13.1: CO_2 Export System Entry Requirements

	Limiting Criterion % Vol		
Component	**Safety Max**	**Integrity Max**	**Hydraulic Efficiency**
CO_2	100	100	96
H_2S	0	0.002[Note 1]	0
CO	0.2	0	0
NO_X	0.01	0	0
SO_X	0.01	0	0
N_2	0	0	[Note 4]
O_2	0	0.001 [Note 3]	[Note 4]
H_2	0	0	[Note 4]
Ar	0	0	[Note 4]
CH_4	0	0	[Note 4]
H_2O	0	0.005[Note 2]	0

Notes:

(1) NACE limit for dense phase CO_2 at a total pressure of 150barg (specified to avoid requirement for sour service materials)

(2) Maximum water content (50 ppmv). Specified to ensure no free water occurs during normal or transient operations.

(3) Maximum oxygen content (10 ppmv). Specified to avoid material selection issues in the well tubing where the dry CO_2 contacts saline aquifer water

(4) The allowable mixture of non-condensable components in the CO_2 stream must be:

Gaseous Phase: $N_2 + O_2 + H_2 + CH_4 + Ar \leq 9.0\%$

Dense Phase: $N_2 + O_2 + H_2 + CH_4 + Ar \leq 4.0\%$, with H_2 no greater than 2.0%

13.1.2 CO_2 Design Composition Range

The entry specification provides a range of acceptable compositions for material selection but does not specify a definitive First Load composition for flow assurance modelling or equipment sizing. A generic oxyfuel capture CO_2 composition has been defined which has been normalised for the removal of oxygen. This composition is shown in Table 13.2. It is expected however that the CO_2 stream from the First Load will contain 99.7% CO_2 and will contain up to 10 ppmv of oxygen.

Table 13.2: Generic CO_2 Composition

Component	Volume %
Carbon dioxide	97.4%
Argon	0.6%
Nitrogen	2.0%
	100.0%

13.2 Pure CO_2 Properties

Pure CO_2 physical properties are summarised below (Table 13.3):

Table 13.3: Pure CO_2 Physical Properties

Property	Value	Units
Molecular Weight	44.01	-
Critical Temperature	31.1	C
Critical Pressure	73.9	Bara
Critical Density	467	kg/m^3
Triple Point Temperature	-56.5	°C
Triple Point Pressure	5.18	Bar
Boiling (sublimation) point (1 atm)	-78.5	°C